

IRE Transactions in Microwave Theory and Techniques



Volume MTT-6

APRIL, 1958

Number 2

In This Issue

Frontispiece	page 130
Guest Editorial	page 131
Contributions	page 133
Correspondence	page 238
Call for WESCON Papers	page 239
1958 National Symposium Program	page 240
Contributors	page 242

TK7800
I23

For complete Table of Contents, see page 129.

PUBLISHED BY THE

Professional Group on Microwave Theory and Techniques

IRE PROFESSIONAL GROUP ON MICROWAVE THEORY AND TECHNIQUES

The Professional Group on Microwave Theory and Techniques is an association of IRE members with professional interest in the field of Microwave Theory and Techniques. All IRE members are eligible for membership and will receive all Group publications upon payment of the prescribed annual fee of \$3.00. Members of the American Physical Society and the Institution of Electrical Engineers of Great Britain may become affiliated with PGM TT and receive all Group publications upon payment of the Affiliate fee of \$7.50 per year.

Administrative Committee

Chairman

W. L. PRITCHARD

Vice-Chairman

T. S. SAAD

Secretary-Treasurer

P. D. STRUM

T. N. ANDERSON

R. E. BEAM

A. C. BECK

A. G. CLAVIER

S. B. COHN

C. W. CURTIS

H. F. ENGELMANN

HENRY MAGNUSKI

W. W. MUMFORD

A. A. OLINER

S. D. ROBERTSON

R. F. SCHWARTZ

GEORGE SINCLAIR

G. C. SOUTHWORTH

KIYO TOMIYASU

ERNEST WANTUCH

H. A. WHEELER

PGMTT Chapters

Albuquerque-Los Alamos

Baltimore

Boston

Buffalo-Niagara

Chicago

Denver

Long Island

Los Angeles

H. D. Finch

W. R. Hom

P. D. Strum

Robert E. Kell

Edward Dervishian

M. C. Thompson, Jr.

Henry Jasik

Dean B. Anderson

New York

Northern New Jersey

Philadelphia

San Diego

San Francisco

Schenectady

Syracuse

Washington

Saul W. Rosenthal

Nat Evans

E. J. Forbes

J. B. Smyth

W. H. Thon

T. R. Bristol

W. T. Whistler

Gustave Shapiro

IRE TRANSACTIONS® on Microwave Theory and Techniques

Published by the Institute of Radio Engineers, Inc., for the Professional Group on Microwave Theory and Techniques, at 1 East 79th Street, New York 21, New York. Responsibility for the contents rests upon the authors, and not upon the IRE, the Group, or its members. Price per copy: IRE PGM TT members, \$2.50; IRE members, \$3.75, nonmembers, \$7.50. Annual subscription price: IRE members, \$8.50; colleges and public libraries, \$12.75; nonmembers, \$17.00.

Address all manuscripts to K. Tomiyasu, PGM TT Editor, General Electric Microwave Laboratory, 601 California Ave., Palo Alto, Calif. Submission of three copies of manuscripts, including figures, will expedite the review.

COPYRIGHT ©1958—THE INSTITUTE OF RADIO ENGINEERS, INC.

All rights, including translations, are reserved by the IRE. Requests for republication privileges should be addressed to the Institute of Radio Engineers, 1 E. 79th St., New York 21, N.Y.

IRE Transactions

on

Microwave Theory and Techniques

Published by the Professional Group on Microwave Theory and Techniques

Volume MTT-6

APRIL, 1958

Number 2

TABLE OF CONTENTS

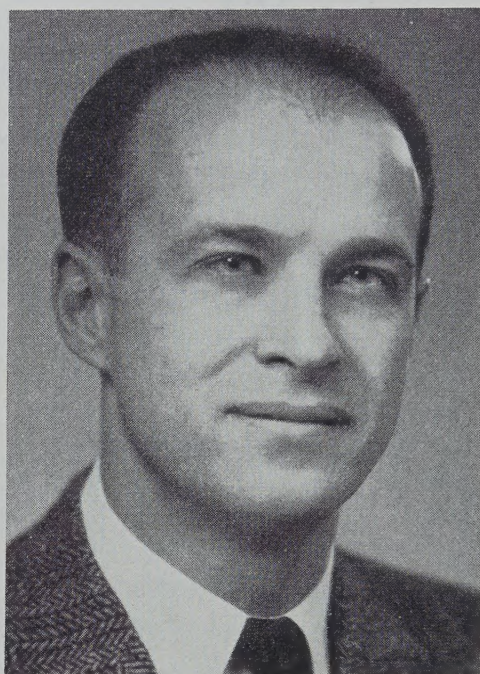
Frontispiece	Nathan Marcuvitz	130
Academic Research Institutes in the Microwave Field	Nathan Marcuvitz	131

CONTRIBUTIONS

A Wide-Band Double-Vane Torque-Operated Wattmeter for 3-cm Microwaves	A. L. Cullen, B. Rogal, and S. Okamura	133
Traveling-Wave Resonators	L. J. Milosevic and R. Vautey	136
Reflection Coefficient of <i>E</i> -Plane Tapered Waveguides	Katsu Matsumaru	143
Propagation in Ferrite-Filled Microstrip	Morris E. Brodwin	150
An Improved Method for the Determination of <i>Q</i> of Cavity Resonators	Amarjit Singh	155
Characteristic Impedances of the Slotted Coaxial Line	Jadwiga Smolarska	161
Velocity Modulation of Electromagnetic Waves	Frederic R. Morgenthaler	167
Heat Loss of Circular Electric Waves in Helix Waveguides	J. A. Morrison	173
The Expansions of Electromagnetic Fields in Cavities	Kaneyuki Kurokawa	178
Broad-Band Calorimeters for the Measurement of Low and Medium Level Microwave Power. I. Analysis and Design	M. Sucher and H. J. Carlin	188
Broad-Band Calorimeters for the Measurement of Low and Medium Level Microwave Power. II. Construction and Performance	A. V. James and L. O. Sweet	195
Amplitude Stabilization of a Microwave Signal Source	Glenn F. Engen	202
A Simple Artificial Anisotropic Dielectric Medium	R. E. Collin	206
Calculation and Measurement of the Noise Figure of a Maser Amplifier	J. C. Helmer and M. W. Muller	210
Propagation in Dielectric Slab Loaded Rectangular Waveguide	P. H. Vartanian, W. P. Ayres, and A. L. Helgesson	215
Parallel-Coupled Transmission-Line-Resonator Filters	Seymour B. Cohn	223
A New Class of Broad-Band Microwave 90-Degree Phase Shifters	B. M. Schiffman	232

CORRESPONDENCE

Fourier Transforms and Directional Couplers	Samuel Sensiper	238
Analysis of the Variable-Ratio Microwave Power Divider	R. M. Vaillancourt	238
Call for WESCON Papers		239
1958 National Symposium Program		240
Contributors		242



N. Marcuvitz

Nathan Marcuvitz was born on December 29, 1913, in New York, N. Y. In 1935 he received the Bachelor's degree in electrical engineering from the Polytechnic Institute of Brooklyn, where he remained as a graduate fellow until 1936. At this time, he joined the RCA Laboratories as a student engineer and subsequently did advanced development work on electron tubes, iconoscopes, and orthicons for television applications. He returned to the Polytechnic Institute of Brooklyn in 1940, where he received the Master's degree in 1941.

He joined the Radiation Laboratory, Massachusetts Institute of Technology, in December, 1941, where he worked on microwaves until 1946.

Returning to the Polytechnic Institute of Brooklyn as an assistant professor in the Department of Electrical Engineering, he completed the requirements for the doctorate in electrophysics in 1947. He was made associate professor in 1949, professor in 1952, and since 1957 has been the director of the Microwave Research Institute.

He edited the "Waveguide Handbook," Volume 10 of the M.I.T. Radiation Laboratory Series, published in 1951 by McGraw-Hill Book Company, Inc.

Dr. Marcuvitz is a Fellow of the IRE, a member of the American Physical Society, Tau Beta Pi, Eta Kappa Nu, and Sigma Xi.

Academic Research Institutes in the Microwave Field

NATHAN MARCUVITZ*

SINCE World War II, large research institutes have burgeoned forth on the campuses of many colleges and universities throughout the United States. Fulfilling at their inception a national need in time of crisis, they have continued in these less critical times to contribute importantly to the national research program. Their impact on academic curricula has been varied but no less important. The effective increase in faculty provided by academic research institutes is permitting the expansion of graduate course programs into ever widening areas of science and engineering in a manner responsive to contemporary scientific and technical developments. Expanded curricula and research facilities make it possible for students in increasing numbers to enter into research programs that attempt to prepare them realistically for the demands our technological society imposes upon them. Despite these evident advantages, research institutes have yet to find a truly permanent place in the academic structure. Financial difficulties, together with related problems of securing balance between research and academic obligations, characterize this paradoxical situation. Since these points bear strongly on the question of the proper utilization of our national scientific and engineering potential, let us examine the role academic research institutes can play on the educational scene with particular stress, by example, on those in the microwave field.

Recent public emphasis on the need for expansion and intensification of our general educational program from the secondary to the graduate school level does not place in proper perspective the influence of such expansion on basic research in this country. For however great is the need for more graduate scientists and engineers, equally great is the need for that specialized and quite small echelon of graduates upon whom falls the disproportionate burden of the exploratory research on which future engineering applications depend. The problem of insuring a properly qualified national supply of scientists and engineers does not necessarily reflect the problems peculiar to the needs of the research minded group with which we are concerned herein. A balanced national educational program demands the separate consideration and solution of the distinct problems involved in the two categories.

Academic research institutes influence mostly the development of the "upper segment" of graduate scientists and engineers, although they are not without influence on the entire body of students and faculty. The staff at such institutes is primarily composed of an admixture

of research scientists and engineers who allocate their time in varying degrees to teaching and research. Such institutes should tend to supplement (but not replace) the classic type of departmental research involving a key professor plus a small group of graduate students. Because of the greater facilities and staff concentrated at research institutes, a broad spectrum of interdepartmental research programs is made available to a large number of graduate students and faculty. The unusual opportunities thereby provided for training and contributing to significant research programs, can and should be incorporated as an integral part of a graduate curriculum. If this potential for creative effort resident in academic research institutes is to be properly exploited, their flexibility of operation should not be hamstrung by an inadequate budget and by their involvement in programs indistinguishable from those in industrial research laboratories.

Since the cost for the training of graduate students is many times higher than for undergraduates, the additional maintenance of research institutes, which appear to be a necessary adjunct of every major graduate school, imposes financial burdens on tuition supported private colleges that are almost impossible to carry without outside cooperation. Up to the present, government sponsorship has been, for the most part, the financial mainstay of this type of academic research activity, but the vagaries of annual congressional budgets impart an aura of uncertainty to this source of research funds. This uncertainty has, in turn, not proven beneficial to the morale and program of academic research staffs. It is to be hoped that the recent re-evaluation of government sponsorship of basic research will result in a policy more conducive to the development of the academic potential in this area.

Consideration of the question of government sponsored research must, of course, include both academic and industrial research. Since the term research has begun to cover an ever widening spectrum of activities, it is of interest to contrast differences in the nature of university and industrial research programs that stem from different motivations. The primary goal of academic research is the pursuit of programs of broad exploratory research that conforms with the basic academic obligation of training scientists. Research in industrial organizations, on the other hand, usually has specific, economically motivated, technological goals. This does not imply an absence of exploratory research; in fact, some industrial organizations engage in fundamental research programs of which any university could well be proud. However, differences in motivation do exist and these should be properly exploited in the

* Director, Microwave Research Institute, Polytechnic Institute of Brooklyn, Brooklyn, N. Y.

national interest by means of academic and industrial programs that complement rather than duplicate one another. This demands a government policy that with proper balance effectively utilizes the potentialities of those programs of academic and industrial research whose development appears indispensable for the healthy growth of our national economy vis-à-vis that of other nations. This, in turn, demands distinct fiscal policies for application to university as against industrial research. The nature of an academic research operation is such that long-term repercussions are created by budgetary changes that would have little influence on an industrial operation.

Not unrelated to the fiscal problem is the nature of the research programs at some existing academic research institutes. For, in order to maintain an effective staff under the present fiscal support structure, contractual obligations are assumed which often run counter to what is considered as proper academic research. Resulting pressures to "produce" and to obtain contracts involve the research faculty in time consuming efforts that inhibit the full utilization of its abilities and talents. This involvement is tolerated only because of the conviction that a research effort is a vital part of a graduate academic program and by the pious hope that some of the defects of the present academic research structure will ultimately be remedied. Hoped for remedies would provide long-term funding on a broad exploratory basis for at least 50 per cent of the total budget of a research institute. This would assure, certainly in the applied science field, the desired flexibility and stability for the development of research programs in keeping with the basic academic obligation of training graduate scientists and engineers. If such programs were carried out on a national scale, it should be possible to insure at key academic institutions throughout the country the existence of centers engaged in specialized and high-level research programs as an integral part of academic activity.

Academic research centers should have a varied nature dependent on the scientific manpower capabilities of specific institutions. Some should be devoted to basic research in the fundamental and classic meaning of the term; others, such as research institutes at engineering colleges, should be devoted to broad spectrum research characteristic of the applied sciences. In the latter category belong the academic research institutes in the microwave field. From these we shall attempt to choose, by way of illustration, a few typical research programs that provide possibilities for graduate training and significant scientific contributions and are, as well, a desirable supplement to related industrial efforts.

About 15 years ago, technical advances in the rapidly growing microwave field created a need for development

of a network theory utilizing distributed and lumped circuit elements more general than the then familiar inductance, capacitance, and resistance elements so effectively employed at the lower frequencies. Under wartime pressure, academic research contributed to a microwave network and mode theoretic viewpoint that conditioned the thinking of microwave engineers and provided valuable assistance to the development of microwave components for numerous radar systems.

At the present time, the advent of novel anisotropic microwave devices incorporating ferrites, plasmas, and other electron beam loaded waveguides is lending impetus to the creation of more general network and fundamental physical viewpoints to provide a corresponding service for present-day microwave engineers. High speed rockets and missiles have given great technical importance to flush mounted "open waveguide" structures of the surface and leaky wave type. Here too, there is room for the development of network techniques for the quantitative description of interacting radiative discontinuity elements, in order to provide stimulation for future applications. Continuing technological penetration into the millimeter part of the electromagnetic spectrum is bringing forth fundamental problems that demand facile multimode network or quasi-optic theories for the quantitative understanding of wave phenomena in this range. Recently developed semiconductor and other solid state structures have placed new classes of active and nonreciprocal microwave network elements at the disposal of microwave engineers. This added versatility creates new horizons for theories in analysis and synthesis of distributed electromagnetic structures.

Of a somewhat different character is the need for broad interdepartmental programs to exploit magnetic resonance and other microwave spectroscopic techniques that promise to yield not only important technological applications, but also useful information at molecular and cellular levels in the fields of biophysics, physics, and physical chemistry. One can continue along these lines but the above are exemplary of a few of the programs that can and are being pursued at academic research institutes in the microwave field.

In summary, it is evident that we have tried to state the case for the establishment and financing of academic research institutes as an integral feature of a graduate school activity. At present, the research viewpoint is an unintegrated supplementary activity frequently hampered by inadequate and academically unbalanced contractual arrangements. If basic research at academic institutions is to be regarded as vital to our national economy, it ought to be effectively utilized by government and industry to permit the realization of its full potential.



A Wide-Band Double-Vane Torque-Operated Wattmeter for 3-CM Microwaves*

A. L. CULLEN†, B. ROGAL‡, AND S. OKAMURA§

Summary—This paper describes a torque-operated wattmeter for waveguide, capable of measuring power in the range of 10 to 200 watts in the wavelength range 3.05–3.45 cm, with an accuracy of about 2 per cent over most of the wave band.

The instrument is an absolute standard since its calibration depends only on measurements of mass, length, and time. Negligible power is absorbed, and the instrument is insensitive to mismatch.

INTRODUCTION

In an earlier paper¹ a torque-operated wattmeter for 3-cm microwaves has been described, and it has been shown that an accuracy of about 1½ per cent can be obtained with the instrument when working into an accurately matched load.

The present instrument has been designed to operate satisfactorily over a wider band of frequencies, and in addition its sensitivity to mismatch is greatly reduced.

CONSTRUCTION

The general arrangement of the instrument is shown in Figs. 1 and 2. The wattmeter consists essentially of a short vertical section *A* of waveguide, connected by *E*-plane bends to horizontal input and output sections, and containing a movable element. The latter consists of a glass tube *B* to which two thin metal vanes are attached. The vanes are separated by one quarter guide wavelength at the midband frequency. A small mirror fixed to the lower end of the glass tube is used in conjunction with a lamp and scale to indicate the angular position of the movable element.

The movement carries also a locking cone used to clamp the suspension by means of the lever *E*, when the instrument is not in use. The lower end of the suspension dips into a dashpot containing silicone oil, thus ensuring "dead-beat" response.

The movement is suspended by a 15-micron-diameter quartz fiber *C* from a vertical shaft *D*.

The shaft *D* is held by a collet in the extension mounted in the center of the shaft of the driven wheel of the worm gearing associated with a slow motion drive.

Two dials and a vernier indicate the angular position of the shaft *D*.

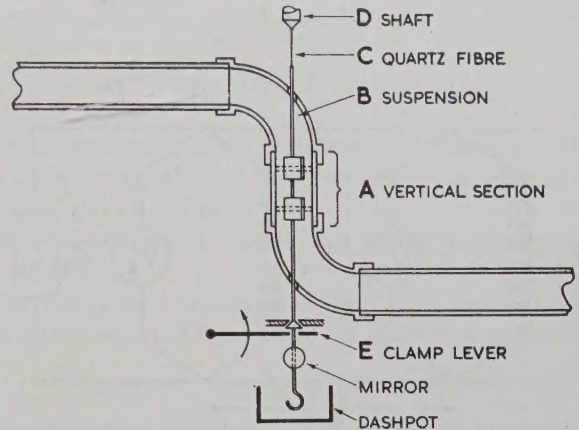


Fig. 1—Construction of the wattmeter.

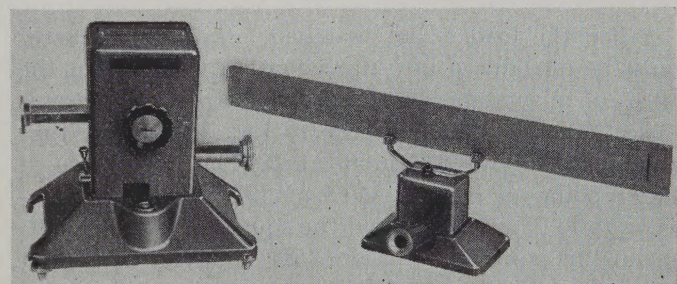


Fig. 2—X-Band wattmeter and scale.

The ends of the horizontal guides are blocked with half guide wavelengths of expanded polythene to screen the vanes from draughts. The base of the wattmeter rests on three leveling screws, and a spirit level is built into the base.

PRINCIPLE OF OPERATION

When microwave power flows through the waveguide, the associated electric field produces a torque tending to rotate the vanes into line with the unperturbed electric field. The torque produced is proportional to the square of the electric field strength magnitude, and hence to the power flow. The resulting deflection of the movement is compensated by turning the torsion head. The angle through which the torsion head must be returned to restore the vane to its initial position is therefore a measure of the microwave power.

A transmission line analog shown in Fig. 3 is helpful in understanding the action of the instrument. Each vane acts like an electrostatic voltmeter connected across a transmission line. The inductive diaphragms

* Manuscript received by the PGMTT, October 1, 1956; revised manuscript received, July 26, 1957.

† University of Sheffield, England.

‡ Wayne-Kerr Labs., Surrey, England.

§ University of Tokyo, Japan.

¹ A. L. Cullen and I. M. Stephenson, "A torque-operated wattmeter for 3 cm microwaves," *Proc. IEE*, vol. 99, pt. 4, p. 294; July, 1952.

shown in Fig. 1 are equivalent to inductances shunted across the electrostatic voltmeters and so chosen as to cancel their capacitive reactances so that the resultant impedance of each shunt is infinite. There is then no discontinuity in the line.

When the load into which the wattmeter works is matched, the relationship between torque and power can be written

$$T = KP. \quad (1)$$

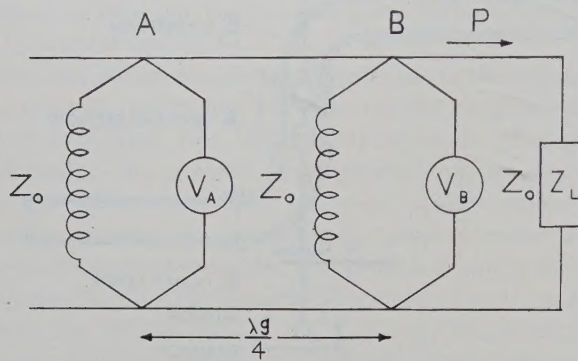


Fig. 3—Equivalent circuit of wattmeter.

When the load is not matched, a correction factor must be introduced into this equation to allow for the effect of mismatch. The mismatch correction factor is easily deduced with reference to Fig. 3. Suppose that there is a voltage minimum at *B*. The impedance at such a point will be $Z_0 \cdot s$, where *s* is the voltage standing-wave ratio (V_{\min}/V_{\max}), and the square of the rms voltage at this point will be $V_B^2 = PZ_0 \cdot s$ where *P* is the net power flow. Because of the quarter-wave separation between *A* and *B*, there will be a voltage maximum at *A* and the square of the voltage at *A* will be $V_A^2 = PZ_0/s$. In the actual wattmeter, the total torque is equal to the sum of the torques on the individual vanes, that is, to $V_A^2 + V_B^2$ in the analog. Hence, the torque is given by

$$T = \frac{1}{2} \left(s + \frac{1}{s} \right) KP. \quad (2)$$

The constant *K* is the electrical calibration constant introduced in (1).

Thus, the mismatch correction factor is

$$F = \frac{1}{2} \left(s + \frac{1}{s} \right). \quad (3)$$

A fuller analysis shows that this factor is valid for any position of the standing-wave pattern. Since $F \geq 1$, the sensitivity of the instrument is increased slightly by mismatch. If $s > 0.9$ the increase is less than $\frac{1}{2}$ per cent.

A single-vane wattmeter may be in error by as much as ± 10 per cent under the same conditions depending on the position of the standing-wave pattern, if no mismatch correction is made.

The correction factor

$$\frac{1}{2} \left(s + \frac{1}{s} \right)$$

for the double-vane instrument is strictly valid only at the design wavelength. At other wavelengths the mismatch correction becomes

$$\frac{1}{2} \left(\frac{1}{s} + s \right) \pm \frac{1}{2} \left(\frac{1}{s} - s \right) \cos \phi \cos \beta l. \quad (4)$$

In this expression ϕ is the phase angle of the reflection coefficient of the load which determines the position of the standing wave relative to the vanes, β is the waveguide phase constant $2\pi/\lambda g$, and *l* is the separation between the centers of the vanes. If, as is often the case, the position of the standing-wave pattern is not known the mismatch correction is uncertain. The limiting values of the mismatch correction factor are

$$\frac{1}{2} \left(\frac{1}{s} + s \right) \pm \frac{1}{2} \left(\frac{1}{s} - s \right) \cos \beta l. \quad (5)$$

The percentage error arising from the second term of (5) depends on the wavelength and on the standing-wave ratio. At 3.3 cm, for example, there is a possible error of ± 1 per cent if $s = 0.9$, or $\pm \frac{1}{2}$ per cent if $s = 0.95$, the design wavelength being 3.20 cm.

CALIBRATION

The calibration of the instrument involves two separate stages.

The first stage is the electrical calibration in which the constant *K* is determined. This constant is equal to the torque per unit power for a matched load. The second stage is the mechanical calibration in which the angular deflection of the movement per unit torque is obtained.

Electrical Calibration

The electrical calibration is obtained from measurements made with a low-power waveguide test bench.

The calibration procedure and its theoretical basis have been dealt with in detail elsewhere² and it is beyond the scope of the present paper to do more than to draw attention to the following points:

- 1) The procedure is still valid if magnetic as well as electrical fields make a significant contribution to the torque.
- 2) Only length (and angle) measurements are involved. No electrical power standards of any kind are involved.
- 3) Any mismatch introduced by the wattmeter in the input guide does not affect the calibration though for functional reasons such mismatch is kept as small as possible.

² A. L. Cullen, "A general method for the absolute measurements of microwave power," *Proc. IEE*, vol. 99, pt. 4, p. 112; February, 1952.

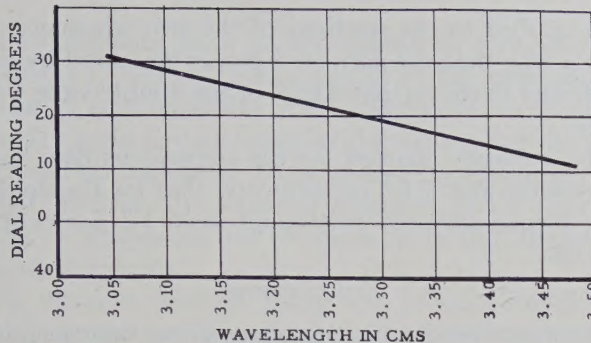


Fig. 4—Matching angle vs wavelength.

4) The constant K is a function of θ , the angular position of the movement and of wavelength.

The calibration procedure must be carried out at a sufficient number of wavelengths in the wave band required to enable a smooth curve of K against λ to be drawn.

The optimum value of θ for best match (the matching angle) is also plotted as a function of wavelength.

Mechanical Calibration

The mechanical calibration consists essentially in determining the specific couple of the quartz fiber suspension. This is done most conveniently by timing torsional oscillations when several rods of known moments of inertia are attached in turn to the movement. If k is the specific couple, the static deflection θ_0 of the movement under the influence of a steady torque T is given by

$$\theta_0 = \frac{T}{k}. \quad (6)$$

This is also the angle through which the torsion head must be turned to restore the movement to its initial position.

The determination of k has involved measurements of mass, length, and time only. Once again, no measurement of power is involved.

Over-All Calibration

Combining (1) and (6), we have the following relationship between torsion-head rotation and power when the load is matched:

$$P = K'\theta_0 \quad (7)$$

where $K' = k/K$.

Eq. (7) is the basic equation of the instrument. The constant K' has the dimensions watts/degree if the angle θ_0 is measured in degrees.

Typical Calibration

Two experimentally determined curves are required for using the double-vane wattmeter. The first is a plot of matching angle against wavelength and for a typical instrument takes the form shown in Fig. 4.

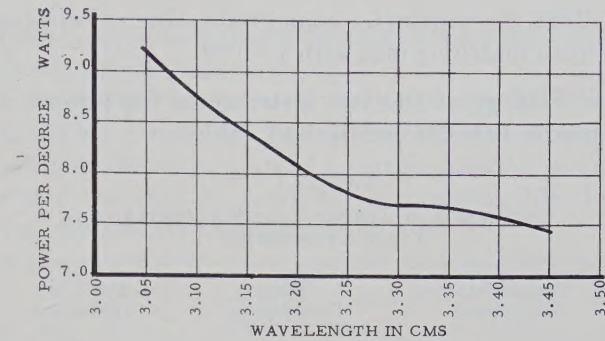


Fig. 5—Power calibration

The second curve gives the power per degree as a function of wavelength and for the same instrument has the form shown in Fig. 5.

The calibration is carried out individually for each instrument.

The errors do not exceed 0.4 per cent for mechanical calibration and 0.25 per cent for electrical calibration.

SPECIFICATION AND PERFORMANCE

The wattmeter will measure power in the range of 10–200 watts. If the source is pulsed, it will measure mean power but the peak power should not exceed about 50 kw.

The mismatch produced by the wattmeter is small, not falling below 0.9 in the band 3.05–3.45 cm. The power lost in the instrument is around 2.5 per cent; it stays relatively constant over the band (to within 0.2 per cent) and compares with about 1.5 per cent loss of power in the same length of normal guide. When making precise measurements this loss has to be taken into consideration as shown later in comparison measurements against a water calorimeter.

The over-all accuracy of the wattmeter is as follows:

in the band	3.10	to 3.35 cm	±2 per cent
	3.05	to 3.10 cm	±3 per cent
	3.35	to 3.45 cm	±3 per cent.

COMPARISON WITH WATER CALORIMETER

Tests have been carried out in which the power of a cw magnetron was measured simultaneously by the torque-vane wattmeter and by a water-calorimeter wattmeter, the latter acting as a termination.

The comparison was carried out at a wavelength of 3.26 cm, the magnetron being capable of maximum output of 10 watts. A continuous flow water calorimeter was used, consisting of a thin pyrex-glass tube extending across the waveguide at a narrow angle in a plane parallel to the broad face. The power was measured in terms of the equivalent mains-frequency power required in an auxiliary heater coil to produce a rise in temperature (about 0.5°C) identical with that due to microwave power.

Two sets of readings were taken as follows:

- 1) With the wattmeter connected directly to the calorimeter with $s = 0.92$.

2) With the wattmeter connected to the calorimeter via a matching unit with $s = 0.99$.

The readings of the two instruments for powers in the range 8-10 watts are given in Table I.

TABLE I

COMPARISON OF TORQUE-VANE WATTMETER AND WATER CALORIMETER

Torque-Vane Wattmeter	Water Calorimeter	Per Cent Difference
1) $s = 0.92$		
9.02 watts	8.89 watts	+1.46
8.94	8.84	+1.13
9.65	9.48	+1.80
9.17	8.85	+3.60
9.10	8.84	+2.94
9.19	9.06	+1.44
Average difference between the two instruments 2.1 per cent.		
2) $s = 0.99$		
9.10 watts	8.97 watts	+1.4
9.02	8.92	+1.1
8.98	8.85	+1.5
9.34	9.33	+0.1
8.94	8.87	+0.8
9.02	8.82	+2.3
Average difference between the two instruments 1.2 per cent.		

These results have been corrected to allow for the measured attenuation in the connecting waveguide. Furthermore, in case 1) above, the wattmeter readings have been corrected for mismatch using (3), and in case 2) above the small loss of power in the matching transformer has been taken into account.

Since the attenuation through the double-vane wattmeter was 2.4 per cent (measured value) a figure of 1.2 per cent was used in estimating the power loss between the vanes and the output flange. All corrections have

been applied to the readings of the two wattmeters in such a way that the corrected power measured by each is referred to the output flange of the double-vane wattmeter.

The accuracy claimed for the continuous flow water calorimeter was ± 1.5 per cent and that for the double-vane torque-operated wattmeter was ± 2 per cent at 3.26 cm.

CONCLUSION

The work described in this paper shows that the initial aim of designing a wide-band torque-operated microwave wattmeter has been achieved. The accuracy claimed has been verified by comparison with the best water calorimeter wattmeter available.

The instrument is an absolute standard of power in the microwave band.

ACKNOWLEDGMENT

The authors wish to express their gratitude to Prof. H. M. Barlow for placing at their disposal laboratory facilities of the Electrical Engineering Department of University College, London, in the early stages of development, and for his interest and encouragement in the work. They thank members of the staff of the Wayne-Kerr Laboratories for help in the design of the instrument. Also, they are grateful to the Director of the Radio Research Station of the Department of Scientific and Industrial Research for providing facilities for comparison of the double-vane wattmeter with a water calorimeter wattmeter and to J. Lane for his invaluable assistance in this part of the work. Finally, author S. Okamura is indebted to the British Council for a scholarship which made his part in the work possible.

Traveling-Wave Resonators*

L. J. MILOSEVIC† AND R. VAUTEY†

Summary—In the first part of the paper, the principles are given which have led to the conception of the traveling-wave resonator, and the calculations enabling its operation to be understood are presented.

The second part describes the apparatus in detail and examines it, bearing in mind its use as high-power testing equipment.

* Manuscript received by the PGM TT, March 26, 1957; revised manuscript received, December 2, 1957.

† Groupe Électronique, Compagnie Française Thomson-Houston, Paris 8, France.

PART I—PRINCIPLE OF OPERATION

INTRODUCTION

THE testing of the power-handling capacity of a microwave transmitter and associated circuit, at far more severe conditions than the nominal ones, has always been considered a very difficult problem for which no valuable solution had been found until the present time.

Two solutions have been proposed to overcome this problem: 1) testing of waveguides at low pressure and 2) testing of waveguides in standing wave. In this case, special hybrid circuits¹ are used for decoupling the magnetron from the circuit to be tested. By means of "cascaded" hybrids the value of apparent power in waveguide is multiplied by 2^n where n is the number of cascaded hybrids.

In the first method, using low pressure conditions, there is no exact relationship between testing and operating conditions. This is due to the fact that the value of breakdown voltage depends upon the nature, pressure, and ionization of the gas, as well as upon the pulse length and repetition rate.

In the second method, using hybrids, the circuit to be tested is placed within the voltage loop of the standing wave. When testing a component, the terminal shorting plunger is moved along $\lambda_g/2$ (where λ_g is the wavelength inside the waveguide) to make sure that every part of the component has actually been subjected to the maximum voltage. In fact, this method suffers from two obvious drawbacks:

- 1) It is necessary to check voltage handling capacity for each part of the component by moving the shorting plunger, which will increase considerably the duration of test. Furthermore, in the case of intricate components there is still considerable doubt as to the exact value of breakdown voltage.
- 2) The hybrid circuit increases the test voltage by a $\sqrt{2}$ ratio only. For higher test voltages, the number of hybrids should be increased. This is rather difficult because of the larger number of adjustments required.

PRINCIPLES OF OPERATION IN THE PROPOSED METHOD

Circuit Using a Hybrid Circuit

A microwave feedback circuit using a hybrid circuit, shown in Fig. 1, has been proposed for use on an electron accelerator.²

In this circuit, the transmitter feeds into leg 3 of the hybrid. Incident energy is divided between legs 1 and 2. Leg 1 is connected to a matched load. Leg 2 loops up through waveguide A on to leg 4. The power transmitted along leg 2 is reinjected, therefore, into the hybrid circuit through leg 4. This power is divided between legs 1 and 2 and the process is repeated indefinitely. Leg 3 (transmitter) is decoupled from leg 4 (reinjection) so that the standing-wave ratio, looking from the trans-

mitter, depends upon the hybrid circuit matching conditions and the load on leg 1.

The proper adjustment of the phases, so that the reinjected power will add to the incident power, will result in the storing up of a certain amount of energy within the ring A . Assuming zero attenuation in the ring, the relative voltage level is

$$\frac{1}{(\sqrt{2} - 1)} \approx 2.42.$$

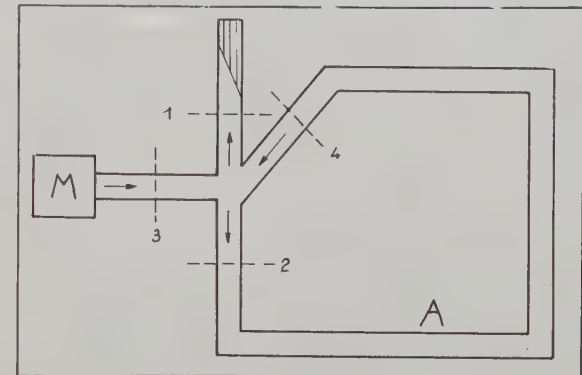


Fig. 1—Microwave feedback circuit.

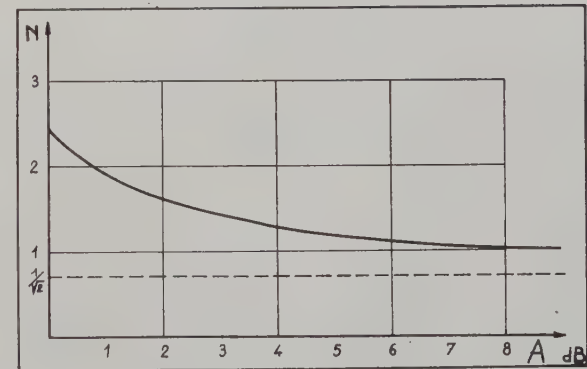


Fig. 2—Overvoltage in the traveling-wave resonator using a hybrid circuit (or a 3-db directional coupler) vs ring attenuation.

For example, with an incident power of 1 mw, the apparent power within the resonator will be

$$1 \text{ mw} \times (2.42)^2 = 5.85 \text{ mw.}$$

When assuming losses equal to A db, the over-voltage coefficient N is given as

$$N = \frac{1}{\sqrt{2} - e^{-\alpha}} \quad \text{with} \quad e^{-\alpha} = 10^{A/20}.$$

The curve showing variation of N vs attenuation is shown in Fig. 2.

For easily obtained attenuation values, the overvoltage is slightly greater than 2, but this value, in many cases, is not sufficiently large.

It has proven possible to get higher overvoltage values by modifying the preceding circuit. This has

¹ L. Young, "A hybrid-ring method of simulating higher powers than are available in waveguides," PROC. IEE, vol. 101, pt. III, pp. 189-190; May, 1954.

² C. W. Miller, "The design of linear accelerators for X-ray therapy," *Metropolitan Vickers Gazette*, pp. 121-125; December, 1953.

been performed by replacing the hybrid circuit with a directional coupler. The coupling coefficient is adjusted according to the ring attenuation. Thus, the system incorporating a hybrid circuit is now a special case in this more general system.

Circuit of Traveling-Wave Resonator Using a Directional Coupler

Two types of circuits might be proposed, as shown in Fig. 3 and Fig. 4. Maximum N values are identical for both circuits, but the values of optimum coupling coefficient differ in each case.

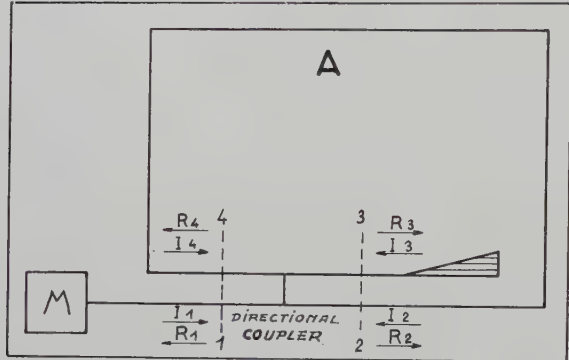


Fig. 3—Microwave feedback circuit with directional coupler—circuit I.

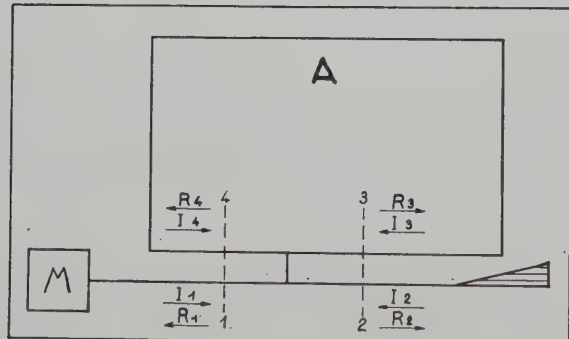


Fig. 4—Microwave feedback circuit with directional coupler—circuit II.

The two circuits in Fig. 3 and Fig. 4 are not grossly different. They could be compared to a conventional resonator connected to a transmission line where the terminals are planes 1 and 3 in Fig. 3, or planes 1 and 2 in Fig. 4.

It is easy to deduce the properties of Fig. 3 from Fig. 4 by inverting planes 2 and 3, which means that C is replaced by $C/(C-1)$. The coupling coefficient C of the directional coupler is expressed as the ratio of the incident power to the transmitted power in the adjacent waveguide. In the design Fig. 3, the greater the losses in the ring, the smaller the coupling coefficient must be for optimum performance.

In the case of Fig. 3, relations between incident and reflected waves are as follows

$$I_4 = R_2 e^{-(\alpha+i\beta)} \quad (1)$$

$$I_3 = R_3 \rho_3 \quad (2)$$

$$I_2 = R_4 e^{-(\alpha+i\beta)}, \quad (3)$$

and in the case of Fig. 4 they are

$$I_4 = R_3 e^{-(\alpha+i\beta)} \quad (4)$$

$$I_2 = R_2 \rho_2 \quad (5)$$

$$I_3 = R_4 e^{-(\alpha+i\beta)} \quad (6)$$

where

I_i = incident-wave amplitudes,

R_i = reflected-wave amplitudes,

ρ_i = reflection coefficients,

$e^\alpha = 10^{A/20}$ = attenuation in the ring (A in db),

β = phase shift (in radians) through the ring.

Traveling-Wave Resonator Characteristics

Taking into account (1)–(6), together with the feedback and matching conditions, the traveling-wave resonator characteristics are computed from the scattering matrix of a directional coupler. The matrix of a directional coupler is as follows:

$$\|S_i\| = \begin{vmatrix} 0 & \frac{\sqrt{C-1}}{\sqrt{C}} & j\frac{1}{\sqrt{C}} & 0 \\ \frac{\sqrt{C-1}}{\sqrt{C}} & 0 & 0 & \frac{j}{\sqrt{C}} \\ j\frac{1}{\sqrt{C}} & 0 & 0 & \frac{\sqrt{C-1}}{\sqrt{C}} \\ 0 & j\frac{1}{\sqrt{C}} & \frac{\sqrt{C-1}}{\sqrt{C}} & 0 \end{vmatrix}. \quad (7)$$

In the case of the circuit in Fig. 3

$$N = \left| \frac{R_2}{I_1} \right| = \frac{\sqrt{C-1}}{\sqrt{C} - e^{-\alpha}} \quad (8)$$

$$C_{\text{opt}} = e^{2\alpha} \quad (9)$$

$$N_{\text{max}} = \frac{1}{\sqrt{1 - e^{-2\alpha}}} = \sqrt{\frac{C_{\text{opt}}}{C_{\text{opt}} - 1}}. \quad (10)$$

In the case of the circuit in Fig. 4

$$N = \left| \frac{R_3}{I_1} \right| = \frac{1}{\sqrt{C} - \sqrt{C-1} \cdot e^{-\alpha}} \quad (11)$$

$$C_{\text{opt}} = \frac{1}{1 - e^{-2\alpha}} \quad (12)$$

$$N_{\text{max}} = \frac{1}{\sqrt{1 - e^{-2\alpha}}} = \sqrt{C_{\text{opt}}}. \quad (13)$$

N_{max} is identical for both circuits for a given amount of ring attenuation. Variations of N_{max} and C_{opt} are illustrated in Fig. 5, as a function of ring attenuation A . N has been plotted (dotted curve) for the particular

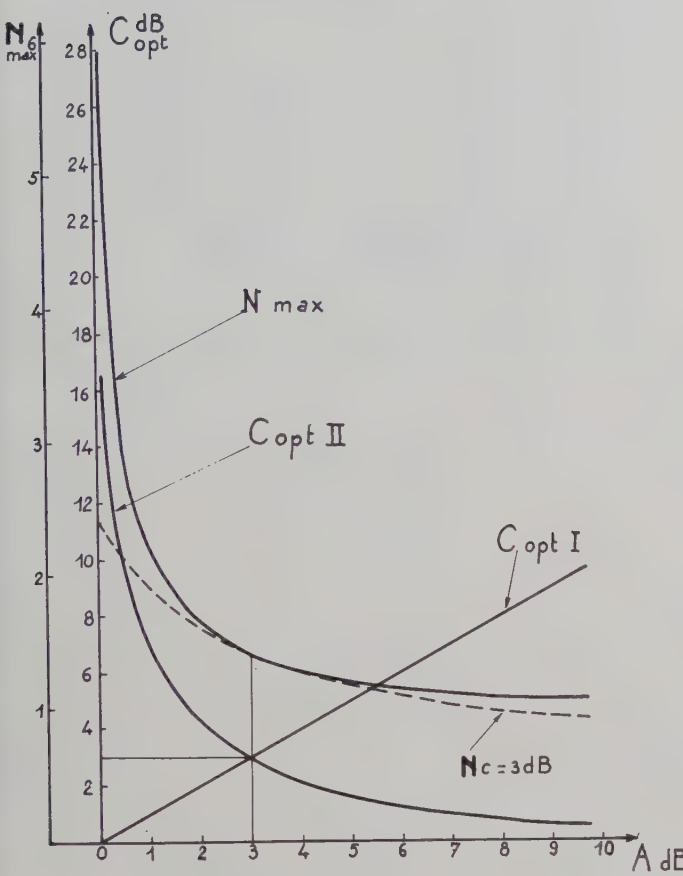


Fig. 5— N_{\max} , C_{opt} , and $C_{\text{opt II}}$ vs ring attenuation.

case where $C = 3 \text{ db}$. It is to be noticed that this curve meets the N_{\max} curve at $A = 3 \text{ db}$.

The microwave resonator is generally of interest when testing low attenuation circuits—say less than 3 db (and even less than 1 db), which is often the case.

In the experimental setup with a variable directional coupler (consisting of, for instance, two 3-db directional couplers and a phase shifter placed in one of the two legs connecting the two 3-db couplers) either circuit may be used depending upon the component to be tested. But, when it is a laboratory model, the first circuit will be preferred because the coupling coefficient is lower and the corresponding directional coupler is easier to make.

The scattering matrix is also useful in studying the reflection coefficient of the ring as seen from the magnetron side.

The reflection coefficient $\rho_1 = (R_1/I_1)$ in relation to reflection coefficient ρ_2 (circuit II) is given as:

$$\rho_1 = \left| \frac{R_1}{I_1} \right| = \left[\frac{\sqrt{1 - \frac{1}{C}} - e^{-\alpha}}{1 - \sqrt{1 - \frac{1}{C}} e^{-\alpha}} \right]^2 \rho_2. \quad (14)$$

This value is always less than ρ_2 and equals zero at optimum coupling, thus demonstrating that at

optimum coupling the whole incident power is transmitted into the feedback ring and no power is sent into the output load. The insertion loss introduced by the feedback ring, in the case of the permanent circuit, is expressed as

$$\left| \frac{I_1}{R_2} \right| = \frac{1 - \sqrt{1 - \frac{1}{C}} e^{-\alpha}}{\sqrt{1 - \frac{1}{C}} - e^{-\alpha}}. \quad (15)$$

For optimum coupling conditions, it can be seen that the insertion loss is infinite.

The reflection coefficient in the feedback ring caused by the output load is expressed as

$$\left| \frac{I_3}{R_3} \right| = e^{-\alpha} \frac{\sqrt{1 - \frac{1}{C}} - e^{-\alpha}}{1 - \sqrt{1 - \frac{1}{C}} e^{-\alpha}} \rho_2$$

$$\left| \frac{I_3}{R_3} \right| \ll \rho_2. \quad (16)$$

This coefficient is always smaller than the reflection coefficient of the load.

In any case, in an experimental setup, output load and waveguide mismatches may be corrected by adding a reactor to the ring. By this means the R_4 wave is cancelled before reaching the component to be tested. A monitoring coupler is placed between the reactance and the component in order to check cancellation.

PART II—DESCRIPTION OF PRACTICAL RESONATOR

TRAVELING-WAVE RESONATOR

The practical design of a traveling-wave resonator for microwave operation is illustrated in Fig. 6. Design of circuits is illustrated by the block diagram in Fig. 7.

In this experimental setup, working since July, 1954, in the Microwave Laboratories of the Compagnie Française Thomson-Houston, TH 5657 and TH 5586 magnetrons have been used with a peak power of approximately 800 kw. Power obtained within the resonator varies from 3 to 8 mw depending upon the component under test.³

The resonator consists of the following microwave parts, all designed for handling high-microwave power and withstanding air pressure of several kg/cm².

³ P. J. Sferrazza, "Traveling-wave resonator," *Tele-Tech.*, p. 84; November, 1955. This paper confirms the CFTH laboratory researches described herein.

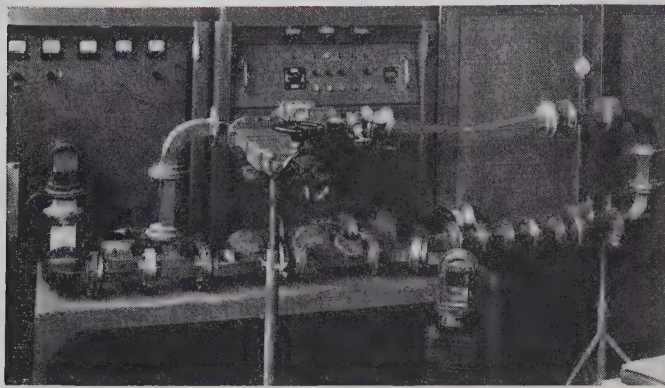


Fig. 6—Photograph of the traveling-wave resonator using a variable directional coupler.

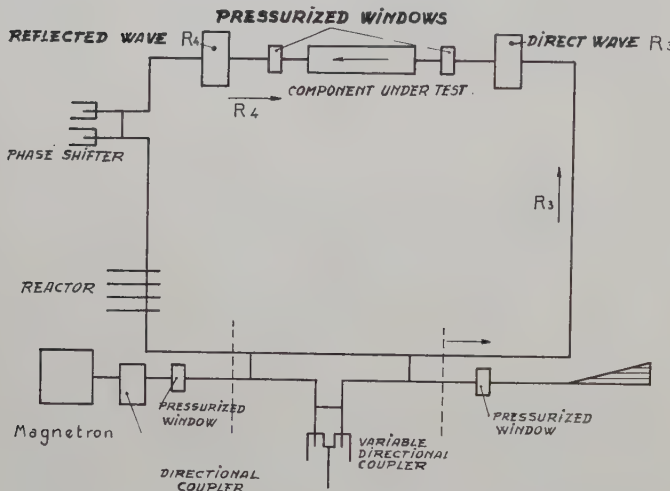


Fig. 7—Schematic diagram of a traveling-wave resonator.

Phase shifter,
Reactor,
Variable directional coupler,
Measuring directional couplers,
Pressurized windows.

Phase Shifter

In traveling-wave resonators, the phase shifter enables the adjustment of the length of the feedback loop to obtain resonance conditions.

The unit consists of a 3-db directional coupler and of two identical plungers simultaneously moved in order to insure a common shorting plane (see Fig. 8).

Assuming that a signal I is sent into leg 1 and that leg 4 is correctly matched, by writing (7) which can be expressed as:

$$\|R\| = \|S_r\| \cdot \|T\|$$

with

$$\|S_r\| = \|S_i^*\|$$

for the 3-db coupler, and allowing for the required connection conditions

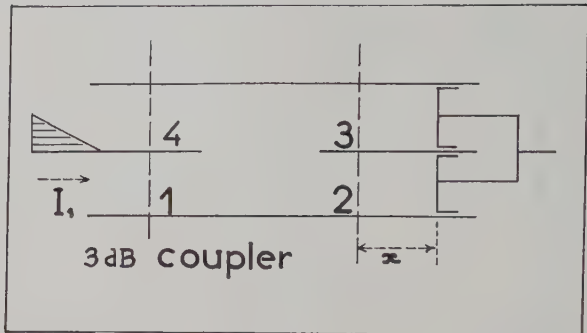


Fig. 8—Circuit diagram of phase shifter.

$$I_2 = R_2 e^{-2j\beta x}$$

$$I_3 = R_3 e^{-2j\beta x}$$

$$I_4 = 0$$

with

$$\beta = \frac{2\pi}{\lambda_g},$$

we obtain

$$\|R\| = \begin{vmatrix} 0 \\ I_1 \\ \frac{I_1}{\sqrt{2}} \\ j\frac{I_1}{\sqrt{2}} \\ jI_1 e^{-2j\beta x} \end{vmatrix}.$$

Therefore, the system is correctly matched ($R=0$) and by moving the plungers by Δx , the following phase shift is obtained

$$\Delta\phi = 2\beta\Delta x,$$

The experimented resonator operates over a 2700 to 3100-mc band: maximum plunger elongation is 100 mm and total phase shift is 400° . Power-handling capacity is good, the only limitation being given by the power handling of the 3-db coupler: approximately 3 mw at atmospheric pressure. With a pressure⁴ of 2 kg/cm^2 8 mw were recorded, without any sign of breakdown discharge.

Reactor

The reactor is used for cancelling wave R_4 (see Fig. 7) before reaching the output plane of component under test. Two types of reactor may be used.

Plunger Reactor: By displacing both plungers of the preceding design in either direction respectively we may use this design as a reactor (see Fig. 9).

⁴ All pressure figures are gauge pressure readings.

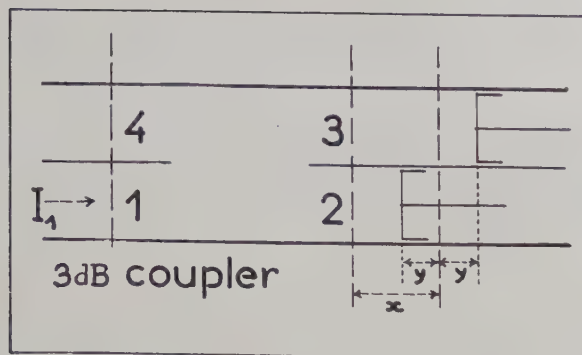


Fig. 9—Circuit diagram of plunger reactor.

In such a case, correct connection conditions are now

$$I_2 = R_2 e^{-2j\beta(x-y)}$$

$$I_3 = R_3 e^{-2j\beta(x+y)}$$

$$I_4 = 0.$$

The same computation, starting from

$$\|R\| = \|S_r\| \cdot \|I\|$$

as before gives

$$\|R\| = \begin{vmatrix} -jI_1 e^{-2j\beta x} \sin 2\beta y \\ I_1 \\ \frac{1}{\sqrt{2}} \\ j \frac{I_1}{\sqrt{2}} \\ jI_1 e^{j\beta x} \cos 2\beta y \end{vmatrix}.$$

The reflection coefficient in leg 1 is therefore:

$$\rho = \frac{R_1}{I_1} = -je^{-2j\beta x} \sin 2\beta y.$$

Plunger offsetting adjustment ($2y$) makes it possible to vary the standing-wave ratio in leg 1.

$$|\rho| = 0 \text{ if } y = 0 \text{ and } |\rho| = 1 \text{ if } y = \frac{\lambda_g}{8}$$

whereas x adjustments alter the phase of the reflected wave.

This circuit shows the advantage of two independent adjustments, namely, as a phase-shifter and reactor.

In the operating reactor shown in Fig. 10, the displacement y can vary over a 0-45 mm range, that is, slightly more than $\lambda_g/8$. Power trials were carried out with a 5-mw magnetron, with a standing-wave ratio of 1.5 and a pressure of 2 kg/cm².

Quartz Rod Reactor: This reactor consists of four cylindrical rods made of fused silica; the diameter of the rods is 12 mm and the length is 80 mm. These silica rods are parallel to the wide side of the waveguide and perpendicular to the propagation direction. Distance between the rods is 17.5 mm which is equal to $\lambda_g/8$ at

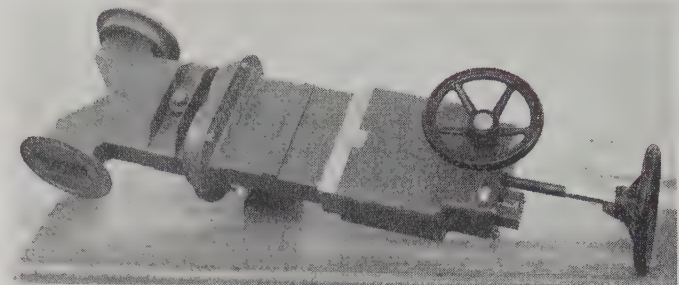


Fig. 10—Photograph of plunger reactor.

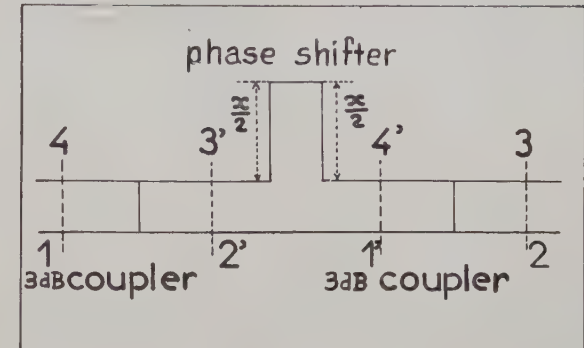


Fig. 11—Circuit diagram of variable directional coupler.

3000 mc. Total displacement is slightly greater than half the width of waveguide. This design insures proper matching of any standing-wave ratio (vswr) up to 2. The power-handling capacity is superior to the conventional reactor (where the dielectric rods are perpendicular to the wide side of waveguide).

Tests have been conducted successfully with a peak power of 2.5 mw (at normal pressure and a vswr equal to 2 before matching).

In the same conditions, the conventional reactor did not operate above 1.7 mw.

Variable Directional Coupler

This directional coupler makes it possible to adjust the coupling between the main guide and the feedback loop, for the optimum value C_{opt} .

The system consists of two 3-db couplers mounted in cascade and a phase shifter inserted in one of the connecting legs of the 3-db couplers.

A study of the diagram in Fig. 11 shows that the system has the same directional properties as an individual 3-db coupler. Now, assuming x , the path difference between legs ($2'-1'$) and ($3'-4'$), coupling conditions are expressed by:

$$I_{1'} = R_{2'} \quad I_{3'} = e^{-j\beta x} \cdot R_{4'}$$

$$I_{2'} = R_{1'} \quad I_{4'} = e^{-j\beta x} \cdot R_{3'}$$

By taking into account the preceding conditions and writing for each 3-db coupler the (7) relation, the following equation is obtained:

$$\begin{vmatrix} I_1 \\ I_2 \\ I_3 \\ I_4 \end{vmatrix} = (S') \begin{vmatrix} R_1 \\ R_2 \\ R_3 \\ R_4 \end{vmatrix}$$

with:

$$C = \frac{1}{\cos^2 \frac{\beta x}{2}}.$$

By simply making x vary between 0 and $\lambda_g/2$ the complete range of coupling values may be covered.

$$(S') = \begin{vmatrix} 0 & e^{j(\pi/2-\beta x/2)} \sin \frac{\beta x}{2} & j e^{-j(\beta x/2)} \cos \frac{\beta x}{2} & 0 \\ e^{j(\pi/2-\beta x/2)} \sin \frac{\beta x}{2} & 0 & 0 & j e^{-j(\beta x/2)} \cos \frac{\beta x}{2} \\ j e^{-j(\beta x/2)} \cos \frac{\beta x}{2} & 0 & 0 & e^{-j(\pi/2+\beta x/2)} \sin \frac{\beta x}{2} \\ 0 & j e^{-j(\beta x/2)} \cos \frac{\beta x}{2} & e^{-j(\pi/2+\beta x/2)} \sin \frac{\beta x}{2} & 0 \end{vmatrix}.$$

With a reference plane shift, as given in the diagonal matrix

$$(P) = \begin{vmatrix} a & 0 & 0 & 0 \\ 0 & b & 0 & 0 \\ 0 & 0 & c & 0 \\ 0 & 0 & 0 & d \end{vmatrix}$$

it is possible to write this new scattering matrix:

$$(S'') = (P)(S')(P).$$

Putting

$$a = 1 \quad b = e^{j(\beta x/2 - \pi/2)}$$

$$c = e^{j(\beta x/2)}$$

and

$$d = e^{j(\pi/2)}$$

the matrix (S'') may be written

$$\|S''\| = \begin{vmatrix} 0 & \sin \frac{\beta x}{2} & j \cos \frac{\beta x}{2} & 0 \\ \sin \frac{\beta x}{2} & 0 & 0 & j \cos \frac{\beta x}{2} \\ j \cos \frac{\beta x}{2} & 0 & 0 & \sin \frac{\beta x}{2} \\ 0 & j \cos \frac{\beta x}{2} & \sin \frac{\beta x}{2} & 0 \end{vmatrix},$$

which proves that the described circuit is working in the same way as a directional coupler having a coupling value of

Pressurized Window

Two materials have been tested. The first one was fused silica; the second one was teflon in the form of a sheet several millimeters thick.

A dielectric window into a waveguide is equivalent to a shunting capacitor. In order to match this over a wide band, the height of guide was increased on each side of the dielectric sheet and the length was adjusted in order to obtain the proper series inductance L_1 . Shunting inductances L_2 consisting of rods, are also inserted at the point of height discontinuity. The corresponding diagram is shown in Fig. 12. All sharp edges due to waveguide section variations have been carefully rounded.

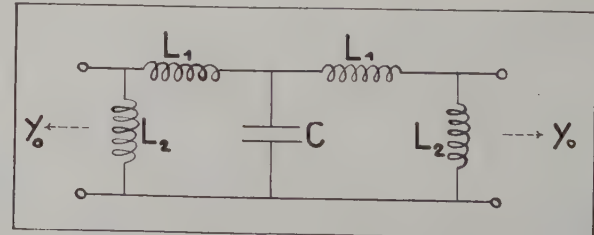


Fig. 12—Matching the pressurized window.

A standing-wave ratio of 1.02 is obtained between 2700 and 3300 mc. Two quartz windows were used during power tests to permit pressurization in the resonator. The test space between the two windows was at atmospheric pressure. Breakdown discharge occurred at a power between 5 and 6 mw.

The teflon window was tested at atmospheric pressure. During test, the window was placed between two quartz windows. The remaining section of the resonator was under higher pressure. At 6 mw, breakdown discharge occurred in the waveguide as well as in the teflon

and quartz windows. The quartz window can withstand relative pressures up to 2 kg/cm² (we experienced quartz failure once at 3.5 kg/cm² and once at 4 kg/cm²). The teflon window has already withstood a relative pressure of 4.5 kg/cm², but further tests are still in progress.

CONCLUSION

The principles of operation of a traveling-wave resonator designed by the authors have been described. Constituent elements have been discussed and the application to high-power tests was mentioned. Now the fact is stressed that power-handling testing is not the sole application of traveling-wave resonators. This cir-

cuit may also be used for other types of measurements. For instance, in the case of optimum coupling, attenuation introduced in the main waveguide is infinite and variation of attenuation within main waveguide around this value is very rapid. This can be applied to measurement of low variations in attenuation when studying surface treatments for waveguide, gas tube losses, etc.

BIBLIOGRAPHY

- [1] Cohn, S. B. and Coale, F. S. "Directional Channel-Separation Filters," *PROCEEDINGS OF THE IRE*, Vol. 44 (August, 1956), pp. 1018-1024.
- [2] Coale, F. S. "A Travelling-Wave Directional Filter," *IRE TRANSACTIONS ON MICROWAVE THEORY AND TECHNIQUES*, Vol. 4 (October, 1956), pp. 256-260.
- [3] Tischer, F. J. "Resonance Properties of Ring Circuits," *IRE TRANSACTIONS ON MICROWAVE THEORY AND TECHNIQUES*, Vol. 5 (January, 1957), pp. 51-56.

Reflection Coefficient of E-Plane Tapered Waveguides*

KATSU MATSUMARU†

Summary—This paper treats the reflection of linearly and sinusoidally tapered waveguides. In the first part, reflection coefficients of linearly tapered waveguides for dominant modes are calculated. Graphs of the vswr of tapers for different impedance ratios are plotted showing that the vswr does not go to unity at multiples of a half wavelength. In the second part, reflection coefficients of sinusoidally tapered waveguides are calculated. Experimental data verify the theory for both kinds of tapers of various lengths at 4 kmc band.

Linear tapers perform almost as well as exponential tapers, and better than shorter hyperbolic tapers. The reflection coefficients of sinusoidal tapers can be about half as small as that of the linear tapers, and these tapers compare favorably with the Dolph-Tchebycheff and the Willis taper of improved design.

INTRODUCTION

REFLECTION coefficients of tapered waveguides can be calculated by formulas described in the references,^{1,2} but these formulas give only rough values. Reflections of several nonuniform transmission lines were theoretically treated by Burrow,³ Scott,⁴

Klopfenstein,⁵ Collin,^{6,7} Willis and Sinha,⁸ Bolinder,^{9,10} and others. Most papers treat the magnitudes of reflection coefficient of particular tapers that are mathematically convenient to analyze, but in microwave circuit we often need practical formulas and convenient graphs to determine the reflection coefficients. These several papers are mainly theoretical, with very limited experimental data on tapered waveguides.

In the first part of this paper, approximate theoretical calculations of the reflection coefficient of linear tapers are presented. From the derived formulas, useful graphs were compiled in terms of the suitable ratios of input-to-output surge impedances. To confirm the formulas experimentally at 4 kmc, we have made two groups of tapers in which the ratios of surge impedances are 2.0 and 2.4. The agreement between calculated and

* Manuscript received by the PGM TT, April 12, 1957; revised manuscript received, October 29, 1957.

† Elec. Commun. Lab., Nippon Telegraph and Telephone Public Corp., Tokyo, Japan.

¹ T. Moreno, "Microwave Transmission Design Data," McGraw-Hill Book Co., Inc., New York, N. Y., p. 53; 1948.

² G. L. Ragan, "Microwave Transmission Circuit," McGraw-Hill Book Co., Inc., New York, N. Y., M.I.T. Rad. Lab. Ser., vol. 9, p. 305; 1948.

³ C. R. Burrow, "The exponential transmission line," *Bell Sys. Tech. J.*, vol. 17, pp. 555-573; October, 1938.

⁴ H. J. Scott, "The hyperbolic transmission line as a matching section," *PROC. IRE*, vol. 41, pp. 1654-1657; November, 1953.

⁵ R. W. Klopfenstein, "A transmission line taper of improved design," *PROC. IRE*, vol. 44, pp. 31-35; January, 1956.

⁶ R. E. Collin, "The theory and design of wide-band multisection quarter-wave transformer," *PROC. IRE*, vol. 43, pp. 179-185; February, 1955.

⁷ R. E. Collin, "The optimum tapered transmission line matching section," *PROC. IRE*, vol. 44, pp. 539-548; April, 1956.

⁸ J. Willis and N. K. Sinha, "Non-uniform transmission lines as impedance transformers," *Proc. IEE*, pt. B, vol. 103, pp. 166-172; March, 1956.

⁹ F. Bolinder, "Fourier transformers in the theory of inhomogeneous transmission lines," *PROC. IRE*, vol. 38, p. 1354; November, 1950.

¹⁰ F. Bolinder, "Fourier transforms in the theory of inhomogeneous transmission lines," *Trans. Roy. Inst. Tech., Stockholm*, No. 48; 1951.

measured values of reflection coefficient was found to be very good.

A sinusoidally tapered waveguide may be used to shorten the length of the taper. In the later part of this paper general formulas for the reflection coefficients of these tapers are described. To confirm the formulas, we made a third group of tapers in which the ratio of input-to-output surge impedance is 2.4. The calculated curve of reflection coefficient of these tapers agreed very well with that of the observed. Bolinder was the first to derive accurate formulas for linear and sinusoidal tapers. While his results are in terms of magnitude of the reflection coefficient, we have derived explicit formulas of complex reflection coefficients of tapered waveguides. By means of our practical charts, we can easily determine the exact reflection coefficient of a tapered waveguide.

CALCULATIONS AND CHARACTERISTICS OF REFLECTION COEFFICIENT OF LINEARLY TAPERED WAVEGUIDE

In Fig. 1(a), W_1 and W_2 are rectangular waveguides, which are connected by an E -plane linear taper. The surge impedances of W_1 and W_2 and the taper are Z_1 , Z_2 , and $Z(x)$, respectively. The origin of x is at the longitudinal center of the taper, and the length of the taper is l . Let us assume that the $Z(x)$ is a linear function of the variable x and Z_1 is larger than Z_2 , *viz.*,

$$Z_1 > Z_2, \quad (1)$$

$$Z(x) = \frac{Z_1 + Z_2}{2} + \frac{Z_2 - Z_1}{l} x. \quad (2)$$

Furthermore, we assume that Z_1 , Z_2 , and $Z(x)$ are positive real. In Fig. 1(b) two transmission circuits whose surge impedances are Z'_1 and Z'_2 , are connected by a step discontinuity. If the electromagnetic wave propagates from left to right, the element of reflection coefficient dR is given by (3) when Z'_1 is only slightly different from Z'_2 . It is

$$dR = \frac{Z'_2 - Z'_1}{Z'_2 + Z'_1} = \frac{dZ'_1}{2Z'_1}. \quad (3)$$

By considering the phase difference, we can obtain R of the taper of Fig. 1(a) by the following integration procedure. With

$$dZ = \frac{Z_2 - Z_1}{l} dx,$$

$$R = \frac{1}{2} \int_{-l/2}^{l/2} \frac{e^{-i2\beta(x+l/2)}}{\frac{Z_1 + Z_2}{2} + \frac{Z_2 - Z_1}{l} x} \cdot \frac{Z_2 - Z_1}{l} dx. \quad (4)$$

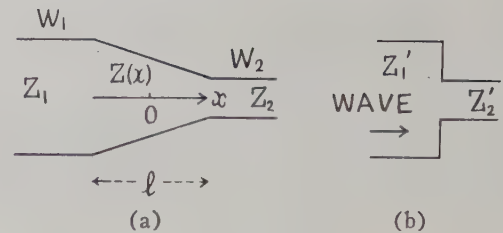


Fig. 1—Illustration of the coordinate in a taper.

The wavelength in the taper, λ_g is constant, and β is $2\pi/\lambda_g$. Putting

$$q \equiv \frac{2(Z_2 - Z_1)}{(Z_1 + Z_2)l},$$

(4) becomes

$$R = \frac{Z_2 - Z_1}{(Z_2 + Z_1)l} \int_{-l/2}^{l/2} \frac{e^{-i2\beta(x+l/2)}}{1 + qx} dx. \quad (5)$$

As a first approximation, we consider (5) when q is negligibly small. In this case, the taper may be considered an exponential one. Then,

$$|R| = \frac{1}{2} \ln \frac{Z_1}{Z_2} \cdot \frac{|\sin(2\pi l/\lambda_g)|}{2\pi l/\lambda_g}. \quad (6)$$

This result is identical with the equation given by Ragan.² Values of $|R|$ derived from (6) show that the reflection coefficient reduces to zero at the minimum points. Eq. (6) is not applicable for general cases when q is not equal to zero. To acquire a more accurate and useful equation, we must integrate (5) by considering q properly.

By using the approximate relation,

$$\frac{1}{1 + qx} \approx 1 - qx + q^2x^2, \quad (7)$$

we have from (5)

$$R = \frac{Z_2 - Z_1}{(Z_2 + Z_1)bl} \left\{ \begin{array}{l} \sin \beta l \cdot \cos \beta l (1 + q^2 l^2 / 4) \\ + (l \cos \beta l - \sin \beta l / \beta) \\ \times (-q \sin \beta l / 2 + q^2 \cos \beta l / 2\beta) \\ - j \left\{ \begin{array}{l} \sin^2 \beta l (1 + q^2 l^2 / 4) \\ + (l \cos \beta l - \sin \beta l / \beta) \\ \times (q \cos \beta l / 2 + q^2 \sin \beta l / 2\beta) \end{array} \right\} \end{array} \right\}. \quad (8)$$

This equation is identical with (6) when we put $q=0$. From the explicit formula (8) we can easily calculate a magnitude of R of a taper. Eq. (8) was derived on the base of assumption (1). We may also use this formula for the case of $Z_2 > Z_1$. However, except for extremely short tapers, the calculated magnitudes of R are equal for both the input and output sides.

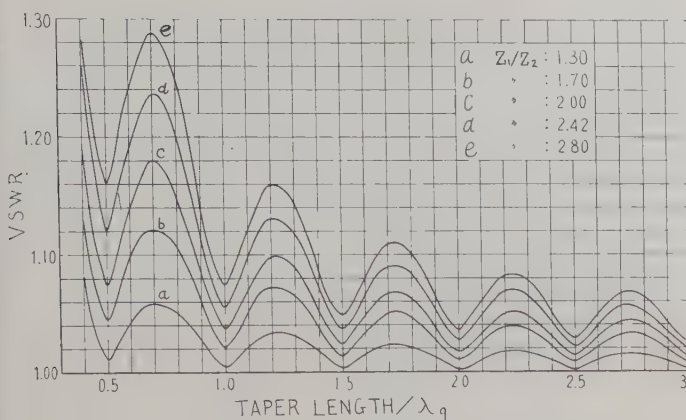


Fig. 2—Curves show vswr's of linearly tapered waveguides calculated from (8) with Z_1/Z_2 as the parameter.

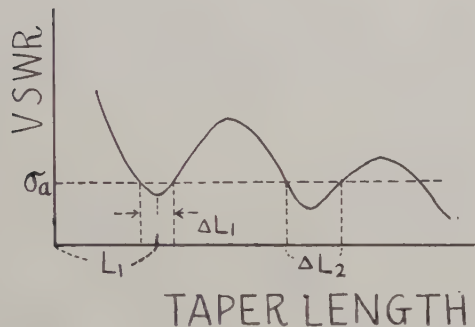


Fig. 3—Method of taper design.

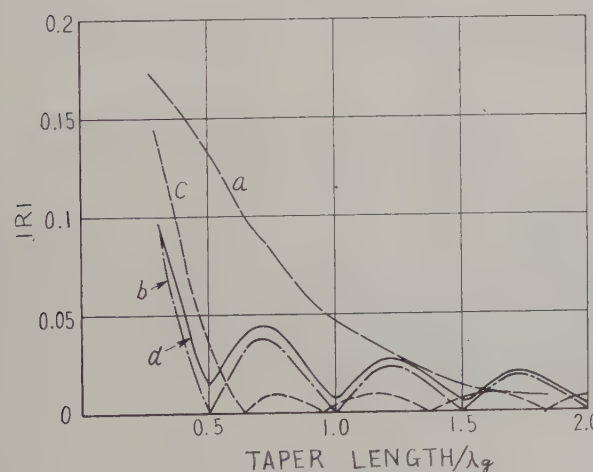


Fig. 4—Performances of linear taper ($Z_1/Z_2 = 1.5$). a:hyperbolic, b:exponential, c:Dolph-Tchebycheff, d:linear.

Placing values of Z_1 , Z_2 , and l in (8), we can calculate the vswr of a taper from the relationship,

$$\text{vswr} = \frac{1 + |R|}{1 - |R|}.$$

Fig. 2 shows graphs of calculated vswr's for various values of Z_1/Z_2 . It is to be noted that usually the required bandwidths for microwave systems are relatively narrow, thus the method of design of a taper will be mentioned here. Let us suppose that for a given value of Z_1/Z_2 , the vswr is as shown in Fig. 3. If the allowable value of the vswr is σ_a , we draw a horizontal line across σ_a . By estimating widths of ΔL_1 , ΔL_2 , etc., we can determine the necessary length of the taper.

Now, we compare the reflection characteristics of a linear taper with that of others. First, we compare the $|R|$ calculated from (8) with that given in Bolinder's paper.¹¹ In Table I, a very good comparison is shown for the case of $Z_1/Z_2 = 2.0$. Bolinder's formula is expressed in terms of complicated Bessel functions and gives only the magnitude of R . It is believed that our formula for R in (8), being simpler and virtually as accurate, will prove to be more practical for designing of a taper. Next, Klopfenstein⁶ described the performances of exponential, hyperbolic, and Dolph-Tchebycheff coaxial tapers for the case of $Z_1/Z_2 = 1.5$. Fig. 4 compares the performance of the linear taper with these

TABLE I

l/λ_g	0.2	0.3	0.4	0.5	0.6	0.7	0.8	0.9	1.0	1.1	1.2	1.3	1.4
$ R $	0.28	0.18	0.09	0.04	0.07	0.08	0.07	0.04	0.02	0.03	0.05	0.04	0.03
Bolinder	0.27	0.17	0.09	0.04	0.07	0.08	0.07	0.04	0.02	0.03	0.05	0.04	0.03

three other types. It is shown that the reflection of a linear taper is not too different from an exponential one. The reflection of the Dolph-Tchebycheff taper is shown to be much better than the linear, but this should be confirmed experimentally. The hyperbolic taper is disadvantageous for waveguide applications. Briefly the conclusion is that, in most cases, a linear taper may be substituted for an exponential.

For microwaves applications, one should use a reflection formula of a tapered transmission line which has been experimentally verified. The reasons are as follows. Most theoretical formulas are approximations derived on the bases of assumptions. For example, the waves propagating in waveguides are not TEM in character. The definition of a surge impedance of a wave-

¹¹ Bolinder, *ibid.*, p. 67 (Fig. 27).

guide is merely formal. Strictly speaking, the equivalent circuit of a taper is composed of many reactances, and hence it is frequency dependent. Moreover, higher modes may be induced in the output or input terminals. For example, Lewin¹² treated the reflection cancellation at junctions between waveguides and horns. The calculated values of reflection coefficient cannot be accurate for extremely short tapers, of course, and it is important to determine the minimum lengths for which the formulas may be used. For these reasons, we determined to get experimental data. We performed experiments at 4 kmc, because this band is most convenient in view of the precision of measurements available at our laboratory.

EXPERIMENTS—PART I ($Z_2/Z_1 = 2.0$)

For a dominant mode in a waveguide of constant width a , the surge impedance is proportional to the height b .¹³ The first experiments were made for the case that Z_2/Z_1 is 2.0. That is, the internal sizes, b and a , of the waveguides were 58.1 mm \times 58.1 mm and 29.1 mm \times 58.1 mm. Lengths of tapers were from 17 cm to 2 cm at intervals of 1 cm. Accuracy of internal sizes in the plane of flanges was approximately ± 0.2 mm. The vswr was measured on the rectangular side using a specially made sliding wooden dummy load on the square side. The residual vswr of this dummy load was approximately 1.01 at this band. We eliminated errors due to this load by shifting its position. The law of the crystal on the standing-wave device was measured. The data were taken at a frequency of 4 kmc ($\lambda_g = 9.82$ cm). Observed and calculated results are shown in Fig. 5, together with other data. Observed points shown by white circles coincide well with the dashed curve for tapers longer than $0.5\lambda_g$. The mean error in the vswr of the tapers longer than $0.5\lambda_g$ was as small as 0.005. In this example Z_2 is larger than Z_1 , so that, the calculated magnitudes of vswr are not equal to the curve c shown in Fig. 2. However, the deviations of vswr from that curve are extremely small. We may use Fig. 2 for this example. It is believed that graphs of Fig. 2 are generally inapplicable for tapers shorter than $0.5\lambda_g$. So, it is important to determine the minimum lengths for which other authors' formulas may be used.

EXPERIMENTS—PART II ($Z_1/Z_2 = 2.4$)

We measured vswr's of another group of tapers connecting waveguides with internal dimensions of 29.1 mm \times 58.1 mm and 12.0 mm \times 58.1 mm, for which Z_1/Z_2 is almost 2.4. Lengths of this group are from 20 cm to 3 cm at intervals of 1 cm. The constructional accuracy of this group is not as good as the first group; namely almost ± 0.35 mm. Measurements were made at a fre-

¹² L. Lewin, "Reflection cancellation in waveguides," *Wireless Eng.*, vol. 10, pp. 258-264; August, 1949.

¹³ A. Schelkunoff, "Electromagnetic Waves," D. Van Nostrand Co., Inc., New York, N. Y., pp. 316-322; 1943.

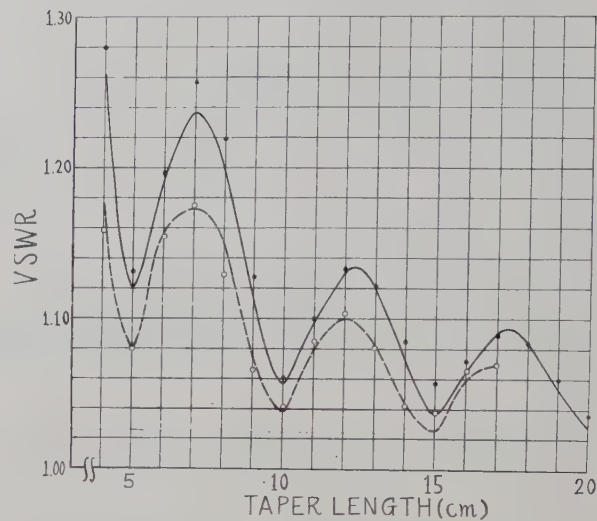


Fig. 5—Results of measurements of vswr of linear tapers. White circles show observed values, and the dashed curve the calculated. The ratio of Z_2/Z_1 is 2.0. Black circles and the solid curve show the corresponding values for the ratio Z_1/Z_2 equal to 2.4.

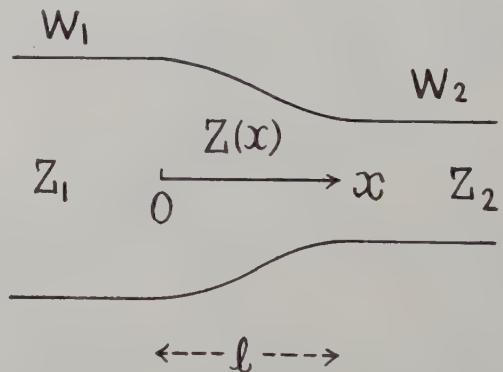


Fig. 6—Illustration of the coordinate in a taper.

quency of 3960 mc; that is, λ_g was almost 10.0 cm. Fig. 5 shows the results. Black circles show observed values and the solid curve the calculated. In this group, again, the results coincide well for tapers longer than $0.5\lambda_g$. Deviations are slightly greater than the first group; the mean error of the vswr is as small as 0.008.

CALCULATION OF REFLECTION COEFFICIENT OF SINUSOIDALLY TAPERED WAVEGUIDE

We calculate the reflection coefficient of a sinusoidally tapered waveguide for the dominant mode in the same way as that for the linearly tapered waveguide. The width a of a rectangular waveguide is constant, and its height b varies sinusoidally as shown in Fig. 6. We assume that Z_1 , Z_2 , and $Z(x)$ are positive real and Z_1 is greater than Z_2 , thus,

$$Z_1 > Z_2. \quad (9)$$

$$Z(x) = \frac{Z_1 + Z_2}{2} - \frac{Z_2 - Z_1}{2} \cos\left(\frac{\pi x}{l}\right). \quad (10)$$

From (10),

$$dZ(x) = \frac{\pi(Z_2 - Z_1)}{2l} \sin\left(\frac{\pi x}{l}\right) dx. \quad (11)$$

Thus, if the electromagnetic wave propagates from left to right, R of the taper in Fig. 6 can be obtained, after considering the phase factor, from

$$R = \frac{\pi(Z_2 - Z_1)}{2l(Z_2 + Z_1)} \int_0^l \frac{e^{-i2\beta x} \sin\left(\frac{\pi x}{l}\right)}{1 - \frac{Z_2 - Z_1}{Z_2 + Z_1} \cos\left(\frac{\pi x}{l}\right)} dx. \quad (12)$$

To evaluate this integral, we put

$$r \equiv \frac{Z_1 - Z_2}{Z_2 + Z_1}.$$

As $|r|$ is smaller than unity, we have

$$\begin{aligned} \frac{1}{1 + r \cos\left(\frac{\pi x}{l}\right)} &\cong 1 - r \cos\left(\frac{\pi x}{l}\right) \\ &+ r^2 \cos^2\left(\frac{\pi x}{l}\right). \end{aligned} \quad (13)$$

Using this approximate relation, we obtain

$$R = \frac{\pi(Z_2 - Z_1)}{2l(Z_2 + Z_1)} \int_0^l e^{-i2\beta x} \sin\left(\frac{\pi x}{l}\right) \cdot \left\{ 1 - r \cos\left(\frac{\pi x}{l}\right) + r^2 \cos^2\left(\frac{\pi x}{l}\right) \right\} dx. \quad (14)$$

On evaluating (14) we find

$$R = \frac{\pi(Z_2 - Z_1)}{2l(Z_2 + Z_1)} \left\{ \begin{aligned} &\cos^2\left(\frac{2\pi l}{\lambda_g}\right) \left\{ \left(1 + \frac{r^2}{4}\right) \frac{-\frac{2\pi}{l}}{\left(\frac{4\pi}{\lambda_g}\right)^2 - \left(\frac{\pi}{l}\right)^2} + \frac{r^2}{4} \frac{-\frac{6\pi}{l}}{\left(\frac{4\pi}{\lambda_g}\right)^2 - \left(\frac{3\pi}{l}\right)^2} \right\} \\ &+ \frac{r}{2} \sin^2\left(\frac{2\pi l}{\lambda_g}\right) \frac{\frac{4\pi}{l}}{\left(\frac{4\pi}{\lambda_g}\right)^2 - \left(\frac{2\pi}{l}\right)^2} \\ &+ j \sin\left(\frac{2\pi l}{\lambda_g}\right) \cos\left(\frac{2\pi l}{\lambda_g}\right) \left\{ \left(1 + \frac{r^2}{4}\right) \frac{\frac{2\pi}{l}}{\left(\frac{4\pi}{\lambda_g}\right)^2 - \left(\frac{\pi}{l}\right)^2} + \frac{r^2}{4} \frac{\frac{6\pi}{l}}{\left(\frac{4\pi}{\lambda_g}\right)^2 - \left(\frac{3\pi}{l}\right)^2} \right. \\ &\left. + \frac{r}{2} \frac{\frac{4\pi}{l}}{\left(\frac{4\pi}{\lambda_g}\right)^2 - \left(\frac{2\pi}{l}\right)^2} \right\} \end{aligned} \right\}. \quad (15)$$

It is clear that (15) is a function of r and l/λ_g . As a check, we put $r = 0$ in (14), and (15) is given by

$$\begin{aligned} R &= \frac{1}{2} \frac{Z_2 - Z_1}{Z_2 + Z_1} \cos\left(\frac{2\pi l}{\lambda_g}\right) \\ &\times \left\{ \cos\left(\frac{2\pi l}{\lambda_g}\right) - j \sin\left(\frac{2\pi l}{\lambda_g}\right) \right\} \\ &\times \left\{ \frac{\pi}{l} / \left\{ \frac{4\pi}{\lambda_g} + \frac{\pi}{l} \right\} - \frac{\pi}{l} / \left\{ \frac{4\pi}{\lambda_g} - \frac{\pi}{l} \right\} \right\}. \end{aligned}$$

In this equation, if l tends to zero, R becomes

$$R = \frac{Z_2 - Z_1}{Z_2 + Z_1}.$$

So, (15) converges to the reflection coefficient of two directly connected waveguides. In Fig. 7, curves show vswr's for various values of Z_1/Z_2 , corresponding to those in Fig. 2. It should be mentioned that the curves of the vswr do not go to unity at the minimum points and their maximum points ascend in accordance with the ratios of Z_1/Z_2 . As for a linear taper, Fig. 7 may be used for the case of $Z_2 > Z_1$. The reflection character described in this chart shows clearly the very high quality of these tapers. It is mentioned that the vswr's increase suddenly for tapers shorter than $0.7\lambda_g$.

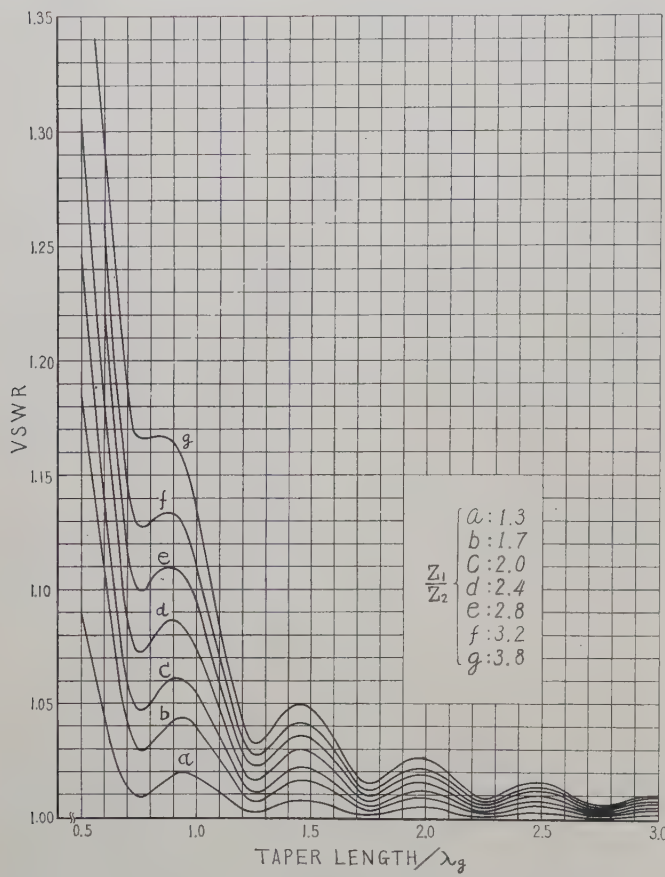


Fig. 7—Curves show vswr's of sinusoidally tapered waveguide as the parameter of Z_1/Z_2 . The impedance ratios are 1.3 to 3.8.

Thus, for approximately equivalent performance, the sinusoidal taper can be made about half as long as the linear taper. Next, we compare the sinusoidal taper with the taper which was described in Willis and Sinha's paper.¹⁵ In this case, Z_1/Z_2 is equal to 2.0. Fig. 8 shows reflection coefficients of both tapers. The length of the sinusoidal tapers is almost $0.65 \lambda_g$ for $|R|$ equal to 0.042 as compared with $0.5 \lambda_g$ for the Willis taper, but this is compensated by a faster reflection drop-off in the sinusoidal taper. Lastly, we compare the sinusoidal taper with the taper which was described in Klopfenstein's paper.¹⁶ Fig. 9 shows reflection performances of both tapers. The Dolph-Tchebycheff taper appears to be somewhat better, but not by a major degree. Thus from Figs. 8 and 9 we see that as to the reflection character, a sinusoidal taper compares well with several kinds of tapers designed by more difficult methods. Consequently, for many applications the sinusoidal taper would be preferable from the standpoint of design simplicity coupled with adequate performance.

EXPERIMENTS—PART III ($Z_1/Z_2 = 2.4$)

As the second group, we experimented for the case that Z_1/Z_2 is 2.4. To confirm the formulas, it appears most favorable to use taper lengths near the first minimum point of the vswr curve, so that lengths from $0.5 \lambda_g$ to $1.0 \lambda_g$ with intervals of 1 cm were used. The accuracy of measurements was, on the whole, improved

TABLE II

l/λ_g	0.5	0.6	0.7	0.8	0.9	1.0	1.1	1.2	1.3	1.4	1.5
VSWR	(15)	1.24	1.14	1.06	1.05	1.06	1.06	1.04	1.02	1.01	1.02
	Bolinder	1.25	1.13	1.07	1.05	1.06	1.06	1.03	1.01	1.02	1.03

TABLE III

Length (cm)	10	11	12	13	14	15	16	17	18	19	20
VSWR	Linear.	1.04	1.07	1.10	1.09	1.05	1.02	1.05	1.07	1.06	1.04
	Sinu.	1.06	1.04	1.02	1.01	1.02	1.02	1.02	1.01	1.01	1.01

COMPARISON WITH OTHER TAPERS

Now, for the case of $Z_1/Z_2 = 2.0$, we show the vswr's from (15) with those calculated from Bolinder's paper¹⁴ in Table III. The agreement of the two sets of values is very good. We next compare sinusoidal tapers with linear tapers. As an example, let us consider a waveguide wavelength λ_g of 10 cm. The vswr of these two tapers are given in Table III for Z_1/Z_2 equal to 2.0.

¹⁴ Bolinder, *op. cit.*, *Trans. Roy. Inst. Tech., Stockholm*, p. 65 (Fig. 26).

compared to that of the two previous groups. Measurements were also made at 3.96 kmc. The results are expressed in Table IV and show excellent agreement. As shown by the curve *d* in Fig. 7, the observed values of vswr yield a minimum near the taper length of $0.75 \lambda_g$ and a maximum near $0.9 \lambda_g$. It is believed that the mean error in the vswr of tapers longer than $0.8 \lambda_g$ is about as small as 0.01.

¹⁵ Willis and Sinha, *op. cit.* (Fig. 3).

¹⁶ Klopfenstein, *op. cit.* (Fig. 6).

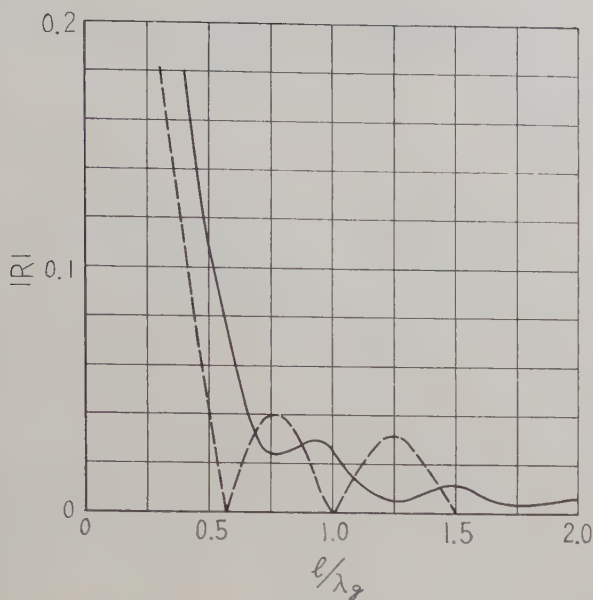


Fig. 8—Reflection coefficient as a function of l/λ_g for the example of Willis and Sinha's paper and sinusoidal taper. Solid line: sinusoidal, and dashed line: the Willis taper.

CONCLUSION

The reflection coefficient of a linearly and a sinusoidally tapered waveguide can be calculated quite accurately by (8) and (15), respectively. Except for extremely short tapers, the calculated magnitudes of R are equal for both the input and output sides. For most cases, however, we may directly determine vswr's by means of the graphs described in Fig. 2 and 7. Both the observed values of the vswr of linear tapers longer than $0.5 \lambda_g$ and sinusoidal tapers longer than $0.8 \lambda_g$ coincide with calculated values at most within the limit of 0.01. The effect of neglecting higher terms in (8) and (15) is very small, so that (8) and (15) are generally sufficient for practical uses.

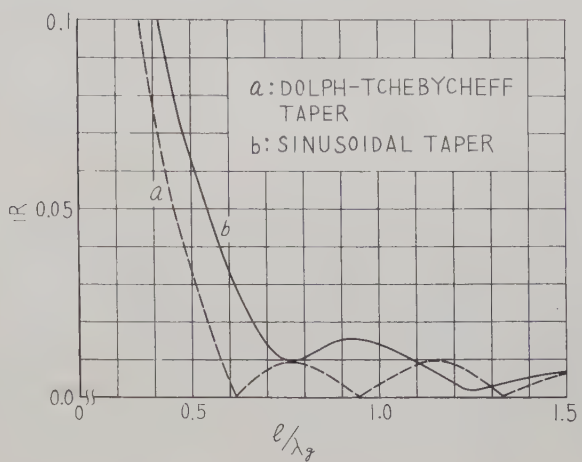


Fig. 9—Reflection coefficient as a function of l/λ_g for the Dolph-Tchebycheff taper and sinusoidal taper.

TABLE IV

l/λ_g	0.5	0.6	0.7	0.8	0.9	1.0
VSWR	Obs.	1.38	1.11	1.06	1.07	1.08
	Cal.	1.26	1.16	1.08	1.07	1.08

The reflection performance of a linear taper is almost as good as an exponential one, and a sinusoidal taper is comparable to the Dolph-Tchebycheff and the Willis taper of improved design.

ACKNOWLEDGMENT

The author is indebted to members of the radio development section of the Electrical Communication Laboratory for assistance in undertaking this research. Thanks are also due to F. Bolinder of Massachusetts Institute of Technology and to Professor E. Löfgren of the Royal Institute of Technology, Stockholm, for sending me a copy of Bolinder's article.



Propagation in Ferrite-Filled Microstrip*

MORRIS E. BRODWIN†

Summary—The propagation constant of a ferrite-filled microstrip is measured as a function of the longitudinal static magnetic field. The results agree with the analysis by Van Trier of the infinite parallel plane waveguide filled with gyromagnetic media. The analysis is extended to anisotropies greater than 0.5. A simple relationship between propagation constant and anisotropy for the quasi-TEM mode with small spacing ($X \ll \lambda_0$) is noted. Cutoff spacings for higher modes are calculated. An apparatus for the measurement of propagation constant independently of interface reflections is described.

INTRODUCTION

PROPAGATION of electromagnetic waves in media possessing tensor permeability has been the subject of considerable investigation. This interest has been stimulated by the development of low-loss ferromagnetic materials called ferrites which easily exhibit electron spin resonance. Van Trier¹ has solved the case of a circular waveguide filled with ferrite and biased in the direction of propagation. He also analyzed in some detail the ferrite-filled parallel plane waveguide with a longitudinal magnetizing field. The case of circular waveguide filled with ferrite material and magnetized in the direction of propagation has also been treated by Kales.² Lax³ has investigated the rectangular waveguide partially filled with ferrite and transversely magnetized.

The principal experimental work with ferrites has been largely restricted to the circular and rectangular waveguide structures. The only reported work in stripline waveguide is that of Fix⁴ and Ardit⁵. Fix⁴ placed the ferrite material between two coupled strip-lines. When the stripline fields are in phase quadrature, a circularly polarized wave is produced in the fringing region. With a longitudinal static magnetic field, the structure exhibited nonreciprocal effects. Ardit⁵ symmetrically located the ferrite slab in a microstrip structure and took measurements of relative attenuation and phase shift. No attempt was made to explain quantitatively the experimental results.

The problem treated in this paper is the determina-

tion of the applicability of the parallel plane waveguide analysis to the wide strip ferrite-filled microstrip. More specifically, we attempt to determine how closely the variation in propagation constant with longitudinal magnetic field for microstrip follows the variation predicted by a parallel plane analysis of the quasi-TEM mode. The analysis of Van Trier is extended to include high values of anisotropy.

A simple relationship between anisotropy and propagation constant is derived for the quasi-TEM mode. Experiments are described for determining the propagation constant independent of the ferrite interface reflections.

ANALYSIS

We consider the medium to be a lossless dielectric with a tensor permeability

$$(\mu) = \begin{bmatrix} \mu_1 & -i\mu_2 & 0 \\ i\mu_2 & \mu_1 & 0 \\ 0 & 0 & \mu_3 \end{bmatrix}. \quad (1)$$

If the ferrite is demagnetized $\mu_3 = \mu_1$ and $\mu_2 = 0$; at saturation $\mu_3 = \mu_0$.

We commence with a cartesian coordinate system with the biasing magnetic field in the z direction. The fields are assumed to be of the form $u(x, y)e^{i\omega t - \Gamma z}$. Following Van Trier, the substitution of the tensor permeability into Maxwell's equations yields the coupled wave equations

$$\nabla_t^2 H_z + aH_z + bE_z = 0 \quad (2a)$$

and

$$\nabla_t^2 E_z + cE_z + dH_z = 0 \quad (2b)$$

where

$$a = \Gamma^2 + \omega^2 \epsilon \mu_1$$

$$b = -\omega \epsilon \frac{\mu_2}{\mu_1} \Gamma$$

$$c = \Gamma^2 + \omega^2 \epsilon \mu_1 \left[1 - \left(\frac{\mu_2}{\mu_1} \right)^2 \right]$$

$$d = \omega \mu_2 \Gamma.$$

By means of a change in variable

$$E_z = \alpha_1 + \alpha_2 \quad (3a)$$

$$H_z = K_1 \alpha_1 + K_2 \alpha_2 \quad (3b)$$

where K_1 and K_2 are chosen to uncouple the equations in α_1 and α_2 .

* Manuscript received by the PGMTT, June 3, 1957; revised manuscript received, October 10, 1957. This research was supported by the USAF through the Office of Scientific Research of ARDC.

† Radiation Lab., The Johns Hopkins University, Baltimore, Md.

¹ A. A. Van Trier, "Guided electromagnetic waves in anisotropic media," *Appl. Sci. Res.*, Vol. B-3, pp. 305-371; December, 1953.

² M. L. Kales, "Modes in waveguide containing ferrites," *J. Appl. Phys.*, vol. 24, pp. 604-608; May, 1953.

³ B. Lax, K. J. Button, and L. M. Roth, "Ferrite Phase Shifters in Rectangular Waveguide," M.I.T., Cambridge, Mass., Tech. Memo. No. 49; November, 1953.

⁴ O. W. Fix, "A balanced stripline isolator," 1956 IRE CONVENTION RECORD, pt. 5, pp. 99-105.

⁵ M. Ardit⁵, "Experimental determination of the properties of microstrip components," 1953 IRE CONVENTION RECORD, pt. 10, pp. 27-37.

Eqs. (2a) and (2b) can be written as

$$\nabla_t^2 \alpha_i + \sigma_i^2 \alpha_i = 0 \quad i = 1, 2 \quad (4)$$

where

$$\begin{aligned} \sigma_{1,2r^2} &= \frac{\sigma_{1,2r}^2}{\omega^2 \epsilon \mu_1} = \Gamma_r^2 + 1 - \frac{1}{2} \left(\frac{\mu_2}{\mu_1} \right)^2 \\ &\pm \left\{ \left(\frac{\mu_2}{\mu_1} \right) \left[\left(\frac{\mu_2}{2\mu_1} \right)^2 - \Gamma_r^2 \right]^{1/2} \right\}. \end{aligned} \quad (5)$$

Application of the boundary condition, $E_{tan} = 0$ yields

$$\alpha_1 + \alpha_2 = 0 \quad (6a)$$

and

$$\begin{aligned} \delta_2 \left[\frac{\partial}{\partial \tau} (\sigma_2^2 \alpha_1 + \sigma_1^2 \alpha_2) \right] - \delta_1 \left[\frac{\partial}{\partial \eta} (\sigma_2^2 \alpha_1 + \sigma_1^2 \alpha_2) \right] \\ + [\delta_1 a + \delta_3 d] \left[\frac{\partial}{\partial \eta} (\alpha_1 + \alpha_2) \right] = 0 \end{aligned} \quad (6b)$$

where

$$\begin{aligned} \delta_1 &= i\omega[\omega^2\epsilon(\mu_2^2 - \mu_1^2) - \mu_1\Gamma^2]/\delta \\ \delta_2 &= \omega\mu_2\Gamma^2/\delta \\ \delta_3 &= -i\omega^2\epsilon\mu_2\Gamma/\delta \\ \delta &= \{ \Gamma^2 + \omega^2\epsilon(\mu_1 + \mu_2) \} \{ \Gamma^2 + \omega^2\epsilon(\mu_1 - \mu_2) \}. \end{aligned}$$

$\partial/\partial\tau, \partial/\partial\eta$ are the tangential and normal derivatives. The symmetrical and antisymmetrical solutions of (4) are substituted into the boundary conditions, (6a) and (6b), and the resulting expressions evaluated on the boundary of Fig. 1. This process leads to two equations which are implicit relations involving the propagation constant and the anisotropy, μ_2/μ_1 .

Restricting the discussion to the antisymmetric solutions leads to the following relation involving Γ_r .

$$O_1 P_2 - O_2 P_1 = 0 \quad (7)$$

where

$$\begin{aligned} O_{1,2} &= \omega^2 \mu_1 \sqrt{\epsilon \mu_1} \sigma_{2,1r} [1 - U \sigma_{1,2r}^2] \\ U &= \frac{1 + \Gamma_r^2 - \left(\frac{\mu_2}{\mu_1} \right)^2}{(\Gamma_r^2 + 1)^2 - \left(\frac{\mu_2}{\mu_1} \right)^2} \\ P_{1,2} &= [e^{i\sigma_{1,2r} X_{or}} + e^{-i\sigma_{1,2r} X_{or}}] [e^{i\sigma_{2,1r} X_{or}} - e^{-i\sigma_{2,1r} X_{or}}] \end{aligned}$$

where

$$X_{or} = X_o \omega \sqrt{\epsilon \mu_1}.$$

Values of the propagation constant Γ_r are determined by choosing a suitable spacing and anisotropy and varying the propagation constant until the left-hand side of (7) is zero. Eq. (7) applies to the odd quasi-TE modes, and even quasi-TM modes as well as the quasi-TEM mode. The ambiguity between a correct

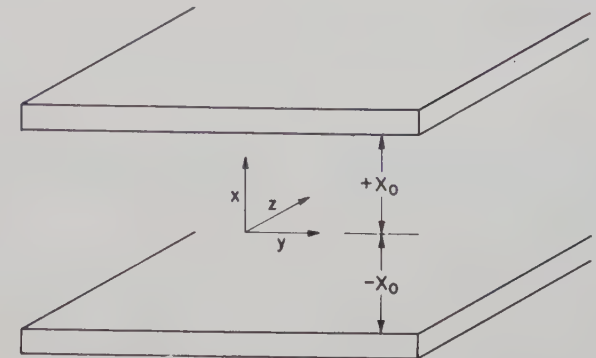


Fig. 1—Coordinates for parallel plane waveguide.

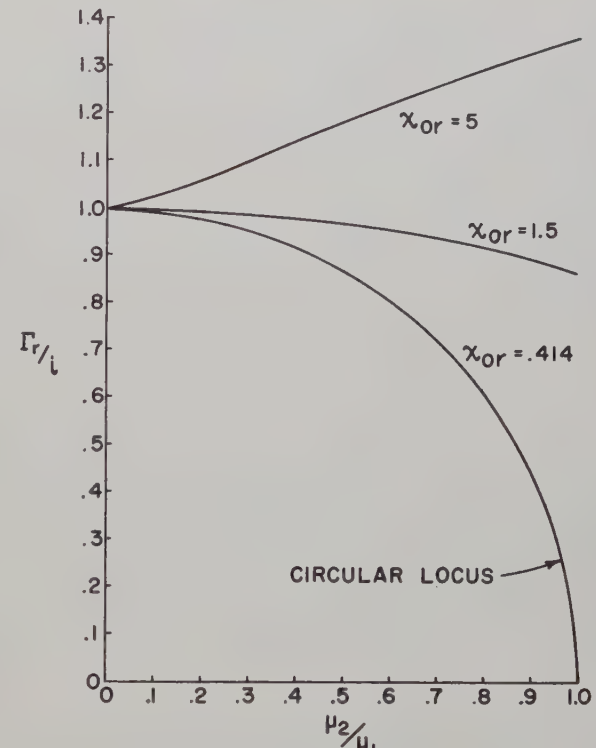


Fig. 2—Propagation constant vs anisotropy—quasi-TEM.

value of propagation constant and the mode with which it is related is resolved by starting the calculations with small anisotropy. The assumed values of propagation constant are chosen in the immediate region of the corresponding isotropic mode.

The propagation constant, Γ_r , for the quasi-TEM mode has been calculated for a range of X_{or} and μ_2/μ_1 , Fig. 2. The curve $X_{or} = 1.5$ corresponds to the behavior of the waveguide with approximately $\lambda/2$ spacing between the parallel planes. The wavelength, λ , is the intrinsic wavelength associated with the material. For spacings less than $\lambda/2$, the dependence of Γ_r on μ_2/μ_1 approaches a circular locus. Additional curves ($X_{or} = 0.1, 0.2, 0.3$) were calculated but are not displayed since they overlap the $X_{or} = 0.414$ curve. This result is useful for design purposes since it relates the propagation constant and anisotropy in a simple fashion.

For small spacing ($X_{or} \leq 0.414$)

$$\left(\frac{\mu_2}{\mu_1}\right)^2 + \left(\frac{\Gamma_r}{i}\right)^2 = 1. \quad (8)$$

The error between points calculated with (8) and points laboriously calculated with (7) is less than 0.9 per cent for small spacing.

For large spacing ($X_{or} = 5$), the trend is reversed. The propagation constant increases with anisotropy instead of decreasing. This peculiar behavior implies that the waveguide acts as a slow wave structure for large spacing and a fast wave structure for small spacing.

When the anisotropy is unity, the corresponding value of the propagation constant is undetermined. This result arises from the behavior of U as $\mu_2/\mu_1 \rightarrow 1$ and $\Gamma_r \rightarrow 0$. U can have any value depending upon the manner in which the variables approach the limit. The trend of the values for anisotropy less than unity and small spacing indicates that the propagation constant tends toward zero as the anisotropy tends toward unity. This result has been verified experimentally. For an anisotropy greater than unity, values of the propagation constant cannot be determined from (7) or its symmetric counterpart. For example, Fig. 3 is a plot of $O_1P_2 - O_2P_1$ vs Γ_r/i with $\mu_2/\mu_1 = 2$, $X_{or} = 0.414$. At low values of Γ_r/i , the function is imaginary and negative. As Γ_r/i increases, the functions tend toward infinity. At a larger value of Γ_r/i , the function starts again with negative real values. Since the function does not pass through zero, the waveguide is beyond cutoff for anisotropies greater than unity.

The critical spacings for the higher modes is determined by setting Γ_r equal to zero in (7) and solving for X_{or}' .

$$X_{or}' = \frac{n\pi}{2 \left[1 - \left(\frac{\mu_2}{\mu_1} \right)^2 \right]^{1/2}} \text{ even } n. \quad (9)$$

When the process is repeated for the symmetric solutions, the same result is obtained, but with odd n . The mode titles are assigned by comparing the result with the solutions for the isotropic case.

The critical spacing for the quasi-TM_n modes are shown in Fig. 4. The critical spacings for the quasi-TE modes are the same as the critical spacings for the quasi-TM modes. This degeneracy in the isotropic case is preserved in the anisotropic case. If we choose a spacing much smaller than $\lambda/2$ to insure that the quasi-TEM mode is the only propagating mode, then an increase in anisotropy does not permit the propagation of higher modes. This result follows from the increase in critical spacing with increasing anisotropy.

EXPERIMENTAL PROCEDURE

The experimental problem is to determine how closely the ferrite-filled microstrip approximates the theoret-

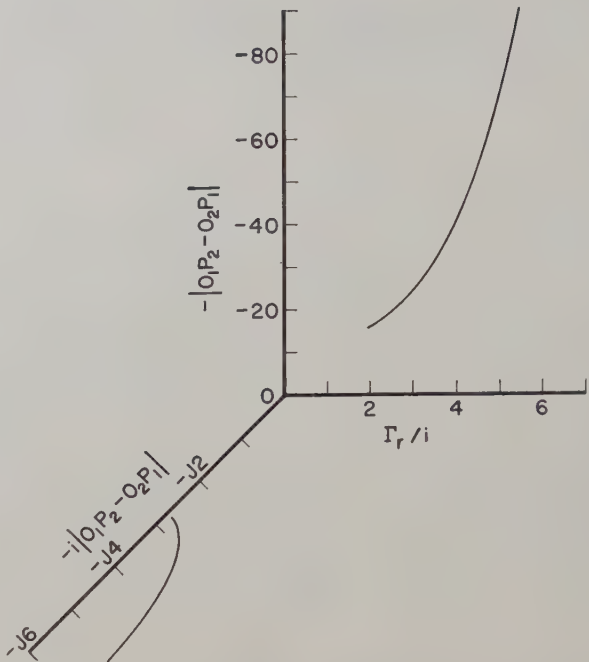


Fig. 3—Behavior for $(\mu_2/\mu_1) > 1$.

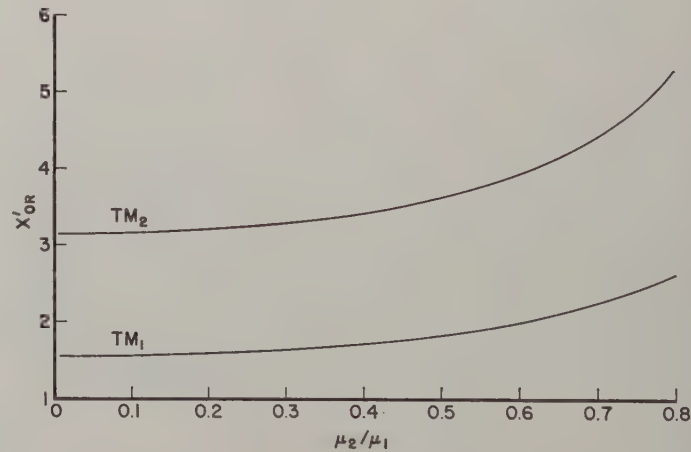


Fig. 4—Critical spacings for the higher modes.

ical predictions of the parallel plane waveguide. The technique consists of placing a ferrite-filled microstrip in a longitudinal magnetic field and determining the relationship between the propagation constant and the magnetic field. In order to approach as closely as possible the parallel plane case, the upper strip width is approximately $\lambda/2$. The microstrip geometry is shown in Fig. 5.

The principal experimental difficulties are caused by the necessity for placing the microstrip within a solenoid. The space limitations prohibit the use of direct field sampling techniques. If measurements are taken external to the ferrite section, the usual phase sensitive bridges are subject to errors caused by variable dielectric-ferrite interface reflections. To avoid these difficulties, a perturbation technique was employed. This apparatus consists of a movable small reflector mounted

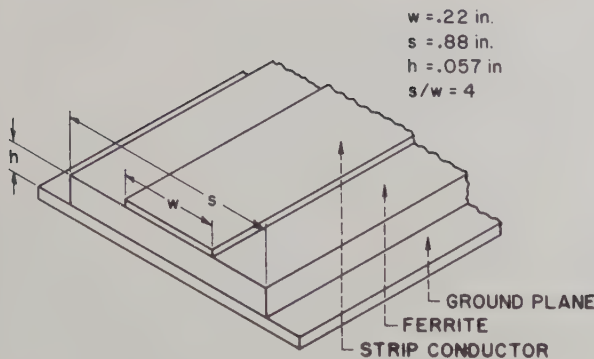


Fig. 5—Microstrip geometry.

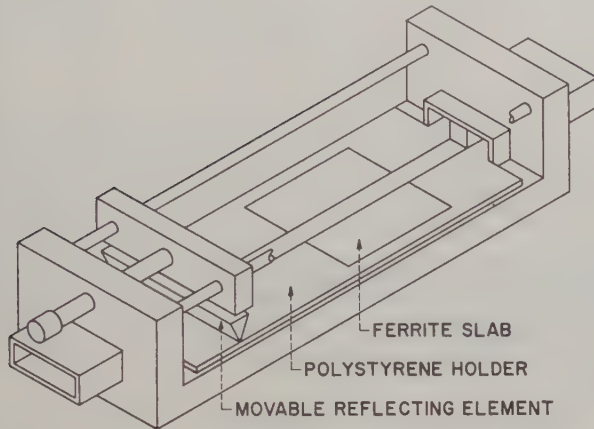


Fig. 6—Apparatus for perturbation technique.

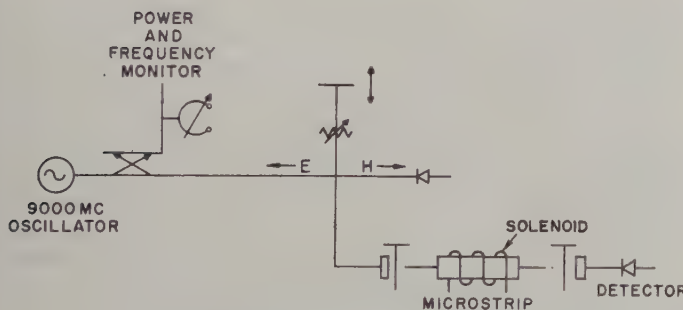


Fig. 7—Phase sensitive bridge.

close to the upper plane of the stripline, Fig. 6. The metal wedge reflects part of the fringing field, and the resultant reflections are determined by a microwave bridge, Fig. 7. The position of the reflecting element is controlled by means of a lead screw. When the reflecting element is displaced by $\lambda_g/2$, the total reflection from the sample is unchanged. In this manner, the interface reflections as well as any reflections from the transitions do not affect the measurement.

The samples were prepared in the following manner. To insure that higher modes would not propagate, the spacing between upper and lower planes of the stripline was chosen as 0.057 inch for a dielectric constant of 7.3. Rectangular samples, $\frac{7}{8} \times 1\frac{1}{2} \times 0.057$ inch, were

prepared and fitted into a polystyrene slab. The dielectric sample holder was cut with linear tapers at each end to reduce reflections from the transitions. The upper and lower conducting planes were prepared by spraying silver paint on the masked sample holder and electroplating a 50-micron copper film. The ferrite employed in these experiments was "R-1," manufactured by General Ceramic and Steatite. The dielectric constant of the ferrite, $\epsilon = 7.3$, was measured by a standard waveguide technique and by the microstrip method previously described. This value is considerably different from the nominal value of 13. The discrepancy is possibly due to the large batch to batch variation of early ferrite materials.

EXPERIMENTAL RESULTS

The phase constant was measured for magnetic fields between 0 and 1700 oersteds. The results of these measurements are shown in Fig. 8. To determine the relative transmission loss, a matched detector was placed at the output transition and the detected energy was noted for different values of applied field. These results are shown in Fig. 9. No significant difference in phase constant or insertion loss was noted when the experiments were repeated with a reversed magnetic field.

DISCUSSION

The variation of phase constant with applied magnetic field agrees, qualitatively, with the predicted behavior of the ferrite-filled parallel plane waveguide. Starting with zero applied field, the phase constant should decrease as the anisotropy is increased, Fig. 2, $X_{or} = 0.414$. At the magnetic field at which the anisotropy is unity, the propagation constant is zero. Above this point, the ferrite section is beyond cutoff. The experimental data shows that the phase constant decreased until a field of 1025 oersteds was reached. The transmission data indicates that the stripline was cut off at 1025 oersteds. The maximum field was 1700 oersteds. The theory, as previously developed, cannot predict losses since it was assumed that μ_1 and μ_2 are real quantities. Consequently, the propagation constant is a pure imaginary and attenuation is not expected. The general trend of the relative transmission, Fig. 9 shows an increase in loss with an increase in magnetic field. From 1025 to 1700 oersteds, the readings remained constant. This small residual transmission is attributed to leakage between the microstrip-waveguide transitions. The fine variation in transmission is produced by the changing wavelength in conjunction with the interface reflections. This is the typical interference phenomenon observed with any resonant structure with varying phase shift.

It is possible to obtain a theoretical expression for the variation of phase constant as a function of the applied magnetic field subject to the following simplifying assumptions:

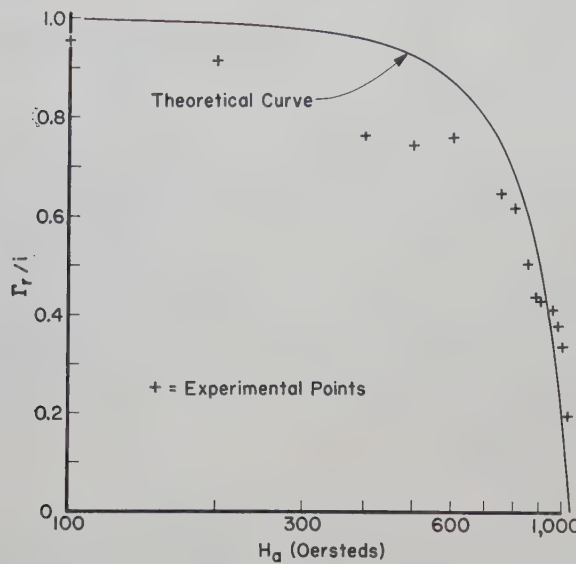


Fig. 8—Phase constant vs applied field.

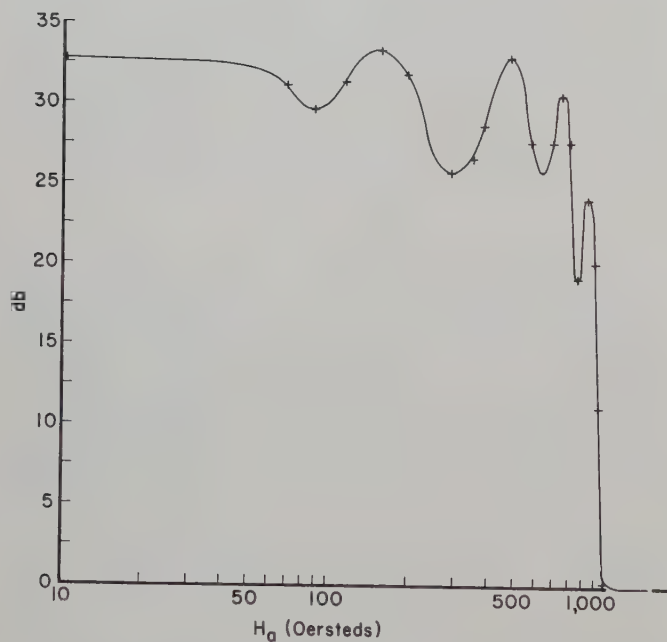


Fig. 9—Relative transmission vs applied field.

1) The static field inside the sample is assumed to be homogeneous. The effects of demagnetization can be expressed by a demagnetizing factor. Since the sample is a rectangular parallelepiped, the internal field is actually inhomogeneous, but this effect is neglected.

2) The magnetic behavior can be expressed by a constant magnetic susceptibility. This assumption is approximately correct only in the region of saturation.

With these assumptions, a relationship between μ_2/μ_1 and the applied field, H_a , can be determined.

The anisotropy is related to the applied field by (see Appendix)

$$\frac{\mu_2}{\mu_1} = \frac{\omega\gamma(1+NK)H_a}{\gamma^2H_a^2(1+K) - \omega^2(1+NK)^2} \quad (10)$$

where

ω = angular frequency

γ = gyromagnetic ratio

K = magnetic susceptibility

N = demagnetization factor

H_a = applied static magnetic field.

If the ferrite slab can be represented by an equivalent ellipsoid of revolution, the demagnetization factor can be calculated. With the dimensions of the slab used in the experiments, $N = 3 \times 10^{-3}$. In the region of saturation, K is on the order of unity and $NK \ll 1$. The demagnetization effects, therefore, are neglected. The relationship between anisotropy and H_a is then given by

$$\frac{\mu_2}{\mu_1} = \frac{\omega\gamma KH_a}{\gamma^2H_a^2(1+K) - \omega^2}. \quad (11)$$

The susceptibility is determined by assuming that cutoff occurs when the anisotropy is unity and solving (11) for K_c for cutoff at 1025 oersteds. The calculated value for K_c is 2.45. When this value of K is substituted into (11), the resultant relationship between μ_2/μ_1 and H_a represents the theoretical behavior of the anisotropy with the applied field. To determine Γ_r/i as a function of H_a , (11) is substituted into (8).

$$\left(\frac{\Gamma_r}{i}\right)^2 = 1 - \left[\frac{\omega\gamma K_c H_a}{\gamma^2 H_a^2 (1 + K_c) - \omega^2} \right]. \quad (12)$$

This equation was employed for drawing the theoretical curve of Fig. 8.

In general, the theoretical curve follows the trend of the data. The principal discrepancy is in the region between 100 and 600 oersteds, where the experimental points are lower than the predicted value. This discrepancy may be a result of the assumption that K remained constant. In the low-field region, where the material is not saturated, K is larger than the chosen value. Increasing K decreases the right-hand side of (12) and would yield a smaller value for Γ_r/i .

A question arises as to how much of the insertion loss is due to a cutoff effect and how much is due to radiation from the microstrip. With this experimental technique, it is not possible to distinguish between the two effects. However, the fact that the experimental points agree very closely with the theoretical values in the region of large insertion loss might indicate that the cutoff effect predominates.

APPENDIX

The relationship between the applied magnetic field and anisotropy is derived from Polder's equations⁶ for μ_1 and μ_2 :

⁶ D. Polder, "On the theory of ferromagnetic resonance," *Phil. Mag.*, vol. 40, pp. 99-115; January, 1949.

$$\mu_1 = \mu_0 \left[1 - \frac{\gamma M \omega_0}{\omega_0^2 - \omega^2} \right] \quad (1)$$

$$\mu_2 = \frac{\mu_0 \gamma M \omega}{\omega_0^2 - \omega^2} \quad (2)$$

where

$$\omega_0 = \gamma H_1$$

H_1 = internal static magnetic field

μ_0 = permeability of free space

γ = gyromagnetic ratio

M = magnetic polarization density

ω = angular frequency.

The anisotropy, μ_2/μ_1 , is related to the internal field by

$$\frac{\mu_2}{\mu_1} = \frac{\gamma M \omega}{\omega_0^2 - \gamma M \omega_0 - \omega^2}. \quad (3)$$

Assuming a demagnetization factor N , the internal field is related to the external field. Expressing the magnetic polarization density in terms of a magnetic susceptibility K , and the internal field, the final equation is

$$\frac{\mu_2}{\mu_1} = \frac{\omega \gamma K (1 + NK) H_a}{\gamma^2 H_a^2 (1 + K) - \omega^2 (1 + NK)^2}. \quad (4)$$

ACKNOWLEDGMENT

The author is indebted to Dr. D. D. King, Dr. M. I. Aissen, and other colleagues for their stimulating discussions and helpful criticism.

An Improved Method for the Determination of Q of Cavity Resonators*

AMARJIT SINGH†

Summary—The various Q factors and circuit efficiency of a cavity resonator can be evaluated from standing-wave measurements on a transmission line or waveguide coupled to the resonator. In the usual method, measurement errors near the half-power points have an unduly large influence on the result. This paper describes a method in which this type of error is avoided.

In the new method, vswr and position of minimum at various frequencies are plotted on a Smith chart and a circle is drawn through the points. This circle is suitably rotated around the center of the chart and a value of equivalent susceptance is read off for each frequency. The graph of susceptance vs frequency is a straight line, from whose slope the Q factors are evaluated.

The underlying theory of the above method is discussed and typical experimental results are presented. Charts of parameters required in the calculations are given.

INTRODUCTION

THE measurement of the Q of cavity resonators finds many applications in the field of microwave electronics, as well as in physical research. Several methods of determination of Q have been developed.¹⁻³ Among these is the method involving measure-

* Manuscript received by the PGMTT, June 19, 1957; revised manuscript received, August 6, 1957.

† Central Electronics Engineering Res. Inst., Pilani, India. Formerly with the Natl. Physical Lab. of India, New Delhi, India.

¹ C. G. Montgomery, "Technique of Microwave Measurements," McGraw-Hill Book Co., Inc., New York, N. Y.; 1947.

² H. M. Barlow and A. L. Cullen, "Microwave Measurements," Constable and Co., London, Eng.; 1950.

³ M. Wind and H. Rapaport, "Handbook of Microwave Measurements," Polytechnic Institute of Brooklyn, Brooklyn, N. Y., vols. I and II; 1955.

ments on standing waves in a transmission line or waveguide coupled to the resonator. The method is not a quick one; however, it has the advantage of supplying the most complete information about the resonator and the coupling system. The losses inside the cavity, the losses in the coupling system, and the power coupled into the transmission line, can all be separated out.⁴ This information is indispensable in such applications as design of microwave tubes, where the circuit efficiency is an important parameter.

After data have been obtained on the variation of vswr and the position of voltage minimum in the line as functions of frequency, it is possible to determine the frequencies which correspond to the half-power points. The Q factors can then be evaluated. The previously developed methods of obtaining the half-power frequencies employ a curve showing vswr vs frequency or one showing the position of the minimum vs frequency. On these curves, one reads off the frequencies which correspond to certain values of vswr or of shift in the position of the minimum. It is to be noted that these curves are not geometrically simple ones, and that any errors in the observations near the half-power points have a large influence on the result. In fact, a discrepancy may be observed between the results obtained

⁴ L. Malter and G. R. Brewer, "Microwave Q measurements in the presence of series losses," *J. Appl. Phys.*, vol. 20, pp. 918-925; October, 1949.

from the vswr curve and the position of minimum curve, based on the same set of observations. It was a rather large discrepancy of this kind which led to the formulation of the method described here.

In the new method, the data yield one set of points which lie on a circle and another set which lie practically on a straight line. Three parameters relating to the circle and the line are used in subsequent calculations. The accuracy of these parameters is thus governed by the readings taken at all frequencies. Also, the observations on vswr as well as position of minimum are utilized simultaneously in the determination of Q . The method has been worked out to take losses in the coupling system into account.

The procedure is illustrated by examples and certain computed parameters are presented in charts. A study relating to the linearity of the curve which is assumed to be a straight line is contained in the Appendix.

EQUIVALENT CIRCUIT AND DEFINITIONS

It has been shown⁵ that a cavity resonator and its coupling system can be represented at frequencies in the vicinity of a resonant mode by an equivalent circuit given in Fig. 1(a). Here the series resistance represents losses in the transmission line and coupling system. The series reactance can be made zero by a suitable choice of the reference plane in the transmission line. With such a choice, the equivalent circuit in the case of a matched line coupled to the resonator is given by Fig. 1(b).

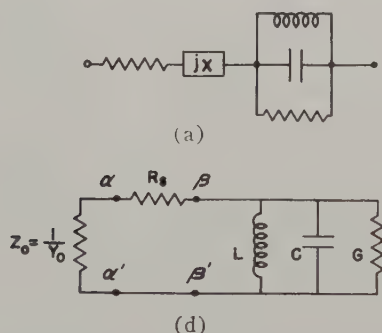


Fig. 1—(a) Equivalent circuit for a cavity resonator near a mode of resonance. (b) Equivalent circuit for a cavity resonator coupled to a matched transmission line, at a reference plane so chosen as to make $X=0$.

Also, it was shown⁵ that if the vswr and position of minimum in the transmission line are determined as functions of frequency near resonance and if the corresponding points are plotted on a Smith chart, they lie on a circle, as shown in Fig. 2. A shift in the location of the reference plane on the transmission line is equivalent to a rotation of this circle around the center of the Smith chart. Let the circle be rotated in such a way

⁵ C. G. Montgomery, R. H. Dicke, and E. M. Purcell, "Principles of Microwave Circuits," McGraw-Hill Book Co., Inc., New York, N. Y., pp. 226-227; 1948.

that its center lies on the radius of the Smith chart passing through the infinity point. The circle then represents either the admittance of an equivalent parallel resonant circuit, or the impedance of an equivalent series resonant circuit. The former representation is used here and the circle is termed the admittance circle.

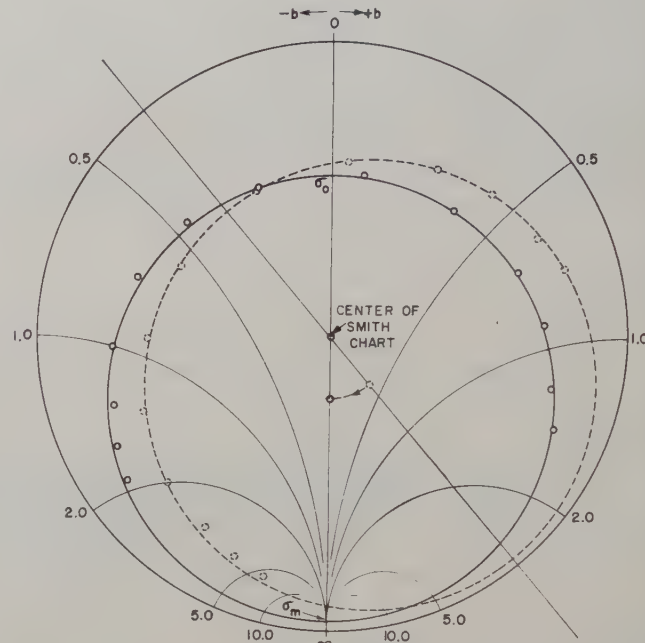


Fig. 2—Admittance circle on Smith chart, as drawn first and after rotation corresponding to suitable choice of reference plane.

At the resonance point, the vswr is a minimum and is denoted by σ_0 . At frequencies very far away from resonance the vswr is a maximum and is denoted by σ_m . Two cases can be distinguished,⁴ depending upon whether or not the circle just described encloses the center of the Smith chart. When the center is enclosed, the power loss in Z_0 is greater than that in R_s and G . When the center is not enclosed, the power loss in Z_0 is less than that in R_s and G . The two cases are referred to as "overcoupled" and "undercoupled" respectively.

The values of σ_m and σ_0 are related to the parameters of the equivalent circuit as follows:

$$\sigma_m = \frac{Z_0}{R_s} = \frac{1}{r_s}, \quad (1)$$

$$\sigma_0 = \left(R_s + \frac{1}{G} \right) / Z_0 = r_s + \frac{1}{g}, \quad (2)$$

in the overcoupled case, and

$$1/\sigma_0 = r_s + \frac{1}{g}, \quad (3)$$

in the undercoupled case, where r_s and g are normalized values of R_s and G respectively.

OUTLINE OF THE METHOD

It is shown in the Appendix that near resonance the normalized susceptance b_α , appearing to the right at terminals $\alpha\alpha'$, varies practically linearly with frequency. The values of b_α at various frequencies and of σ_0, σ_m can be determined from the admittance circle drawn on a Smith chart. If b_α is plotted as a function of f , an accurate value of df/db_α can be obtained from the slope of the curve.

Next, the Q factor denoted by Q_{00} by Malter and Brewer is evaluated. Q_{00} takes into account only the losses within the resonator proper (represented by G in the equivalent circuit). It can be determined as follows:

$$Q_{00} = \frac{f_0}{f_2 - f_1}, \quad (4)$$

where f_1 and f_2 are the frequencies at which $b_\beta = \pm g$, b_β being the normalized susceptance appearing towards the right at the terminals $\beta\beta'$. Let the value of b_α , when $b_\beta = g$, be denoted by $(b_\alpha)_{00}$. Then Q_{00} is given by

$$Q_{00} = \frac{f_0}{2 \frac{df}{db_\alpha} (b_\alpha)_{00}}. \quad (5)$$

The other Q factors can be evaluated from a knowledge of $Q_{00}, \sigma_m, \sigma_0$, through the use of a procedure which is the reverse of that described by Malter and Brewer.⁴ The circuit efficiency can also be determined in the usual way.

EVALUATION OF $(b_\alpha)_{00}$

From the equivalent circuit of Fig. 1(b), it can be seen that the normalized admittance y_α appearing to the right at terminals $\alpha\alpha'$ is given by:

$$y_\alpha = \left(r_s + \frac{1}{g + jb_\beta} \right)^{-1}. \quad (6)$$

This gives

$$b_\alpha = \frac{b_\beta}{(1 + r_s g)^2 + r_s^2 b_\beta^2}. \quad (7)$$

The value of b_α , when b_β takes the value g , is given by:

$$(b_\alpha)_{00} = \frac{g}{1 + 2r_s g + 2r_s^2 g^2}. \quad (8)$$

Also, from (1) through (3), we have:

$$g = \begin{cases} \sigma_m/(\sigma_0\sigma_m - 1), & \text{for overcoupled case,} \\ \sigma_m\sigma_0/(\sigma_m - \sigma_0), & \text{for undercoupled case,} \end{cases} \quad (9)$$

and

$$r_s g = \begin{cases} 1/(\sigma_0\sigma_m - 1) & \text{for overcoupled case,} \\ \sigma_0/(\sigma_m - \sigma_0), & \text{for undercoupled case.} \end{cases} \quad (10)$$

Substituting (9) and (10) in (8), we get:

$$(b_\alpha)_{00} = \begin{cases} \frac{\sigma_m(\sigma_0\sigma_m - 1)}{(\sigma_m^2\sigma_0^2 + 1)}, & \text{for overcoupled case,} \\ \frac{\sigma_0\sigma_m(\sigma_m - \sigma_0)}{(\sigma_m^2 + \sigma_0^2)}, & \text{for undercoupled case.} \end{cases} \quad (11)$$

In the limiting case of zero series losses, σ_m is infinity and $(b_\alpha)_{00}$ is equal to $1/\sigma_0$ for the overcoupled case and to σ_0 for the undercoupled case. For finite σ_m , one may put

$$(b_\alpha)_{00} = \begin{cases} \frac{F_0}{\sigma_0}, & \text{for overcoupled case,} \\ F_u \sigma_0, & \text{for undercoupled case,} \end{cases} \quad (12)$$

where

$$F_0 = \frac{\sigma_0\sigma_m(\sigma_0\sigma_m - 1)}{(\sigma_m^2\sigma_0^2 + 1)}, \quad (13)$$

$$F_u = \frac{\sigma_m(\sigma_m - \sigma_0)}{\sigma_m^2 + \sigma_0^2}. \quad (14)$$

The values of the factors F_0 and F_u have been computed for various combinations of the values of σ_m and σ_0 , and are given in Fig. 3(a) and 3(b) (next page).

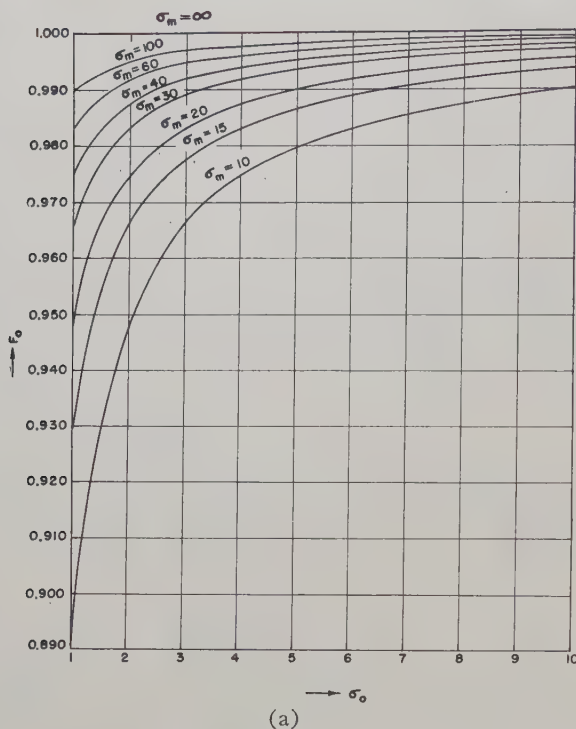
EXPERIMENTAL PROCEDURE

Observations are first taken on the variation of vswr and the position of the minimum with frequency in the vicinity of resonance. The position of the minimum on the transmission line at a frequency near resonance is arbitrarily chosen as a reference point. The shift of the minimum with respect to this point is determined and is corrected for dispersion in the portion of transmission line between the cavity and the probe.⁶ The corrected shift is expressed in terms of wavelength. With these data, points corresponding to various frequencies are plotted on a Smith chart. A circle is drawn through these points. When the best circle is drawn through the points, any large errors in standing-wave measurements tend to be smoothed out. The points and the circle are then swung around the center of the Smith chart, so as to bring the center of the admittance circle on that radius of the Smith chart which passes through the infinity point.

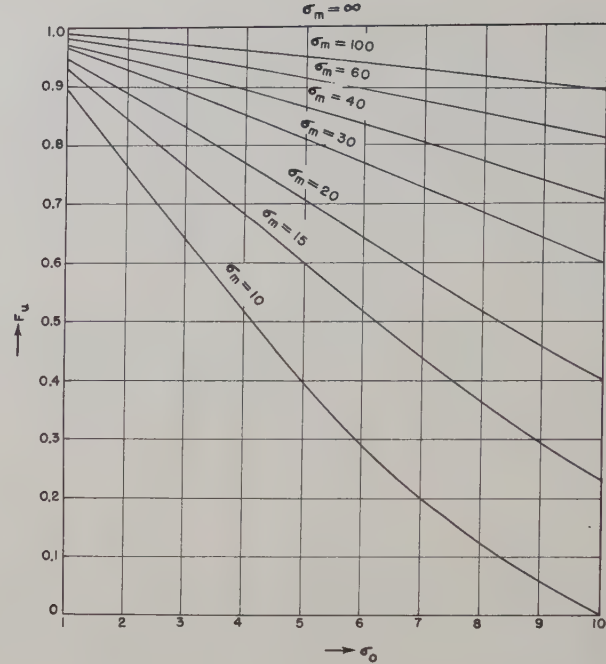
The above mentioned procedure involving rotation of the admittance circle can be conveniently performed if a piece of tracing paper is attached to the Smith chart. The points, the circle, and the center of the Smith chart are plotted on the tracing paper, which can then be easily rotated about the center of the Smith chart.

The values of b_α corresponding to each frequency, and

⁶ *Ibid.*, p. 339.



(a)



(b)

Fig. 3—Functions to evaluate normalized susceptance as seen from terminals $\alpha\alpha'$, when that seen from $\beta\beta'$ is equal to g :(a) for overcoupled case, $(b_\alpha)_{00} = F_0/\sigma_0$, where

$$F_0 = \frac{\sigma_0 \sigma_m (\sigma_0 \sigma_m - 1)}{(\sigma_m^2 \sigma_0^2 + 1)},$$

(b) for undercoupled case, $(b_\alpha)_{00} = F_u \sigma_0$, where

$$F_u = \frac{\sigma_m (\sigma_m - \sigma_0)}{\sigma_m^2 + \sigma_0^2}.$$

also the values of σ_0 , σ_m , can now be read off from the Smith chart.

The values of b_α are plotted as a function of frequency. In drawing a straight line through them, any large errors in frequency determination also tend to be smoothed out. The slope of the line gives db_α/df and the value of f at $b_\alpha = 0$, gives f_0 .

After it is decided whether the case is one of overcoupling or undercoupling, as explained earlier, the value of $(b_\alpha)_{00}$ is determined from (12) and Fig. 3(a) and 3(b). Q_{00} is obtained by a substitution of the values found for df/db_α , f_0 , and $(b_\alpha)_{00}$ in (5).

Q_0 and Q_L can then be derived from the following relations given by Malter and Brewer.⁴

$$Q_0 = \begin{cases} Q_{00}/D_0, & \text{for overcoupled case,} \\ Q_{00}/D_u, & \text{for undercoupled case,} \end{cases} \quad (15)$$

where

$$D_0 = 1 + \frac{\sigma_0 \sigma_m - 1}{(1 + \sigma_m)^2}, \quad (16)$$

and

$$D_u = 1 + \frac{\sigma_m - \sigma_0}{\sigma_0 (1 + \sigma_m)^2}. \quad (17)$$

Also,

$$Q_L = \begin{cases} Q_0/(1 + \sigma_0)H_0, & \text{for overcoupled case,} \\ Q_0/(1 + 1/\sigma_0)H_u, & \text{for undercoupled case,} \end{cases} \quad (18)$$

where

$$H_0 = \frac{\sigma_m + 1}{\sigma_m + \sigma_0 + 2}, \quad (19)$$

and

$$H_u = \frac{\sigma_m + 1}{\frac{1}{\sigma_m + \frac{1}{\sigma_0}} + 2}. \quad (20)$$

EXAMPLES

The procedure just described has been tried out in a large number of cases in *S* band and also in the uhf region. The admittance circle and the b_α vs f curve obtained in a typical case, in the uhf region, are shown in Figs. 2 and 4, respectively. Fig. 2 shows the admittance circle as plotted in its initial position and also after rotation. Fig. 4 shows the b_α vs f curve which is nearly a straight line over a range of frequencies about six times ($f_1 - f_2$). Relevant parameters for this case are tabulated in Table I.

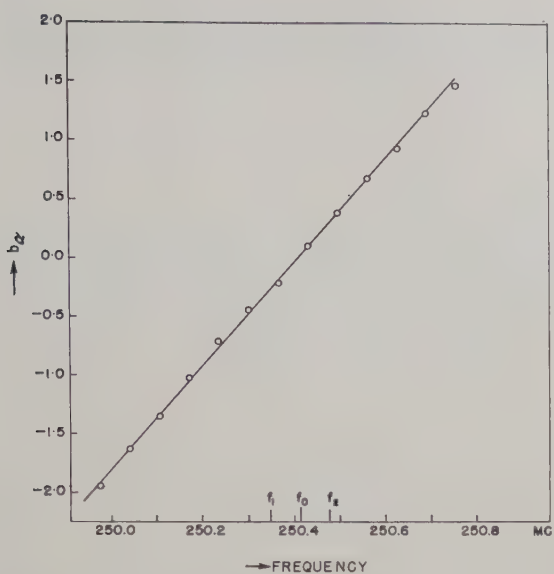


Fig. 4—Plot of normalized susceptance seen at reference plane as a function of frequency.

than 2 per cent between the half-power frequencies, for $Q_L = 25$, $\sigma_m = 1$, and $\sigma_n = 20$. Under normal conditions the values of Q_L , σ_m , and coupling are greater than those assumed above. Thus b_α varies linearly with f over a frequency range substantially larger than the separation between half-power frequencies.

All the data over this extended frequency range contribute to the accuracy of the final result. The accuracy is somewhat reduced by the fact that error can be introduced when rotating the admittance circle on the Smith chart and in reading off susceptance values. However, it can be seen from the results presented in Table II and Table III that there is an over-all decrease in the standard deviation, when the new method is used.

The difference between the mean values obtained by using the two methods needs further investigation. Errors in the absolute values of vswr can cause such a difference. It is also possible that the difference arises

TABLE I

f_0	σ_m	σ_0	F_0	$(b_\alpha)_{00}$	df/db_α	Q_{00}	Q_0	Q_L	Circuit efficiency
250.4 mc	100	3.45	0.996	0.288	0.226 mc	1931	1875	434	76.8 per cent

TABLE II

VALUES OF Q_L FOR THE INDIVIDUAL SETS OF READINGS

Set no.	Q_L as determined by the new method	Q_L as determined by the method of Malter and Brewer
1	999	975
2	978	1045
3	1010	1065
4	1020	1112
5	977	976
6	1050	1060
7	1012	1155
8	990	1011
9	996	1125
10	1025	1047

In order to determine the accuracy obtained by using the new method, as compared with that obtained by using the method given by Malter and Brewer,⁴ ten sets of observations were taken on a cavity with a resonant mode in the *S* band. The values of Q_L obtained from the individual sets of data, using the two methods, are tabulated in Table II. The values of parameters deduced from all the sets are given in Table III. It can be seen that the standard deviation (also referred to as root mean square deviation) obtained by the new method is less than one half of that obtained by the half-power point method.

DISCUSSION OF ACCURACY

An analysis given in the Appendix shows that the variation of b_α with f deviates from linearity by less

TABLE III

VALUES OF PARAMETERS DEDUCED FROM ALL THE SETS

Parameter	Value from new method	Value from Malter and Brewer's method
f_0 (overcoupled case)	2.892 kmc	
σ_0	2.46 to 2.57	
σ_m	100 or above	
Mean Q_L	1006	1057
Standard deviation of Q_L	21	58
Mean Q_0	3470	3640
Standard deviation of Q_0	80	190
Mean Q_{00}	3520	3700
Standard deviation of Q_{00}	90	210

because the simplified equivalent circuit used as a common starting point for the two methods is not an exact representation of the cavity resonator.

CONCLUSION

A method of evaluating the Q of cavity resonators from vswr data has been presented. The accuracy of the final result does not depend unduly on readings taken close to the half-power points, but upon all the readings of vswr as well as position of minimum. Any large errors are smoothed out at two stages in the procedure. This procedure has been worked out to cover the case in which losses in the transmission line and the coupling system are taken into account, and these losses can be isolated from other losses. The method is particularly suitable for applications in which accurate values of Q_L , Q_0 , Q_{00} , Q_{ext} , and the circuit efficiency are required.

APPENDIX

LINEARITY OF VARIATION OF b_α WITH FREQUENCY

Let us first consider the variation of b_β with frequency

$$b_\beta = \frac{1}{Y_0} \left(\omega C - \frac{1}{\omega L} \right)$$

$$= \frac{1}{Y_0} \sqrt{\frac{C}{L}} \frac{2\delta}{f_0} \left(1 + \frac{\delta}{2f_0} \right) \left(1 + \frac{\delta}{f_0} \right)^{-1},$$

where

$$\delta = f - f_0.$$

or

$$b_\beta = \frac{1}{Y_0} \sqrt{\frac{C}{L}} \frac{2\delta}{f_0} \left(1 - \frac{\delta}{2f_0} + \text{higher order terms in } \frac{\delta}{f_0} \right)$$

$$= \frac{1}{Y_0} \sqrt{\frac{C}{L}} \frac{2\delta}{f_0} \left(1 - \frac{\delta}{\delta_L} \frac{1}{4Q_L} + \dots \right), \quad (21)$$

where $2\delta_L = f_0/Q_L$ = difference between half-power frequencies. Also, from (7) we have

$$b_\alpha = \frac{b_\beta}{(1 + r_s g)^2 + r_s^2 b_\beta^2}$$

$$= \frac{b_\beta}{(1 + r_s g)^2} \left[1 - \left(\frac{r_s b_\beta}{1 + r_s g} \right)^2 + \dots \right].$$

In the second term in the square brackets, a first-order approximation for b_β can be used since the second term will be small in comparison with the first term. As shown by (21), b_β is proportional to δ , to a first approximation, and also $b_\beta \approx (1+g)$, for $\delta = \delta_L$. Thus to a first approximation, $b_\beta = (1+g)\delta/\delta_L$.

Making this substitution in the second term in the square brackets, we get:

$$b_\alpha = \frac{b_\beta}{(1 + r_s g)^2} \left[1 - \left(\frac{r_s}{1 + r_s g} \right)^2 (1 + g)^2 \left(\frac{\delta}{\delta_L} \right)^2 + \dots \right].$$

Substituting for r_s and g from (1) and (9), and for the remaining factor b_β from (21), and neglecting⁷ higher order terms in $1/\sigma_m$, we get:

⁷ The exact expressions for coefficients of $(\delta/\delta_L)^2$ are

$[(\sigma_0\sigma_m + \sigma_m^{-1})/(\sigma_0\sigma_m^2)]^2$ and $[(\sigma_m + \sigma_m\sigma_0 - \sigma_0)/\sigma_m^2]^2$

for the overcoupled and undercoupled cases, respectively. The simpler expressions mentioned above give good approximations since σ_m is normally $\gg 1$, and since the coefficients in question are themselves correction terms.

$$b_\alpha = K_0 \delta \left(1 - \frac{\delta}{\delta_L} \frac{1}{4Q_L} + \dots \right)$$

$$\cdot \left[1 - \left(\frac{\sigma_0 + 1}{\sigma_0\sigma_m} \right)^2 \left(\frac{\delta}{\delta_L} \right)^2 + \dots \right], \quad (22)$$

for the overcoupled case, and

$$b_\alpha = K_u \delta \left(1 - \frac{\delta}{\delta_L} \frac{1}{4Q_L} + \dots \right)$$

$$\cdot \left[1 - \left(\frac{1 + \sigma_0}{\sigma_m} \right)^2 \left(\frac{\delta}{\delta_L} \right)^2 + \dots \right], \quad (23)$$

for the undercoupled case, where,

$$K_0 = \frac{1}{Y_0} \sqrt{\frac{C}{L}} \frac{2}{f_0} \left(\frac{\sigma_0\sigma_m - 1}{\sigma_0\sigma_m} \right)^2, \quad (24)$$

and

$$K_u = \frac{1}{Y_0} \sqrt{\frac{C}{L}} \frac{2}{f_0} \left(\frac{\sigma_m - \sigma_0}{\sigma_m} \right)^2. \quad (25)$$

As K_0 and K_u do not depend upon f , it can be seen that b_α is proportional to δ to a first approximation. The correction terms have been expressed as functions of the ratio of $(f-f_0)$ to the difference between half-power frequencies, δ/δ_L . It is also seen that the corrections are smaller for larger values of Q_L , for smaller series losses (i.e., larger σ_m), and for greater coupling between cavity and line (i.e., larger σ_0 for overcoupled case and smaller σ_0 for undercoupled case).

In particular, if $Q_L = 25$, then the correction due to the first factor is less than 1 per cent over a range of frequencies lying between the half-power points. Similarly if $\sigma_m = 20$, then at critical coupling, $\sigma_0 = 1$, the correction due to the second factor is less than 1 per cent over the same range. The deviations from linearity would be largest when coupling is small and at the same time the series losses are appreciable.

Thus for most practical purposes, the variations of b_α with frequency may be considered linear to a good approximation, over frequency ranges of interest.

ACKNOWLEDGMENT

The author is grateful to K. S. Krishnan and K. N. Mathur for their kind encouragement. He is also indebted to N. C. Vaidya, M. S. Kunchitham, and R. A. Rao who used the method in a large number of cases and thus helped in its verification.



Characteristic Impedances of the Slotted Coaxial Line*

JADWIGA SMOLARSKA†

Summary—The characteristic impedance for the two possible TEM modes is calculated for a slotted coaxial line whose outer walls have a zero thickness. Conformal mapping is used in the calculations. The characteristic impedance for a slotted coaxial line is calculated in an approximate way for outer wall thickness different from zero.

INTRODUCTION

As is known, in a cylindrical system of conductors having the cross section in Fig. 1(a) two modes of TEM waves can propagate. These modes correspond to the solution of the Laplace equation in the plane of the cross section for the boundary values shown in Fig. 1(b) and 1(c).

The wave impedance of the first of these modes was calculated by Collin¹ who used a variational method of analysis in which he neglected the thickness of the outer walls.

Bochenek² calculated the wave impedance for this first mode by using a conformal mapping method in which he neglected the inside conductor, but took into account the thickness of the outer walls.

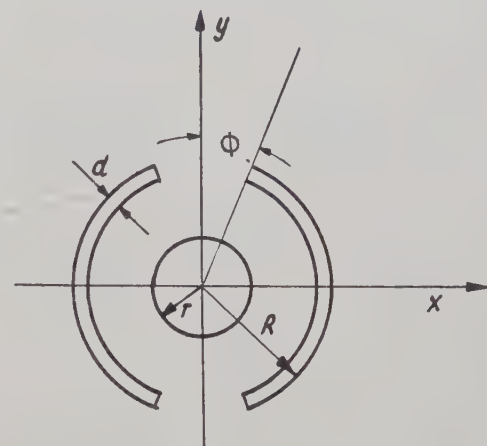
The method of conformal mapping leads to the determination of the wave impedance in the previous case as well; *i.e.*, when we neglect the thickness of the outer walls and take into account the central conductor, the mapping can be performed in an exact way. At the same time, by making simplifying assumptions which do not give rise to any reservations in cases of practical interest, the approximate value of the impedance may be found without neglecting either the central conductor or the thickness of the walls.

In the case of the other mode of transmission [Fig. 1(c)] the conformal mapping method also leads to the determination of the impedance.

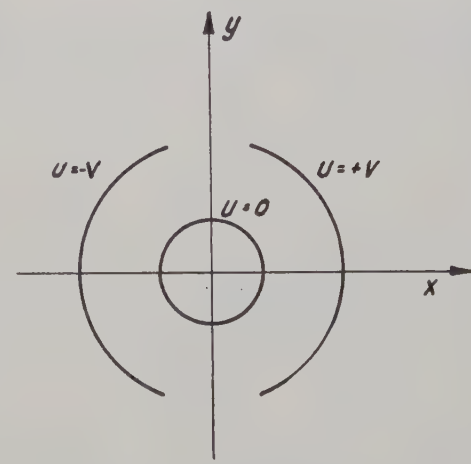
The subject of this report is to present the results of an analysis made along these lines and to compare them with the results published in both of the above-mentioned articles.

MODE OF THE FIRST TYPE

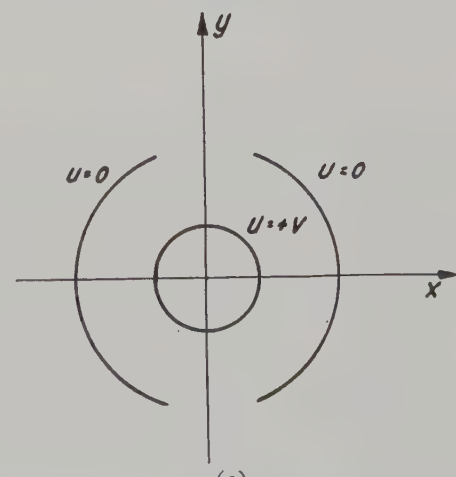
The boundary problem for Laplace's equation [Fig. 1(b)] is transformed successively, by means of conformal mapping,³ into boundary problems I, II, III



(a)



(b)



(c)

Fig. 1—System of conductors and the TEM modes examined. (a) Cross section of the system of conductors, (b) first transmission mode, (c) second transmission mode.

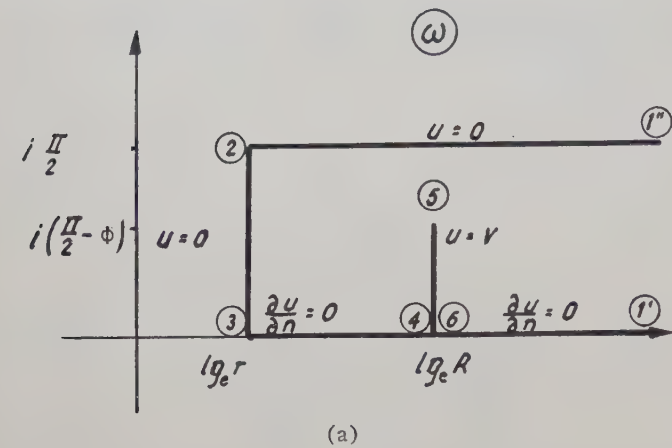
* Manuscript received by the PGM TT, July 1, 1957.

† Institute of Basic Technical Problems, Palace of Culture and Science, Warsaw, Poland.

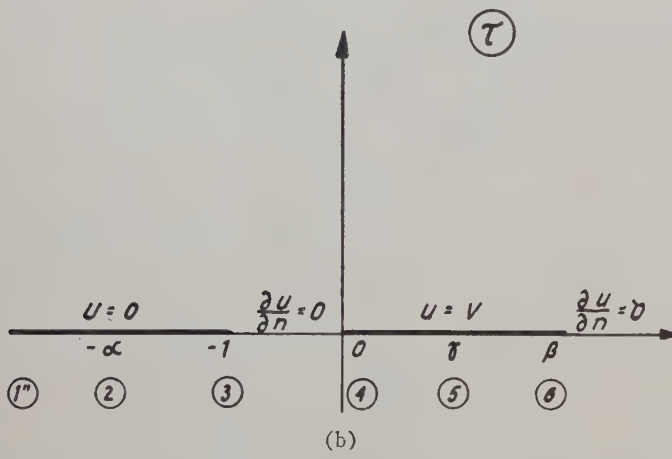
¹ R. E. Collin, "The characteristic impedance of a slotted coaxial line," IRE TRANS., vol. MTT-4, pp. 4-8; January, 1956.

² K. Bochenek, "Impedancia falowa linii wystepujacej w jednym z rodzajow symetryzatora," Arch. Elektrotech., vol. 4, pp. 135-147; 1956.

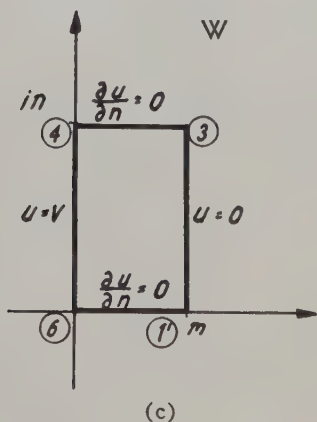
³ E. Weber, "Electromagnetic Fields, Theory and Applications," John Wiley & Sons, Inc., New York, N. Y.; 1950.



(a)



(b)



(c)

Fig. 2—Boundary problems obtained by successive conformal mappings. Arabic numerals in the circles refer to points corresponding to each other. The boundary conditions for the function u are also given. (a) Boundary problem I—plane ω , (b) boundary problem II—plane τ , (c) boundary problem III—plane W .

[Fig. 2(a)–2(c)]. The splitting into successive transformations permits a better orientation as regards their character.

The first mapping has the form

$$\omega = \lg_e z. \quad (1)$$

The second is the Christoffel-Schwarz integral:

$$\omega = \frac{1}{2} \int_0^\tau \frac{(t - \gamma) dt}{\sqrt{(t - \beta)(t - 0)(t + 1)(t + \alpha)}} + \lg_e R. \quad (2)$$

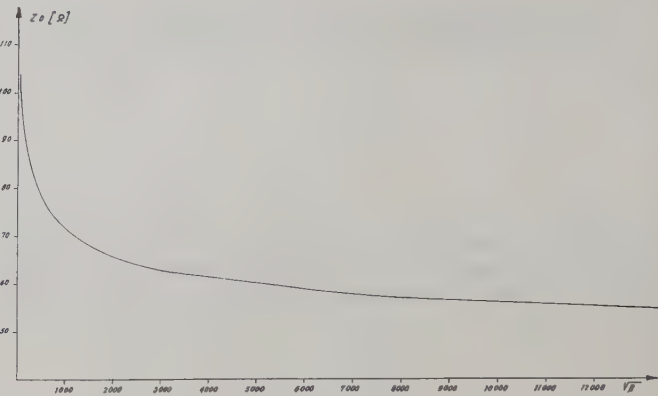


Fig. 3—Characteristic impedance as a function of the parameter β .

In the system corresponding to boundary problem II the wave impedance is defined by only one parameter β . The value of this impedance is readily found by means of the third mapping, which is also of the Christoffel-Schwarz type, and which reduces this system to the system of a plane ideal line (without boundary distortions). This mapping has the form

$$\Psi = C_1 \int_0^\tau \frac{dt}{\sqrt{(t - 0)(t - \beta)(t + 1)}} + in. \quad (3)$$

A simple calculation gives a formula for the wave impedance as a function of β :

$$Z_0 = \sqrt{\frac{\mu_0}{\epsilon_0}} \frac{K(k)}{K(k')} \quad (4)$$

where

$$k = \sqrt{\frac{1}{1 + \beta}} \quad k' = \sqrt{\frac{\beta}{1 + \beta}}$$

and which is given in Fig. 3. $K(k)$ and $K(k')$ are complete elliptic integrals of the first kind.

The finding of β as a function of the angle ϕ and the ratio of the radii R/r of the line presents a basic difficulty. To find this relation, mapping II should be studied more closely.

To the arbitrarily selected values of the parameters α , β , and γ there corresponds the region ω in which points 4 and 6 may not coincide, as in the case in Fig. 4. Hence, in the case of interest to us, α , β , and γ should be determined by means of the three conditions: 1) $\lg_e R/r$ has the selected value, 2) the angle ϕ has the selected value, 3) points 4 and 6 coincide.

These conditions written in analytical form appear as follows:

$$\lg_e \frac{R}{r} = \frac{1}{2} \int_{-1}^0 \frac{(t - \gamma) dt}{\sqrt{(t - \beta)(t - 0)(t + 1)(t + \alpha)}} \quad (5)$$

$$i\left(\frac{\pi}{2} - \phi\right) = \frac{1}{2} \int_0^\tau \frac{(t - \gamma) dt}{\sqrt{(t - \beta)(t - 0)(t + 1)(t + \alpha)}} \quad (6)$$

$$i\frac{\pi}{2} = \frac{1}{2} \int_{-1}^{-\alpha} \frac{(t - \gamma) dt}{\sqrt{(t - \beta)(t - 0)(t + 1)(t + \alpha)}}. \quad (7)$$

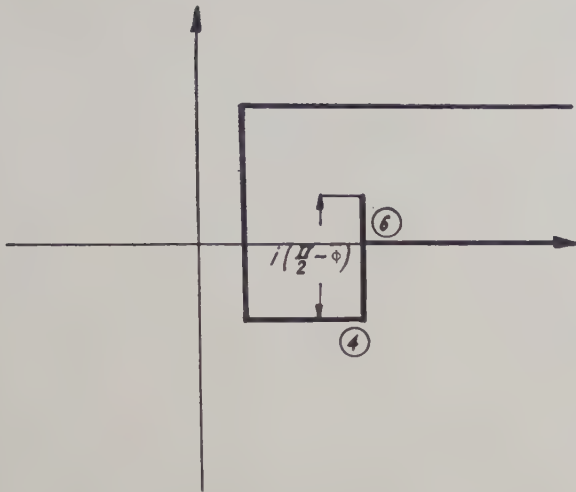


Fig. 4—Displacement of points 4 and 6.

With the help of classical transformations we express these relations by means of elliptic integrals:⁴

$$\lg_e \frac{r}{R} = \frac{1}{\sqrt{\alpha(\beta + 1)}} [(\alpha - 1)\Pi(\rho_1, k) - (\alpha + \gamma)K(k')] \quad (8)$$

$$k' = \sqrt{\frac{\beta + \alpha}{(\beta + 1)\alpha}} \quad \rho_1 = -\frac{1}{\alpha}$$

$$\frac{\pi}{2} - \phi = \frac{1}{\sqrt{\alpha(\beta + 1)}} [(1 + \gamma)F(\Psi, k) - \Pi(\Psi, \rho_2, k)] \quad (9)$$

$$k = \sqrt{\frac{\beta(\alpha - 1)}{(\beta + 1)\alpha}} \quad \rho_2 = -\frac{\beta}{\beta + 1}$$

$$\Psi = \arcsin \sqrt{\frac{(\beta + 1)\gamma}{\beta(\gamma + 1)}}$$

$$\frac{\pi}{2} = \frac{1}{\sqrt{\alpha(\beta + 1)}} [(\gamma - \beta)K(k) + (\beta + \alpha)\Pi(\rho_3, k)] \quad (10)$$

$$k = \sqrt{\frac{\beta(\alpha - 1)}{(\beta + 1)\alpha}} \quad \rho_3 = -\frac{\alpha - 1}{\beta + 1}.$$

In these equations $K(k)$ is the complete elliptic integral of the first kind, $F(\Psi, k)$ is the incomplete elliptic integral of the first kind, $\Pi(\rho, k)$ is the complete elliptic integral of the third kind, and $\Pi(\Psi, \rho, k)$ is the incomplete elliptic integral of the third kind. The mathematical procedure leading to the finding of the values of β , α , and γ (unfortunately, the latter two parameters must also be evaluated) corresponding to the values of R/r and ϕ which interest us is presented in Appendix I.

The values obtained for the impedance as a function of the angle 2ϕ are shown in Fig. 5 for ratios $R/r = 3.37$, 2.72 , 2.6 , 2.3 .

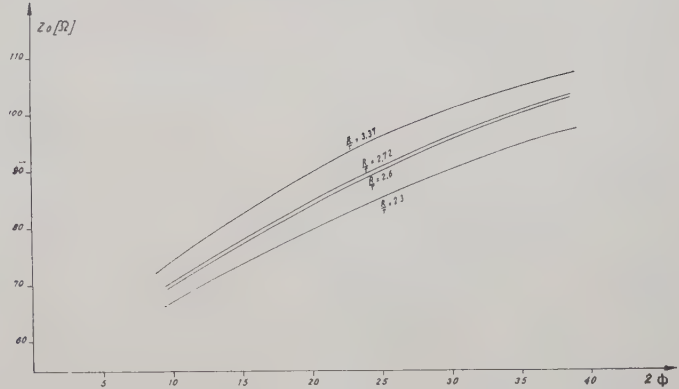
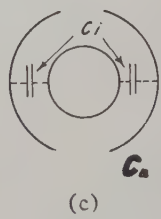
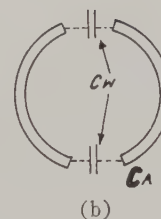
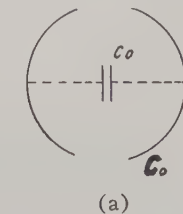
Fig. 5—Characteristic impedance as a function of the angle 2ϕ for various values of the ratios R/r . $d=0$.

Fig. 6—Capacity distribution. (a) C_0 —capacity between the thin outer conductors, (b) C_A —total capacity of the system without the inner conductor, $C_W = C_A - C_0$ capacity introduced by thickening the walls. (c) C_B —total capacity of the system with thin outer walls. $C_C = C_B - C_0$ —capacity introduced by the central conductor.

When the thickness of the walls is not neglected; *i.e.*, the line shown in Fig. 1(a), the capacity introduced by the central conductor and the capacity introduced by the thickening of the walls may be considered as adding to each other (Fig. 6) as long as the increase in wall thickness does not affect the field distribution in the vicinity of the central conductor and the introduction of the central conductor does not affect the field distribution in the gaps between the outer conductors. The greater the radius of the outer conductor in relation to both the radius of the central conductor and the thickness of the walls of the outer conductor, the more correct this assumption seems.

The impedance calculations presented below are based on the determination of the additional capacity introduced into the system by the thickening of the walls of the outer conductor on the basis of formulas derived by Bochenek² and the additional capacity introduced by the central conductor on the basis of the results obtained here.

⁴ See; *e.g.*, P. Byrd and M. Friedman, "Handbook of Elliptic Integrals for Engineers and Physicists," Springer-Verlag, Berlin, Germany; 1954.

W. Gröbner and N. Hofreiter, "Integraltafel," Springer-Verlag, Berlin, Germany; 1949.

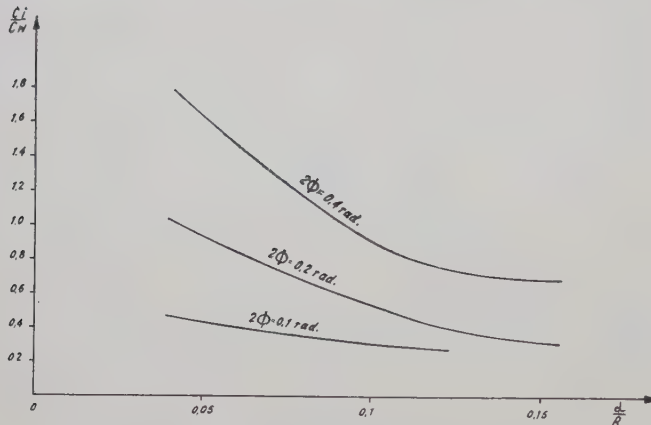


Fig. 7—Ratio of capacity introduced by the inner conductor to the capacity introduced by thickening the walls for various angles (2ϕ).

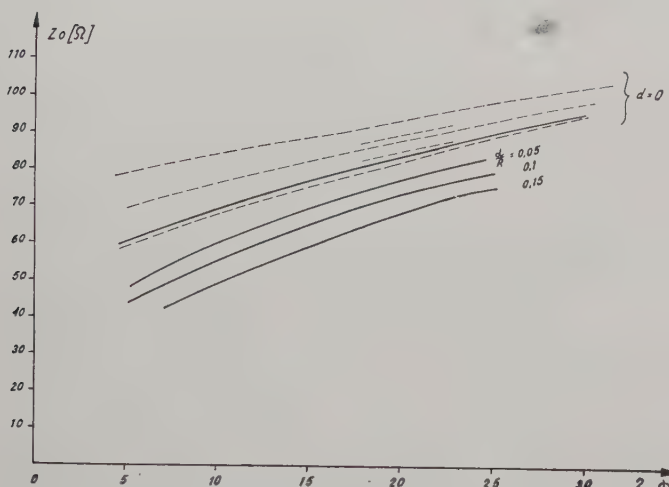


Fig. 8—Solid line—characteristic impedance as a function of the angle 2ϕ for $R/r=2.6$ and the various values of d/R . Dotted lines—approximations obtained by a variational method for $d=0$.

The ratio of the capacity introduced by the inner conductor C_i to the capacity introduced by the thickening of the walls C_w is represented in Fig. 7. This curve gives an idea of the influence of both factors on the values of the impedance.

The next curve (Fig. 8) represents the impedance for the ratio $R/r=2.6$, wall thickness $d/R=0, 0.05, 0.1$, and 0.15 as a function of the angle 2ϕ . For comparison, the curves obtained by Collin¹ for the case $d=0$ are also given in the figure.

Fig. 9 presents a comparison of the approximate value of the characteristic impedance obtained by Collin¹ by a variational method for $r=0$ and $d=0$ with the exact value obtained by means of homographic mapping.

MODE OF THE SECOND TYPE

This mode [Fig. 1(c)] corresponds to the basic mode in a coaxial line distorted by the slotting of the outer conductor. It seems of interest to investigate the effect of this distortion on the values of the wave impedance.

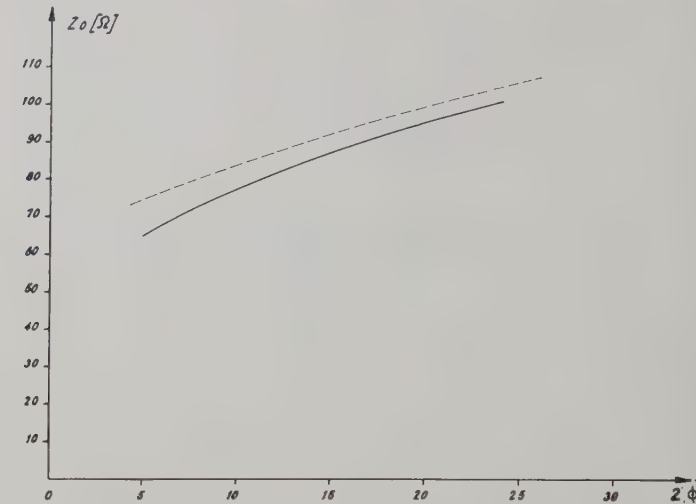


Fig. 9—Solid line—characteristic impedance as a function of angle 2ϕ for $R/r=2.6$ and $d=0$. Dotted line—approximation obtained by a variational method. (See reference 1.)

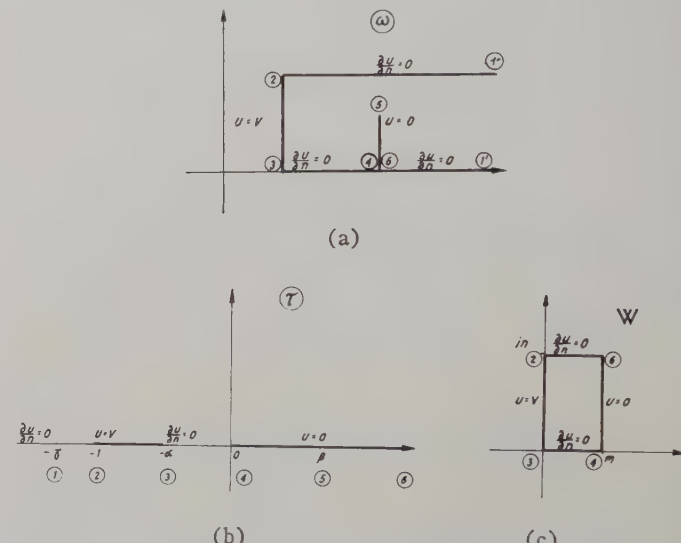


Fig. 10—Boundary problems obtained by successive conformal mappings. Arabic numerals in the circles denote points corresponding to each other. Boundary conditions for the function u are also given. (a) Boundary conditions problem I—plane ω , (b) boundary problem II—plane τ , (c) boundary problem III—plane W .

As in the preceding case, we use three successive conformal mappings:

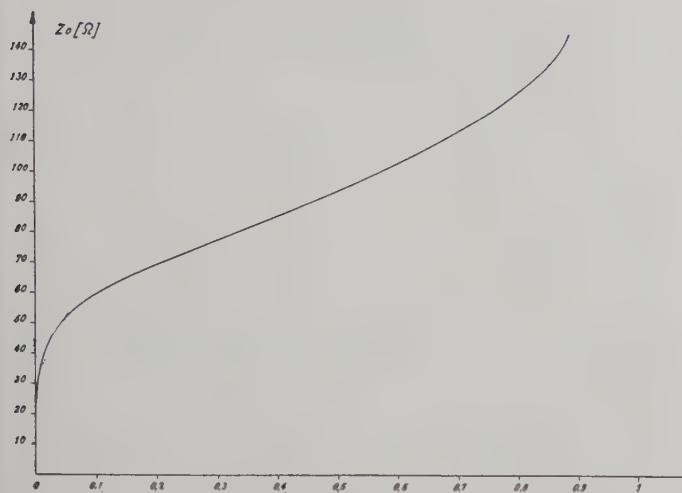
$$\omega = \lg_e z \quad (11)$$

$$\omega = -i \frac{\sqrt{(\gamma-1)(\gamma-\alpha)\gamma}}{2(\gamma+\beta)} \cdot \int_0^r \frac{(t-\beta)dt}{(t+\gamma)\sqrt{(t+0)(t+\alpha)(t+1)}} + \lg_e R; \quad (12)$$

$$\omega = C_1 \int_0^r \frac{dt}{\sqrt{(t-0)(t+\alpha)(t+1)}} + m. \quad (13)$$

The boundary problems corresponding to these mappings are shown in Fig. 10.

The impedance in system II [Fig. 10(b)] is defined by only one parameter α . Its value is found by means of

Fig. 11—Characteristic impedance as a function of parameter α .

mapping in the system III, identically as in the preceding case.

The dependence of the impedance on α is expressed by the formula:

$$Z_0 = \frac{1}{4} \sqrt{\frac{\mu_0}{\epsilon_0}} \frac{K(k)}{K(k')} \quad (14)$$

where

$$k = \sqrt{\alpha} \quad k' = \sqrt{1 - \alpha}.$$

This relation is shown in Fig. 11.

Similarly as in the previous case, the calculations lead us to the following system of equations giving the relation between the parameters α, β, γ and the quantities R/r and ϕ :

$$\lg_e \frac{R}{r} = \frac{\sqrt{\gamma(\gamma - \alpha)}}{(\gamma + \beta)\sqrt{\gamma - 1}} \left[(1 + \beta)K(k) - \frac{1 - \alpha}{\gamma - \alpha} (\gamma + \beta)\Pi(\rho_1, k) \right]; \quad (15)$$

$$k = \sqrt{\alpha} \quad \rho_1 = -\frac{\alpha(\gamma - 1)}{\gamma - \alpha}$$

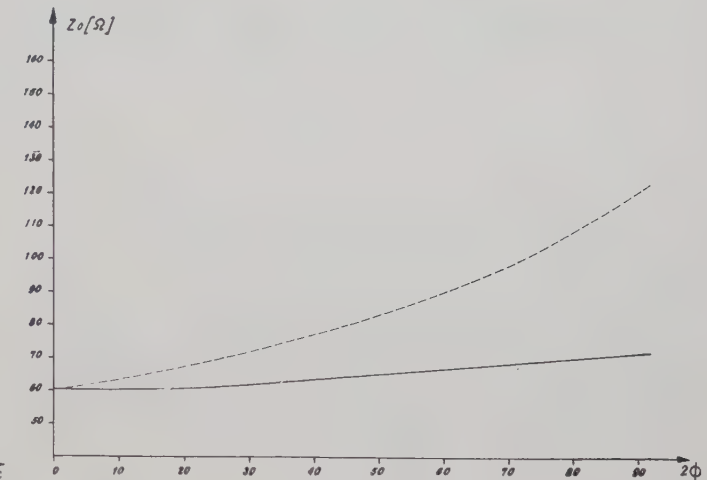
$$\frac{\pi}{2} - \phi = \frac{\sqrt{(\gamma - 1)\gamma}}{(\gamma + \beta)\sqrt{\gamma - \alpha}} \left[(\beta + \alpha)F(\Psi, k') - \frac{(\beta + \gamma)\alpha}{\gamma} \Pi(\Psi, \rho_2, k') \right]; \quad (16)$$

$$k' = \sqrt{1 - \alpha} \quad \rho_2 = -\frac{\gamma - \alpha}{\gamma}$$

$$\Psi = \arcsin \sqrt{\frac{\beta}{\beta + \alpha}}$$

$$\frac{\pi}{2} = \frac{\sqrt{(\gamma - 1)(\gamma - \alpha)\gamma}}{\gamma + \beta} \left[\frac{\beta + \gamma}{\gamma - 1} \Pi(\rho_3, k') - K(k') \right] \quad (17)$$

$$k' = \sqrt{1 - \alpha} \quad \rho_3 = -\frac{\alpha - 1}{\gamma - 1}.$$

Fig. 12—Solid line—characteristic impedance of the second mode as a function of the angle 2ϕ . Dotted line—result of the simplified calculation (see text).

The procedure for determining α, β , and γ for the values of the ratio R/r and the angle ϕ , of interest to us, is given in Appendix II.

The values obtained for the ratio $R/r = 2.72$ as a function of the angle 2ϕ are given in Fig. 12. Also given in this figure is the curve of the impedance calculated by assuming that the capacity of the coaxial line changes proportionally to the angle subtended by the cross section of the outer conductor. As may be seen, this type of simplification of the impedance calculation gives results which depart considerably from reality; the actual impedance increases more slowly than the impedance calculated in the above approximative manner. This should have been expected when one considers that the field lines become more dense at the boundary of the gap.

In the case of the type of wave being considered here, it seems that the influence of the thickness of the outer conductor on the impedance will be considerably smaller than in the preceding case since both parts of the outer conductor are at the same potential.

APPENDIX I

CALCULATION OF THE FIRST TRANSMISSION MODE

In the range of the values of the parameters of interest to us, (8)–(10) can be replaced, for purposes of calculation, by simplified formulas which are derived from the assumption that

$$\beta \gg 1, \quad \beta \gg \gamma, \quad \text{and} \quad \beta \gg \alpha.$$

$$\lg_e \frac{r}{R} \cong \frac{1}{\sqrt{\alpha \cdot \beta}} [\alpha E(k') - (\alpha + \gamma)K(k')] \quad (18)$$

$$\frac{\pi}{2} - \phi \cong \frac{1}{\sqrt{\alpha \cdot \beta}} [\gamma F(\Psi, k) + \alpha E(\Psi, k) - \sqrt{\alpha} \operatorname{tg} \Psi] \quad (19)$$

$$\frac{\pi}{2} \cong \frac{1}{\sqrt{\alpha \cdot \beta}} [(\gamma + \alpha)K(k)]. \quad (20)$$

$E(k')$ is the complete elliptic integral of the second kind.

$$k = \sqrt{\frac{\alpha-1}{\alpha}} \quad k' = \sqrt{\frac{1}{\alpha}}$$

$$\rho = -1 \quad \Psi = \arcsin \sqrt{\frac{\gamma}{\gamma+1}}.$$

For the range of the angle ϕ and ratios R/r , of interest to us, these assumptions are correct and can be directly verified by substituting the results obtained into the exact formulas.⁵

We insert in (18) the expression for $\gamma+\alpha$ obtained from (20) and we obtain (21)

$$\sqrt{\beta} = \frac{\sqrt{\alpha}E(k')}{\lg_e \frac{r}{R} + \frac{\pi}{2} \frac{K(k')}{K(k)}}. \quad (21)$$

The system (19) through (21) obtained in this way is a convenient point of departure for the numerical calculations.

The computational procedure is as follows: we assume a value for R/r and a value for α . In this way the parameters of the system are uniquely defined. Only the corresponding value of the angle ϕ has to be found. To do this, we insert the values taken for α and R/r into (21) and determine β from this equation. We insert the value found for β and the value taken for α into (20) and obtain γ . We substitute the values of α , β , and γ into (19) and obtain the angle ϕ . By taking different values of α we can change ϕ in the interval of interest to us. The value of β obtained in the course of the computations uniquely determines the impedance (4),

$$\text{for } \beta \gg 1: \quad Z_0 = \frac{591.4}{\lg_e 4 \sqrt{\beta}}.$$

As may be seen, the calculations are quite simple, since they reduce to looking up the elliptic integrals in the tables and to making some arithmetical calculations.

⁵ The correctness of the assumption that $\beta \gg 1$ can also be checked in the following way: β is a parameter which uniquely determines the impedance; with an increase in β the impedance decreases. The impedance for the system with the central conductor is smaller (and therefore β is greater) than the impedance (the value of β) for the system without the central conductor. For the system without the central conductor, the corresponding value of impedance can be readily found by means of homographic mapping.

APPENDIX II

CALCULATION OF THE SECOND TRANSMISSION MODE

In the ranges of the angle ϕ and the ratios R/r of interest to us, $\gamma \gg 1$, and therefore (15) through (17) can be replaced for purposes of calculation by simplified formulas:

$$\lg_e \frac{R}{r} = \frac{\sqrt{\gamma}}{\gamma + \beta} \cdot \left[\frac{\gamma[K(k) - E(k)] + \beta[\gamma K(k) - \alpha K(k) - E(k)]}{\gamma} \right]; \quad (22)$$

$$\frac{\pi}{2} - \phi = \frac{\sqrt{\gamma}}{\gamma + \beta} \left[(\beta + \alpha)F(\Psi, k') - \frac{\gamma + \beta}{\gamma} \cdot \alpha \Pi(\Psi, \rho, k') \right]; \quad (23)$$

$$\frac{\pi}{2} = \frac{\sqrt{\gamma}}{\gamma + \beta} K(k')[1 + \beta] \quad (24)$$

$$k = \sqrt{\alpha} \quad k' = \sqrt{1 - \alpha} \quad \rho = -1$$

$$\Psi = \arcsin \sqrt{\frac{\beta}{\beta + \alpha}}.$$

We insert in (22) the expression for β obtained from (24) and we obtain (25):

$$\gamma \left[K(k') \lg_e \frac{R}{r} - \frac{\pi}{2} K(k) \right] + \sqrt{\gamma} E(k) K(k') + \frac{\pi}{2} K(k)(1 + \alpha) - K(k') \lg_e \frac{R}{r} = 0. \quad (25)$$

The calculations are made as follows: we assume a value for R/r and a value for α . To find the angle ϕ , we insert the values taken for R/r and α into (25) and from this equation determine γ . We insert the value found for γ and that taken for α into (24) and obtain β . We put the values of α , β , and γ into (23) and obtain the angle ϕ . By taking various values for α we can change ϕ into the interval in which we are interested. The value of α uniquely determines the impedance (14).

ACKNOWLEDGMENT

The author would like to thank Professor K. Bochenek for his suggestions and aid and the members of the staff of the Department of Communications Theory of the Institute of Basic Technical Problems for their encouragement.



Velocity Modulation of Electromagnetic Waves*

FREDERIC R. MORGENTHALER†

Summary—This paper deals with electromagnetic wave propagation through dielectric media whose propagation constants vary as a function of time.

If the parameters of the medium cannot respond to changes in the electric and magnetic fields of the propagating wave, the fields within such media will be linear. Maxwell's equations are solved for cases in which the scalar permittivity and permeability vary independently with time. When the impedance is constant, an exact solution is obtained. When the impedance varies, a closed form approximation is found since an exact solution is not always possible. The field energy and electromagnetic momentum are derived for a velocity transient and it is seen that, in general, the energy changes and the momentum remains constant.

The frequency deviation that results when a monochromatic wave is passed through a section of dielectric with nonconstant velocity of propagation is discussed in detail. An approximate solution is obtained for the case in which the electrical length of such a section is small; it is found that essentially linear phase modulation occurs. The general solution is found for the case in which the electrical length of section is long and the permittivity of the medium sinusoidally modulated. The optimum length found to give the greatest frequency deviation is shown to be generally impracticable.

It appears that ferroelectric or ferrimagnetic velocity-modulated dielectrics are feasible, at least for low-power modulators.

I. INTRODUCTION

THIS paper considers the problem of modulating the velocity of propagation of dielectric media and the effects which arise when electromagnetic waves travel through such media.

A time-varying velocity of propagation implies time-variable permittivity and/or permeability. This immediately suggests that ferroelectrics or ferrimagnetics, respectively under the influence of external electric or magnetic fields, might be suitable means of obtaining velocity-modulated media.

Section II contains the mathematical solution to Maxwell's equations for the general case of independently time-varying μ and ϵ . The special case of a velocity step transient is considered by physical reasoning and the energy densities of the modulated waves are evaluated in Section III. The frequency variation of monochromatic waves passing through a dielectric slab whose velocity of propagation varies homogeneously as a function of time is derived in Section IV. Numerical results based on the published parameters of a particular ferroelectric are given.

* Manuscript received by the PGM TT, July 2, 1957; revised manuscript received, August 5, 1957. This paper is based on a Master of Science thesis submitted to the Electrical Engineering Department of the Massachusetts Institute of Technology, Cambridge, Mass.; June, 1956.

† Air Force Cambridge Res. Center, Air Res. and Dev. Command, Bedford, Mass.

II. SOLUTION OF MAXWELL'S EQUATIONS WHEN THE PERMITTIVITY AND PERMEABILITY VARY WITH TIME

The behavior of an electromagnetic wave passing through a dielectric with time-varying velocity of propagation can be predicted if the solution to Maxwell's equations is known when the permittivity and permeability are functions of time.

Assume a charge- and current-free region where μ and ϵ of the medium are functions of time. The wave equations for a TEM mode propagating in the z direction become¹

$$\frac{\partial^2 E_y}{\partial z^2} = \mu \epsilon \ddot{E}_y + (\dot{\mu} \epsilon + 2\mu \dot{\epsilon}) \dot{E}_y + (\mu \ddot{\epsilon} + \dot{\mu} \epsilon) E_y, \quad (1)$$

and

$$\frac{\partial^2 H_x}{\partial z^2} = \mu \epsilon \ddot{H}_x + (\dot{\mu} \epsilon + 2\dot{\mu} \epsilon) \dot{H}_x + (\ddot{\mu} \epsilon + \dot{\mu} \epsilon) H_x. \quad (2)$$

The fields may be written in the form

$$E = \frac{W_E}{\epsilon \sqrt{\mu}} (A e^{+i\beta z} + B e^{-i\beta z}), \quad (3a)$$

where W_E is given by

$$\ddot{W}_E + \left[\frac{\beta^2}{\mu \epsilon} + \frac{1}{4} \left(\frac{\dot{\mu}}{\mu} \right)^2 - \frac{1}{2} \left(\frac{\ddot{\mu}}{\mu} \right) \right] W_E = 0; \quad (3b)$$

and

$$H = \frac{W_H}{\mu \sqrt{\epsilon}} (A e^{+i\beta z} + B e^{-i\beta z}), \quad (4a)$$

where W_H is given by

$$\ddot{W}_H + \left[\frac{\beta^2}{\mu \epsilon} + \frac{1}{4} \left(\frac{\dot{\epsilon}}{\epsilon} \right)^2 - \frac{1}{2} \left(\frac{\ddot{\epsilon}}{\epsilon} \right) \right] W_H = 0. \quad (4b)$$

Special Case

From the form of (3) and (4) it is obvious that W_E will equal W_H only if μ and ϵ are constants or if their ratio is always constant. If $[\mu(t)/\epsilon(t) = \eta^2]$ is constant, then it is seen that the ratio of the electric field to the magnetic field will likewise be invariant and so the two fields are in space and time phase. Under these conditions an exact solution of the fields is

¹ F. R. Morgenthaler, "Velocity modulation of electromagnetic waves," M.S. thesis submitted to M.I.T., Cambridge, Mass.; June, 1956.

$$E(z, t) = \eta H(z, t) = \frac{A}{\epsilon} e^{\pm i\beta z} e^{\pm i(\beta/\eta) f(dt/\epsilon)}, \quad (5)$$

where β takes on eigenvalues subject to the boundary conditions; a series of terms like (5) is the general solution which can be verified by direct substitution. There will be no reflections as long as the impedance of the dielectric remains constant and strictly progressive waves are possible.

It is seen that

$$V(t) = \frac{1}{\sqrt{\mu(t)\epsilon(t)}} = \frac{1}{\eta\epsilon(t)}. \quad (6)$$

The velocity of propagation is given by the same form as when μ and ϵ are constant.

The total phase of the wave given by (5) is

$$\phi = \frac{\beta}{\eta} \int \frac{dt}{\epsilon},$$

and the instantaneous frequency is given by

$$\omega(t) = \frac{d\phi}{dt} = \beta v(t). \quad (7)$$

Eq. (7) indicates that the frequency is simply proportional to the velocity of propagation and this is true if it is remembered that the derivation is based on the assumption that μ and ϵ do not vary with position. This implies that the medium is infinite in extent and, moreover, that any wave now in the dielectric has always been there and has been influenced by any variation in velocity that has occurred since the infinite past. It is appropriate to point out here that the separation of the partial differential equation implies that the space variation of the wave is unaffected by any changes in μ and ϵ . Consider in connection with this that at some point in the distant past a wave train of length L and frequency f_1 was started in the medium and that at that time μ and ϵ were stationary with time. This wave train is characterized by the frequency f_1 and some constant velocity of propagation v_1 . It therefore has a wavelength $\lambda_1 = v_1/f_1$. Now suppose that the velocity of propagation suddenly changes to some new value v_2 . All portions of the original wave train will be acted upon simultaneously, that is, slowed down or speeded up together. The new wave train will therefore still be of length L and the space waveform will not have changed. This means that the wavelength still has the same value λ_1 but because $v=f\lambda$ it follows that the frequency must have changed to a value $f_2 = v_2/\lambda_1$; hence, $f_2/f_1 = v_2/v_1$. Eq. (7) is merely expressing this fact in general terms. So long as the original wave stays in the medium its frequency will follow the velocity changes of the medium. If a fresh wave enters the dielectric, it will not, of course, become subject to the past history of the medium. For example, if a new wave train of length L and frequency f_1 (as before) enters the dielectric after the velocity has changed from v_1 to v_2 , then its frequency will still be f_1 and its wavelength will change to $\lambda_2 = (v_2/v_1)\lambda_1$. The

total length will be $(v_2/v_1)L$ instead of L . If the velocity now changes to some new value, the frequency will change accordingly and the wavelength will remain constant.

The exact solution obtained for the special case of constant impedance is illuminating but not very useful since in practice the impedance will not remain constant. It is desirable to solve (3) and (4) for the general case when μ and ϵ vary independently with time. No exact solution is possible and the task remains to find a suitable approximation. A series solution is difficult to interpret physically and so a closed form solution is preferable. Since the equation to be solved is a second-order linear differential equation, the Liouville approximation² offers hope and turns out to be entirely suitable.

The fields are then given by

$$E(z, t) \simeq \frac{A}{\sqrt[4]{\mu\epsilon^3}} e^{\pm i\beta z} e^{\pm i\beta f(dt/\sqrt{\mu\epsilon})} \quad (8)$$

and

$$H(z, t) \simeq \frac{A}{\sqrt[4]{\mu^3\epsilon}} e^{\pm i\beta z} e^{\pm i\beta f(dt/\sqrt{\mu\epsilon})}. \quad (9)$$

For slowly varying μ and ϵ , reflections are small and progressive waves are possible. As was shown previously for the special case of constant impedance, the instantaneous frequency is proportional to the velocity of propagation. The physical interpretation given before is also applicable in this situation. The previous remarks concerning eigenvalues of β apply here also so that (8) and (9) are, in general, infinite series.

III. SOLUTION OF STEP TRANSIENT FROM PHYSICAL REASONING

The fact that the general partial differential (1) and (2) were separable led to the physical interpretation that the space variation of a wave is invariant after it once enters a dielectric having time-varying parameters. The transition across the boundary will certainly cause space distortion but once this has happened no further perturbations of space waveform will occur until the wave leaves the medium. During the journey through the dielectric, all of the individual frequency components of the wave will follow the variations of the velocity of propagation. The physical picture of the phase variations of the electric and magnetic fields is clear: since the wavelength remains constant and the velocity does not, the frequency must change to fulfill the condition $v=f\lambda$. The important point to be realized is that the frequency does not necessarily remain invariant as a wave passes through a series of different dielectrics. That this is so in the usual case is only because the velocity of propagation is not a function of time.

It is desirable to understand why the amplitudes of

² S. Schelkunoff, "Applied Mathematics for Engineers and Scientists," D. Van Nostrand Co., Inc., New York, N. Y.; p. 210, 1948.

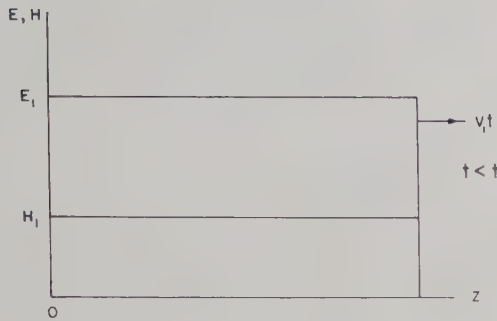


Fig. 1

the electric and magnetic fields vary as they do. Consideration of the instantaneous flux and charge offers a convenient method of obtaining this physical picture. The simple step transient in Fig. 1 offers an easily analyzed example that demonstrates all the relevant principles. The transient electromagnetic wave is propagated through a variable dielectric whose constants are given as functions of time. Both μ and ϵ are assumed to step from their initial values μ_1 and ϵ_1 to μ_2 and ϵ_2 , respectively (Fig. 2). The initial velocity of propagation is $v_1 = 1/\sqrt{\mu_1\epsilon_1}$ and the final value is $v_2 = 1/\sqrt{\mu_2\epsilon_2}$. Since the velocity is constant except at the jump, the standard wave equation must apply except at the discontinuity. From the previous discussion it is clear that the space waveform, but not the amplitude of the transient, will be invariant.

At the instant of the jump the total charge Q and the total flux ψ must remain constant. An invariant Q and ψ imply that D and B , respectively, do not change instantaneously.

Before the step ($t < t_0$)

$$B = \mu_1 H_1, \quad (10a)$$

$$D = \epsilon_1 E_1. \quad (10b)$$

After the step ($t > t_0$)

$$B = \mu_2 H_2, \quad (11a)$$

$$D = \epsilon_2 E_2. \quad (11b)$$

The most general form of E_2 and H_2 is for both fields to have a backward as well as a forward traveling-wave component.

$$H_2 = H_2^+ - H_2^-, \quad (12a)$$

$$E_2 = E_2^+ + E_2^-. \quad (12b)$$

The characteristic impedances of the dielectric are

$$\eta_1 = \sqrt{\frac{\mu_1}{\epsilon_1}} = \frac{E_1}{H_1} \quad t < t_0, \quad (13a)$$

$$\eta_2 = \sqrt{\frac{\mu_2}{\epsilon_2}} = \frac{E_2}{H_2} \quad t > t_0. \quad (13b)$$

The combination of (10a) through (11b) yields

$$B = \mu_1 H_1 = \mu_2 (H_2^+ - H_2^-), \quad (14a)$$

$$D = \epsilon_1 E_1 = \epsilon_2 (E_2^+ + E_2^-). \quad (14b)$$

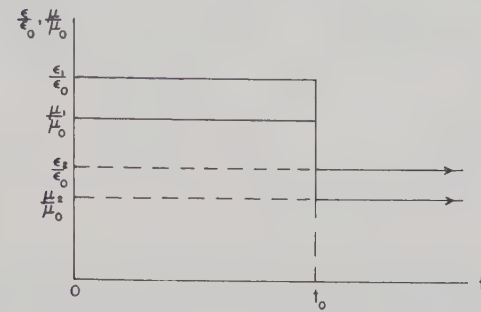


Fig. 2

The solution for this pair of equations gives

$$E_2^+ = \frac{1}{2} \left(\frac{\epsilon_1}{\epsilon_2} + \sqrt{\frac{\mu_1 \epsilon_1}{\mu_2 \epsilon_2}} \right) E_1 \\ = \frac{\eta_2}{2} \left(\frac{\mu_1}{\mu_2} + \sqrt{\frac{\mu_1 \epsilon_1}{\mu_2 \epsilon_2}} \right) H_1 = \eta_2 H_2^+, \quad (15a)$$

$$E_2^- = \frac{1}{2} \left(\frac{\epsilon_1}{\epsilon_2} - \sqrt{\frac{\mu_1 \epsilon_1}{\mu_2 \epsilon_2}} \right) E_1 \\ = \frac{\eta_2}{2} \left(\frac{\mu_1}{\mu_2} - \sqrt{\frac{\mu_1 \epsilon_1}{\mu_2 \epsilon_2}} \right) H_1 = \eta_2 H_2^-. \quad (15b)$$

For the special case when $\eta_1 = \eta_2 = \eta_0$, or equivalently $\mu_1/\mu_2 = \epsilon_1/\epsilon_2$, (15a) and (15b) reduce to

$$E_2^+ = \frac{\epsilon_1}{\epsilon_2} E_1 = \frac{\mu_1}{\mu_2} \eta_0 H_1 = \eta_0 H_2^+, \quad (16a)$$

$$E_2^- = H_2^- = 0. \quad (16b)$$

Under these conditions of constant impedance there is no reflected wave.

For the case where $\mu_1 = \mu_2$, (15a) and (15b) become

$$E_2^+ = \frac{1}{2} \left(\frac{\epsilon_1}{\epsilon_2} + \sqrt{\frac{\epsilon_1}{\epsilon_2}} \right) E_1 = \eta_2 H_2^+, \quad (17a)$$

$$E_2^- = \frac{1}{2} \left(\frac{\epsilon_1}{\epsilon_2} - \sqrt{\frac{\epsilon_1}{\epsilon_2}} \right) E_1 = \eta_2 H_2^-. \quad (17b)$$

If ϵ_1 and ϵ_2 do not differ greatly, E_2^- will be small compared to E_2^+ and may be neglected without great loss of accuracy. In that event E_2^+ can be approximated by

$$E_2^+ \simeq \frac{\epsilon_1}{\epsilon_2} E_1 \simeq \eta_2 H_2^+. \quad (18)$$

Eq. (18) indicates that the exact solution obtained for the case of constant impedance may be a reasonable approximation when one of the dielectric parameters remains invariant. The Liouville approximation is of slightly different form in that the amplitudes of D and B are not constant.

Energy Density

The uniform step transient of Fig. 1 has a total energy given by

$$U = \frac{1}{2} \int (\epsilon E^2 + \mu H^2) dV, \quad (19)$$

where the integration extends throughout the entire volume. Prior to t_0 the initial energy U_1 is given by

$$U_1 = \frac{1}{2}(\epsilon_1 E_1^2 + \mu_1 H_1^2)V. \quad (20)$$

The volume energy density is defined as $u = dU/dV$. For the initial wave

$$u_1 = \epsilon_1 E_1^2 = \mu_1 H_1^2. \quad (21)$$

After the velocity transient ($t > t_0$), the fields are given by $E_2 = E_2^+ + E_2^-$, and $H_2 = H_2^+ - H_2^-$. The energy density is then

$$u_2 = \frac{1}{2} \epsilon_1 E_1^2 \left(\frac{\epsilon_1}{\epsilon_2} + \frac{\mu_1}{\mu_2} \right). \quad (22)$$

The energy gain is defined as u_2/u_1 and given by

$$\frac{u_2}{u_1} = \frac{1}{2} \left(\frac{\epsilon_1}{\epsilon_2} + \frac{\mu_1}{\mu_2} \right). \quad (23)$$

The apparent violation of the conservation of energy is reconciled when it is remembered that the difference in energies is needed to do work upon the fields within the dielectric and μ and ϵ are changing. It is apparent that here is a mechanism for changing the energy level of an electromagnetic wave. That the frequency changes as well has already been shown.

Electromagnetic Momentum³

The electromagnetic momentum \vec{g} of a field is given by

$$\vec{g} = \frac{1}{v^2} \vec{S}, \quad (24)$$

where v is the velocity of propagation and \vec{S} is Poynting's vector. With reference to the problem just discussed, the original fields are described by (15a) and (15b). It is obvious that

$$g_1 = \epsilon_1 \sqrt{\mu_1 \epsilon_1} E_1^2. \quad (25)$$

Since $S_2 = (\mu_1 \epsilon_1 / \mu_2 \epsilon_2) E_1^2$, the final value of momentum is given by

$$g_2 = \epsilon_1 \sqrt{\mu_1 \epsilon_1} E_1^2 = g_1. \quad (26)$$

This important result, derived for the special case of the step transient, is also true for the general case; even though energy may be added or subtracted from the electromagnetic field by varying the velocity of propagation of the medium through which it passes, the electromagnetic momentum of the field is unchanged.

Since the momentum is associated only with the propagated field and not the standing-wave field, it is clear that the Liouville approximation should predict conservation of momentum also. The fact that the exact \vec{S}_2 is given by the approximation ensures that this is indeed true.

³ J. Stratton, "Electromagnetic Theory," McGraw Hill Book Co., Inc., New York, N. Y., pp. 103-104; 1941.

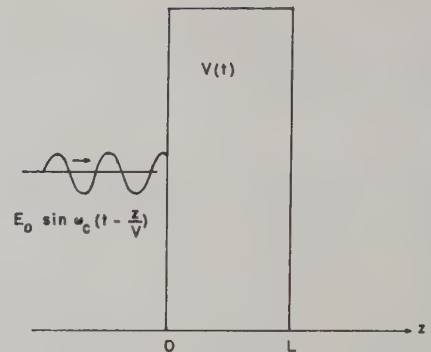


Fig. 3

IV. THE DIELECTRIC MODULATOR

A time-variable dielectric (Fig. 3) extends from $z=0$ to $z=L$ and is assumed homogeneous throughout. A monochromatic wave passes through the section.

It can be shown that the equation for a wavefront propagating with nonconstant velocity⁴ is

$$E = E_0 \sin \left[\omega_c \left(t - \int \frac{dz}{v} \right) \right]. \quad (27)$$

The transit time is defined as

$$T = \int \frac{dz}{v}. \quad (28)$$

Since the total phase of the wave is given by

$$\phi = \omega_c \left(t - \int \frac{dz}{v} \right), \quad (29)$$

the instantaneous frequency is

$$\omega(t) = \omega_c \left(1 - \frac{d}{dt} T \right). \quad (30)$$

Thin Sections

If the dielectric slab is very thin, the velocity can be approximated as constant for any given wavefront and dependent only upon the time that the wavefront entered the medium during the modulating cycle.⁵ Under these conditions

$$T = \int_0^L \frac{dz}{v} \simeq \frac{L}{v(t)}. \quad (31)$$

The instantaneous frequency is approximated by

$$\omega(t) \simeq \omega_c \left(1 + \frac{L}{v^2} \frac{dv}{dt} \right). \quad (32)$$

General Solution

In practical situations the approximation (32) is nearly always valid. It is, however, instructive to con-

⁴ J. C. Slater, "Microwave Electronics," D. Van Nostrand Co., Inc., New York, N. Y., pp. 268-269; 1950.

⁵ This is analogous to the situation found in klystrons where the velocity of an electron is assumed to be constant while it passes through the narrow accelerating gap but dependent on the time that it entered the gap.

sider the general case when the velocity cannot be assumed constant for the transit interval. The transit time for the entire length L is given by

$$T = \int_0^L \frac{dz}{v} = t_1 - t_0. \quad (33)$$

In this equation, t_0 is the entrance time of a wavefront and t_1 is the exit time of the same wavefront. The integral may be evaluated as follows:

$$\int_{t_0}^{t_1} v(t) dt = \int_0^L dz = L. \quad (34)$$

$$\begin{aligned} \omega(t_1) \simeq & \frac{\sec^2\left(\frac{\omega_m t_1}{2}\right)}{\left[1 + \left\{\frac{2 \tan\left(\frac{\omega_m t_1}{2}\right) + b}{\sqrt{4 - b^2}}\right\}^2\right]} \\ & \times \frac{\sec^2\left[\tan^{-1}\left\{\frac{2 \tan\left(\frac{\omega_m t_1}{2}\right) + b}{\sqrt{4 - b^2}}\right\} - \frac{\omega_m L \sqrt{4 - b^2}}{4v_0}\right] \omega_c}{\left[1 + \left\{\frac{\sqrt{4 - b^2}}{2} \tan\left[\tan^{-1}\left\{\frac{2 \tan\left(\frac{\omega_m t_1}{2}\right) + b}{\sqrt{4 - b^2}}\right\} - \frac{\omega_m L \sqrt{4 - b^2}}{4v_0}\right] - \frac{b}{2}\right\}^2\right]}, \end{aligned} \quad (43)$$

Therefore, $f(t_1, t_0) = L$, or $t_0 = g(t_1, L)$ and

$$T = t_1 - g(t_1, L). \quad (35)$$

Sinusoidal Modulation

In the case of monochromatic waves passing through a homogeneous dielectric slab whose permittivity is a sinusoidal function of time, if ϵ is given by

$$\epsilon = K' \epsilon_0 (1 + b \sin \omega_m t), \quad (36)$$

and $\mu = \mu_0$, then the velocity of propagation is given by

$$v = \frac{v_0}{\sqrt{1 + b \sin \omega_m t}}; \quad v_0 = \frac{1}{\sqrt{K' \mu_0 \epsilon_0}}, \quad (37)$$

where K' is the dielectric constant at the chosen operating point.

If the dielectric is electrically thin, then the approximation (32) can be used. Under these circumstances the instantaneous frequency of the wave emerging from the dielectric is

$$\omega(t) \simeq \omega_c \left[1 - \frac{bL}{2v_0} \frac{\cos \omega_m t}{\sqrt{1 + b \sin \omega_m t}} \right], \quad (38)$$

and the total variation of frequency

$$\Delta\omega(t) \simeq - \frac{bL \omega_m \omega_c \cos \omega_m t}{2v_0 \sqrt{1 + b \sin \omega_m t}}. \quad (39)$$

If b is very small, (39) becomes

$$\Delta\omega(t) \simeq - \frac{bL \omega_m \omega_c}{2v_0} \cos \omega_m t, \quad (40)$$

which is the form of linear phase modulation where

$$\omega_d = \frac{b \omega_m \omega_c L}{v_0}, \quad (41)$$

and

$$\theta_d = \frac{\omega_d}{\omega_m} = \frac{b \omega_c L}{v_0}. \quad (42)$$

If L is electrically long so that the velocity cannot be assumed constant over the transit time interval, then the integral (34) must be evaluated. The instantaneous frequency may be shown to be approximately¹

when $(b^2 \ll 2)$. Note that if $(\omega_m L \sqrt{4 - b^2})/4v_0 = K\pi$ ($K = 0, 1, 2, 3, \dots$), the frequency will be constant and equal to ω_c . This means that if the length L is such as to require an integral number of modulating cycles to elapse before a wavefront passes completely through, then surely all wavefronts will have exactly the same transit time. Since the frequency variation is proportional to the rate of change of transit time, it is obvious that no frequency variation will take place. These null lengths are given by

$$L = \frac{4K\pi v_0}{\omega_m \sqrt{4 - b^2}} \quad (K = 0, 1, 2, 3, \dots). \quad (44)$$

Since the frequency behavior is periodic, there is no advantage to be gained in making L any longer than some value within the first interval. The optimum length modulator that will result in the greatest frequency variation is evidently somewhere within the interval

$$0 < L_{\text{opt}} < \frac{4v_0}{\omega_m \sqrt{4 - b^2}}.$$

Straightforward maximization shows that the midpoint of the interval yields the optimum length.

It was assumed in the derivation of (43) that $b^2 \ll 2$. It is therefore permissible to write

$$L_{\text{opt}} \simeq \frac{v_0}{2} \tau_m = \frac{c}{2\sqrt{K'}} \tau_m, \quad (45)$$

where c is the free space velocity of light, and τ_m is the modulating period.

The maximum and minimum values of ω for this optimum length may be shown to be

$$\frac{2+b}{2-b} \omega_e \quad \text{and} \quad \frac{2-b}{2+b} \omega_e$$

respectively.

It is obvious that the optimum length modulator is feasible only when the modulating frequency is very high. For low modulating frequencies, a modulator of any physically practical length is well within the assumptions used in deriving (40), and the frequency variation is essentially pure phase modulation.

Numerical Results

Davis and Rubin⁶ have published data on SrTiO₃—BaTiO₃ (27 per cent SrTiO₃) ceramics at 3000 mc. Their results show that the relaxation spectrum reported by Powles and Jackson⁷ has not been reached and that at room temperature the dielectric constant is approximately 5000, with a loss tangent of 0.1 (with no bias field applied). If a field strength of 10 kv per cm is maintained, the loss decreases slightly and the dielectric constant drops to about 2000.

On the basis of Rubin and Davis's data it is possible to predict the performance of an SrTiO₃—BaTiO₃ modulator operating with a carrier frequency of 3000 mc. If the ambient temperature is about 25°C, then $\tan \delta \approx 0.1$ and K' varies between 4000 and 2000 for zero kv per cm and 10 kv per cm, respectively. Assuming a linear change of K' with field strength, it is obvious that a dc bias of 5 kv per cm in series with an ac voltage of magnitude 10 kv per cm peak-to-peak will produce a permittivity given by

$$\epsilon \approx 3000\epsilon_0(1 + \frac{1}{3} \sin \omega_m t). \quad (46)$$

If the values of b and K' in (46) are substituted into (45) the length of the "optimum modulator" is given by

$$L_{\text{opt}} \approx \frac{3 \times 10^8}{f_m} \text{ cm.} \quad (47)$$

With a loss tangent of 0.1 the loss at 3000 mc is approximately 15 db per cm. If the maximum allowable loss through the modulator is 3 db, then $f_m \geq 15 \times 10^8$ cps. Therefore, as predicted earlier, the optimum modulator is probably not realizable. If a lower value of ω_m is picked and a short L is used so as to keep the loss down, then (41) and (42) apply. The phase deviation at 3000 mc is

$$\theta_d \approx \frac{11\pi L}{3}, \quad (48)$$

where L is in centimeters.

⁶ L. G. Rubin and L. Davis, Jr., "Some dielectric properties of barium-strontium titanate ceramics at 300 megacycles," *J. Appl. Phys.*, vol. 24, pp. 1194-1197; September, 1953.

⁷ J. G. Powles and W. Jackson, "The measurement of the dielectric properties of high-permittivity materials at centimeter wavelengths," *Proc. IEE (London)*, vol. 96, part III, pp. 383-389; 1949.

V. CONCLUSION

The analysis has indicated that essentially linear phase modulation may be expected from a dielectric modulator. The electromagnetic momentum of a wave going through such a modulator is unaffected by the modulation process but the energy level will, in general, be increased. This energy is provided by the modulating source which on the average does work upon the electromagnetic field.

Dielectrics that appear suitable for velocity modulation include ferroelectric ceramics such as the BaTiO₃—SrTiO₃ compositions. There is a temperature range above the Curie point where these ceramics are still nonlinear and where the losses are substantially reduced. The Curie temperature can be moved over a wide range by altering the concentration of the strontium atoms.

Ferrimagnetic dielectrics are, of course, also applicable for such use. Although these materials are characterized by tensor rather than scalar permeabilities, the main results of the analysis can be applied if effective scalar permeabilities can be determined for the various directions of propagation.

When an electrostatically controlled ferroelectric is used in an FM modulator to vary the capacitance of a tuned circuit, the operating point value of K' determines the operating point capacitance, which in turn determines the carrier frequency. If the value of K' changes because of temperature or other variations, then the carrier will also drift. Observe that in the dielectric velocity modulator that has been discussed, the carrier frequency is not affected by changes in K' and will always be as stable as the generating source. The phase deviation is, of course, sensitive to changes in the dielectric constant, and drift owing to temperature changes may be important.

The maximum modulating rate to which the ferroelectric ceramics will respond is unknown. The extent to which the piezoelectric effect enters the modulation problem is also unknown.

It should be realized that these results assume that the velocity of propagation of the dielectric medium is modulated, *not* by the electromagnetic field passing through it, but by the modulating bias. If this is true, the linear analysis derived is valid; if not, the field relations are nonlinear and much more difficult to solve.

The velocity will not be modulated by the microwave field if the medium cannot respond to microwave frequencies, and this apparently is the case. Even if it is not, the results are applicable if the microwave field is not sufficiently strong to make significant changes in the permittivity.

VI. ACKNOWLEDGMENT

The author wishes to express his gratitude to L. J. Chu of the Massachusetts Institute of Technology for his guidance and helpful criticism.

Heat Loss of Circular Electric Waves in Helix Waveguides*

J. A. MORRISON†

Summary—This paper presents a theoretical calculation of the eddy current losses of circular electric waves in a closely-wound helix waveguide. The wire diameter is assumed large compared to the skin depth, but small compared to the guide diameter and the operating wavelength, so that the fields near the wire are quasi-static and may be determined by conformal mapping.

When the wires are in contact, the waveguide wall is effectively a metal surface with grooves of semicircular cross section, the current flow being parallel to the direction of the grooves. The power loss for this case is computed to be about 8.5 per cent higher than in a waveguide with smooth metal walls. When the wires are not in contact, the wall is treated as a grating of parallel, round wires. The increase in power loss over a smooth surface is approximately 22.5 per cent when the wires are separated by a distance equal to their diameter.

I. INTRODUCTION

IT is well established experimentally¹ that circular electric waves can be propagated in a closely-wound helix waveguide of small round wires, with total losses only slightly higher than the losses in a conventional round waveguide of the same size. In practice the wire diameter will be large compared to the eddy current skin depth, but small compared to the diameter of the guide and the operating wavelength. Under these assumptions, Marcatili² has recently used an inverse technique to estimate the increase in eddy current loss in the special case when the wires of the helix are touching, so that the waveguide wall is effectively a metal surface with grooves of semicircular cross section. It is the purpose of this paper to show that the quasi-static problem associated with Marcatili's problem can be solved exactly by conformal mapping, leading to an approximate calculation of the heat loss, and that the eddy current loss can also be calculated approximately when the wires of the helix are not in contact with one another.

II. BOUNDARY WITH SEMICIRCULAR GROOVES

For a circular electric wave in an ordinary round waveguide the wall currents are purely circumferential, the electric field at the wall is essentially zero, and the magnetic field is in the axial direction. Since helix waveguides are wound with as small a pitch as possible, we may regard the magnetic field at the wall as perpendicular to the wires and the current as parallel to

the wires. Since the wires are small compared to the guide radius and the wavelength, we may neglect curvature effects and propagation effects, and consider the two-dimensional problem of a quasi-static magnetic field bounded on one side by a grating of perfectly conducting round wires, and uniform at great distances on the other side. The basic assumption here is that the magnetic field outside the metal is essentially that which would exist outside a smooth perfectly conducting guide wall. The power dissipated by eddy currents is then approximately proportional to the integral of the square of the tangential magnetic field over the conducting surfaces.

A two-dimensional quasi-static magnetic field $H e^{i\omega t}$ in the x - y plane may be derived from a complex potential function³ $W(z)$ by

$$H = \text{grad} (\text{Re } W), \quad (1)$$

if W is an analytic function of the complex variable $z = x + iy$. The condition that the normal component of H vanishes on a perfectly conducting boundary is satisfied if $\text{Im } W$ is constant on such a boundary.

Thus in the case of the periodic semicircular grooves the problem becomes one of finding an analytic function W whose imaginary part is constant on the conducting boundary of Fig. 1 and is such that $W \sim H_0 z$, as $y \rightarrow \infty$, for then, from (1), $H_x \rightarrow H_0$ and $H_y \rightarrow 0$, so that at a great distance from the conducting surface there is a magnetic field of constant strength in the direction indicated in Fig. 1.

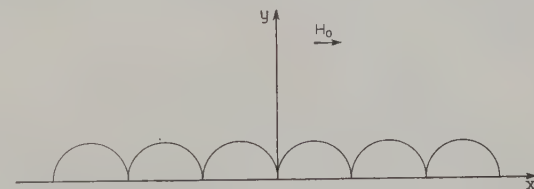


Fig. 1—Cross section of semicircular grooves.

Because of the periodicity of the shape of the conducting surface, it is sufficient to consider just a strip in the z plane as shaded in Fig. 2(a). It is shown in Appendix I that by means of the conformal transformation⁴ which

* Manuscript received by the PGMTT, July 5, 1957; revised manuscript received, October 21, 1957.

† Bell Telephone Labs., Inc., Murray Hill, N. J.

¹ S. P. Morgan and J. A. Young, "Helix waveguide," *Bell Syst. Tech. J.*, vol. 35, pp. 1347-1384; November, 1956.

² E. A. Marcatili, "Heat loss in grooved metallic surface," *PROC. IRE*, vol. 46, pp. 1134-1139; August, 1957.

³ S. P. Morgan, "Effect of surface roughness on eddy current losses," *J. Appl. Phys.*, vol. 20, pp. 352-362; April, 1949.

⁴ Z. Nehari, "Conformal Mapping," McGraw-Hill Book Co., Inc., New York, N. Y.; 1952.

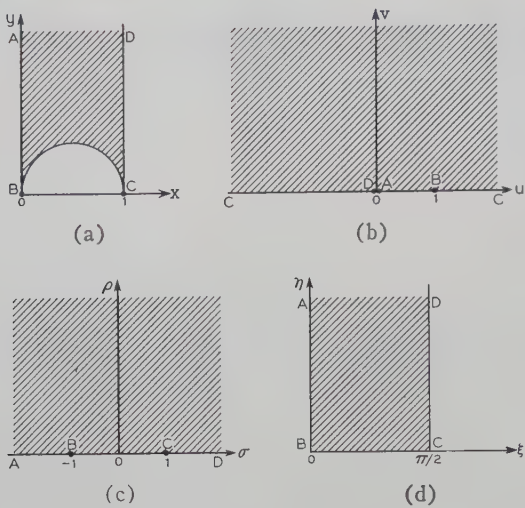


Fig. 2—Conformal transformation from grooved to flat strip.
(a) z plane, (b) w plane, (c) τ plane, (d) ξ plane.

maps the upper half-plane into this strip and some elementary transformations, the flat strip $ABCD$ in the $\xi = \xi + i\eta$ plane, Fig. 2(d), is mapped into the strip in the z plane by the conformal transformation,

$$z = \frac{iK(i \tan \xi)}{K(\sec \xi)}, \quad (2)$$

where $K(w)$ is the complete elliptic integral of the first kind⁵ and modulus w .

In the ξ plane

$$W = \frac{2H_0}{\pi} \xi, \quad (3)$$

for this makes $\text{Im } W = 0$ on $\eta = 0$, and hence on the semi-circle BC of the conducting surface and further, since the strip in the z plane is of unit width whilst that in the ξ plane is of width $\pi/2$, $W \sim H_0 z$ as $y \rightarrow \infty$.

Now the power dissipated by eddy currents in a surface S of conductivity g , whose radius of curvature is large compared to the skin depth δ , is given approximately³ by

$$P = \frac{1}{2g\delta} \int_S |H_t|^2 ds = \frac{1}{2g\delta} \int_S \frac{dW}{dz} \frac{d\bar{W}}{d\bar{z}} ds, \quad (4)$$

where H_t is the amplitude of the tangential component of the magnetic field on the conducting surface, and the second expression follows by using the quasi-static magnetic field given by (1) and the Cauchy-Riemann relations.⁴

For a plane conducting surface, $W = H_0 z$. Hence, from (3) and (4) the ratio of the power dissipated in the semi-circular groove of unit diameter to that dissipated in a plane strip is

$$\frac{P}{P_0} = \frac{4}{\pi^2} \int_B^C \frac{d\xi}{dz} \frac{d\bar{\xi}}{d\bar{z}} ds, \quad (5)$$

where the contour in the z plane is the semicircle in Fig. 2(a). From the relation between z and ξ given in (2) it is shown in Appendix I that

$$\begin{aligned} \frac{P}{P_0} &= \frac{8}{\pi^3} \int_0^1 [K(k)]^2 dc \\ &= \frac{8}{\pi^3} \left[2 \int_0^1 (1-c)[K(k)]^2 dc + 1 \right], \end{aligned} \quad (6)$$

where $c = k^2$ and $K(k)$ is the complete elliptic integral of the first kind and modulus k . Numerical integration gives

$$\frac{P}{P_0} = 1.085. \quad (7)$$

This may be compared with Marcattili's estimate, $P/P_0 = 1.09 \pm 0.01$.

We now determine the position of the effective smooth waveguide wall, which enables the phase constant of the propagating wave to be correctly calculated. In Appendix I it is shown that $\xi \sim (\pi z/2) - i \log 2$, as $y = \text{Im } z \rightarrow +\infty$. Hence, from (3),

$$W \sim H_0 \left(z - \frac{2i}{\pi} \log 2 \right) = W_0, \text{ as } y \rightarrow +\infty. \quad (8)$$

Thus $\text{Im } W_0 = 0$ on $y = 2/\pi \log 2 = d$, which is therefore the position of the effective smooth waveguide wall. Since the wire radius is here supposed to be $\frac{1}{2}$, the ratio D of the displacement of the effective smooth waveguide wall from the trough of the groove to the radius of the groove cross section is

$$D = 2d = \frac{4}{\pi} \log 2 = 0.88. \quad (9)$$

III. BOUNDARY OF CYLINDRICAL WIRES

Turning now to the case when the pitch of the helix is greater than the wire diameter we are concerned with the plane grating of parallel cylindrical wires, as shown in Fig. 3. There is supposed to be an impressed magnetic field $H_0 e^{i\omega t}$ parallel to and on one side of the plane containing the axes of the wires and perpendicular to the wires. There will be leakage through the wires but to the order of the quasi-static approximation this may be neglected. (The circular electric wave can be resolved into conical waves which are reflected on the waveguide walls. In the rectified model this means plane waves incident on the grating and from the equivalent circuit⁶ for this problem it follows that the grating acts as a short-circuit in the limit as the ratio of pitch to

⁵ P. F. Byrd and M. D. Friedman, "Handbook of Elliptic Integrals for Engineers and Physicists," Springer-Verlag, Berlin, Germany; 1954.

⁶ N. Marcuvitz, "Waveguide Handbook," McGraw-Hill Book Co., Inc., New York, N. Y., M.I.T. Rad. Labs. Ser., vol. 10, p. 286, 1951.

wavelength tends to zero.) The actual leakage is soaked up by a lossy external sheath.

Thus, on the side of the impressed field, the quasi-static magnetic field is of constant strength H_0 at a great distance from the wires, whilst on the other side, the field vanishes at a great distance from the wires. The problem is then one of finding an analytic function W whose imaginary part is constant on the conducting cylinders and is such that $W \rightarrow 0$ as $x \rightarrow -\infty$ and $W \sim iH_0z$, as $x \rightarrow +\infty$ so that, from (1), $H_x \rightarrow 0$ and $H_y \rightarrow -H_0$. But Smythe⁷ gives the solution to the equivalent electrostatic problem wherein the surfaces $\text{Im } W = 0$ are circular cylinders within two per cent provided that $b \geq 2c$ in Fig. 3, the error decreasing as b/c increases and increasing as b/c decreases. Here $2b$ is the distance between the axes of successive wires and $2c$ is the diameter of the wires both in the direction along the line of axes and in the direction perpendicular to that. As b/c approaches unity, the cylinder becomes a square of side $2c$. The maximum deviation from a circle is quoted later for the three values of the ratio b/c for which numerical results are given.

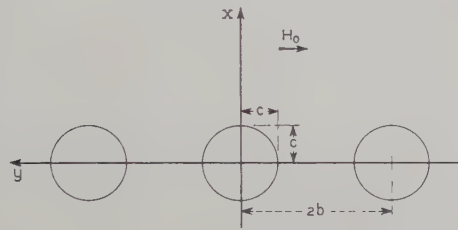


Fig. 3—Cross section of cylindrical wires.

In the present notation, from Smythe,⁷

$$W = \frac{H_0 b}{2\pi} \left(\sin^{-1}(\xi) + \sin^{-1} \left[\frac{2\xi + a - 1}{a + 1} \right] \right), \quad (10)$$

where

$$z = \frac{2b}{\pi(1 + \lambda)} \left(\tanh^{-1} \left[\frac{(\xi - 1)^{1/2}}{(\xi + a)^{1/2}} \right] + \lambda \tanh^{-1} \left[\frac{(\xi + 1)^{1/2}}{(\xi + a)^{1/2}} \right] \right), \quad (11)$$

and appropriate values are given to the inverse functions and the square roots. The ξ plane is cut along the real axis from -1 to $+\infty$, and from $-a$ to $-\infty$. The quantity λ is the smallest positive root of

$$\sin \left[\frac{\pi c}{2b} (1 + \lambda) \right] = \tanh \left[\frac{\pi c}{2b} \left(1 + \frac{1}{\lambda} \right) \right], \quad (12)$$

and

$$a = \coth^2 \left[\frac{\pi c}{2b} \left(1 + \frac{1}{\lambda} \right) \right] + \cot^2 \left[\frac{\pi c}{2b} (1 + \lambda) \right]. \quad (13)$$

⁷ W. R. Smythe, "Static and Dynamic Electricity," McGraw-Hill Book Co., Inc., New York, N. Y., p. 98; 1950.

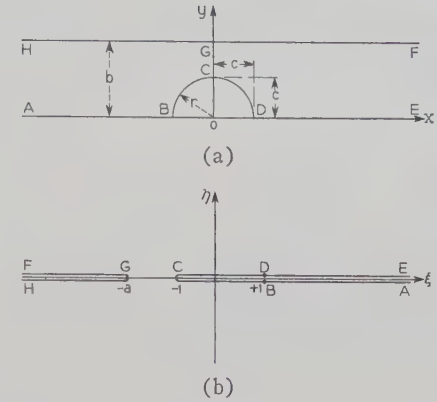


Fig. 4—Conformal transformation of the strip with semicircular intrusion into cut plane. (a) z plane, (b) ξ plane.

These equations arise from the condition that $OC = c = OD$, in Fig. 4(a).

From (4) the ratio of the power dissipated in the parallel grating of cylindrical wires to that dissipated in a plane grating is

$$\frac{P}{P_0} = \frac{1}{bH_0^2} \int_B^D \frac{dW}{dz} \frac{d\bar{W}}{d\bar{z}} ds, \quad (14)$$

since for the plane grating $W = iH_0z$, $x \geq 0$ and $W = 0$, $x \leq 0$. From (10), (11), and (14) it is shown in Appendix II that

$$\frac{P}{P_0} = (1 + \lambda) \left(\frac{[1 - \Lambda_0(\sin^{-1} \lambda, k)]}{\sqrt{1 - \lambda^2}} + \cos \left[\frac{\pi c}{2b} (1 + \lambda) \right] \cot \left[\frac{\pi c}{2b} (1 + \lambda) \right] \frac{K(k)}{\pi \lambda} \right), \quad (15)$$

where

$$k' = \sqrt{1 - k^2} = \frac{\cos \left[\frac{\pi c}{2b} (1 + \lambda) \right]}{\lambda}. \quad (16)$$

Here $\Lambda_0(\beta, k)$ is Heuman's Lambda function⁵ and $K(k)$ is as before. The displacement

$$d = \lim_{x \rightarrow +\infty} \left[x - \frac{\text{Im } W}{H_0} \right]$$

of the effective smooth waveguide wall is found in Appendix II, (39), and the ratio $D = d/c$, where c is the axial radius of the wire, is thus

$$D = \frac{b}{\pi c(1 + \lambda)} \left((1 - \lambda) \log \tanh \left[\frac{\pi c}{2b} \left(1 + \frac{1}{\lambda} \right) \right] + 2\lambda \log \tan \left[\frac{\pi c}{2b} (1 + \lambda) \right] \right). \quad (17)$$

Eq. (12) was solved numerically for three values of b/c and the quantities P/P_0 and D were then calculated from (15) and (17). These values are tabulated below, together with the values r_{\max}/c , where r_{\max} is the largest value of the radius r of the cylinders forming the grat-

ing, as given by Richmond.⁸ It is to be expected that as b/c decreases the values of P/P_0 are smaller than those for exactly circular wires and conversely for the values of D .

b/c	P/P_0	D	r_{\max}/c
2	1.225	0.64	1.018
3/2	1.140	0.80	1.063
4/3	1.105	0.86	1.11

Since for $b/c=1$ and exactly circular wires the calculated value of P/P_0 is 1.085, (7), the value of P/P_0 for $b/c=4/3$ as given above is about one per cent low. In extrapolating for b/c between 1 and 2 the values calculated for $b/c=1$, 3/2, and 2 should be used. Thus the extrapolated value of P/P_0 for $b/c=6/5$ is 1.10. This compares favorably with the experimental value of 1.13 for the power loss ratio, obtained by J. A. Young of these Laboratories in the case of a helix waveguide with wire diameter 0.0045" and separation 0.0009."

IV. CONCLUSION

An approximate theoretical calculation of heat losses in a metallic waveguide surface with boundary of periodic semicircular grooves and of cylindrical wires has been made, using the magnetic field of a perfect smooth guide. Also calculated was the displacement of the effective smooth waveguide wall from the wire axes. From comparison with experiment it appears that the theory gives quite a good prediction of the heat loss when it is borne in mind that the experimental value will be slightly higher due to leakage into the outer jacket and the presence of a dielectric coating on the wire which presumably tends to concentrate the fields slightly and increase the eddy currents.

It should also be noted that the results apply to any low-loss mode in a helix of finite pitch; *i.e.*, any mode for which, either by accident or design, the wall currents follow the direction of the wires.¹

APPENDIX I

We first give the conformal transformation $z=z(\xi)$ which maps the flat strip in the ξ plane, Fig. 2(d), into the strip with the semicircular groove in the z plane, Fig. 2(a). The successive transformations from the ξ plane are given by⁴

$$\begin{aligned} \tau &= -\cos(2\xi), \quad w = \frac{2}{(1-\tau)}, \\ z &= i \frac{K(\sqrt{1-w})}{K(\sqrt{w})}, \end{aligned} \quad (18)$$

where

$$K(\sqrt{w}) = \int_0^1 \frac{dt}{\sqrt{(1-t^2)(1-wt^2)}} \quad (19)$$

is the complete elliptic integral of the first kind and

⁸ W. R. Richmond, "On the electrostatic field of a plane or circular grating formed of thick round wires," *Proc. Lond. Math. Soc. Ser. 2*, vol. 22, p. 389; 1923.

modulus \sqrt{w} . Combining the transformation of (18) we obtain

$$z = i \frac{K(i \tan \xi)}{K(\sec \xi)}. \quad (20)$$

We calculate here the expression for P/P_0 given in (5). On the semicircle in the z plane, *Fig. 2(a)*, setting $\xi=\xi$, $0 \leq \xi \leq (\pi/2)$ in (20), it is found that

$$z = \frac{K}{(K - iK')}, \quad k = \sin \xi, \quad (21)$$

where K , K' are the complete elliptic integrals of the first kind⁵ with complementary moduli k and $k' = \sqrt{1-k^2}$, respectively. From (21), it follows that

$$\frac{dz}{d\xi} = -\frac{i\pi}{2 \sin \xi \cos \xi (K - iK')^2}, \quad (22)$$

where use has been made of the identity⁶

$$\frac{d}{dk} \left(\frac{K'}{K} \right) = -\frac{\pi}{2K^2 k k'^2}. \quad (23)$$

From (5) and (22),

$$\begin{aligned} \frac{P}{P_0} &= \frac{8}{\pi^3} \int_0^{\pi/2} (K^2 + K'^2) \sin \xi \cos \xi d\xi \\ &= \frac{8}{\pi^3} \int_0^1 [K(k)]^2 dc; \quad c = k^2. \end{aligned} \quad (24)$$

Since⁵

$$\begin{aligned} \int_0^1 (2c-1)K^2 dc \\ = [(c-1)(2c-1)K^2 + 2(c-1)KE + E^2]_0^1 = 1, \end{aligned} \quad (25)$$

(24) may be written

$$\frac{P}{P_0} = \frac{8}{\pi^3} \left(2 \int_0^1 (1-c)K^2 dc + 1 \right). \quad (26)$$

Finally, as $\text{Im } (\xi) \rightarrow +\infty$, $\sec \xi \rightarrow 0$ and $i \tan \xi \sim -(1-2e^{2i\xi})$. Hence (5), from (20),

$$\frac{\pi}{2} z \sim i(\log 2 - i\xi), \quad \text{as } \text{Im } (\xi) \rightarrow +\infty. \quad (27)$$

APPENDIX II

We here determine P/P_0 as given by (14), where W and z are given as functions of ξ by (10) and (11). The quantities λ and a are given by (12) and (13) which arise from the condition that $OC=OD=c$ in *Fig. 4(a)*, namely, with

$$0 < \tan^{-1} \sqrt{\frac{2}{(a-1)}} < \frac{\pi}{2},$$

$$\frac{2b}{\pi(1+\lambda)} \tan^{-1} \sqrt{\frac{2}{(a-1)}} = c = \frac{2b\lambda}{\pi(1+\lambda)} \tanh^{-1} \sqrt{\frac{2}{(a+1)}}. \quad (28)$$

The points A, B, C, D, E, F, G, H in the z plane correspond to the points with the same letters in the ξ plane, Fig. 4(b), which is cut along the real axis from -1 to $+\infty$ and from $-a$ to $-\infty$. From (10), $\text{Im}(W) = 0$ for $\xi = \xi \pm i0$, $-1 < \xi \leq 1$; i.e., on the section BCD . In the z plane this section is close to a semicircle if b/c is not close to 1 in which case the section is closer to a square. For $b=2c$ the distance r from the origin O is equal to c within two per cent and for $b=4/3c$ the error is a little over ten per cent.⁸

In differential form (10) and (11) are

$$\frac{dW}{d\xi} = \frac{iH_0b}{2\pi} \frac{[(\xi+1)^{1/2} + (\xi+a)^{1/2}]}{(\xi-1)^{1/2}(\xi+1)^{1/2}(\xi+a)^{1/2}}, \quad (29)$$

$$\frac{dz}{d\xi} = \frac{b}{\pi(1+\lambda)} \frac{[(\xi+1)^{1/2} + \lambda(\xi-1)^{1/2}]}{(\xi-1)^{1/2}(\xi+1)^{1/2}(\xi+a)^{1/2}}, \quad (30)$$

where appropriate values are to be given to the square roots.

Dividing (29) by (30) we obtain

$$\frac{dW}{dz} = \frac{iH_0(1+\lambda)}{2} \frac{[(\xi+1)^{1/2} + (\xi+a)^{1/2}]}{[(\xi+1)^{1/2} + \lambda(\xi-1)^{1/2}]} \quad (31)$$

As $x \rightarrow \pm \infty$, $|\xi| \rightarrow \infty$, and assigning the appropriate values to the square roots,

$$\frac{dW}{dz} \rightarrow iH_0, \text{ as } x \rightarrow +\infty$$

$$\frac{dW}{dz} \rightarrow 0, \text{ as } x \rightarrow -\infty, \quad (32)$$

the difference arising because of the cuts in the ξ plane. This is the desired behavior for W at great distances from the wires.

From (14), (30), and (31),

$$\frac{P}{P_0} = \frac{1}{bH_0^2} \int_{-1}^1 \left(\left[\frac{dW}{dz} \frac{d\bar{W}}{d\bar{z}} \sqrt{\frac{dz}{d\xi} \frac{d\bar{z}}{d\xi}} \right]_{\xi=\xi+i0} + \left[\frac{dW}{dz} \frac{d\bar{W}}{d\bar{z}} \sqrt{\frac{dz}{d\xi} \frac{d\bar{z}}{d\xi}} \right] \right)_{\xi=\xi-i0} d\xi$$

$$= \frac{(1+\lambda)}{2\pi} \cdot \int_{-1}^1 \frac{[(a+1) + 2\xi]}{\sqrt{(1-\xi^2)(a+\xi)[(1+\lambda^2) + (1-\lambda^2)\xi]}} d\xi. \quad (33)$$

By means of standard transformations⁵ and after considerable reductions it is found that

$$\frac{P}{P_0} = (1+\lambda) \left(\frac{[1 - \Lambda_0(\sin^{-1} \lambda, k)]}{\sqrt{1-\lambda^2}} + \cos \left[\frac{\pi c}{2b} (1+\lambda) \right] \cot \left[\frac{\pi c}{2b} (1+\lambda) \right] \frac{K(k)}{\pi \lambda} \right), \quad (34)$$

where $\Lambda_0(\beta, k)$ is Heuman's Lambda function,⁵ λ is the smallest positive root of (12), and

$$(1-k^2) = \frac{\cos^2 \left[\frac{\pi c}{2b} (1+\lambda) \right]}{\lambda^2}. \quad (35)$$

Finally, we determine the length

$$d = \lim_{x \rightarrow \infty} \left(x - \frac{\Psi}{H_0} \right), \quad \Psi = \text{Im } W. \quad (36)$$

Since this is independent of y , it is sufficient to take $y=0$ and consider the behavior as $x \rightarrow \infty$ along DE in Fig. 4(a) or, equivalently, as $\xi \rightarrow \infty$ on $\xi = \xi + i0$, Fig. 4(b). From (29), the square roots all being positive on $\xi = \xi + i0$, $\xi > 1$,

$$\Psi = \frac{H_0 b}{2\pi} \left(\log [\xi + \sqrt{\xi^2 - 1}] + \log \left[\frac{(2\xi + a - 1) + 2\sqrt{(\xi + a)(\xi - 1)}}{(a + 1)} \right] \right), \quad (37)$$

since $\Psi = 0$ at $\xi = 1$; i.e., on the grating. Also, from (11), for $\xi = \xi + i0$, $\xi > 1$,

$$= x \frac{b}{\pi(1+\lambda)} \left(\log \left[\frac{(2\xi + a - 1) + 2\sqrt{(\xi + a)(\xi - 1)}}{(a + 1)} \right] + \log \left[\frac{(2\xi + a + 1) + 2\sqrt{(\xi + a)(\xi + 1)}}{(a - 1)} \right] \right). \quad (38)$$

Thus, from (36)–(38), letting $\xi \rightarrow \infty$,

$$d = \frac{b}{2\pi(1+\lambda)} \left((1-\lambda) \log \left[\frac{2}{(a+1)} \right] + 2\lambda \log \left[\frac{2}{(a-1)} \right] \right)$$

$$= \frac{b}{\pi(1+\lambda)} \left((1-\lambda) \log \tanh \left[\frac{\pi c}{2b} \left(1 + \frac{1}{\lambda} \right) \right] + 2\lambda \log \tan \left[\frac{\pi c}{2b} (1+\lambda) \right] \right), \quad (39)$$

using (28).

V. ACKNOWLEDGMENT

The writer wishes to thank S. P. Morgan for bringing this problem to his attention and for many helpful discussions during the preparation of this paper.

The Expansions of Electromagnetic Fields in Cavities*

KANEYUKI KUROKAWA†

Summary—In the theory of cavity resonators, the assumptions are frequently made that every irrotational function can be represented as the gradient of a scalar and that every divergenceless function can be represented as the rotation of a vector. These are, however, not necessarily correct. This paper corrects these misleading assumptions and describes “the theory of cavity resonators” which supplement the classical theory of Slater.

I. INTRODUCTION

EXPANDING the electromagnetic fields in terms of complete orthonormal functions, we can reduce the problem of solving Maxwell's equations in a cavity to that of determining all the expansion coefficients. In this way, Slater¹ succeeded in giving the input impedance of a cavity. However, he did not use the correct set of functions and missed a capacitance term in the input impedance expression. Furthermore he stated that for the expansion of the magnetic field \mathbf{H} in a cavity we did not need the irrotational functions. The reason for this statement seems to be that \mathbf{H} is itself solenoidal, namely $\nabla \cdot \mathbf{H} = 0$. In this regard Teichmann and Wigner² pointed out that the component expressed as the gradient of a scalar was necessary to expand \mathbf{H} , in addition to the functions corresponding to the natural resonance modes. The contribution of this component to the input admittance is a term proportional to ω^{-1} , that is, an inductance term, where ω is the angular frequency. These functions, however, still remain incomplete in the most general case, for the assumption was made that every irrotational function can be represented as the gradient of a scalar. The function which is denoted by the symbol \mathbf{G}_0 in this paper is the missing one. In a fairly recent paper, Schelkunoff³ made some comments on Teichmann and Wigner's work. His illustration shows that the set of natural modes is not incomplete if use is made of a short circuit which conforms to the impressed field. However, the complete sets of orthonormal functions defined in Section II of this paper are more suitable for a general discussion. These functions already have been well studied by Müller.⁴ In his treatment, however, the incorrect

assumption mentioned above is again taken for granted, though his final result is undoubtedly correct.

This paper describes “the theory of cavity resonators” which serves as a supplement to the classical theory of Slater. The emphasis is placed on correcting widely held assumptions that, when a function is divergenceless, we need no irrotational functions to expand the function and that, when the rotation of a function vanishes, the function can be expressed as the gradient of a scalar.

II. COMPLETE SETS OF ORTHONORMAL FUNCTIONS

For the expansion of functions defined in a closed region V , enclosed by a surface (or surfaces) S , we first have to set up appropriate complete sets of orthonormal functions in V . It is well known that the solutions of the wave equation with the boundary condition

$$\begin{aligned} \nabla^2 \psi_\alpha + k_\alpha^2 \psi_\alpha &= 0 & (\text{in } V) \\ \psi_\alpha &= 0 & (\text{on } S) \end{aligned} \quad (1)$$

are capable of forming a complete set of orthonormal functions ψ_α ($\alpha = 1, 2, 3, \dots$) which is used in expanding an arbitrary piecewise continuous scalar function in V . Similarly the solutions of

$$\begin{aligned} \nabla^2 \phi_\lambda + k_\lambda^2 \phi_\lambda &= 0 & (\text{in } V) \\ \frac{\partial \phi_\lambda}{\partial n} &= 0 & (\text{on } S), \end{aligned} \quad (2)$$

where the derivative is taken in a direction normal to the surface S , are capable of forming another complete set ϕ_λ ($\lambda = 0, 1, 2, \dots$) for the expansion of a scalar function.

For the expansion of an arbitrary piecewise continuous vector function defined in V , in like manner, we have two complete sets of orthonormal functions Ψ_p ($p = 0, 1, 2, \dots$) and Φ_q ($q = 0, 1, 2, \dots$), each of which satisfies

$$\begin{aligned} \nabla^2 \Psi_p + k_p^2 \Psi_p &= 0 & (\text{in } V) \\ \mathbf{n} \times \Psi_p &= 0, \quad \nabla \Psi_p = 0 & (\text{on } S) \end{aligned} \quad (3)$$

and

$$\begin{aligned} \nabla^2 \Phi_q + k_q^2 \Phi_q &= 0 & (\text{in } V) \\ \mathbf{n} \times \nabla \times \Phi_q &= 0, \quad \mathbf{n} \cdot \Phi_q = 0 & (\text{on } S). \end{aligned} \quad (4)$$

It is worth noting that two boundary conditions are necessary to define these vector functions.

Some of Ψ_p and Φ_q have the common eigenvalues k_a' ($a = 1, 2, 3, \dots$) and are related to each other by

$$k_a \Psi_p = \nabla \times \Phi_q, \quad k_a \Phi_q = \nabla \times \Psi_p.$$

* Manuscript received by the PGM TT, August 16, 1957.

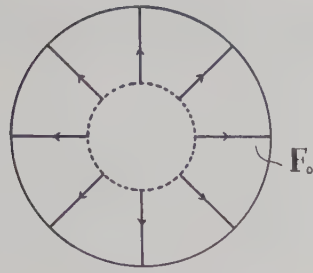
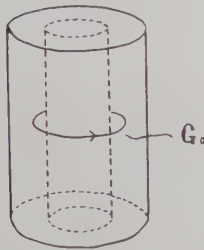
† Institute of Industrial Science, University of Tokyo, Chiba City, Japan.

¹ J. C. Slater, “Microwave Electronics,” D. Van Nostrand Co., Inc., New York, N. Y., pp. 57-83; 1950.

² T. Teichmann and E. P. Wigner, “Electromagnetic field expansions in loss-free cavities excited through holes,” *J. Appl. Phys.*, vol. 24, pp. 262-267; March, 1953.

³ S. A. Schelkunoff, “On representation of electromagnetic fields in cavities in terms of natural modes of oscillation,” *J. Appl. Phys.*, vol. 24, pp. 262-267; March, 1953.

⁴ G. Goubaul, “Electromagnetische Wellenleiter und Holräume,” Wissenschaftliche Verlagsgesellschaft M.B.H., Stuttgart, Germany, pp. 80-97; 1955.

Fig. 1— F_0 functions.Fig. 2— G_0 functions.

Let us denote these Ψ_α and Φ_λ as E_α and H_α respectively hereafter. The above relations become

$$k_\alpha E_\alpha = \nabla \times H_\alpha, \quad k_\alpha H_\alpha = \nabla \times E_\alpha. \quad (5)$$

All the other Ψ_α and Φ_λ will be denoted as F_α ($\alpha = 0, 1, 2, \dots$) and G_λ ($\lambda = 0, 1, 2, \dots$). Then it can be shown that the rotations of F_α and G_λ vanish.

$$\nabla \times F_\alpha = 0, \quad \nabla \times G_\lambda = 0. \quad (6)$$

F_α and G_λ with nonzero eigenvalues satisfy the relations

$$k_\alpha F_\alpha = \nabla \psi_\alpha, \quad k_\lambda G_\lambda = \nabla \phi_\lambda \quad (7)$$

where ψ_α and ϕ_λ are the functions defined by (1) and (2). If the closed region V has two or more than two separate boundaries, F_α with $k_\alpha = 0$ can exist and will be denoted by the symbol F_0 . An example of such a region V is the space between two concentric spheres. F_0 satisfies

$$\begin{aligned} \nabla \times F_0 &= 0, & \nabla \cdot F_0 &= 0 \quad (\text{in } V) \\ n \times F_0 &= 0 & & \quad (\text{on } S). \end{aligned}$$

Therefore, by Helmholtz's theorem, F_0 can be set equal to the gradient of a scalar function ψ .

$$F_0 = \nabla \psi$$

where ψ satisfies Laplace's equation $\nabla^2 \psi = 0$ in V and the boundary condition $n \times \nabla \psi = 0$ on S . ψ can be considered as an electrostatic potential and F_0 as the electrostatic field. In a multiply connected region (the region in which there are contours which cannot be shrunk away to nothing) G_λ with $k_\lambda = 0$ can exist and will be denoted by the symbol G_0 . An example of such a region is the space between two coaxial cylinders closed at both ends. In this case, G_0 corresponds to the magnetic field produced by the dc current flowing through the circuit which con-

sists of the center conductor, the short ends, and the outer conductor. G_0 satisfies

$$\begin{aligned} \nabla \times G_0 &= 0, & \nabla \cdot G_0 &= 0 \quad (\text{in } V) \\ n \cdot G_0 &= 0 & & \quad (\text{on } S). \end{aligned}$$

Therefore, by Helmholtz's theorem, G_0 can be set equal to the rotation of a vector function but not to the gradient of a scalar function. If we want to set G_0 equal to the gradient of a scalar function, we have either to introduce "a cut" in the region or to use a multivalued function.

In some cases, there are many independent F_0 's and G_0 's; however they can all be grouped in the sets of F_α 's and G_λ 's, respectively, for all of them satisfy (6).

III. THE EXPANSIONS OF ELECTROMAGNETIC FIELDS

We shall use the set of functions E_α and F_α in expanding the electric field, for E_α and F_α have boundary conditions similar to those of the actual field E in a cavity. For the same reason, we shall expand H in a series in terms of the H_α 's and G_λ 's; the current J in the E_α 's and F_α 's; and the charge density ρ in the ψ_α 's. Thus we have

$$\begin{aligned} E &= \sum_a E_\alpha \int E \cdot E_\alpha dv + \sum_\alpha F_\alpha \int E \cdot F_\alpha dv, \\ H &= \sum_a H_\alpha \int H \cdot H_\alpha dv + \sum_\lambda G_\lambda \int H \cdot G_\lambda dv, \\ J &= \sum_a E_\alpha \int J \cdot E_\alpha dv + \sum_\alpha F_\alpha \int J \cdot F_\alpha dv, \\ \rho &= \sum_\alpha \psi_\alpha \int \rho \psi_\alpha dv. \end{aligned} \quad (8)$$

Since $\nabla \times E$ behaves like H , the H_α 's and G_λ 's will be used to expand $\nabla \times E$.

$$\begin{aligned} \nabla \times E &= \sum_a H_\alpha \int \nabla \times E \cdot H_\alpha dv \\ &\quad + \sum_\lambda G_\lambda \int \nabla \times E \cdot G_\lambda dv. \end{aligned} \quad (9)$$

From the vector relation

$$\begin{aligned} \nabla \cdot (E \times \nabla \times E_\alpha) &= \nabla \times E \cdot \nabla \times E_\alpha - E \cdot \nabla \times \nabla \times E_\alpha \\ &= k_\alpha H_\alpha \cdot \nabla \times E - k_\alpha^2 E_\alpha \cdot E \end{aligned}$$

and Gauss' theorem we have

$$\int n \times E \cdot H_\alpha dS = \int \nabla \times E \cdot H_\alpha dv - k_\alpha \int E \cdot E_\alpha dv. \quad (10)$$

Similarly from

$$\begin{aligned} \nabla \cdot (E \times G_\lambda) &= G_\lambda \cdot \nabla \times E - E \cdot \nabla \times G_\lambda \\ &= G_\lambda \cdot \nabla \times E \end{aligned}$$

we have

$$\int \mathbf{n} \times \mathbf{E} \cdot \mathbf{G}_\lambda dS = \int \nabla \times \mathbf{E} \cdot \mathbf{G}_\lambda dv. \quad (11)$$

Inserting (10) and (11) into (9), we obtain

$$\begin{aligned} \nabla \times \mathbf{E} &= \sum_a \mathbf{H}_a \left\{ k_a \int \mathbf{E} \cdot \mathbf{E}_a dv + \int \mathbf{n} \times \mathbf{E} \cdot \mathbf{H}_a dS \right\}, \\ &+ \sum_\lambda \mathbf{G}_\lambda \int \mathbf{n} \times \mathbf{E} \cdot \mathbf{G}_\lambda dS. \end{aligned} \quad (12)$$

In a corresponding way, expanding $\nabla \times \mathbf{H}$ in a series in terms of the \mathbf{E}_a 's and \mathbf{F}_α 's and using the boundary conditions $\mathbf{n} \times \mathbf{E}_a = 0$ and $\mathbf{n} \times \mathbf{F}_\alpha = 0$ on S , we have

$$\nabla \times \mathbf{H} = \sum_a \mathbf{E}_a k_a \int \mathbf{H} \cdot \mathbf{H}_a dv. \quad (13)$$

For the expansion of $\nabla \cdot \mathbf{B}$ we shall use the ϕ_λ 's.

$$\nabla \cdot \mathbf{B} = \sum_\lambda \phi_\lambda \int \nabla \cdot \mathbf{B} \phi_\lambda dv. \quad (14)$$

From the relation

$$\begin{aligned} \nabla \cdot \phi_\lambda \mathbf{B} &= \phi_\lambda \nabla \cdot \mathbf{B} + \mathbf{B} \cdot \nabla \phi_\lambda \\ &= \phi_\lambda \nabla \cdot \mathbf{B} + k_\lambda \mathbf{B} \cdot \mathbf{G}_\lambda \end{aligned}$$

and Gauss' theorem we have

$$\int \phi_\lambda \mathbf{B} \cdot \mathbf{n} dS = \int \nabla \cdot \mathbf{B} \phi_\lambda dv + k_\lambda \int \mathbf{B} \cdot \mathbf{G}_\lambda dv. \quad (15)$$

Substituting in (14), we obtain

$$\nabla \cdot \mathbf{B} = \sum_\lambda \phi_\lambda \left\{ -k_\lambda \int \mathbf{B} \cdot \mathbf{G}_\lambda dv + \int \mathbf{B} \cdot \mathbf{n} \phi_\lambda dS \right\}. \quad (16)$$

Similarly for $\nabla \cdot \mathbf{D}$, expanding in series in the ψ_α 's and using the boundary condition $\psi_\alpha = 0$ on S , we have

$$\nabla \cdot \mathbf{D} = \sum_\alpha \psi_\alpha \left\{ -k_\alpha \int \mathbf{D} \cdot \mathbf{F}_\alpha dv \right\}. \quad (17)$$

We have now set up the series for the various quantities appearing in Maxwell's equations. Assuming that ϵ and μ are constant throughout in the region V , we next substitute these series in Maxwell's equations. From

$$\nabla \times \mathbf{E} + \frac{\partial \mathbf{B}}{\partial t} = 0$$

we have

$$\begin{aligned} \sum_a \mathbf{H}_a \left(k_a \int \mathbf{E} \cdot \mathbf{E}_a dv + \int \mathbf{n} \times \mathbf{E} \cdot \mathbf{H}_a dS \right) \\ + \sum_\lambda \mathbf{G}_\lambda \int \mathbf{n} \times \mathbf{E} \cdot \mathbf{G}_\lambda dS \\ + \mu \frac{d}{dt} \left\{ \sum_a \mathbf{H}_a \int \mathbf{H} \cdot \mathbf{H}_a dv + \sum_\lambda \mathbf{G}_\lambda \int \mathbf{H} \cdot \mathbf{G}_\lambda dv \right\} = 0. \end{aligned} \quad (18)$$

Multiplying (18) by \mathbf{H}_a and integrating over V , on account of the orthonormal conditions, we obtain

$$k_a \int \mathbf{E} \cdot \mathbf{E}_a dv + \mu \frac{d}{dt} \int \mathbf{H} \cdot \mathbf{H}_a dv = - \int \mathbf{n} \times \mathbf{E} \cdot \mathbf{H}_a dS. \quad (19)$$

Multiplying (18) by \mathbf{G}_λ and integrating over V , we have

$$\mu \frac{d}{dt} \int \mathbf{H} \cdot \mathbf{G}_\lambda dv = - \int \mathbf{n} \times \mathbf{E} \cdot \mathbf{G}_\lambda dS. \quad (20)$$

Similarly from

$$\nabla \times \mathbf{H} - \frac{\partial \mathbf{D}}{\partial t} = \mathbf{J},$$

we have

$$k_a \int \mathbf{H} \cdot \mathbf{H}_a dv - \epsilon \frac{d}{dt} \int \mathbf{E} \cdot \mathbf{E}_a dv = \int \mathbf{J} \cdot \mathbf{E}_a dv \quad (21)$$

$$- \epsilon \frac{d}{dt} \int \mathbf{E} \cdot \mathbf{F}_\alpha dv = \int \mathbf{J} \cdot \mathbf{F}_\alpha dv. \quad (22)$$

The equation $\nabla \cdot \mathbf{B} = 0$ gives

$$k_\lambda \int \mathbf{H} \cdot \mathbf{G}_\lambda dv = \int \mathbf{H} \cdot \mathbf{n} \phi_\lambda dS. \quad (23)$$

Finally $\nabla \cdot \mathbf{D} = \rho$ gives

$$-k_\alpha \epsilon \int \mathbf{E} \cdot \mathbf{F}_\alpha dv = \int \rho \psi_\alpha dv. \quad (24)$$

From (19)–(24), the expansion coefficients $\int \mathbf{E} \cdot \mathbf{E}_a dv$, $\int \mathbf{E} \cdot \mathbf{F}_\alpha dv$, $\int \mathbf{H} \cdot \mathbf{H}_a dv$, $\int \mathbf{H} \cdot \mathbf{G}_\lambda dv$ will be obtained. Substituting these coefficients in the first two equations in (8), the desired electric and magnetic fields will be given in the series expansion.

As shown by Slater, (22) and (24) lead to the same result if we have the equation of continuity

$$\nabla \cdot \mathbf{J} + \frac{d}{dt} \rho = 0.$$

The only exception is the equations with the subscript $\alpha = 0$, where \mathbf{F}_0 has no corresponding ψ_0 .

To get a relation between (20) and (23) corresponding to the continuity equation, we take the time derivative of (23) and substitute in (20).

$$\begin{aligned} \mu \frac{d}{dt} \int \mathbf{H} \cdot \mathbf{n} \phi_\lambda dS &= -k_\lambda \int \mathbf{n} \times \mathbf{E} \cdot \mathbf{G}_\lambda dS \\ &= - \int \mathbf{n} \times \mathbf{E} \cdot \nabla \phi_\lambda dS. \end{aligned} \quad (25)$$

Here we introduce a differential operator ∇_S on the surface S which is equivalent to the operator $(\nabla - \mathbf{n}(\partial/\partial n))$. Integrating

$$\nabla_S \cdot (\phi_\lambda \mathbf{n} \times \mathbf{E}) = \phi_\lambda \nabla_S \cdot \mathbf{n} \times \mathbf{E} + \mathbf{n} \times \mathbf{E} \cdot \nabla_S \phi_\lambda$$

over S and using the relation $\nabla \phi_\lambda = \nabla_S \phi_\lambda$ [for $(\partial \phi_\lambda / \partial n) = 0$ on S], we have

$$\oint \phi_\lambda \mathbf{n} \times \mathbf{E} \cdot d\mathbf{l} = \int \phi_\lambda \nabla_S \cdot \mathbf{n} \times \mathbf{E} dS + \int \mathbf{n} \times \mathbf{E} \cdot \nabla \phi_\lambda dS.$$

The line integral is over the perimeter of S and is equal to zero, for the surface S is a closed surface and its perimeter vanishes. Substituting in (25), we find

$$\mu \frac{d}{dt} \int \mathbf{H} \cdot \mathbf{n} \phi_\lambda dS = \int (\nabla_S \cdot \mathbf{n} \times \mathbf{E}) \phi_\lambda dS. \quad (26)$$

This is true because of

$$\nabla_S \cdot \mathbf{n} \times \mathbf{E} = \frac{d}{dt} \mathbf{B} \cdot \mathbf{n}. \quad (27)$$

Eq. (27) is the continuity for the fictitious surface magnetic charge $-\mathbf{B} \cdot \mathbf{n}$ and the fictitious surface magnetic current $\mathbf{n} \times \mathbf{E}$. It expresses the conservation of the fictitious magnetic charge. Eqs. (20) and (23) lead to the same result using (27), as in the case of (22) and (24). The only exception is the equation with the subscript $\lambda=0$.

IV. THE INPUT ADMITTANCE OF A CAVITY

We next take up a cavity with an output which couples the cavity to an outside system, and which is assumed to take the form of a waveguide (or a coaxial line). Let S_0 be the cross section of the waveguide, which forms the boundary surface between the cavity and the output (see Fig. 3). The cavity now consists of the natural cavity plus the part of the waveguide out to the surface S_0 . The cavity wall S and the surface S_0 form a closed surface inside which we are solving Maxwell's equations. We assume that the tangential component of electric field, \mathbf{E}_{\parallel} , is given on S_0 by excitation from the outside system, and we expand it in terms of the complete orthonormal modes of the waveguide.

$$\mathbf{E}_{\parallel} = \sum_n \mathbf{E}_{tn} V_n \quad (28)$$

where the \mathbf{E}_{tn} 's are the orthonormal eigenfunctions for the transverse electric field in the waveguide and the V_n 's are the expansion coefficients. V_n can be considered as a voltage associated with n th mode in the waveguide.

Next we shall expand the functions \mathbf{H}_a and \mathbf{G}_λ on S_0 in series in the \mathbf{E}_{tn} 's.

$$\mathbf{H}_a = \sum_n \mathbf{k} \times \mathbf{E}_{tn} I_{an}, \quad (29)$$

$$\mathbf{G}_\lambda = \sum_n \mathbf{k} \times \mathbf{E}_{tn} I_{\lambda n}, \quad (30)$$

where the I_{an} 's and $I_{\lambda n}$'s are the expansion coefficients, \mathbf{k} is the longitudinal unit vector of the waveguide and is equal to $-\mathbf{n}$. From (28) and (29), we have

$$-\int_{S_0} \mathbf{n} \times \mathbf{E} \cdot \mathbf{H}_a dS = \int_{S_0} \mathbf{k} \times \mathbf{E} \cdot \mathbf{H}_a dS.$$

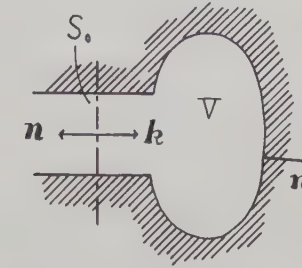


Fig. 3.—Reference plane S_0 .

$$\begin{aligned} &= \int_{S_0} \sum_n \mathbf{k} \times \mathbf{E}_{tn} V_n \cdot \sum_m \mathbf{k} \times \mathbf{E}_{tm} I_{am} dS \\ &= \sum_n V_n I_{an}. \end{aligned} \quad (31)$$

Similarly from (28) and (30), we have

$$-\int_{S_0} \mathbf{n} \times \mathbf{E} \cdot \mathbf{G}_\lambda dS = \sum_n V_n I_{\lambda n}. \quad (32)$$

For simplicity, we shall further assume that the angular frequency ω of the exciting field is in the vicinity of the resonant frequency $\omega_a = k_a / \sqrt{\epsilon_a}$ of the \mathbf{E}_a , \mathbf{H}_a mode, which is well separated from other resonant frequencies. Then \mathbf{H}_a component will be dominant in the magnetic field and the tangential component of \mathbf{E} on S will be given by the approximation⁵

$$\mathbf{n} \times \mathbf{E} \doteq Z_S \mathbf{H} \doteq (1 + j) \sqrt{\frac{\omega_a \mu}{2\sigma_S}} \mathbf{H}_a \int \mathbf{H} \cdot \mathbf{H}_a d\mathbf{v} \quad (33)$$

where Z_S and σ_S are the characteristic impedance and the conductivity of the wall conductor, respectively. From (33), we have

$$-\int_S \mathbf{n} \times \mathbf{E} \cdot \mathbf{H}_a dS \doteq (1 + j) \frac{\omega_a \mu}{Q_{Sa}} \int \mathbf{H} \cdot \mathbf{H}_a d\mathbf{v}, \quad (34)$$

where

$$\frac{1}{Q_{Sa}} = \frac{1}{2} \sqrt{\frac{2}{\omega_a \mu \sigma_S}} \int_S \mathbf{H}_a^2 dS. \quad (35)$$

⁵ If we take the surface roughness and irregularities of the wall into account, (34) and (35) are rewritten in the forms

$$\begin{aligned} \int_S \mathbf{n} \times \mathbf{E} \cdot \mathbf{H}_a dS &\doteq (1 + j S_a) \frac{\omega_a \mu}{Q_{Sa}} \int \mathbf{H} \cdot \mathbf{H}_a d\mathbf{v} \\ \frac{1}{Q_{Sa}} &\doteq \frac{F_a}{2} \sqrt{\frac{2}{\omega_a \mu S_a \sigma}} \int_S \mathbf{H}_a^2 dS \end{aligned}$$

where F_a and $F_a S_a$ are the factors which measure the apparent increases in the surface resistance and surface reactance.

Measurements show that the relations $F_a > 1$, $S_a > 1$ usually hold. ω_a' in (39) is replaced by

$$\omega_a' = \omega_a \left(1 - \frac{S_a}{2Q_{Sa}} \right).$$

Assuming that $J = \sigma E$, we eliminate $\int \mathbf{E} \cdot \mathbf{E}_a dv$ from (19) and (21).

$$\begin{aligned} \epsilon\mu \frac{d^2}{dt^2} \int \mathbf{H} \cdot \mathbf{H}_a dv + \sigma\mu \frac{d}{dt} \int \mathbf{H} \cdot \mathbf{H}_a dv + k_a^2 \int \mathbf{H} \cdot \mathbf{H}_a dv \\ + \left(\epsilon \frac{d}{dt} + \sigma \right) \int_S \mathbf{n} \times \mathbf{E} \cdot \mathbf{H}_a dS \\ = - \left(\epsilon \frac{d}{dt} + \sigma \right) \int_{S_0} \mathbf{n} \times \mathbf{E} \cdot \mathbf{H}_a dS. \quad (36) \end{aligned}$$

$(d/dt) = j\omega$, for we assumed the time factor $e^{j\omega t}$. If $j\omega\epsilon \gg \sigma$, as is usually the case, from (31), (34), and (36), we have

$$\begin{aligned} \int \mathbf{H} \cdot \mathbf{H}_a dv \left\{ k_a^2 - \omega^2 \epsilon\mu + j\omega\sigma\mu + (1+j)j\omega\epsilon\omega_a\mu \frac{1}{Q_{Sa}} \right\} \\ = j\omega\epsilon \sum_n V_n I_{an} \quad (37) \end{aligned}$$

from which we obtain

$$\int \mathbf{H} \cdot \mathbf{H}_a dv \doteq \frac{\sum_n V_n I_{an} / \omega_a \mu}{j \left(\frac{\omega}{\omega_a'} - \frac{\omega_a'}{\omega} \right) + \frac{1}{Q_a'}} \quad (38)$$

where

$$\begin{aligned} k_a^2 = \omega_a^2 \epsilon\mu, \quad \omega_a' = \omega_a \left(1 - \frac{1}{2Q_{Sa}} \right), \\ \frac{1}{Q_a'} = \frac{1}{Q_a} + \frac{1}{Q_{Sa}}, \quad \frac{1}{Q_a} = \frac{\sigma}{\omega_a \epsilon}. \quad (39) \end{aligned}$$

Next from (20) we have

$$\begin{aligned} \mu \frac{d}{dt} \int \mathbf{H} \cdot \mathbf{G}_\lambda dv + \int_S \mathbf{n} \times \mathbf{E} \cdot \mathbf{G}_\lambda dS \\ = - \int_{S_0} \mathbf{n} \times \mathbf{E} \cdot \mathbf{G}_\lambda dS. \quad (40) \end{aligned}$$

We neglect the second term on the left-hand side of (40) in comparison with the first term, for $\mathbf{n} \times \mathbf{E}$ is sufficiently small on S . [In (36) the large terms on the left-hand side cancel each other and the surface integral $\int_S \mathbf{n} \times \mathbf{E} \cdot \mathbf{H}_a dS$ cannot be neglected in the vicinity of the resonant frequency.] Inserting (30) into (40), we have

$$j\omega\mu \int \mathbf{H} \cdot \mathbf{G}_\lambda dv \doteq \sum_n V_n I_{\lambda n} \quad (41)$$

from which we obtain

$$\int \mathbf{H} \cdot \mathbf{G}_\lambda dv \doteq \frac{\sum_n V_n I_{\lambda n}}{j\omega\mu}. \quad (42)$$

Substituting (38) and (42) into (8), we have

$$\begin{aligned} \mathbf{H} \doteq \sum_a \mathbf{H}_a \frac{\sum_n V_n I_{an} / \omega_a \mu}{j \left(\frac{\omega}{\omega_a'} - \frac{\omega_a'}{\omega} \right) + \frac{1}{Q_a'}} \\ + \sum_\lambda \mathbf{G}_\lambda \frac{\sum_n V_n I_{\lambda n}}{j\omega\mu}. \quad (43) \end{aligned}$$

This is the desired magnetic field in the form of series expansion.

For the electric field, from (21) and (22) we have, taking into account that there is no steady-state solution for $\int \mathbf{E} \cdot \mathbf{F}_a dv$,

$$\mathbf{E} \doteq -j\sqrt{\frac{\mu}{\epsilon}} \sum_a \mathbf{E}_a \frac{\sum_n V_n I_{an} / \omega_a \mu}{j \left(\frac{\omega}{\omega_a'} - \frac{\omega_a'}{\omega} \right) + \frac{1}{Q_a'}}. \quad (44)$$

Thus we have solved Maxwell's equations in the cavity.

The tangential magnetic field on S_0 is given by

$$\begin{aligned} \mathbf{H}_{\parallel 1} = \sum_{a,\lambda} \sum_n \sum_m \mathbf{k} \times \mathbf{E}_{tm} \left\{ I_{am} \frac{V_n I_{an} / \omega_a \mu}{j \left(\frac{\omega}{\omega_a'} - \frac{\omega_a'}{\omega} \right) + \frac{1}{Q_a'}} \right. \\ \left. + I_{\lambda m} \frac{V_n I_{\lambda n}}{j\omega\mu} \right\}. \quad (45) \end{aligned}$$

We are considering the cavity which has only one output with only one transmission mode. The component $\mathbf{H}_{\parallel 1}$ of this mode is

$$\mathbf{H}_{\parallel 1} = \sum_a \mathbf{k} \times \mathbf{E}_{t1} \left\{ \frac{V_1 I_{a1}^2 / \omega_a \mu}{j \left(\frac{\omega}{\omega_a'} - \frac{\omega_a'}{\omega} \right) + \frac{1}{Q_a'}} + \frac{V_1 I_{\lambda 1}^2}{j\omega\mu} \right\}. \quad (46)$$

On the other hand, $\mathbf{H}_{\parallel 1}$ is expressible in the form

$$\mathbf{H}_{\parallel 1} = \mathbf{k} \times \mathbf{E}_{t1} I_1 \quad (47)$$

where I_1 is the current associated with the transmission mode. From (46) and (47), we have

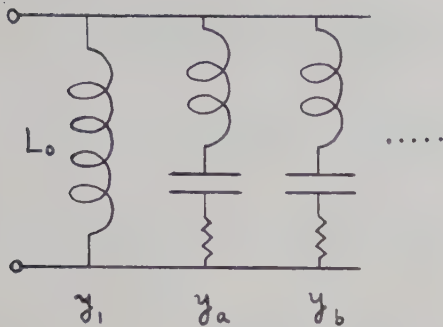
$$I_1 = \sum_a \frac{V_1 I_{a1}^2 / \omega_a \mu}{j \left(\frac{\omega}{\omega_a'} - \frac{\omega_a'}{\omega} \right) + \frac{1}{Q_a'}} + \sum_\lambda \frac{V_1 I_{\lambda 1}^2}{j\omega\mu}. \quad (48)$$

The input admittance is, therefore,

$$Y = \frac{I_1}{V_1} = \sum_a \frac{I_{a1}^2 / \omega_a \mu}{j \left(\frac{\omega}{\omega_a'} - \frac{\omega_a'}{\omega} \right) + \frac{1}{Q_a'}} + \sum_\lambda \frac{I_{\lambda 1}^2}{j\omega\mu}. \quad (49)$$

Similarly for cavities with two output leads, we have

$$\begin{aligned} I_1 &= Y_{11} V_1 + Y_{12} V_2, \\ I_2 &= Y_{12} V_1 + Y_{22} V_2, \end{aligned} \quad (50)$$



$$y_1 = \frac{1}{j\omega\mu} \sum I_{\lambda 1}^2 = \frac{1}{j\omega L_0}$$

$$y_a = \frac{1}{j\left(\omega L_a - \frac{1}{\omega C_a}\right) + R_a}$$

$$L_a = \frac{\omega_a \mu}{\omega_a' I_{a1}^2}, \quad C_a = \frac{1}{\omega_a'^2 L_a}, \quad R_a = \frac{\omega_a' L_a}{Q_a'}$$

where

Fig. 4—Equivalent circuit of one-entry cavity with well-separated ω_a 's.

where

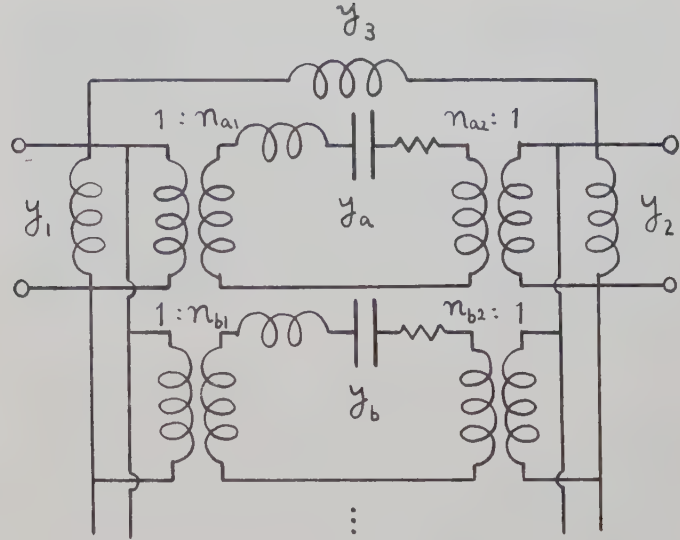
$$Y_{ij} = \sum_a \frac{I_{ai} I_{aj} / \omega_a \mu}{j\left(\frac{\omega}{\omega_a'} - \frac{\omega_a'}{\omega}\right) + \frac{1}{Q_a'}} + \sum_{\lambda} \frac{I_{\lambda i} I_{\lambda j}}{j\omega\mu} \quad (i, j = 1, 2). \quad (51)$$

I_1, I_2 are the currents and V_1, V_2 are the voltages associated with the transmission modes in the output leads No. 1 and No. 2, respectively. The equivalent circuit of (49) is shown in Fig. 4 and that of (51) in Fig. 5. The generalization of the above discussion to cavities with many output leads is easy.

V. \mathbf{G}_{λ} FUNCTIONS

Although the relation $\nabla \cdot \mathbf{H} = 0$ holds in the region V , we need the \mathbf{G}_{λ} functions to expand \mathbf{H} , because the condition $\nabla \cdot \mathbf{H} = 0$ does not necessarily mean the vanishing of the irrotational part of \mathbf{H} , as shown by Helmholtz's theorem.

We have seen that both the \mathbf{H}_a and \mathbf{G}_{λ} functions are necessary to set up a complete set of orthonormal functions and that an inductance term $\sum_{\lambda} I_{\lambda 1}^2 / j\omega\mu$ from the \mathbf{G}_{λ} 's appears in the input admittance besides the familiar resonance terms from the \mathbf{H}_a 's. The \mathbf{G}_{λ} 's ($\lambda \neq 0$) are related to the conservation law of magnetic charge as explained before. If the magnetic field enters the cavity through a part of S_0 and returns into the waveguide through the other part of S_0 , and if an observer does not see the outside of the cavity, he thinks that the magnetic charge $+|\mathbf{n} \cdot \mathbf{B}|$ is at the entrance of the field lines through S_0 , and $-|\mathbf{n} \cdot \mathbf{B}|$ is at their exit from S_0 , and that the magnetic current $\mathbf{n} \times \mathbf{E}$ flows between them. Such a magnetic field cannot be expressed by the \mathbf{H}_a 's alone but requires the \mathbf{G}_{λ} 's as



$$y_1 = \frac{1}{j\omega\mu} \sum (I_{\lambda 1}^2 + I_{\lambda 1} I_{\lambda 2}), \quad y_2 = \frac{1}{j\omega\mu} \sum (I_{\lambda 2}^2 + I_{\lambda 1} I_{\lambda 2})$$

$$y_3 = -\frac{1}{j\omega\mu} \sum I_{\lambda 1} I_{\lambda 2},$$

$$1:n_{a1} = 1:n \sqrt{\frac{I_{a1}}{I_{a2}}}, \quad 1:n_{a2} = 1:-n \sqrt{\frac{I_{a2}}{I_{a1}}}$$

$$y_a = \frac{1}{j\left(\omega L_a - \frac{1}{\omega C_a}\right) + R_a}$$

$$L_a = n^2 \frac{\omega_a \mu}{\omega_a' I_{a1} I_{a2}}, \quad C_a = \frac{1}{\omega_a'^2 L_a}, \quad R_a = \frac{\omega_a' L_a}{Q_a'}$$

Fig. 5—Equivalent circuit of two-entry cavity with well-separated ω_a 's.

well. If we neglect the \mathbf{G}_{λ} 's, we have to assume that there is no magnetic field through S_0 .

For illustration, let us consider a cavity with the smallest ω_a satisfying $\omega_a \gg \omega$. The input admittance can now be written in the form

$$Y = \sum_a \frac{I_{a1}^2 / \omega_a \mu}{j\left(\frac{\omega}{\omega_a'} - \frac{\omega_a'}{\omega}\right) + \frac{1}{Q_a'}} + \sum_{\lambda} \frac{I_{\lambda 1}^2}{j\omega\mu} \doteq j\omega C_0 + \frac{1}{j\omega L_0} \quad (52)$$

where

$$C_0 = \sum_a \frac{I_{a1}^2}{\omega_a'^2 \mu}, \quad \frac{1}{L_0} = \sum_{\lambda} \frac{I_{\lambda 1}^2}{\mu}. \quad (53)$$

If the \mathbf{G}_{λ} 's were neglected, the inductive term $1/j\omega L_0$ would not appear and we might come to the conclusion that the input admittance must be always capacitive when $\omega_a \gg \omega$ ($a = 1, 2, 3, \dots$). The input admittance can be both inductive and capacitive depending on the magnitudes of C_0 and L_0 . If $\omega C_0 = 1/\omega L_0$, the cavity

shows a resonance which is different from the resonance of \mathbf{E}_a and \mathbf{H}_a . A length of waveguide short-circuited at one end and shunted by a window at the other end can be considered as a cavity. S_0 may be placed just in front of the window. If the length of the cavity is $\lambda_g/4$, certainly we have $\omega_a \gg \omega$. The input admittance of the cavity is, in this case, the shunt admittance of the window and it can be inductive, capacitive, or resonant, depending on the type of the window. This shows that we need the term $1/j\omega L_0$ in (52) and hence the \mathbf{G}_λ functions to expand \mathbf{H} .

In a certain type of cavities, we need the \mathbf{G}_0 function as well. Though the fictitious magnetic current may close upon itself and there may be no fictitious magnetic charge on S_0 , this function can contribute an inductance term to the input admittance. The cavity with a coupling loop and a coaxial line output lead is an example (Fig. 6). S_0 may be placed in the coaxial line some distance away from the coupling loop. In this case, we have the \mathbf{G}_0 function corresponding to the magnetic field produced by the dc circuit which consists of S_0 , the outer and inner conductors of the coaxial line and the loop. If the TEM wave is the only transmission mode in the output lead, the normal component of \mathbf{H} on S_0 is vanishingly small. Still, we have an inductance term in the input admittance, for $\mathbf{n} \times \mathbf{E}$ on S_0 can induce the \mathbf{G}_0 component of \mathbf{H} in the cavity. The necessity for the inductance term is easily seen, if we consider the admittance at a very low frequency.

Every \mathbf{H}_a has a corresponding \mathbf{E}_a , but \mathbf{G}_0 has not. Hence, \mathbf{G}_0 is not a resonance mode. \mathbf{G}_0 has no relation to the fictitious magnetic charge on S_0 and in this respect \mathbf{G}_0 is distinct from all the other \mathbf{G}_λ 's.

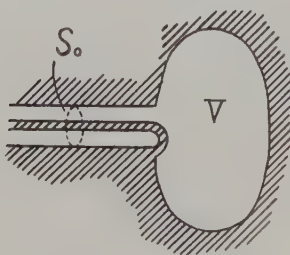


Fig. 6—Cavity with loop.

VI. EXAMPLES

To justify our conclusion about the \mathbf{G}_λ functions, we shall calculate the input admittance of simple cavities. First, the input admittance of a short-circuited rectangular waveguide ($l_x \times l_y$) will be taken up. The reference plane S_0 is l_z away from the shorted end. This example was discussed in detail in Schelkunoff's paper,³ still it might be instructive to follow our steps in the same example.

Considering the waveguide from the shorted end up to S_0 as a cavity, we have two types of \mathbf{H}_a functions.

$$\begin{aligned} \mathbf{H}_a = & -iA \left(\frac{\pi m_y}{l_y k_m} \right) \sin \frac{\pi m_x x}{l_x} \cos \frac{\pi m_y y}{l_y} \cos \frac{\pi m_z z}{l_z} \\ & + jA \left(\frac{\pi m_x}{l_x k_m} \right) \cos \frac{\pi m_x x}{l_x} \sin \frac{\pi m_y y}{l_y} \cos \frac{\pi m_z z}{l_z} \end{aligned} \quad (54)$$

$$\begin{aligned} \mathbf{H}_a = & -iA \left(\frac{\pi m_z}{l_z k_m} \right) \left(\frac{\pi m_x}{l_x k_m} \right) \sin \frac{\pi m_x x}{l_x} \cos \frac{\pi m_y y}{l_y} \cos \frac{\pi m_z z}{l_z} \\ & - jA \left(\frac{\pi m_z}{l_z k_m} \right) \left(\frac{\pi m_y}{l_y k_m} \right) \cos \frac{\pi m_x x}{l_x} \sin \frac{\pi m_y y}{l_y} \cos \frac{\pi m_z z}{l_z} \\ & + kA \frac{1}{k_m^2} \left[\left(\frac{\pi m_x}{l_x} \right)^2 + \left(\frac{\pi m_y}{l_y} \right)^2 \right] \\ & \cdot \cos \frac{\pi m_x x}{l_x} \cos \frac{\pi m_y y}{l_y} \sin \frac{\pi m_z z}{l_z} \end{aligned} \quad (55)$$

where

$$k_m^2 = \left(\frac{\pi m_x}{l_x} \right)^2 + \left(\frac{\pi m_y}{l_y} \right)^2 + \left(\frac{\pi m_z}{l_z} \right)^2 = \left(\frac{\omega_a}{c} \right)^2 \quad (56)$$

$$A = \sqrt{\frac{\epsilon_{m_x} \epsilon_{m_y} \epsilon_{m_z}}{l_x l_y l_z}} \frac{k_m}{\sqrt{\left(\frac{\pi m_x}{l_x} \right)^2 + \left(\frac{\pi m_y}{l_y} \right)^2}}. \quad (57)$$

The \mathbf{G}_λ functions are

$$\begin{aligned} \mathbf{G}_\lambda = & \sqrt{\frac{\epsilon_{m_x} \epsilon_{m_y} \epsilon_{m_z}}{l_x l_y l_z}} \frac{1}{k_\lambda} \left\{ i \left(\frac{\pi m_x}{l_x} \right) \sin \frac{\pi m_x x}{l_y} \cos \frac{\pi m_y y}{l_y} \cos \frac{\pi m_z z}{l_z} \right. \\ & + j \left(\frac{\pi m_y}{l_y} \right) \cos \frac{\pi m_x x}{l_x} \sin \frac{\pi m_y y}{l_x} \cos \frac{\pi m_z z}{l_z} \\ & \left. + k \left(\frac{\pi m_z}{l_z} \right) \cos \frac{\pi m_x x}{l_x} \cos \frac{\pi m_y y}{l_y} \sin \frac{\pi m_z z}{l_z} \right\}, \end{aligned} \quad (58)$$

where

$$k_\lambda^2 = \left(\frac{\pi m_x}{l_x} \right)^2 + \left(\frac{\pi m_y}{l_y} \right)^2 + \left(\frac{\pi m_z}{l_z} \right)^2. \quad (59)$$

The ϵ_m 's are the Neumann factors. The cavity is excited by the TE_{10} mode in the waveguide. The tangential component \mathbf{E}_{t1} of this mode is

$$\mathbf{E}_{t1} = j \sqrt{\frac{2}{l_x l_y}} \sin \frac{\pi x}{l_x} \quad (60)$$

where $\sqrt{2/l_x l_y}$ is the normalizing factor. In this case, we need \mathbf{H}_a with $m_x = 1, m_y = 0, m_z = 1, 2, 3, \dots$ in (55) and \mathbf{G}_λ with $m_x = 1, m_y = 0, m_z = 0, 1, 2, \dots$ only. These are the functions used by Schelkunoff in his second approach. From (29) and (30), we obtain

$$I_{a1} = \sqrt{\frac{2}{l_z}} \frac{\pi m_z}{l_z k_m} \cos m_z \pi, \quad (61)$$

$$I_{\lambda 1} = -\frac{1}{k_\lambda} \sqrt{\frac{\epsilon m_z}{l_z}} \frac{\pi}{l_x} \cos m_z \pi. \quad (62)$$

Hence

$$\begin{aligned} I_{a1}^2 &= \frac{2}{l_z} \left(\frac{\pi m_z}{l_z k_m} \right)^2 \\ \sum I_{\lambda 1}^2 &= \sum_{m_z=0}^{\infty} \frac{1}{k_\lambda^2} \frac{\epsilon m_z}{l_z} \left(\frac{\pi}{l_x} \right)^2 \\ &= \frac{1}{l_x} \left\{ 1 + 2 \sum_{m_z=1}^{\infty} \frac{\left(\frac{\pi}{l_x} \right)^2}{\left(\frac{\pi}{l_x} \right)^2 + \left(\frac{\pi m_z}{l_z} \right)^2} \right\}. \end{aligned}$$

Inserting these values in (49) and neglecting the effect of losses, we have

$$\begin{aligned} Y &= \frac{1}{j\mu} \frac{1}{l_z} \left[\sum_a \frac{2\omega \left(\frac{\pi m_z}{l_z} \right)^2 / k_m^2}{\omega^2 - \omega_a^2} \right. \\ &\quad \left. + \frac{1}{\omega} \left\{ 1 + 2 \sum_{m_z=1}^{\infty} \frac{\left(\frac{\pi}{l_x} \right)^2}{\left(\frac{\pi}{l_x} \right)^2 + \left(\frac{\pi m_z}{l_z} \right)^2} \right\} \right]. \quad (63) \end{aligned}$$

On the other hand, from transmission line theory, we have

$$Y = \sqrt{\frac{\epsilon}{\mu}} \frac{\sqrt{\omega^2 - \omega_c^2}}{j\omega} \cot \beta l_z \quad (64)$$

where

$$\beta = \sqrt{\epsilon\mu} \sqrt{\omega^2 - \omega_c^2}$$

$$\omega_c^2 = \left(\frac{\pi}{l_x} \right)^2 c^2 = \left(\frac{\pi}{l_x} \right)^2 / \epsilon\mu.$$

Using the relation

$$\cot \theta = \frac{1}{\theta} \left\{ 1 + \sum_{n=1}^{\infty} \frac{2}{1 - \left(\frac{n\pi}{\theta} \right)^2} \right\}$$

(64) is rewritten in the form

$$Y = \frac{1}{j\omega\mu l_z} \left\{ 1 + \sum_{n=1}^{\infty} \frac{2 \left\{ \omega^2 - \left(\frac{\pi}{l_x} \right)^2 c^2 \right\}}{\omega^2 - c^2 \left\{ \left(\frac{\pi}{l_x} \right)^2 + \left(\frac{n\pi}{l_z} \right)^2 \right\}} \right\}. \quad (65)$$

Eqs. (63) and (65) can be shown to be identical by a little algebra, leading to the conclusion that (63) is equal to (64). Eqs. (63) and (64) represent the same admittance and hence this conclusion is quite reasonable. However, if we neglect the G_λ functions from the beginning, the ω^{-1} term will not appear in (63) and the two admittances differ from each other.

Next, we shall take up a short-circuited coaxial line, showing the contribution of the G_0 function. The distance between the reference plane S_0 and the short end is L . The tangential component E_{t1} of the exciting field is

$$E_{t1} = i_r \frac{1}{\sqrt{2\pi \log b/a}} \frac{1}{r} \quad (66)$$

where a is the radius of inner conductor and b is the inner radius of outer conductor. The induced H_a 's by this field are

$$H_a = i_\phi \frac{1}{\sqrt{2\pi \log b/a}} \sqrt{\frac{2}{L}} \frac{1}{r} \cos \frac{n\pi z}{L} \quad (n = 1, 2, 3, \dots) \quad (67)$$

and the G_0 is

$$G_0 = i_\phi \frac{1}{\sqrt{2\pi \log b/a}} \sqrt{\frac{1}{L}} \frac{1}{r}. \quad (68)$$

From (29) and (30), we obtain

$$I_{a1} = \sqrt{\frac{2}{L}} \cos n\pi$$

$$I_{\lambda 1} = \sqrt{\frac{1}{L}}.$$

Using the relation

$$\omega_a = \frac{n\pi}{L} \frac{1}{\sqrt{\epsilon\mu}}$$

and (49), we have a well known expression of the input admittance.

$$\begin{aligned} Y &= \sum_a \frac{\frac{2}{L} / \omega_a \mu}{j \left(\frac{\omega}{\omega_a} - \frac{\omega_a}{\omega} \right)} + \frac{1}{j\omega\mu} \\ &= \frac{1}{j\omega\mu L} \left\{ 1 + \sum_{n=1}^{\infty} \frac{2}{1 - \left(\frac{n\pi}{\omega L \sqrt{\epsilon\mu}} \right)^2} \right\} \end{aligned}$$

$$= -j \sqrt{\frac{\epsilon}{\mu}} \cot \frac{2\pi}{\lambda_0} L. \quad (69)$$

If we neglect the G_0 function, we have again a faulty result in this case.

These examples show that we need the G_λ 's as well as the H_a 's to expand the magnetic field, though $\nabla \cdot H = 0$ throughout in the cavity.

VII. APPENDIX

Helmholtz's Theorem

Let V be a region inside a closed surface (or surfaces) S . Then any vector function F defined in V can be expressed as the sum of the gradient of a scalar and the rotation of a vector.

$$\begin{aligned} F(\mathbf{r}) = \nabla \left\{ \oint_S \frac{F(\mathbf{r}')}{4\pi R} \cdot n dS' - \int_V \frac{\nabla' \cdot F(\mathbf{r}')}{4\pi R} dV' \right\} \\ + \nabla \times \left\{ \oint_S \frac{F(\mathbf{r}')}{4\pi R} \times n dS' \right. \\ \left. + \int_V \frac{\nabla' \times F(\mathbf{r}')}{4\pi R} dV' \right\} \quad (70) \end{aligned}$$

where

$$R = |\mathbf{r} - \mathbf{r}'|,$$

∇' is a differential operator on \mathbf{r}' , and n is the outer normal on S . Eq. (70) shows that if we have two conditions $\nabla \cdot F = 0$ in V and $n \cdot F = 0$ on S , then F can be set equal to the rotation of a vector. If we have two conditions $\nabla \times F = 0$ in V and $n \times F = 0$ on S , then F can be set equal to the gradient of a scalar. $\nabla \times F = 0$ in V does not necessarily mean that $F = \nabla \phi$ where ϕ is a scalar function of position. In a corresponding way $\nabla \cdot F = 0$ in V does not necessarily mean $F = \nabla \times A$ where A is a vector function of position. The examples are the G_0 and F_0 functions defined in Section II.

Completeness of Ψ and Φ

Consider the relevance

$$\begin{aligned} k^2 \int \Psi^2 dV = \int \{(\nabla \times \Psi)^2 + (\nabla \cdot \Psi)^2\} dV \\ - 2 \int n \times \Psi \cdot \nabla \times \Psi dS \quad (71) \end{aligned}$$

and take the variation. A little manipulation shows that

$$\begin{aligned} \delta k^2 \int \Psi^2 dV = -2 \int \delta \Psi \cdot (\nabla^2 \Psi + k^2 \Psi) dV \\ + 2 \int \{\Psi \times n \cdot \nabla \times \delta \Psi + \nabla \cdot \Psi n \cdot \delta \Psi\} dS. \quad (72) \end{aligned}$$

Therefore

$$\begin{aligned} k^2 = \frac{\int \{(\nabla \times \Psi)^2 + (\nabla \cdot \Psi)^2\} dV - 2 \int n \times \Psi \cdot \nabla \times \Psi dS}{\int \Psi^2 dV} \quad (73) \end{aligned}$$

⁶ P. M. Morse and H. Feshback, "Methods of Theoretical Physics," McGraw-Hill Book Co., Inc., New York, N. Y., p. 54; 1953.

is the appropriate variational expression for the eigenvalue of Ψ . We can choose Ψ_p one by one, each of which makes

$$\begin{aligned} \Omega = \int \{(\nabla \times \Psi_p)^2 + (\nabla \cdot \Psi_p)^2\} dV \\ + 2 \int \Psi_p \times n \cdot \nabla \times \Psi_p dS \quad (74) \end{aligned}$$

a minimum under the normalizing condition and the orthogonal conditions.

$$\int \Psi_p^2 dV = 1, \quad \int \Psi_p \cdot \Psi_q dV = 0 \quad q < p. \quad (75)$$

An infinite set of functions thus selected forms a complete set of orthonormal functions as the conventional proof shows.⁷ Every Ψ_p satisfies (3). Hence, we come to the conclusion that the solutions of (3) are capable of forming a complete set of orthonormal functions.

The variational expression for the eigenvalue of Φ is

$$k^2 = \frac{\int \{(\nabla \times \Phi)^2 + (\nabla \cdot \Phi)^2\} dV - 2 \int (n \cdot \Phi) (\nabla \cdot \Phi) dV}{\int \Phi^2 dV}. \quad (76)$$

In a similar way as for Ψ , we easily verify that the solutions of (4) are capable of forming another complete set of orthonormal functions.

With the aid of Helmholtz's theorem, it can be shown that the Ψ_p 's are divided into two groups, the E_a 's and the F_a 's and the Φ_q 's into the H_a 's and the G_λ 's.

Eq. (72) and $k_0^2 = 0$ shows that F_0 satisfies $\nabla \times F_0 = 0$ and $\nabla \cdot F_0 = 0$ in V since $n \times \Psi = 0$ on S . Similarly (75) and $k_0^2 = 0$ shows that G_0 satisfies $\nabla \times G_0 = 0$ and $\nabla \cdot G_0 = 0$ in V .

Mixed Boundary Conditions

The sets of functions Ψ and Φ defined in Section II are not the only sets for the expansions of the electric and magnetic fields in a cavity. We can impose the mixed boundary conditions, short and open, upon the functions. Let $S + S'$ be a closed surface (or surfaces) in which we are solving Maxwell's equations. The solutions of

$$\nabla^2 \Psi + k^2 \Psi = 0$$

$$\begin{cases} n \times \Psi = 0 \\ n \cdot \Psi = 0 \end{cases} \quad \text{(on } S\text{)} \quad \begin{cases} n \times \nabla \times \Psi = 0 \\ n \cdot \Psi = 0 \end{cases} \quad \text{(on } S'\text{)} \quad (77)$$

are capable of forming a complete set of orthonormal functions. Similarly, the solutions of

⁷ P. M. Morse and H. Feshback, *loc. cit.*, pp. 738-739. Also see R. Courant and D. Hilbert, "Methods of Mathematical Physics," Interscience Publishers, New York, N. Y., vol. 1, pp. 424-429; 1953.

$$\nabla^2 \Phi + k^2 \Phi = 0$$

$$\left. \begin{aligned} \mathbf{n} \times \nabla \times \Phi = 0 \\ \mathbf{n} \cdot \Phi = 0 \end{aligned} \right\} \text{(on } S) \quad \left. \begin{aligned} \mathbf{n} \times \Phi = 0 \\ \nabla \cdot \Phi = 0 \end{aligned} \right\} \text{(on } S') \quad (78)$$

form another complete set of orthonormal functions.

The Ψ 's can be divided into two groups, the E_a 's and the F_α 's, and the Φ 's into the H_a 's and the G_λ 's. E_a and H_a satisfy the relations

$$k_a E_a = \nabla \times H_a, \quad k_a H_a = \nabla \times E_a$$

and the boundary conditions

$$\left. \begin{aligned} \mathbf{n} \times E_a = 0 \\ \mathbf{n} \cdot H_a = 0 \end{aligned} \right\} \text{(on } S) \quad \left. \begin{aligned} \mathbf{n} \cdot E_a = 0 \\ \mathbf{n} \times H_a = 0 \end{aligned} \right\} \text{(on } S').$$

Those are the functions used by Slater. For F_α ($\alpha \neq 0$), we have

$$k_\alpha F_\alpha = \nabla \psi_\alpha$$

where ψ_α is the solution of

$$\nabla^2 \psi_\alpha + k_\alpha^2 \psi_\alpha = 0$$

$$\psi_\alpha = 0 \text{ (on } S) \quad \frac{\partial \psi_\alpha}{\partial n} = 0 \text{ (on } S').$$

Slater, however, took the boundary condition $\psi_\alpha = 0$ on S and S' . As a result of this fault, he missed in the input impedance a capacitance term which corresponds to the inductance term in (49). In a certain type of cavities, there exists the function F_0 . The best example may be a cavity with a coupling probe and a coaxial line output as shown in Fig. 7. For G_λ ($\lambda \neq 0$), we have

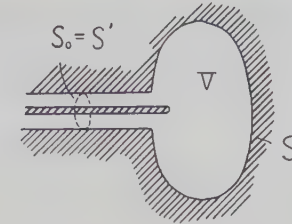


Fig. 7—Cavity with probe.

$$k_\lambda G_\lambda = \nabla \phi_\lambda$$

where ϕ_λ is the solution of

$$\nabla^2 \phi_\lambda + k_\lambda^2 \phi_\lambda = 0$$

$$\phi_\lambda = 0 \text{ (on } S') \quad \frac{\partial \phi_\lambda}{\partial n} = 0 \text{ (on } S).$$

Besides the multiply connected region, we have G_0 in the region where S separates S' into two or more than two independent parts. If we take a cross section of the output guide as S' and the cavity wall as S and impose a tangential magnetic field on S' as Slater did, we can easily show that the G_λ components of \mathbf{H} are all very small and can be neglected. But it does not justify the statement that we need no G_λ functions to start with.

VIII. ACKNOWLEDGMENT

The author wishes to thank David L. Bobroff whose lecture at M.I.T. gave the impetus without which this paper would have never been published. The continued support and encouragement of M. Hoshiai, N. Takagi, and S. Saito have been greatly appreciated.



Broad-Band Calorimeters for the Measurement of Low and Medium Level Microwave Power.

I. Analysis and Design*

M. SUCHER† AND H. J. CARLIN†

Summary—Design considerations for a group of broad-band calorimetric power meters, capable of accurately measuring low (zero to one milliwatt) and medium (zero to 100 milliwatts) power levels over a frequency range from zero to 75,000 mc, are presented. The power meters are of the nonadiabatic, twin, dry-load type and utilize the substitution of dc power. The conflicting requirements imposed upon the design by the need to realize broad-band performance, adequate sensitivity, reasonably short response time, negligibly small rf-dc equivalence error, freedom from "zero" drift and from other types of error are discussed. An analysis is given of the known sources of error which enables the accuracy of the individual instruments to be reliably estimated.

THREE is a definite need for a more accurate method of measuring microwave power at low and medium levels than is at present afforded by bolometers. The latter, in addition to being subject to pulse power¹ and rf-dc substitution (or equivalence)² errors^{3,4} are also subject to errors which are caused by mount inefficiency.⁵⁻⁷ Calorimetry naturally suggests itself as an alternative. In recent years calorimetric techniques have been extended to the direct measurement of microwave power in the same range for which bolometers are generally used.⁸⁻¹³ Three basically different calorimeter types—flow, adiabatic, and nonadiabatic—have been employed for this purpose, all utilizing the substitution principle. The calorimeters of Carter⁸ and

Strom⁹ are flow devices, the Naval Research Laboratory calorimeter described by Fellers¹⁰ is of the adiabatic type, and those described by Ernst and Schusse,¹¹ by Macpherson and Kerns,¹² and by Sharpless¹³ are nonadiabatic.

The present paper is concerned with the basic design principles which underlie a broad-band nonadiabatic calorimeter of the twin dry-load type. A schematic diagram of the rectangular waveguide version of this device is shown in Fig. 1. Units covering the frequency band 0-75,000 mc per sec have been built with a power measuring range of approximately 100 microwatts-100 milliwatts and the design data and operating characteristics are described in a companion paper.¹⁴

The basic equation defining the operation of an idealized nonadiabatic calorimeter (*i.e.*, where heat losses

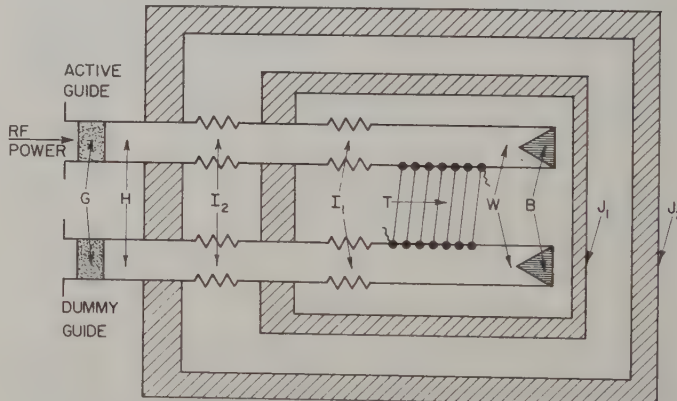


Fig. 1.—Schematic diagram of calorimeter in rectangular waveguide. J_2 , outer jacket; J_1 , inner jacket; W , thin-walled waveguide calorimeter termination; B , broad-band load; T , thermopile; I_1 , inner isolating section; I_2 , outer isolating section; H , entry waveguide; G , polyfoam plug.

* Manuscript received by the PGMTT, July 29, 1957; revised manuscript received, September 29, 1957. The work reported here was done under contracts AF-30(602)-988 and DA36-039sc-645 with the Rome Air Dev. Ctr., Rome, N. Y., and the U. S. Army Signal Eng. Labs., Fort Monmouth, N. J., respectively.

† Microwave Research Institute, Polytechnic Institute of Brooklyn, Brooklyn, N. Y.

¹ M. Sucher and H. J. Carlin, "The operation of bolometers under pulsed power conditions," *IRE TRANS. ON MICROWAVE THEORY AND TECHNIQUES*, vol. 3, pp. 45-52; July, 1955.

² The substitution error occurs when the rf and dc power distributions differ over the absorbing load. Because of this, rf and dc powers may produce different heating effects and thereby produce an error in the dc calibration.

³ H. J. Carlin and M. Sucher, "Accuracy of bolometric power measurements," *PROC. IRE*, vol. 40, pp. 1042-1048; September, 1952.

⁴ E. Weber, "On microwave power measurements," *Elektrotech u. Maschinenbau*, vol. 71, pp. 254-259; September, 1954.

⁵ J. A. Lane, "The Measurement of power at a wavelength of 3 cm by thermistors and bolometers," *Proc. IEE*, vol. 102, pt. B, pp. 819-825; November, 1955.

⁶ J. Collard, G. R. Nicoll, and A. W. Lines, "Discrepancies in the measurement of microwave power at wavelengths below 3 cm," *Proc. Phys. Soc. (London)*, vol. B63, pp. 215-216; March, 1950.

⁷ M. Sucher, "A Comparison of Microwave Power Measurement Techniques," *Proc. Symp. on Modern Advances in Microwave Techniques*, New York, N. Y., pp. 309-323; June, 1955.

⁸ C. J. Carter, "Calorimeter Type Power Meters," The Ohio State Univ. Res. Foundation, Columbus, Ohio, Engineering Rep., Wright Air Dev. Ctr. Contract W33-038-ac-15162, ASTIA AD No. 26873; August, 1953.

⁹ L. D. Strom, "A calorimeter for microwave low level power measurements," *1955 Aeronautical Electronics Digest*, IRE Dayton Chapter, pp. 158-159; May, 1955.

¹⁰ R. G. Fellers, "Measurement Techniques at Millimeter Wavelengths," *Proc. Symp. on Modern Advances in Microwave Techniques*, New York, N. Y., pp. 355-367; June, 1955.

¹¹ E. W. Ernst and J. H. Schusse, "Conduction Calorimeter Power Meter," University of Illinois, Urbana, Ill., Tech. Rep. No. 3, Elec. Eng. Res. Lab., Contract W33-0380-ac-014538; April, 1951.

¹² A. C. Macpherson and D. N. Kerns, "A microwave microcalorimeter," *Rev. Sci. Instrum.*, vol. 26, pp. 27-33; January, 1955.

¹³ W. M. Sharpless, "A calorimeter for power measurements at millimeter wavelengths," *IRE TRANS. ON MICROWAVE THEORY AND TECHNIQUES*, vol. 2, pp. 45-47; September, 1954.

¹⁴ A. V. James and L. O. Sweet, "Broad-band calorimeters for the measurement of low and medium level microwave power. II—Construction and performance," this issue, p. 195.

are not effectively eliminated as in the adiabatic type, but taken care of by appropriate calibration, usually by substitution of known amounts of low-frequency power) is

$$P(t) = C \frac{d\theta}{dt} + \frac{\theta}{R} \quad (1)$$

where

$P(t)$ = power input in watts,

C = heat capacity of calorimetric body in joules per $^{\circ}\text{C}$,

θ = temperature rise of body with respect to its surroundings in $^{\circ}\text{C}$

$\frac{d\theta}{dt}$ = time rate of temperature rise of body with respect to its surroundings in $^{\circ}\text{C}$ per sec.,

R = thermal resistance of the body to its surroundings in $^{\circ}\text{C}$ temperature rise per watt.

This equation assumes Newton's law of cooling, and further, that the body is at uniform temperature throughout, with C and R independent of temperature.

For constant power input P , the solution of (1) is

$$\theta = \theta_0(1 - e^{-t/\tau}) \quad (2)$$

where θ_0 is the steady-state temperature rise due to a power P and τ is the thermal time constant of the body. Here

$$\theta_0 = RP \quad (3)$$

$$\tau = RC \quad (4)$$

$$R = \frac{1}{G}, \quad G = \text{thermal conductance.} \quad (5)$$

If the steady-state temperature rise is used as a measure of the applied power, as is generally the case, then the power sensitivity of the calorimeter (defined as temperature rise per unit power input) is equal to R . The relation between measurement time and time constant may be illustrated by the fact that a waiting time equivalent to four, five, and six time constants results in a corresponding temperature rise which is 98.2, 99.3 and 99.8 per cent of the steady-state value, respectively, if the temperature build-up is truly exponential. To achieve a short measurement time, the large value of R , associated with high sensitivity, must be counteracted by a small heat capacity, C , so that the time constant, RC , shall be sufficiently short. The sensitive nonadiabatic calorimeters reported in the literature achieve their small heat capacity by use of thin-walled construction of the metal casing which houses the rf power absorbing load. Generally, the necessary thermal isolation (large R) is obtained by a substantial reduction of the conductive heat loss, which would otherwise be the major portion of the total heat loss. This had been accomplished earlier by using a short air gap^{12,13} in the entry waveguide leading to the casing, but a broad-band tech-

nique is used in the present design consisting of thermally isolating sections in the entry waveguide made of suitable dielectric coated with a thin metal film.¹¹ In this isolator the conductive flow of heat is impeded without appreciable attenuation of the rf power flow. Convective and radiative heat losses from the casing are kept reasonably small by limiting the size of the casing to the degree permitted by other design considerations.

Since the minimum detectable power is as much dependent on the background thermal fluctuations and temperature drift as on the calorimeter sensitivity, great attention is paid to thermally shielding the calorimeter against external temperature variations. Thus, the NBS calorimeter reported in the literature¹² was enclosed in a massive brass can which was immersed in a large oil bath. The limit of resolution in this design is imposed by random fluctuations of temperature experienced by the shield can in contact with the agitated oil bath and is equivalent to about 10 microwatts of power.

The calorimeters described in this paper achieve a power resolution of less than 10 microwatts without the necessity of oil bath stabilization. The techniques required are described in the following sections.

BASIC DESCRIPTION OF MRI CALORIMETERS

Performance Characteristics

These calorimeters have their thermal isolating systems and rf power absorbing loads so designed that they operate over broad frequency bands. Furthermore, the design has been deliberately developed so as to minimize errors over the operating frequency band caused by such things as rf-dc substitution, rf attenuation and rf leakage of thermal isolating sections, and drift of zero setting due to fluctuation of ambient temperature. The models were constructed for the Air Force¹⁵ and the Department of the Army¹⁶ as standards of microwave power measurement in the milliwatt range. The calorimeters are portable but are intended primarily for laboratory use under ordinary laboratory conditions; temperature regulation of the laboratory, although helpful, is not required. The minimum detectable power, as limited by thermal fluctuation and drift under typical laboratory conditions, ranges from several tenths of a microwatt for the millimeter wavelength models to about 5 microwatts for the larger waveguide sizes. The maximum power range is 100 to 300 milliwatts depending on the model. The vswr does not exceed 1.3 over the

¹⁵ Under Contract No. AF-30(602)-988, six discrete units, one coaxial and five in waveguide, collectively covering the range from 0 to 40,000 mc were delivered by the Microwave Res. Inst. of the Polytechnic Institute of Brooklyn, Brooklyn, N. Y., to the Rome Air Dev. Ctr., Rome, N. Y.

¹⁶ Under Contract No. DA36-039sc-64579, three discrete waveguide units collectively covering the range from 26,500 to 75,000 mc were delivered to the Signal Corps Eng. Labs., Fort Monmouth, N. J., by the Microwave Res. Inst. of the Polytechnic Institute of Brooklyn, Brooklyn, N. Y.

entire operating frequency band of a standard waveguide size. Collectively the instruments cover practically the entire microwave spectrum in use today—a range from zero to 75,000 mc. The broad-band rf loads are rugged, and the calorimeters are not subject to a pulsed power error as is the case for some bolometer elements. Calibration is accomplished with dc power with an equivalence error of less than several tenths per cent. The over-all accuracy (root mean square of maximum errors from independent sources), based on a careful error analysis, ranges from ± 1 per cent for the lowest frequency waveguide calorimeters to $\pm 2\frac{1}{2}$ per cent for the highest frequency waveguide units at the most favorable power levels. The coaxial calorimeter has an over-all accuracy of 2 per cent at the most favorable power levels. The numerical data for individual sources of error of coaxial and waveguide units are presented in the companion paper.¹⁴ The thermopile outputs of the various calorimeters range from 23 microvolts to 51 microvolts per milliwatt. Ordinary potentiometric measurements can provide a power resolvability of from five to two microwatts. The time constants range from little over one minute to four minutes.

DESIGN CONSIDERATIONS

The following were the calorimeter design objectives: 1) good inherent sensitivity, 2) short time-constant, 3) well-matched rf loads (maximum vswr of 1.3 for the entire operating band of a waveguide), 4) minimal rf-dc equivalence error, 5) suppression of temperature drift and temperature fluctuation effects. It will become clear from the following discussion that the realization of the first four aims places conflicting demands on the design of the waveguide termination and the rf load located within it so that design compromises must be made.

Since the calorimeters were intended to serve as standards of microwave power measurement, a primary design requirement was that the rf-dc equivalence error be bracketed within narrow and determinable limits. The conditions for minimizing this error become almost intuitively evident if one considers a distribution of power sources inside a closed, perfectly (thermally)-conducting envelope. Because of its perfect conductivity the envelope must be an isothermal. Because the rate of heat loss from the envelope to the surroundings is proportional to its temperature elevation, the steady-state temperature rise of the envelope must be proportional to the total power dissipated within it. The proportionality constant is actually the thermal resistance of the envelope to its surroundings and is entirely independent of the distribution of power sources.¹⁷ In this ideal case, it is clear, no equivalence error is possible.

¹⁷ The situation is exactly analogous to that of a closed perfectly conducting shell enclosing a distribution of electric charge. Potential, capacitance, and charge in the electrical case correspond to temperature rise, thermal conductance, and power, respectively, in the thermal case.

Now let the envelope take the form of a long thin-walled metallic cylinder of finite thermal conductivity from whose ends there is no leakage of heat and which contains within it an axially located point source of power. If it is assumed that heat is lost radially from the surface at a rate proportional to the temperature rise and area of the surface element from which it is escaping, then it can be shown that the envelope is no longer an isothermal but possesses a temperature distribution which depends on the location of the source. However, the *integrated* temperature rise (and therefore the average surface temperature rise) is still proportional to the strength of the source and independent of its position along the axis. Again there is no equivalence error if the *integrated* temperature rise is used as an index of the power. If heat is now permitted to escape from the ends of the cylinder, not only does the temperature rise per unit power input (averaged over the surface of the cylinder) decrease, but it becomes a function of the source position as well. Qualitative reasoning (as well as analytic treatment) shows that the longer the cylinder, the smaller the end losses, the greater the cross-sectional thermal conductivity of the cylinder, the less sensitive is the integrated temperature rise to source position, and the smaller is the equivalence error produced by dissimilar distributions of power sources of equal total strength. It follows that the terminating calorimeter waveguides should be long relative to the rf loads located within them, should be constructed of metal having the highest thermal conductivity, and should be conductively well isolated from the metal jacket in which they are enclosed. An approximate ratio of four to one in waveguide to load length was found satisfactory for a 0.015-inch wall thickness of silver waveguide well-isolated by suitable spacers from the enclosing metal jacket. Experimental data on the equivalence error is presented further on.

An rf load which closely resembles a point source will produce negligible substitution error when the thermal detectors are remote from the source. Requirements of ruggedness, power handling capacity, and broad-banding rule out bolometer wires and thermistor beads. Tapered resistive strips axially oriented in the waveguide suggest themselves as broad-band loads. These must be sufficiently long to give a broad-band match, but for reasons of calorimeter sensitivity must be kept as short as possible, so that the associated waveguide termination will be correspondingly short. With increasing frequency, as the attenuation per unit length of the resistive material increases, shorter strips may be used, together with shorter waveguides for containing them.

The thermal conductance G of the waveguide to the surrounding metal jacket (whose reciprocal R determines the temperature rise per unit power input) is composed of the sum of four conductances G_I , G_T , G_L , and G_S . The first three of these, respectively, represent the

conductive heat loss through the thermally isolating section of guide connecting the termination to the jacket, the conductive heat loss through the thermocouple wires attached to the waveguide, and the conductive heat loss through the wire leads which connect the rf load to the dc calibrating circuit. The last of these represents the combined heat loss from the waveguide surface due to free convection and radiation. If end effects are neglected the latter is given (in watts per °C) by

$$G_S = gpl$$

where pl is the outer surface area of the waveguide as determined by the waveguide cross section perimeter p and length l (in centimeters) and where the factor g (which is approximately 10^{-3}) represents the convective and radiative heat loss per square centimeter per °C of exposed waveguide surface. Once the minimum value of l has been established (by considerations of load length and equivalence error as described above) the value of G_S is fixed for a given waveguide cross section and frequency band. The isolating section is so designed that G_I is small relative to G_S while the thermocouple wires and dc load leads contribute additional conductances which are less than about 10 per cent of the total. The dominating term in G is therefore G_S , which, for a given waveguide cross section, is proportional to the waveguide length l . As the operating frequency band increases, both p and l decrease, causing a corresponding increase in the calorimeter sensitivity.

The time constant τ of the calorimeter is given by C/G , where C is the total heat capacity and G the total conductance. The former is the sum of C_S , the heat capacity of the terminating waveguide, C_L , that of the load and load holder, C_T , that of the thermopile and attached wires, and C_I , the effective heat capacity contributed by the waveguide isolating section because of its partial heating by the absorbed power. Accordingly,

$$\tau = \frac{C_S + C_L + C_T + C_I}{G_S + G_L + G_T + G_I}.$$

The ultimate time constant τ_u may be defined as C_S/G_S , that belonging to a perfectly (conductively) isolated piece of waveguide unencumbered by load or thermopile. Here

$$C_S = \rho c_h pl t$$

$$G_S = gpl,$$

ρ and c_h being the density and specific heat of the waveguide metal, respectively, and t its thickness. Accordingly

$$\tau_u = \frac{\rho c_h t}{g}$$

and is therefore proportional to the thickness t of metal used, being equal to approximately 100 seconds for

silver waveguide of 0.015-inch wall thickness.¹⁸

In an effort to shorten the time constant the thickness cannot be made arbitrarily small because a small rf-dc equivalence error is dependent on good cross-sectional heat conductivity which increases with thickness. Furthermore, in seeking to reduce the time constant one ultimately reaches a point where any further reduction in wall thickness is accompanied by a significant increase in equivalence error with no substantial decrease in time constant. This occurs when the contributory heat capacities C_I , C_L and C_T (as well as those of flanges which are sometimes required at the ends of the waveguide) begin to dominate the total heat capacity. (In this connection it may be pointed out that a resistive strip load is superior to a volume absorbing load because of the smaller associated thermal mass and time constant.)

To sum up, a short waveguide termination is desirable in order to maximize the calorimeter sensitivity and a thin-walled construction to minimize the thermal time constant. However, the waveguide must be long relative to the rf load and sufficiently thick so as to keep the rf-dc equivalence error within desired limits. Good conductive isolation of the waveguide from the enclosing jacket is desirable both to minimize the equivalence error and to improve the calorimeter sensitivity. A reduction in convective and radiative heat loss from the waveguide increases both sensitivity and time constant. However, the gain in sensitivity might well be offset by the larger errors (e.g., those due to temperature drift) which are associated with the necessarily longer measurement time. At higher frequencies increased sensitivity and more compact construction are obtained because of the accompanying reduction in waveguide cross section and in rf load length.

The suppression of temperature drift and random temperature fluctuations in the calorimeter is accomplished through use of thermal symmetry and massive double shielding. The design seeks to achieve, to the maximum degree possible, identical thermal behavior on the part of the twin calorimetric bodies and identity of the thermal forces impressed upon them because of external temperature variations. If these two aims are realized, then, theoretically at least, any arbitrary change in outside temperature would produce equal and in-phase temperature variations in both bodies without any effect on the temperature difference between them. The first objective requires identical construction of the twin terminations, while the second requires that they be surrounded by an isothermal envelope of very long (theoretically infinite) time constant so that both bodies see a uniform and unvarying temperature around them. A thermally massive aluminum jacket approximates

¹⁸ Silver is best because its heat capacity per unit volume is smaller than that of most other suitable metals and therefore gives the shortest time constant. Because of its superior thermal conductivity, silver also gives the smallest equivalence error for a given thickness.

such an envelope by virtue of its high thermal conductivity and large thermal mass. The former property minimizes temperature gradients along the jacket and the latter prevents the jacket from appreciably following the external temperature variations. The purpose of an outer jacket is to surround the inner one with a similar isothermal envelope, thereby enhancing the total shielding effect. The two jackets are conductively insulated from each other by special waveguide sections whose combined thermal conductance G_I is small relative to the shunting convective and radiative conductances G_S existing between the jacket walls. The combined conductance G , in conjunction with the thermal capacities of the two jackets, forms a low-pass filter with a very low-cutoff frequency, the approximate electrical analog for which is the π section filter shown in Fig. 2. This analog is particularly appropriate in representing the behavior of the shielding system in the transient case. The capacitances C_1 and C_2 represent the thermal capacities of the inner and outer jacket, respectively, and the electrical ground corresponds to the temperature of the reference or "dummy" calorimetric body.

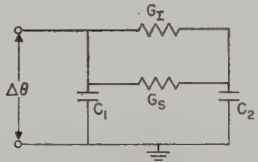


Fig. 2—Simplified equivalent circuit of calorimeter shielding system for transient conditions. C_1 , C_2 are the thermal capacities of the inner and outer shielding jackets, respectively; G_I is the combined thermal conductance of the waveguide isolating sections; G_S is the thermal conductance between the walls of the inner and outer jackets; ground represents the temperature of the reference calorimetric body; $\Delta\theta$ is an impressed temperature change on the entry waveguide of the "active" calorimetric body.

With the above type of construction, the effect of external temperature variations is reduced by a factor of from two to ten thousand. As a result, internal drift rates of approximately 5×10^{-4} to 10^{-4} °C per hour are obtained for external ambient temperature variations having a rate of 1°C/hour. (A double shield system of the type described is ten or more times "quieter" thermally than a single jacket immersed in a stirred bath. The latter has a "graininess" of temperature, due to the impact of the stirred liquid on the jacket, which introduces an unnecessarily large amplitude of thermal noise.)

SOURCES OF ERROR

The main sources of measurement error are those due to 1) lack of exact equivalence between rf and dc heating, 2) attenuation of rf power between input and calorimetric termination, 3) drift of temperature caused by external temperature variation, 4) nonlinear relationship between thermopile emf and input power, and 5) errors in associated dc instrumentation.

EQUIVALENCE ERROR

The rf-dc equivalence error is attributable to differences in the dc and rf power distribution along the tapered load strip. Such differences cannot altogether be avoided if only for the reason that the power distribution generally varies somewhat with rf frequency. Because of the complexity of the problem, experimental evaluation of the error is much easier and probably more accurate than an analytic determination. Therefore, the former approach was used.

The experimental technique was as follows: first the steady-state thermopile output was measured as a function of the axial position of a point-like source¹⁹ inside the thin-walled guide. A typical curve showing the percent deviation from maximum thermopile reading as a function of source position is shown in Fig. 3 for a length of RG-52/U waveguide of 0.015-inch wall thickness of either silver or brass construction. (It is seen that the maximum occurs near the half-way point in the guide for both metals, the curve for silver being much flatter than that for brass because of the larger thermal conductivity of the former metal.) If the different power distributions in the strip were known, the curve of Fig. 3 could be used to estimate the equivalence error for a given position of the strip at a given frequency. Even without a detailed knowledge of the distribution, however, limits of error can be estimated from the length of the strip. For example, the RG-52/U loads are about $\frac{5}{8}$ inch (1.6 cm) in length. Such a load, when situated in a silver waveguide so that its midpoint coincides with the source position yielding maximum thermopile reading, would be subject to a maximum error of only 0.3 percent for the most extreme rf and dc power distribution (e.g., all of the rf power concentrated at the center of the strip and all of the dc power at either end, or vice versa).

To delimit the error still further, studies²⁰ were next made of the temperature distribution along the strip at various rf frequencies and for various dc input power arrangements. (Because the heat loss from the strip is mainly convective and radiative, the temperature rise at any point is essentially proportional to the power density at that point, the proportionality constant being independent of position. The temperature distribution may therefore be taken as a fair approximation to the actual power density distribution.) In one type of experiment the temperature profile was measured by means of an array of six equally spaced iron-constantan thermojunctions embedded in the bakelite backing of the strip along the latter's longitudinal axis. Tests of this ar-

¹⁹ In the experiments a point source of power was variously approximated by a small piece of IRC resistance card mounted in a bakelite block which was free to slide in the guide, an evaporated metallic film of short length on a piece of glass tubing riding on a movable axially positioned bakelite rod, or a short length of deplated Wollaston wire similarly mounted.

²⁰ S. Satinsky, "Minimizing substitution errors in a microwave calorimeter," M.E.E. thesis, Polytechnic Institute of Brooklyn, Brooklyn, N. Y.; June, 1955.

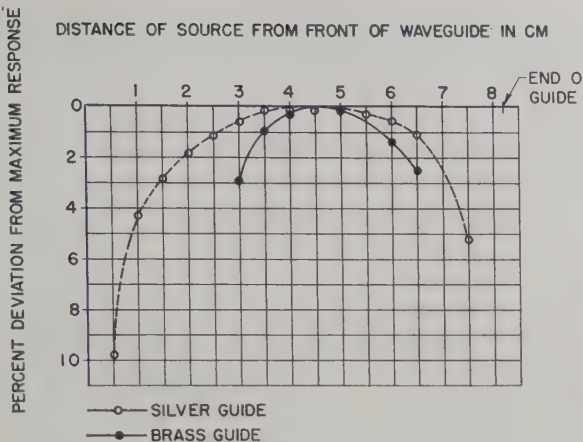


Fig. 3—Curves used in estimating calorimeter equivalence error. The thermopile output of the calorimeter, expressed in per cent deviation from maximum response, is plotted as a function of the axial position of a quasi-point source of power inside the waveguide. Results are for two RG-52/U waveguides of 0.015-inch wall thickness, one brass, the other silver.

arrangement showed that the presence of the wires did not appreciably disturb the temperature profile. A typical RG-52/U calorimeter strip load was used which, with wires attached, had a vswr of 1.3 or better over the entire operating band of the waveguide. The thermocouple wires were brought out perpendicular to the plane of the strip through small holes in the side walls of the waveguide in which the strip was mounted. The wires were therefore at right angles both to the E lines and to the axis of propagation and thus presented the least disturbance to the rf field. (Measurement of the effect of the wires alone showed that their attenuation was negligible and their insertion vswr very small.) Provision was made for applying dc power in different distributions by scratching an appropriate contour in the resistive material. Temperature distributions were obtained at 500-mc intervals over a band from 8200 to 12,400 mc. A continuous but not very strong shift in temperature distribution was observed as a function of frequency, the power concentration tending to a maximum at the center of the strip. If a longitudinal dividing scratch, extending part way from the back end toward the tapered end of the strip, was engraved in the resistive material and dc current circulated around this barrier, a temperature distribution could be obtained which resembled in a general way that due to rf power absorption. The dc temperature maximum tended to coincide with the end of the scratch mark where the dc current density was a maximum. By adjustment of the length of the scratch (which incidentally had no observable effect on the rf properties of the strip) the dc temperature maximum could be made to coincide with the average position of the rf maxima at the different frequencies.

The equivalence error was obtained by comparing the expected calorimeter reading per unit power input for the experimentally determined dc load temperature distribution with that for the rf distribution which gave

the most widely different result. This was done by computing the weighted mean calorimeter reading for a given temperature distribution (taking the latter as the impressed power distribution for the thin-walled waveguide) using the ordinates of the curve of Fig. 3 as weighting factors. The error evaluation was made for the optimum strip position (center of strip near center of waveguide) and also for a displacement of the strip by one centimeter from the optimum position. The result for these two cases was an indicated error of 0.005 and 0.07 per cent, respectively, for silver waveguide and of 0.013 and 0.26 per cent, respectively, for brass waveguide. Even allowing for imperfect scaling of waveguide models of different frequency range, minor variations in power distributions from load to load, and imperfect positioning of load strips, one obtains an equivalence error, based on the above data, well below 0.3 per cent in the case of the silver waveguide calorimeters which collectively cover the range from 7000 to 26,500 mc.

For the higher frequency calorimeters, separate experiments were performed in which the dc temperature profile was determined by probing the strip with a single movable thermocouple. (The loads were tapered thin mica strips on which a resistive metallic film had been evaporated.) The region of rf power concentration was determined by an auxiliary experiment in which the attenuation of rf power at three typical frequencies (at band limits and midrange) was determined as a function of film length. The peak of the dc power distribution was adjusted so as to coincide approximately with the peak of the rf power distribution. From an experimentally obtained curve of thermopile reading vs point source position, together with the information on rf and dc power distributions, the rf-dc equivalence error is estimated to be less than 0.3 per cent for the higher frequency models.

In the case of the coaxial calorimeter a disk-type concentric resistive film load is used oriented in a plane transverse²¹ to the axis of propagation. Theoretically, the rf and dc power distributions should be identical because of the identity of the rf and dc electromagnetic field configurations. Actually, there will be some variation because of the distributed reactances associated with the load and any auxiliary matching structures. However, because of the transverse orientation of the disk these minor dissimilarities in distribution will produce an almost negligible equivalence error.

ATTENUATION OF RF POWER

Since any attenuation of rf power between input to the calorimeter and the site of rf power dissipation (the termination; *i.e.*, the terminating waveguide with its resistive load strip) can be applied as a correction, the error from this cause is basically the uncertainty in the

²¹ A transverse film would also have been advantageous in waveguide from the point of view of substitution error. However, the longitudinally oriented load is more readily matched over a broad band in rectangular guide.

measured attenuation. The problem is, however, complicated by two factors—the non-negligible reflection factor of the termination and the equally non-negligible insertion vswr of the rf line connecting the calorimeter input to the termination. Even if the attenuation (*i.e.*, insertion loss between matched generator and matched load) of the latter were measured perfectly there would still be an uncertainty in the correction because of the above two factors. Therefore, in estimating the total error, due attention must be paid to this problem. This is treated in more detail in the companion paper.¹⁴

DRIFT ERROR

The error due to drift of calorimeter "zero" tends to increase with the physical size of the calorimeter and the rate of change of the external temperature. Also, the longer the time constant the larger is the error because of the longer measurement time required. The magnitude of this error for the different calorimeters is given in Table III¹⁴ for an assumed ambient temperature drift of 1°C/hour. (This error would, of course, be much less in a temperature-controlled room.) The drift error, in any event, may be substantially reduced by means of a measurement procedure¹⁴ which corrects for the zero drift. This procedure involves the measurement of the input power in terms of the *arithmetic mean* of the *change* in output emf during the heating and cooling of the termination. Any steady drift is thereby cancelled out of the measurement while any reversal in drift direction during the measurement leaves the error uncorrected. In the latter case, however, the correction is unimportant because the drift is generally quite small during a reversal in drift direction.

NONLINEARITY ERROR

The steady-state power sensitivity (thermopile output per unit power input) is found to decrease with in-

creasing power level. This shows that the relation between calorimeter reading and input power must be a nonlinear one. Actually, the relation is approximated by the expression $E = KP^n$, where E is the thermopile emf, P the power input, and K and n constants for a particular calorimeter. The exponent n varies with the physical size of the calorimeter termination but is always less than unity. (In the case of the RG-52/U model, for example, n is approximately 0.93.) The reason for this behavior can be traced to the predominantly convective cooling of the calorimeter which is a nonlinear phenomenon.⁴ The nonlinearity may be responsible for a calibration error unless the calibrating power is very closely equal to the unknown rf power. For some calorimeters this error may exceed one per cent at high power levels, where the nonlinearity is greatest, if the calibrating power differs by more than 10 per cent from the unknown power.

INSTRUMENTATION ERROR

The instrumentation error, defined as the error in measuring the calibrating dc power, can be kept to a very small value (better than 0.25 per cent) relative to the other errors, by using precision dc measurement techniques. This is discussed in the companion paper.¹⁴

CONCLUSION

This paper has presented the basis for the design of a series of accurate, dry, broad-band calorimeters of high sensitivity. Of particular importance is the fact that all sources of error are clearly delimited so that a definite precision measure can be given when the devices are used in microwave power measurements. These instruments can therefore readily be used as power standards within the accuracy limits stated.



Broad-Band Calorimeters for the Measurement of Low and Medium Level Microwave Power.

II. Construction and Performance*

A. V. JAMES† AND L. O. SWEET†

Summary—The construction and performance of a series of rugged, broad-band twin-Joule calorimeters, using dry loads, are described. These calorimeters operate over the frequency range of 0 to 75,000 mc. The over-all measurement error, computed as the rms value of the maximum individual errors from known independent sources, is shown to lie between 1 and 2½ per cent for power levels between 1 and 100 mw. Power measuring techniques are discussed and a method using the heating and cooling cycle of the calorimeter is described in detail. Power comparison measurements between the calorimeters and several bolometer mounts illustrate the increasing inefficiency of bolometer mounts with increasing frequency.

INTRODUCTION

THIS paper describes the operating characteristics and gives design data for a series of broad-band microwave calorimeters of the "twin-Joule" type which cover the frequency band 0 to 75 kmc and directly measure powers from about 50 μ w to 200 mw. In these units a broad-band dry load absorbs microwave power and the temperature rise of a casing surrounding this load is compared with the temperature of an identical reference unit at ambient temperature. The fundamental ideas which form the basis of this design are discussed in a companion article.¹ That paper presents a theoretical analysis of the sources of error such as, substitution effects, ambient temperature drift, etc. The present article shows how the basic analysis is applied to the actual design of the operating instruments and discusses the performance features of the various meters.

DESCRIPTION

Basic Calorimeter Structure

A sketch of the basic structure of the calorimetric power standard is shown in Fig. 1. Two sections of waveguide ① extend through the outer metal jacket ②. Thermal isolators ③ are interposed between the input waveguides and the inner metal jacket ④. A second set of thermal isolators ⑤ separates the thin-

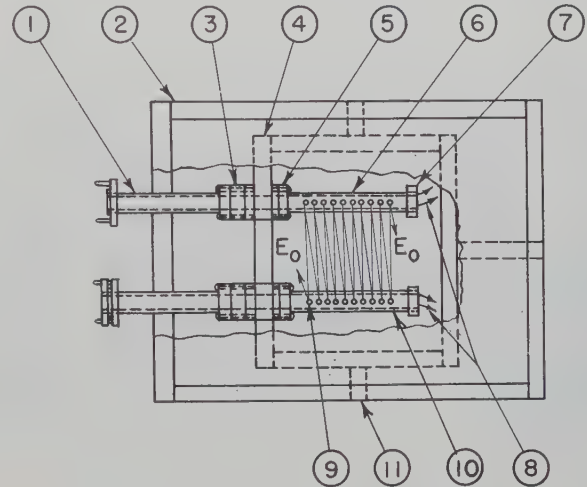


Fig. 1—Basic calorimeter structure.

walled waveguides ⑥ ⑩ from the inner metal jacket. Broad-band tapered loads (not shown in the figure) are held in place inside the thin-walled waveguides by load holders ⑦. Either low-frequency or dc power is applied to the loads by means of copper wires ⑧ which pass through the two metal jackets. Iron-constantan thermojunctions ⑨ are bonded in pairs to the active ⑥ and reference ⑩ waveguides. The inner metal jacket is supported by standoff insulators ⑪. The output leads of the thermojunctions, E_0 , pass through the metal jackets in a common cable with the load wires. A cut-away view of the calorimeter in guide size RG-96/U is shown in Fig. 2 (next page).

That portion of the calorimeter from the input waveguides up to, but not including the flanges of the thin-walled waveguide, will be called the "entry-waveguide system"; this includes the input waveguides, thermal isolators, and all thermal conductive paths shunting the input waveguides. The term "termination" will be given to that part of the calorimeter that is connected to the entry-waveguide system; it includes the loads and the thin-walled waveguides to which the thermojunctions are attached.

In the ideal case, the active termination will experience the same average temperature rise when rf power is dissipated in it as when dc power is used. This temperature rise is very nearly proportional to the input

* Manuscript received by the PGM TT, July 29, 1957; revised manuscript received, September 25, 1957. This work was sponsored under Contract No. AF-30(602)-988 for the Rome Air Dev. Ctr., Rome, N. Y., and No. DA36-039-sc-64579 for the Signal Corps Eng. Labs., Fort Monmouth, N. J.

† Polytechnic Res. and Dev. Co., Brooklyn, N. Y.; formerly with the Polytechnic Institute of Brooklyn, Brooklyn, N. Y.

¹ M. Sucher and H. J. Carlin, "Broad-band calorimeters for the measurement of low and medium level microwave power. I. Analysis and design," this issue, p. 188.

power and causes the thermo junctions to generate an output voltage very nearly proportional to the input power. However, an output voltage can be produced by other means as well. Any temperature difference between the two input waveguides will cause a temperature difference between the two thin-walled waveguides. Temperature differences can be caused by ambient temperature variations or by handling. The ability of a calorimeter to measure small rf powers is limited by these unwanted temperature differences.

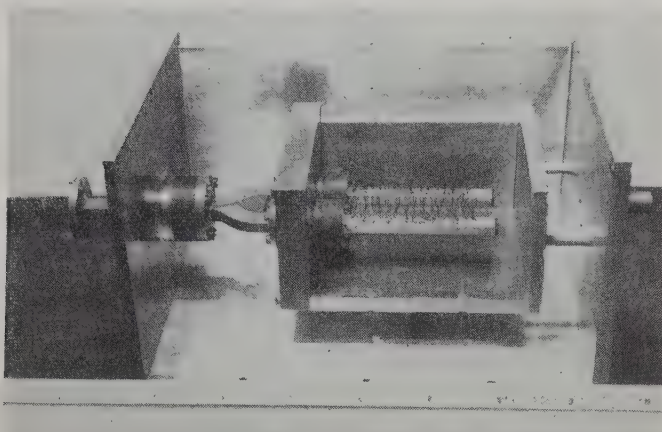


Fig. 2—Cut-away view of 26,500-40,000-mc (RG-96/U Waveguide Size) calorimeter.

An analysis of the thermal circuit of the calorimeter shows that the entry-waveguide system, along with the terminations and associated thermo junctions, forms an electric bridge circuit analog of the thermal system.² A simplified schematic of the thermal circuit of the calorimeter is shown in Fig. 3. R_1 and R_2 represent the thermal resistances associated with the two input waveguides, and R_3 is the thermal resistance between these guides. R_4 and R_5 are the thermal resistances of the thermal isolators and R_6 is the shunt thermal path between them. G_1 and G_2 are the two thin-walled waveguides and associated thermo junctions. R_7 and R_8 are the thermal resistances from the thin-walled waveguides to the inner metal jacket, while R_9 represents the thermal resistance between the inner jacket and the external environment. P_{dc} and P_{rf} represent the dc and rf power sources, respectively. ΔT represents the temperature difference between the two thin-walled waveguides.

It is clear that whenever the dc power, P_{dc} , or the rf power, P_{rf} , is applied to the active termination, a temperature difference, ΔT , will exist between the terminations. Also, if the temperature balance between the input waveguides, terminals 1 and 2, is disturbed in any

way whatsoever, a ΔT will be developed. By making the thermal resistance R_3 very small in comparison with R_4 and R_5 , ΔT will be very small. It is obvious that if input terminals 1 and 2 were connected together, ΔT would be zero for P_{dc} and P_{rf} equal to zero.

The calorimeters were designed to have a low-thermal resistive path between the input waveguides; this was accomplished by using thick copper cover plates for the inner jacket and by placing the input waveguides close together.

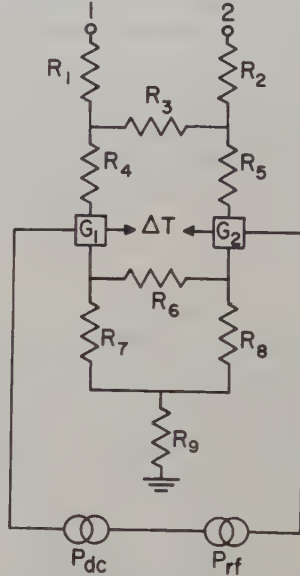


Fig. 3—Simplified equivalent thermal circuit of calorimeter.

The calorimeters in guide sizes RG-52/U, RG-96/U, RG-97/U, and RG-98/U were designed using a symmetrical "Y."^{2,3} The "Y" effectively connects terminals 1 and 2 together (thermally, but not rf-wise) and gives additional reduction in temperature drift. Some of the various calorimetric powermeters are shown in Fig. 4.

Isolating Sections

Four types of thermal isolators were used. These were silver sprayed bakelite, electroplated bakelite, electro-formed pieces, and thin-walled brass tubing. The silver sprayed bakelite spacers were used in the RG-51/U, RG-52/U, and RG-107/U calorimeters, and they were fabricated by spraying two or three coats of an air drying silver paint on the bakelite. Electroplated bakelite was used in the RG-96/U, RG-97/U, and RG-98/U calorimeters. These spacers were made by evaporating a coating of silver onto the bakelite and then electroplating silver onto the coating. The over-all thickness of the silver was about 0.0003 inch. Electroformed spacers

² A. V. James, "Broadband, Rugged Calorimeter Powermeters", Polytechnic Institute of Brooklyn, Brooklyn, N. Y., First Quar. Rep. R-414.3-55, PIB-346.3; April, 1955.

³ A. V. James, "A sensitive millimeter calorimetric powermeter," M.E.E. thesis, Polytechnic Institute of Brooklyn, Brooklyn, N. Y.; April, 1956.

were used in the RG-66/U and coaxial calorimeters. The recommended electroforming procedure is to successively plate 0.0003 inch of copper, 0.001 inch of nickel, and a copper flash on a polished aluminum mandrel. The mandrel is then cast in an araldite resin, and after the resin hardens the mandrel is slowly dissolved with hydrochloric acid. Thin-walled brass sections 0.003 inch thick also were used as isolators in the coaxial calorimeter. These sections were fabricated by careful machining. Different types of isolators are shown in Fig. 5.

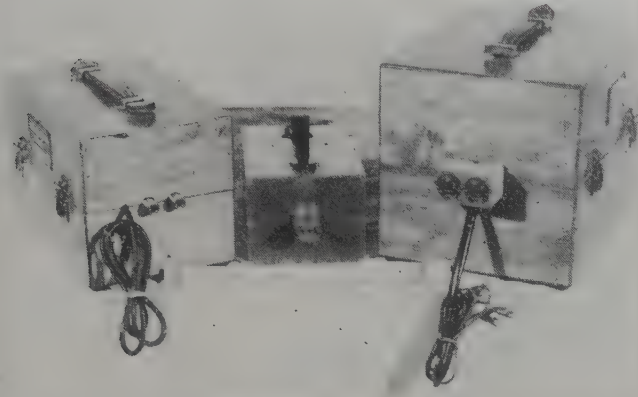


Fig. 4—Calorimeter power heads—coaxial model and waveguide sizes RG-66/U, RG-96/U.

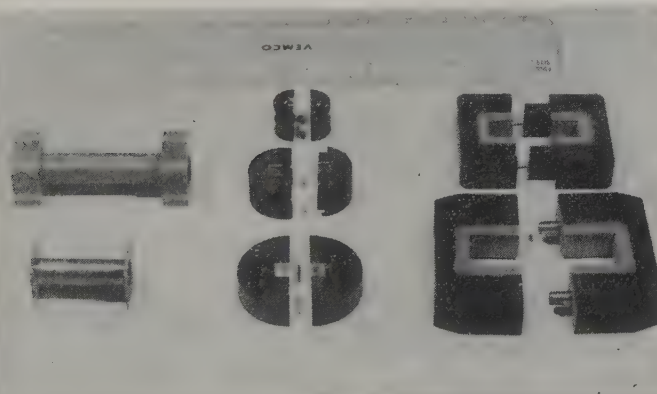


Fig. 5—Construction of various thermal isolating sections.

Loads

The waveguide loads were made of resistance⁴ cards or a chromium film evaporated on mica, and each load was terminated by a short circuit. A scratch that extends most of the length of the resistive material was made to provide an approximately even distribution of dc power. The coaxial load resistor took the form of a concentric resistive film on mica. The resistive material consisted of a mixture of 1 part liquid bright platinum

No. 5 and 3 parts gold essence No. 31. These solutions are manufactured by the Hanovia Chemical Company.

Thermopiles

The iron-constantan thermojunctions were made of number 30 and 33 wires depending on the calorimeter, and each junction had a sensitivity of about $52 \mu\text{V}/^\circ\text{C}$. The junctions were insulated by gluing strips of insulated copper squares to the waveguide and soldering the thermojunctions to these squares. Care was taken to avoid the use of excessive heat, and for this reason a low melting point solder was used. The squares were fabricated by first bonding 0.0027-inch thick copper to a 12" \times 12" sheet of epoxy-glass 0.006-inch thick and tinning the copper with solder. The squares were then formed by photo-etching the spaces between the squares down to the epoxy-glass surface. The strips were then cut from the 12" \times 12" sheet.

POWER MEASUREMENT TECHNIQUES

The measurement of rf power depends essentially on a comparison of the thermopile output of the calorimeter when rf power is applied to the termination with that obtained when equal dc power is dissipated in the same termination; *i.e.*, on the use of dc-rf substitution. This may be accomplished in a number of different ways, the most accurate of which is to calibrate the calorimeter with dc power either immediately before or after the calorimeter response to the unknown rf power has been measured.

For greatest accuracy (at levels exceeding one milliwatt) the following procedure was used. The calorimeter termination was first allowed to reach a steady-state temperature with the unknown rf power applied. The resulting thermopile emf was then measured and converted into an approximate power reading with the aid of a previously obtained graph of *input power vs thermopile emf*. The purpose of this step was to determine the level of dc power to be used in the ensuing exact calibration. The rf power was then cut off, the termination allowed to cool, and the residual thermopile emf, e_1 , measured. An accurately known amount of stable dc calibrating power, P_{dc} (equal to the rf power within ten per cent), was then applied and the resultant emf, e_2 , measured. The dc power was then cut off and the residual emf, e_3 , measured. Finally, the rf power was again applied and the final emf, e_4 , measured. The rf power, P_L , was then determined from

$$\frac{P_L}{P_{dc}} = \left(\frac{e_4 - e_3}{e_2 - e_1} \right). \quad (1)$$

A standard waiting interval of five time-constants was allowed between the application or removal of power and the reading of the resultant thermopile output.

⁴ Manufactured by the International Resistance Co., Philadelphia, Pa.

Such an interval is sufficient for a temperature rise or fall to reach 0.993 of its steady-state value in an exponential buildup or decay process such as occurs in the heating and cooling of the termination. The time sequence of operations is illustrated in Fig. 6.

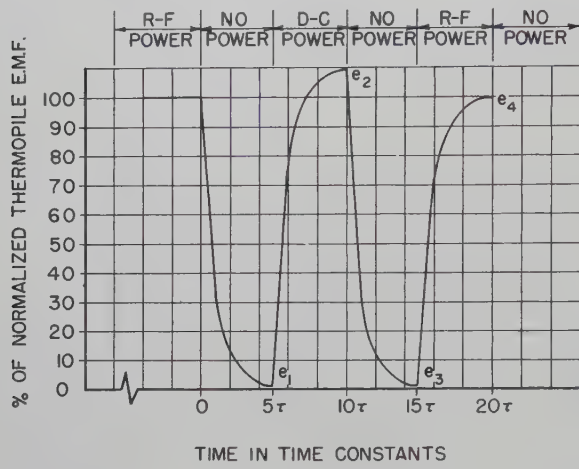


Fig. 6—Time sequence of operations in calibration of calorimeter, τ is the thermal time constant.

The above method has two advantages. It serves to reduce the error due to "zero" drift in the calorimeter, which is particularly important at low power levels, and to calibrate the calorimeter anew for each measurement, thus making the result independent of any long-time changes in the properties of the calorimeter or of day to day changes in the ambient temperature at which the measurement is performed. Approximate equality of dc calibrating and rf power helps to minimize errors due to the somewhat nonlinear relation between output emf and input power which is particularly noticeable in most calorimeters at power levels above 10 mw.⁵ Obviously the success of this procedure depends a good deal on the stability of the rf source.

A type K-2 Leeds and Northrup potentiometer in conjunction with a Minneapolis-Honeywell "ElectroniK" null indicator was found satisfactory for output emf measurements at power levels above one milliwatt. (The "ElectroniK" null indicator is equal in sensitivity to the conventional galvanometer but much faster in its response.) For lower power levels it is almost essential to use a high-gain, stable dc amplifier of low-internal noise, such as the Perkin-Elmer Model 53 or Liston-Becker Model 14 breaker type. Such an amplifier permits the measurement of emf with a resolution of better than 0.01 μ v so that the ultimate limitation on the de-

⁵ The nonlinearity is attributable to the fact that the termination is predominantly cooled by "free-convection." The convective heat loss is proportional to the temperature elevation above ambient raised to the 1.2 power, hence the nonlinearity. (See Sucher and Carlin, *op. cit.*)

tectable power is determined purely by the thermal fluctuation and zero drift of the calorimeter.

A convenient method of obtaining an accurately determinable dc calibrating power is to incorporate the active calorimeter load in one arm of a balanced precision Wheatstone bridge as shown in Fig. 7 and to determine the dc power from a precision measurement of the voltage across the bridge and the value of the load resistance. The same potentiometer which is used to measure the thermopile emf also can be used to measure the bridge voltage with the aid of a volt-box or precision potential divider. Alternatively, the power can be determined from a measurement of the bridge current with the aid of a multirange precision milliammeter (0.1 per cent full-scale accuracy). The latter method (for reasons of convenience) was used in one of the calibration setups with an accuracy of better than 0.5 per cent. Even better precision can be obtained with the potentiometer method.

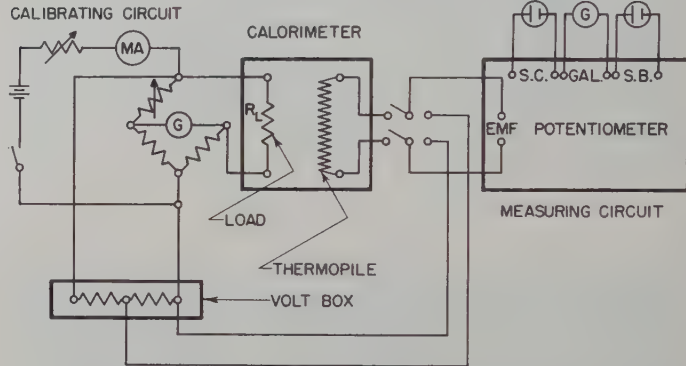


Fig. 7—Schematic diagram of a calorimeter calibrating and measuring circuit.

Additional power measurement methods include reading the thermopile output on a sensitive galvanometer (e.g., the Rubicon 3412 spotlight galvanometer or equivalent) in conjunction with an Ayrton shunt for accurate range switching or on a stable electronic microvoltmeter (such as the L. & N. 9835-A) equipped with a suitable range switch and referring to a previously obtained calibration curve of power versus instrument deflection. Another method is to feed adjustable dc power into the dummy load so as to balance out the effect of the unknown rf power in the active load, a sensitive null indicator being used to detect the thermopile output. The deflection methods are not as accurate as the potentiometric methods, while the balance technique, in addition to demanding some experience from the operator, also requires a determination of the correction factor to be applied to the measurement because of a slight (usually one or two per cent) difference in the response of the dummy and active terminations to equal amounts of dc power.

ERRORS AND OVER-ALL ACCURACY

The types of errors that occur when the heating and cooling cycle method is used to measure rf power can be divided into two categories, those that are independent of rf power level and those that depend upon the amount of rf power being measured. Among the former are attenuation, 4-pole, substitution, and dc power measurement errors, while the latter kind of errors are caused by thermal drift, limit of resolution, and non-linearity. These errors were analyzed in the companion article¹ and methods of measurement, as well as measured data on the values encountered in practice, will be given here. The calorimeter can only indicate the power dissipated in the termination itself, and any power dissipated in the entry waveguide system is not directly measured. It is, therefore, necessary to measure the attenuation of the connecting section of waveguide (this section can be considered a 4-pole) and apply this as a correction to the power indicated. The attenuation of this connecting 4-pole was measured for the waveguide calorimeters covering the range from 7–40 kmc by terminating the 4-pole in a lossy movable short, varying the position of this short, and accurately determining the radius of the resulting circular locus of the input reflection coefficient.⁶ Since the attenuation is a slowly varying function of frequency, it was sufficient to make the measurement at three frequencies to define it over the entire band. By using this technique the attenuation was determined with an error of 1 per cent or less for the entire operating bands of the calorimeters. The attenuation of the RG-97/U and RG-98/U calorimeters was measured by noting the change in output level of a bolometer biased with dc and fed from a square wave modulated rf source. By making many repeated measurements at 2-kmc intervals, the attenuation was determined with an error of about 2 per cent. The attenuation of the 4-pole in the coaxial calorimeter was measured with equipment supplied by the Weinschel Engineering Company, Kensington, Md. In this method, square-wave modulated rf power was split and fed to two bolometers. The outputs of the bolometers were amplified in separate channels and then subtracted to obtain a null. One of the channels contained a precision audio attenuator and the change in this attenuator that was necessary to reproduce a null after the 4-pole had been inserted was the attenuation of the 4-pole. This method has the advantage that the measurement is largely independent of power fluctuations of the rf source. Furthermore, the sensitivity of the equipment was such that a 0.01-db change could be readily distinguished. The attenuation of the coaxial 4-pole over the frequency band was obtained with an error of 1 per cent.

⁶ H. M. Altschuler and A. A. Oliner, "A shunt technique for microwave measurements," IRE TRANS., vol. MTT-3, pp. 29–30; July, 1955.

The ratio⁷ of power absorbed in the termination to the total power absorbed in the calorimeter is given by

$$K = \frac{P_L}{P_T} = \frac{|S_{12}|^2 + S_{22}(\Gamma_{in} - S_{11})|^2 - |\Gamma_{in} - S_{11}|^2}{|S_{12}|^2(1 - |\Gamma_{in}|^2)}, \quad (2)$$

where P_L and P_T are the powers absorbed in the termination and entire calorimeter, respectively; Γ_{in} is the input reflection coefficient of the calorimeter; and S_{11} , S_{22} , and S_{12} are the scattering parameters of the connecting 4-pole. In general, the value of K depends upon both the phases and magnitudes of the scattering and reflection coefficients. In practice, only the magnitudes of these quantities would be known at best, and so there will be an uncertainty in the value of K . For practical purposes one can take

$$K = |S_{12}|^2 \quad (3)$$

which is more or less midway between the maximum and minimum possible values of K . The maximum error in K that is incurred by using (3) is termed the "4-pole error." One obtains $|S_{12}|^2$ from the attenuation of the 4-pole since the attenuation equals $-10 \log |S_{12}|^2$. The measured 4-pole error ranged from 0.7 per cent to about 2 per cent, depending on the calorimeter.

When using dc power to calibrate a calorimeter, one actually assumes that equal amounts of dc and rf powers will produce equal thermopile output voltages. The amount by which this assumption is incorrect is the substitution error. The analysis made by Sucher and Carlin¹ shows that the substitution error is quite small and is of the order of 0.1 per cent. The substitution error for the coaxial calorimeter is essentially zero, since the load is a planar resistive ring perpendicular to the direction of propagation and rf and dc powers distribute similarly.

When calibrating a calorimeter with dc power, the load was connected in a Wheatstone bridge. With such an arrangement and by using a milliammeter of 0.1 per cent accuracy to measure the bridge current, it was possible to measure the dc calibrating power to within ± 0.5 per cent.

Because of asymmetry in the thermal structure, there usually was a thermopile output with no power incident on the calorimeter, and ambient temperature variations caused this output to vary or drift. The amount of drift was determined by means of two tests. For the first test the thermocouple output and room temperature were recorded over a period of about 18 hours. The second type of test involved recording the thermopile voltage variation that occurred after the calorimeter was connected to a typical rf setup including all associated

⁷ L. O. Sweet and M. Sucher, "The available power of a matched generator from the measured load power in the presence of small dissipation and mismatch of the connecting network," IRE TRANS., vol. MTT-5, pp. 167–168; April, 1957.

equipment. Sufficient attenuation was used so that there was essentially zero rf power incident on the calorimeter. Based on these tests and assuming a maximum room temperature change of 1°C per hour, the largest possible drift error ranges from 6 to 12 μw for the calorimeters covering the range up to 26.5 kmc and is 1 μw or less for the remaining calorimeters. The drift error was considered to be approximately $1\frac{1}{2}$ times the maximum drift in a five time constants period of time.

The resolution error depends on the microvolt per milliwatt sensitivity (this ranged from 25 to 50 $\mu\text{v}/\text{mw}$) of the calorimeter which in turn depends on the thermal sensitivity of the calorimeter (temperature rise per unit power input) and the number of thermojunctions used. The error was taken to be a power equivalent to twice the minimum detectable change of thermopile emf of about 0.15 μv when the L. & N. Type K-2 potentiometer is used. The resolution error for the series of calorimeters was close to 10 μw .

The nonlinearity error is illustrated in Fig. 8. If e_{dc} is the thermopile emf corresponding to a calibrating power P_{dc} and e_{rf} that corresponding to the unknown rf power, then the rf power would be computed (on the assumption of a linear relationship between thermopile emf and power) as

$$P_{L'} = P_{dc} + \frac{e_{rf} - e_{dc}}{\tan \phi} \quad (4)$$

where

$$\tan \phi = \frac{e_{dc}}{P_{dc}} \quad (5)$$

The correct value, P_L , which is obtained from the true curvilinear relation, differs from $P_{L'}$ by an amount ΔP (shown greatly exaggerated in the figure). In practice, ΔP is relatively small because the curve is actually very nearly a straight line and P_{dc} is chosen close to P_L . If P_{dc} is within 5 per cent of $P_{L'}$, the nonlinearity error is negligible up to power levels of 20 mw. The error increases with increasing power level, but even at the 100 mw level it is less than one per cent.

The accuracy of a calorimeter is taken as the rms value of the different errors cited. The drift and resolution errors contribute most to the over-all error at low power levels (less than 1 mw), while at high levels (100 mw) the nonlinearity error is a significant factor in the over-all error. The best accuracy ($1-2\frac{1}{2}$ per cent) is achieved at levels of about 10 mw.

Since the heating and cooling cycle method is the most accurate, the errors applicable to this technique were mentioned. However, the discussion of attenuation, 4-pole, substitution, and dc power measurement errors also applies to any of the other possible measurement methods. Table I gives a breakdown of the errors associated with the various power meters.

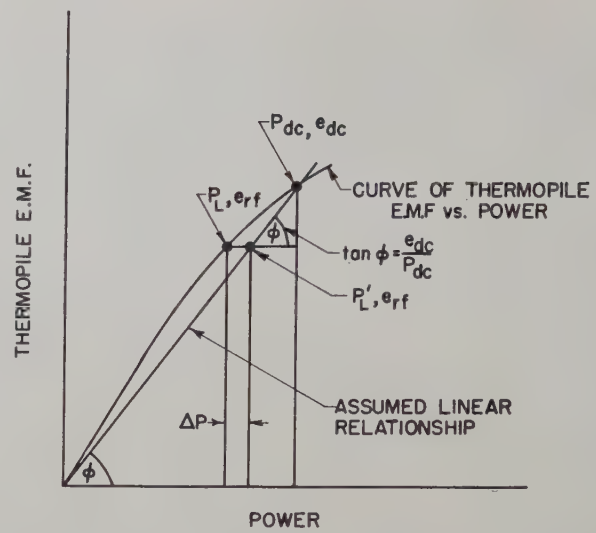


Fig. 8—Illustration of calorimeter nonlinearity error. P_L is the actual rf power corresponding to a measured thermopile emf, e_{rf} , and $P_{L'}$ is the calculated value based on a calibrating power, P_{dc} , and an assumed linear relationship between thermopile emf and power. The measurement error is ΔP .

EXPERIMENTAL POWER COMPARISONS

Power comparisons between the calorimeters and bolometer mounts were made, and the results are summarized in Table II. The results and accuracies are given to the nearest 0.5 per cent. The comparisons take into account any difference in the vswr of the bolometer and calorimeter, and the uncertainties in the measurements caused by a mismatched generator were included on the accuracy figure.⁸

The coaxial and RG-107/U calorimeters were checked against the 627-A and 616-A bolometer mounts respectively, manufactured by the Polytechnic Research and Development Company. RG-51/U and RG-52/U calorimeters were compared against a Hewlett-Packard 485B tunable X-Band mount; a $\frac{1}{2}$ -inch brass adapting section was used with this mount for the comparison with the RG-51/U calorimeter. The RG-66/U, RG-96/U, and RG-97/U calorimeters were compared against bolometer mounts made by the Microwave Research Institute of the Polytechnic Institute of Brooklyn.

The results of the different power comparisons seem to show a definite trend toward greater bolometer mount inefficiencies as the frequency increases. Part of the difference between the powers measured with a bolometer mount and a calorimeter at 10.5 kmc might be attributed to the modulation of the barretter with modulated rf power, but this effect is probably not greater than 2 per cent.⁹

⁸ R. W. Beatty and A. C. Macpherson, "Mismatch errors in microwave power measurements," Proc. IRE, vol. 41, pp. 1112-1119; September, 1953.

⁹ T. Moreno and O. C. Lundstrom, "Microwave power measurement," Proc. IRE, vol. 35, pp. 514-518; May, 1947.

TABLE I
BREAKDOWN OF ERRORS

Calorimeter	Power Level	$ S_{12} ^2$	4-Pole	DC Power	Drift	Potentiometer	Substitution	Non-linearity	Total rms Error
Coaxial	10^{-3} watts	1 per cent	1.7 per cent	0.5 per cent	0.6 per cent	1.0 per cent	0 per cent	0 per cent	2.4 per cent
	10^{-2} watts				0.1 per cent	0.1 per cent		0 per cent	2.0 per cent
	10^{-1} watts				0 per cent	0 per cent		1 per cent	2.3 per cent
RG-51/U	10^{-3} watts	0.7 per cent	0.7 per cent	0.5 per cent	1.2 per cent	1.0 per cent	0.3 per cent	0 per cent	1.9 per cent
	10^{-2} watts				0.1 per cent	0.1 per cent		0 per cent	1.1 per cent
	10^{-1} watts				0 per cent	0 per cent		1 per cent	1.5 per cent
RG-52/U	10^{-3} watts	0.7 per cent	0.7 per cent	0.5 per cent	0.7 per cent	1.3 per cent	0.3 per cent	0 per cent	1.9 per cent
	10^{-2} watts				0.1 per cent	0.1 per cent		0 per cent	1.1 per cent
	10^{-1} watts				0 per cent	0 per cent		1 per cent	1.5 per cent
RG-107/U	10^{-3} watts	0.7 per cent	0.7 per cent	0.5 per cent	0.6 per cent	1.0 per cent	0.3 per cent	0 per cent	1.6 per cent
	10^{-2} watts				0.1 per cent	0.1 per cent		0 per cent	1.1 per cent
	10^{-1} watts				0 per cent	0 per cent		1 per cent	1.5 per cent
RG-66/U	10^{-3} watts	0.7 per cent	0.7 per cent	0.5 per cent	0.8 per cent	0.9 per cent	0.3 per cent	0 per cent	1.7 per cent
	10^{-2} watts				0.1 per cent	0.1 per cent		0 per cent	1.2 per cent
	10^{-1} watts				0 per cent	0 per cent		1 per cent	1.5 per cent
RG-96/U*	10^{-3} watts	0.7 per cent	1.1 per cent	0.5 per cent	0.1 per cent	0.7 per cent	0.3 per cent	0 per cent	1.6 per cent
	10^{-2} watts				0 per cent	0.1 per cent		0 per cent	1.4 per cent
	10^{-1} watts				0 per cent	0 per cent		1 per cent	1.7 per cent

* Errors of RG-97/U and RG-98/U calorimeters are essentially the same as those of the RG-96/U size except for $|S_{12}|^2$ which was determined with a precision of ± 2 per cent.

TABLE II
POWER COMPARISONS*

Calorimeter	Frequency (kmc)	Modulation	Power Level in Milliwatts	Comparison Against	Result	Accuracy of Comparison
Coaxial	9.0	cw	1.5	PRD 627-A Bolometer Mount†	calorimeter was 6 per cent higher	± 3 per cent
RG-51/U	9.0	1000 cps square wave	4.7	HP-485B Tunable Bolometer Mount‡	calorimeter and bolometer were the same	± 2.5 per cent
RG-52/U	10.5	1000 cps square wave	8.4		calorimeter was 5 per cent higher	± 3.5 per cent
RG-107/U	12.6	1000 cps square wave	1.3	PRD 616-A Bolometer Mount	calorimeter was 3 per cent higher	± 3 per cent
RG-66/U	23.3	1000 cps square wave	0.7	MRI Bolometer Mounts§	calorimeter was 4.5 per cent higher	± 2 per cent
RG-96/U	29.7	1000 cps square wave	1.0		calorimeter was 7.5 per cent higher	± 3 per cent
RG-97/U	42.0	1000 cps square wave	0.4		calorimeter was 8 per cent higher	± 3 per cent

* Data for frequencies above 50 kmc were not available at the time this table was prepared.

† Polytechnic Research & Development Co., Brooklyn, N. Y.

‡ Hewlett-Packard Co., Palo Alto, Calif.

§ Microwave Research Institute, Polytechnic Institute of Brooklyn, Brooklyn, N. Y.

CONCLUSION

A series of broad-band calorimetric powermeters which are suitable for use as laboratory standards and covering the frequency range from dc to 75 kmc have been designed and constructed. These calorimeters enable one to make absolute power measurements with an accuracy

of from 1 to $2\frac{1}{2}$ per cent at power levels of from 1 to 100 mw.

They thus can be used to calibrate a bolometer directly without resorting to the use of directional couplers. Furthermore, the calorimeters can be used to measure pulsed power without the attendant error

TABLE III
SUMMARY OF CALORIMETER CHARACTERISTICS

Guide Size	Frequency Range (kmc)	Entry Waveguide	Sensitivity ($\mu\text{v}/\text{mw}$)	Time Constant (minutes)	Power Handling Capacity (mw)	Minimum Measurable Power With 5 Per Cent Accuracy* (in microwatts)
3/8" Coaxial	0 - 10	twin	32	1.2	100	140
RG-51/U	7.5-10	twin	30	4.0	100	250
RG-52/U	8.2-12.4	Y	23	2.6	100	140
RG-107/U	12.4-18	twin	29	2.7	100	140
RG-66/U	18 -26.5	twin	41	1.7	100	170
RG-96/U	26.5-40	Y	46	1.8	300	50
RG-97/U	33 -50	Y	41	1.1	200	50
RG-98/U	50 -75	Y	51	1.1	100	50

* Based on use of Liston-Becker Model 14 Breaker-Amplifier or equivalent.

present when bolometers are used.¹⁰ If one desires, the calorimeters can be calibrated and used as field instruments since they are rugged devices. Sensitivities are such that powers of as low as 50 to 100 μw can be measured with reduced accuracies of the order of 5-10 per cent. Table III is a summary of calorimeter characteristics.

¹⁰ M. Sucher and H. J. Carlin, "The operation of bolometers under pulsed power conditions," IRE TRANS. ON MICROWAVE THEORY AND TECHNIQUES, vol. 3, pp. 45-52; July, 1955.

ACKNOWLEDGMENT

In connection with the material reported in this and the companion paper¹ credit is due E. Barcomb for much of the detailed design work and Miss M. Zusman, E. Molloy and S. Kanarek for many of the rf measurements.

Thanks are also due Miss M. Eschwei and Mrs. C. Ruch for their valuable work in preparing the various thermal isolating sections and film loads.

Amplitude Stabilization of a Microwave Signal Source *

GLENN F. ENGEN†

Summary—Recent developments in the microwave field have provided new tools for use in regulating the output amplitude of a microwave signal source. An amplitude or power stabilizer has been constructed at the National Bureau of Standards Boulder Laboratories, using the recently developed self-balancing dc bolometer bridge and a commercially available, electrically controlled, ferrite attenuator which achieves power stabilities of a few parts in 10^4 per hour.

Use of a high directivity directional coupler permits stabilization of the forward traveling component of the signal, thus providing the equivalent of a *matched*, stable generator. In practice, a broad-band source match of vswr less than 1.05 is achieved, and this figure may be further improved, at a given frequency, by suitable tuning. In addition, the device has applications as a precision broad-band attenuator, since known changes in power level may be achieved by switching certain of the associated dc components.

* Manuscript received by the PGMTT, August 12, 1956; revised manuscript received, October 11, 1957.

† National Bureau of Standards, Boulder, Colo.

THE recent and continuing advances in the microwave measurements art are continually imposing greater demands upon the stability of the microwave signal source. Except for the use of regulated power supplies, and stabilized environmental conditions, the problem of amplitude or power stability has received comparatively little attention—much less than the companion problem of frequency stability, and such efforts as have been made in this field^{1,2} have apparently stopped short of recognizing all of the potential advantages of this technique. On the general philosophy of stabilization a recent author has appropriately

¹ I. K. Munson, "Microwave power stabilizer," *Rev. Sci. Instr.*, vol. 21, p. 622; July, 1950.

² J. P. Vinding, "An automatic gain control system for microwaves," IRE TRANS. ON MICROWAVE THEORY AND TECHNIQUES, vol. 4, pp. 244-245; October, 1956.

commented, "that voltage and temperature regulators are themselves feedback or servo systems. It therefore is logical to apply the feedback loop directly to the output. The extreme precision in the control of contributory factors can be relaxed."³

GENERAL DESCRIPTION

The power stabilizer to be described in the following paragraphs follows this general plan (Fig. 1). A portion of the output signal is split off by the directional coupler, detected, a correction signal is derived, and following amplification, this portion is used to drive the electrically controlled ferrite attenuator in the required direction to maintain a constant output.

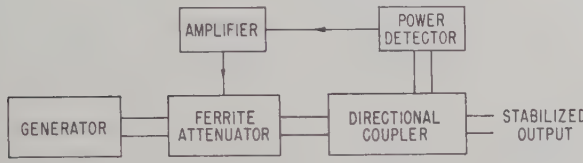


Fig. 1—Block diagram of power stabilizer.

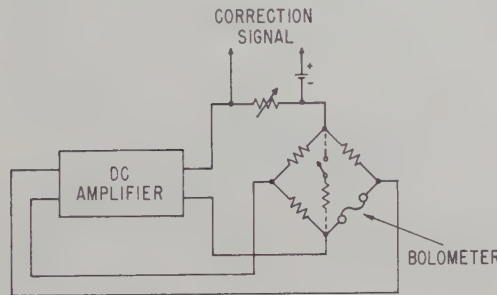


Fig. 2—Basic circuit of power detector.

Power detection is achieved by means of a self-balancing dc bolometer bridge which has been described in an earlier paper.⁴ The basic circuit is shown in Fig. 2. Fluctuations in the microwave signal are reflected as changes in the current required to maintain the bridge balance, and comparison of this current with the potential of a mercury cell by use of a suitable variable resistor yields the desired correction signal.

The absolute stability which may be achieved by a system of this type is limited, for practical purposes, by the detector stability. Because a bolometer (barretter) has a higher inherent stability than a crystal, it was chosen for this application; in addition, the use of a bolometer makes possible a novel attenuator to be described later. The bolometer does require, however, a temperature controlled environment, in this case to $\pm 0.005^\circ\text{C}$.

³ D. D. King, "Measurements at Centimeter Wavelength," D. Van Nostrand Co., New York, N. Y., p. 167; 1952.

⁴ G. F. Engen, "A self-balancing dc bridge for accurate bolometric power measurements," *J. of Res., Natl. Bureau of Standards*, vol. 59, p. 101; August, 1957, R.P. 2776.

EQUIVALENT CIRCUIT

The use of a directional coupler to sample the output signal has been described. But the output signal provided by the side arm of an ideal coupler connected in the indicated manner is a measure only of the *forward* traveling component of the signal. Accordingly, it is this forward component which is held constant by the stabilizer. But this is characteristic of a matched generator, thus it is recognized intuitively that not only does this technique provide the equivalent of a *stable* generator, but that of a *matched* generator as well.

In order to put these ideas in more definite form, reference is first made to the circuit of a conventional generator feeding an arbitrary line. In Fig. 3 let \mathbf{b} and \mathbf{a} represent the amplitudes of the forward and reverse voltage waves respectively, with the other quantities defined in the usual manner. Then

$$\mathbf{b} = \frac{e}{2} (1 - \Gamma_g) + \mathbf{a} \Gamma_g \quad (1)$$

where

$$\Gamma_g = \frac{Z_g - Z_0}{Z_g + Z_0}.$$

In particular it is noted that even though a stable generator, e , is postulated, \mathbf{b} has, in general, a functional dependence upon \mathbf{a} through the factor Γ_g . Only for the special case $\Gamma_g = 0$ is \mathbf{b} independent of \mathbf{a} .

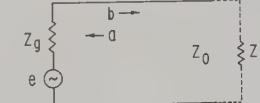


Fig. 3—Circuit for (1).

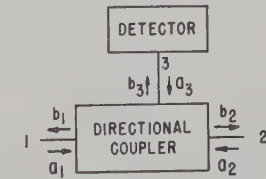


Fig. 4—Circuit for (2).

Consider next the relationships that prevail at the terminal surfaces of the directional coupler. In Fig. 4 the \mathbf{a} 's and \mathbf{b} 's represent the amplitudes of the incident and emergent waves respectively. It can be shown that⁵

$$\begin{aligned} \mathbf{b}_2 = \mathbf{b}_3 & \left[\frac{S_{12}}{S_{13}} + \Gamma_d \left(S_{23} - \frac{S_{12}S_{33}}{S_{13}} \right) \right] \\ & + \mathbf{a}_2 \left(S_{22} - \frac{S_{12}S_{23}}{S_{13}} \right) \end{aligned} \quad (2)$$

⁵ The derivation is a straightforward solution of the scattering equations of a three-arm junction.

where Γ_d is the reflection coefficient of the power detector, and the $S_{m,n}$ are the scattering coefficients of the coupler.

The first term on the right is a measure of the signal delivered to the detector and is held constant by the stabilizer. Thus it is noted that the output, or outgoing wave is given by the sum of a constant term and a term proportional to the reverse wave. Comparison of (2) with (1) indicates that the factor

$$\left(S_{22} - \frac{S_{12}S_{23}}{S_{13}} \right)$$

plays the role of Γ_g in the stabilized output.

The term S_{22} is the reflection coefficient of Arm 2 with the first and third arms terminated in matched loads. For a main guide vswr of 1.05, S_{22} has a magnitude of approximately 0.025. In addition, $|S_{12}| < 1$ while

$$\left| \frac{S_{23}}{S_{13}} \right| = 0.01$$

for a coupler directivity of 40 db. Assuming these values combine in the worst phase, the equivalent $|\Gamma_g|$ has a value less than 0.035, which corresponds to a source vswr of 1.07.

The term

$$\left(S_{22} - \frac{S_{12}S_{23}}{S_{13}} \right)$$

may also be measured experimentally by the following technique. Arm 1 of the coupler is terminated in a variable load which is adjusted to produce a null in the output of Arm 3 with Arm 2 connected to the signal source. It can be shown, subject to this adjustment, that the input reflection coefficient at Arm 2 is just the desired quantity,

$$S_{22} - \frac{S_{12}S_{23}}{S_{13}}.$$

Measurement of a commercially available coupler yielded for this quantity corresponding values of $\text{vswr} < 1.05$ over an entire waveguide band.

Finally, if a tuning transformer is included in Arm 2, this term may be reduced at a given frequency to as low a value as the state of the impedance measuring art permits by tuning for an impedance match at Arm 2 after the previous adjustment has been made.

Thus far the analysis has assumed that the first term on the right in (2) is held constant by the stabilizer action. This assumption is in error on two distinct counts: first the feedback loop does not have infinite gain and second, no method of adjusting the phase of this term is provided. A change in the phase of b_s is equivalent, however, to a shift in phase of the generator, and thus is of no concern since in practice the signal source has in general a frequency or phase instability far in excess of what could be introduced by the stabilizer.

lizer operation. The treatment of noninfinite gain will be reserved for the Appendix where it will be shown that the deterioration in performance due to this effect is negligible in this instrument.

PERFORMANCE

The performance of the system is shown in Fig. 5 and Fig. 6 which are recordings of the fluctuations in power output of the main guide as measured by a dc bridge⁴ of the type referenced. In Fig. 5 the improvement in performance over an unstabilized klystron is shown, where the klystron was operated with stabilized beam, reflector, and heater potentials, and in a stabilized environment. The result of introducing a 3-db power change (by means of an attenuator) ahead of the stabilizer is shown in Fig. 6, where the time scale has been reduced to one minute per division instead of one hour as in Fig. 5. It will be noted that the change in power level is just discernible. The stabilization factor as determined from these measurements is approximately 10,000.

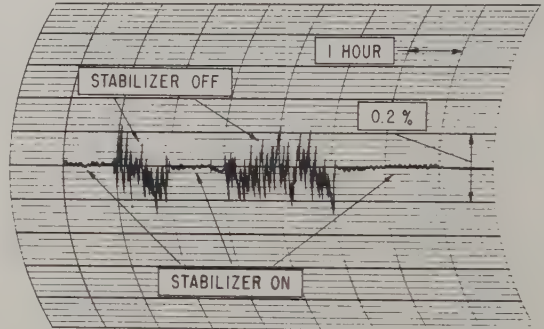


Fig. 5—Improvement in performance over an unstabilized klystron.

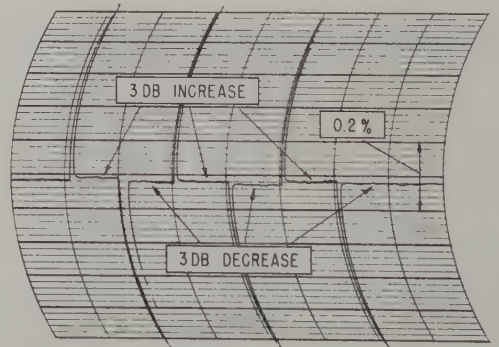


Fig. 6—Response of stabilizer to a 3-db change in input power.

These records also indicate a time constant for the stabilizer of about $\frac{1}{2}$ second. This could be reduced, if required, at the expense of the stabilization factor, but operating experience to date indicates that this value is satisfactory.

A PRECISION ATTENUATOR

With suitable modification the instrument can also be used to produce known changes in power level, and

thus serve as an attenuator, in the following manner. For definiteness, assume that the bolometer employed as power detector requires a total of 4 mw of power to bring it to the nominal operating resistance, and that the stabilizer has been so adjusted that this power is comprised of 3 mw of dc and 1 mw of rf. If a resistor is now shunted across the bridge as indicated by the dotted lines in Fig. 2, some of the dc power will be diverted from the bolometer and the action of the stabilizer will replace this with rf power. Thus by a proper choice of resistor the rf power can be made to increase from 1 mw to 2 mw or any other value within limits, and a load connected to the main arm of the directional coupler will experience a proportional increase in power. The accuracy of this result will depend in practice primarily upon the accuracy with which the initial conditions can be established and is expected to be of the order of 0.01 db for attenuations of 3 db with decreasing accuracy at larger values.

It should be noted that this accuracy is independent of the characteristics of the microwave components such as load vswr, etc. provided that these characteristics are independent of power level, and the frequency of the signal source remains constant. The accuracy is also independent, to a first approximation, of the bolometer substitution error.⁶

CONCLUSION

The amplitude or power stabilization technique has thus been shown to produce a variety of useful results. In conclusion, these are,

- 1) Stable amplitude—A stability of a few parts in 10^4 per hour is achieved.
- 2) Broad-band source match—A match of vswr ≤ 1.05 is obtained over an entire waveguide frequency band. This match may be further improved at a given frequency to a degree limited for practical purposes only by the state of the art in recognizing a matched load.
- 3) Constant source impedance—The technique holds the source impedance constant, regardless of its value, which is useful in certain applications.
- 4) Increased available power—In order to achieve a matched source it is common practice to pad the generator by 20 db or more, although ferrite isolators are finding a growing use for this purpose. The stabilizer to a large degree eliminates the need for this padding, although it does introduce a nominal 3-db loss in the control element. The generator padding cannot be entirely eliminated in general because of the possibility of pulling the os-

cillator frequency, although operating experience to date indicates that in practice this effect is usually negligible. The ultimate system would employ frequency stabilization of the oscillator and hence completely eliminate the need of padding. The power stabilizer can thus provide an effective increase in the available power of as much as 17 db or more over conventional dissipative pads.

- 5) Precision attenuator—Over a 0-10-db range or greater, the technique provides a precision attenuator which requires no calibration.

APPENDIX

A rigorous treatment of the effect of changes in magnitude of \mathbf{b}_0 in (2) is tedious, and in its place the following intuitive treatment will be supplied.

It has been observed in connection with (1) that \mathbf{b} has in general a functional dependence in both amplitude and phase upon \mathbf{a} , while the phase of \mathbf{b} is ordinarily of no interest. The existing state of the art is such, in fact, that the phases of the various quantities in (1) do not permit ready measurement; it is rather the magnitudes of these quantities which are usually observed.

If the generator is connected to a passive load of reflection coefficient Γ_g , then $\mathbf{a} = \mathbf{b}\Gamma_g$ and (1) becomes:

$$\mathbf{b}(1 - \Gamma_g\Gamma_g) = \frac{e}{2} (1 - \Gamma_g)$$

from which it follows:

$$\frac{\left| \frac{e}{2} (1 - \Gamma_g) \right|}{1 + |\Gamma_g\Gamma_g|} \leq |\mathbf{b}| \leq \frac{\left| \frac{e}{2} (1 - \Gamma_g) \right|}{1 - |\Gamma_g\Gamma_g|}.$$

Thus if the load is matched ($\Gamma_g = 0$), and

$$|\mathbf{b}| = \left| \frac{e}{2} (1 - \Gamma_g) \right|$$

while for $\Gamma_g \neq 0$ there is an uncertainty in the magnitude of \mathbf{b} by the factor $1/1 \pm |\Gamma_g\Gamma_g|$. In practice the interest in Γ_g stems from the role it plays in determining the uncertainty in $|\mathbf{b}|$. Define $\delta\mathbf{b}_1$ and $\delta\mathbf{b}_2$ such that

$$|\mathbf{b}_0| + |\delta\mathbf{b}_1| = \frac{|\mathbf{b}_0|}{1 - |\Gamma_g\Gamma_g|}$$

and

$$|\mathbf{b}_0| - |\delta\mathbf{b}_2| = \frac{|\mathbf{b}_0|}{1 + |\Gamma_g\Gamma_g|}$$

where \mathbf{b}_0 is the value of \mathbf{b} when $\Gamma_g = 0$. $|\delta\mathbf{b}_1|$ and $|\delta\mathbf{b}_2|$ thus represent the uncertainty in $|\mathbf{b}|$ when the generator is connected to other than a matched load. Solving for $|\Gamma_g|$ yields:

⁶ The accuracy is independent of the bolometer dc-rf substitution error provided that the bolometer resistance law, at a constant ambient temperature can be expressed in the form $r = f(P_{dc} + KP_{rf})$ where K is constant and P_{dc} and P_{rf} are the dc and microwave power dissipated in the bolometer, respectively.

$$|\Gamma_g| = \frac{1}{|\Gamma_l|} \frac{|\delta b_1|}{|\mathbf{b}_0| + |\delta \mathbf{b}_1|},$$

$$|\Gamma_g| = \frac{1}{|\Gamma_l|} \frac{|\delta b_2|}{|\mathbf{b}_0| - |\delta \mathbf{b}_2|},$$

or if Γ_g is small $|\delta \mathbf{b}_1| \ll |\mathbf{b}_0|$, $|\delta \mathbf{b}_1| = |\delta \mathbf{b}_2| = |\delta \mathbf{b}|$, and

$$|\Gamma_g| \approx \frac{1}{|\Gamma_l|} \frac{|\delta \mathbf{b}|}{|\mathbf{b}_0|}. \quad (3)$$

An upper limit to $|\Gamma_g|$ due to noninfinite gain of the feedback loop may be obtained by the following experimental technique. First a matched load is connected to the stabilized output and the magnitude of \mathbf{b}_3 (2) observed. The matched load is then replaced by a sliding short which is adjusted to produce the maximum change in $|\mathbf{b}_3|$.

Since \mathbf{b}_2 is a linear function of \mathbf{b}_3 , the value of $|\mathbf{b}_3|$ and $|\delta \mathbf{b}_3|$ as thus obtained may be substituted in (3) to obtain an upper limit to the equivalent $|\Gamma_g|$ due to finite gain.

Application of this technique to the stabilizer yielded a corresponding vswr of less than 1.001 which indicates this term is negligible in comparison with

$$\left(S_{22} - \frac{S_{12}S_{23}}{S_{13}} \right).$$

ACKNOWLEDGMENT

The author acknowledges the contributions of R. W. Beatty who proposed the application as a precision attenuator, and thanks him for his valuable criticism in the preparation of the manuscript.

A Simple Artificial Anisotropic Dielectric Medium*

R. E. COLLIN†

Summary—The anisotropic properties of an infinite stack of thin dielectric sheets separated by another set of thin sheets with a different dielectric constant is investigated. It is shown that the anisotropic properties are brought about because of the two distinct modes of propagation which can exist in such a stacked array of sheets. The limiting forms of the wave solutions and second-order results for the equivalent dielectric constants are given.

INTRODUCTION

LECTROMAGNETIC wave propagation in homogeneous anisotropic dielectric media is well understood and discussed in most text books on optics.¹ At optical frequencies, one has to rely on naturally occurring crystalline media with anisotropic properties. At microwave frequencies where the wavelength is much greater, it is possible to construct artificial dielectric media having either isotropic or anisotropic properties. For example, nonsymmetrical metallic obstacles arranged in a cubical array or symmetrical (also unsymmetrical) obstacles arranged in a noncubical array in a suitable binder will produce an artificial dielectric with anisotropic properties.² However, this paper will consider only the anisotropic properties of an

infinite stack of dielectric sheets as illustrated in Fig. 1. Each sheet of thickness t and relative dielectric constant κ_a is separated by a sheet of thickness d and relative dielectric constant κ_b . In order to behave essentially as a homogeneous medium, the spacing S must be small in comparison with the wavelength λ_0 of the radiation. Conditions on S will be given later. Because of the similar disposition of the sheets with respect to the y and z axis, it can be anticipated that this medium will have the same effective dielectric constant along the y and z axis, but a different effective dielectric constant in the x direction and therefore corresponds to a uniaxial crystalline medium.

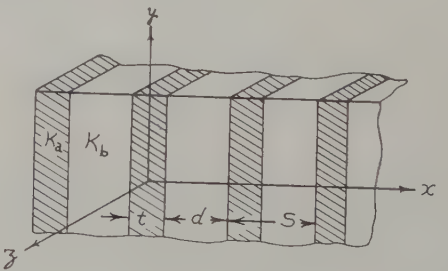


Fig. 1—An artificial anisotropic dielectric medium.

* Manuscript received by the PGMTT, August 23, 1957.
† Elec. Eng. Dept., Case Institute of Technology, Cleveland, Ohio; formerly with Canadian Armament Res. and Dev. Estab., Valcartier, P. Q., Can.

¹ G. Joos, "Theoretical Physics," Blackie and Son, Ltd., London, 2nd ed., ch. 19; 1951.

² G. Estrin, "The effects of anisotropy in a three-dimensional array of conducting disks," PROC. IRE, vol. 39, pp. 821-826; July, 1951.

Before considering propagation in this stacked dielectric sheet medium, the theory of wave propagation in a homogeneous uniaxial crystalline medium will be briefly reviewed for later comparison.

PROPAGATION IN AN HOMOGENEOUS ANISOTROPIC DIELECTRIC

Let the principal dielectric constants be $\kappa_1, \kappa_2, \kappa_3$ along the principal axes and let these axes coincide with the x, y , and z axis, respectively. For plane wave propagation, the electric field has the following form

$$\mathbf{E} = \mathbf{E}_0 e^{-i\beta n \cdot \mathbf{r}}, \quad (1)$$

where \mathbf{E}_0 is a constant vector, \mathbf{n} is a unit vector along the wave normal, and \mathbf{r} is the position vector $\mathbf{a}_{xz} + \mathbf{a}_{yz} + \mathbf{a}_{zz}$. From Maxwell's equations one obtains

$$-j\omega\mu\mathbf{H} = \nabla \times \mathbf{E} = -j\beta n \times \mathbf{E}, \quad (2a)$$

$$j\omega\mathbf{D} = \nabla \times \mathbf{H} = \frac{j\beta^2}{\omega\mu} [\mathbf{E} - \mathbf{n}(\mathbf{n} \cdot \mathbf{E})]. \quad (2b)$$

Eq. (2b) shows that \mathbf{D} is always normal to \mathbf{n} , but that \mathbf{D} and \mathbf{E} are not, in general, colinear. If $\mathbf{n} \cdot \mathbf{E} = 0$, then \mathbf{D} and \mathbf{E} are colinear and must lie in the yz plane. In this case $\beta^2 = \kappa_2 k_0^2$, where k_0 is the free-space propagation factor. In general, $\mathbf{n} \cdot \mathbf{E} \neq 0$ and hence replacing the components of \mathbf{E} in the first term on the right-hand side of (2b) by

$$\frac{D_x}{\kappa_1 \epsilon_0}, \quad \frac{D_y}{\kappa_2 \epsilon_0}, \quad \frac{D_z}{\kappa_3 \epsilon_0},$$

and solving for the components of \mathbf{D} gives

$$\mathbf{D} = \epsilon_0 \mathbf{n} \cdot \mathbf{E} \frac{\beta^2}{k_0^2} \left[\frac{\mathbf{a}_x n_z k_1^2}{\beta^2 - k_1^2} + k_2^2 \frac{\mathbf{a}_y n_y + \mathbf{a}_z n_z}{\beta^2 - k_2^2} \right], \quad (3)$$

where $k_i^2 = \kappa_i k_0^2$. Using the result $\mathbf{n} \cdot \mathbf{D} = 0$ one obtains the following eigenvalue equation from (3).

$$\beta^2 = \frac{k_1^2 k_2^2}{n_x^2 k_1^2 + (1 - n_x^2) k_2^2}. \quad (4)$$

For every direction of the wave normal, except along the optical axis (x axis), two values of the phase velocity are possible. For one mode, \mathbf{E} lies in the yz plane and $\beta = k_2$, while for the other mode \mathbf{E} has components along all three axis in general and β is given by (4). The dielectric displacement \mathbf{D} for the two modes are mutually orthogonal and make the same angle with the electric field as the normal \mathbf{n} makes with the direction of the Poynting vector.

From the above properties of the two modes of propagation, it is readily seen that they may be derived from a magnetic type and an electric type of Hertzian potential having a single component along the optical axis. The ordinary wave is obtained from the magnetic type Hertzian potential as follows

$$\mathbf{E} = -j\omega\mu\nabla \times \mathbf{\Pi}_M, \quad (5a)$$

$$\mathbf{H} = \nabla \times \nabla \times \mathbf{\Pi}_M, \quad (5b)$$

and $\mathbf{\Pi}_M$ is a solution of

$$\nabla^2 \mathbf{\Pi}_M + k_2^2 \mathbf{\Pi}_M = 0. \quad (5c)$$

The extraordinary wave is obtained from the electric type of Hertzian potential as follows

$$\mathbf{E} = k_0^2 \mathbf{\Pi}_E + \frac{1}{\kappa_2} \nabla \nabla \cdot \mathbf{\Pi}_E, \quad (6a)$$

$$\mathbf{H} = j\omega\epsilon_0 \nabla \times \mathbf{\Pi}_E, \quad (6b)$$

and $\mathbf{\Pi}_E$ is a solution of

$$\nabla^2 \mathbf{\Pi}_E + k_1^2 \mathbf{\Pi}_E + \frac{\kappa_1 - \kappa_2}{\kappa_2} \frac{\partial^2 \mathbf{\Pi}_E}{\partial x^2} = 0. \quad (6c)$$

When $\mathbf{n} = \mathbf{a}_x n_x$; *i.e.*, coincides with the optical axis, the solutions generated by $\mathbf{\Pi}_M$ and $\mathbf{\Pi}_E$ vanish. However, the solution in this case is a simple plane wave transverse to the x axis and with a propagation constant k_2 .

PROPAGATION IN A STACKED DIELECTRIC SHEET MEDIUM

If the x axis is considered as the axis of propagation in the medium illustrated in Fig. 1, then the modes of propagation are the E and H modes. These modes are derivable from the electric and magnetic Hertzian potentials, respectively, as follows³

for E modes,

$$\mathbf{E} = \frac{1}{\kappa(x)} \nabla \times \nabla \times \mathbf{\Pi}_E, \quad (7a)$$

$$\mathbf{H} = j\omega\epsilon_0 \nabla \times \mathbf{\Pi}_E, \quad (7b)$$

$$\nabla^2 \mathbf{\Pi}_E - \frac{1}{\kappa(x)} \nabla \kappa(x) \nabla \cdot \mathbf{\Pi}_E + \kappa(x) k_0^2 \mathbf{\Pi}_E = 0, \quad (7c)$$

while for H modes

$$\mathbf{E} = -j\omega\mu \nabla \times \mathbf{\Pi}_M, \quad (8a)$$

$$\mathbf{H} = \nabla \times \nabla \times \mathbf{\Pi}_M, \quad (8b)$$

$$\nabla^2 \mathbf{\Pi}_M + \kappa(x) k_0^2 \mathbf{\Pi}_M = 0, \quad (8c)$$

where

$$\kappa(x) = \begin{cases} \kappa_a, & mS - \frac{t}{2} \leq x \leq mS + \frac{t}{2}, \\ \kappa_b, & mS + \frac{t}{2} \leq x \leq (m+1)S - \frac{t}{2}, \end{cases}$$

and m is any integer. $\mathbf{\Pi}_E$ and $\mathbf{\Pi}_M$ have components along the x axis only. In view of the periodic nature of $\kappa(x)$, the solutions for $\mathbf{\Pi}_E$ and $\mathbf{\Pi}_M$ are of the form⁴

$$\mathbf{\Pi}_E = \mathbf{a}_x e^{-i\beta n \cdot \mathbf{r}} F_E(x), \quad (9a)$$

$$\mathbf{\Pi}_M = \mathbf{a}_x e^{-i\beta n \cdot \mathbf{r}} F_M(x), \quad (9b)$$

³ R. E. Collin and R. M. Vaillancourt, "Application of Rayleigh-Ritz method to dielectric steps in waveguides," IRE TRANS., vol. MTT-5, pp. 177-184; July, 1957.

⁴ R. E. Collin, "Reflection and transmission at a slotted dielectric interface," Can. J. Phys., vol. 34, pp. 398-411; April, 1956.

where F_E and F_M are periodic functions of x with a period S . The boundary conditions are continuity of

$$\Pi_M, \frac{\partial \Pi_M}{\partial x}, \frac{1}{\kappa(x)} \frac{\partial \Pi_E}{\partial x}, \text{ and } \Pi_E.$$

The fundamental solutions for Π_E and Π_M are readily constructed from the independent even and odd solutions of the wave equation. The details are given by Collin⁴ for a case corresponding to a solution for Π_M . A similar procedure may be used for Π_E but account must be taken of the modified boundary condition on $\partial \Pi_E / \partial x$. The solutions for the general case will not be given here, but rather the limiting forms of these solutions as $k_0 S$ approaches zero. It is found that

$$\Pi_E \rightarrow a_x e^{-j\beta n \cdot r} F_E(x), \quad (10a)$$

where

$$F_E(x) = F_E(x + mS)$$

$$= \begin{cases} 1 - j\beta n_x \frac{\kappa_a - \kappa_b}{\kappa_2} \left(1 - \frac{t}{S}\right) x, & -\frac{t}{2} \leq x \leq \frac{t}{2}, \\ 1 - j\beta n_x \frac{\kappa_a - \kappa_b}{\kappa_2} \frac{t}{S} \left(\frac{S}{2} - x\right), & \frac{t}{2} \leq x \leq S - \frac{t}{2}, \end{cases} \quad (10b)$$

$$\beta^2 = \frac{k_1^2 k_2^2}{n_x^2 k_1^2 + (1 - n_x^2) k_2^2}, \quad (10c)$$

$$\kappa_1 = \left[\frac{1}{\kappa_b} - \frac{\kappa_a - \kappa_b}{\kappa_a \kappa_b} \frac{t}{S} \right]^{-1}, \quad (10d)$$

$$\kappa_2 = \kappa_b + (\kappa_a - \kappa_b) \frac{t}{S}, \quad (10e)$$

and that

$$\Pi_M \rightarrow a_x e^{-jk_2 n \cdot r}, \quad (11)$$

where $k_2^2 = \kappa_2 k_0^2$ and κ_2 is given by (10e). The limiting solution for Π_M is thus a plane wave corresponding to the ordinary wave in the equivalent homogeneous anisotropic dielectric. The limiting solution for Π_E is essentially also a plane wave. It is modified by a small oscillating phase function. The field components are derivable from Π_E by means of (7a)–(7c). If these field components, apart from the propagation factor $e^{-j\beta n \cdot r}$, are averaged over one period along the x axis, one finds that the average values are the same as would be obtained for a homogeneous anisotropic dielectric with relative dielectric constants given by (10d) and (10e). Thus, in the limit as $k_0 S$ approaches zero the stacked dielectric sheet medium becomes identical with a homogeneous anisotropic dielectric. The maximum anisotropic effect is obtained when

$$\frac{t}{S} = 0.50, \quad (12a)$$

and for this value of t/S the ratio of the two dielectric constants is

$$\frac{\kappa_2}{\kappa_1} = \frac{(\kappa_a + \kappa_b)^2}{4\kappa_a \kappa_b}. \quad (12b)$$

This ratio is not critically dependent on t/S . As κ_a becomes much larger than κ_b , this ratio approaches $\kappa_a/4\kappa_b$. For polystyrene sheets separated by polyfoam sheets and the optimum value of t/S , $\kappa_2/\kappa_1 = 1.22$.

Even for large values of $k_0 S$ this medium has anisotropic properties, because of the existence of two distinct modes of propagation with different phase velocities. In fact, for arbitrary large values of $k_0 S$, there are many modes of propagation. However, provided that $k_0 S$ satisfies the following inequality, only the two fundamental modes will propagate with a wave normal having real direction cosines,

$$k_0 S < \frac{2\pi}{\sqrt{\kappa}}, \quad (13)$$

where κ is the largest value of κ_a or κ_b . This relation is obtained by imposing the condition that no higher order mode having the required periodic behavior should propagate in a homogeneous material with a dielectric constant κ .

The plane wave approximations for Π_E and Π_M are accurate for that range of $k_0 S$ for which the equivalent dielectric constants are well approximated by (10d) and (10e). For general values of $k_0 S$, second-order approximations for the equivalent dielectric constants are,

$$\kappa_1' = \kappa_1 + \frac{\kappa_b^2 [(P_{11} + P_{00})^2 - 4\Delta]}{4\Delta P_{00}(2P_{00} - P_{11})} \frac{S^2}{\lambda_0^2}, \quad (14a)$$

where

$$\begin{aligned} \Delta &= P_{00} P_{11} - P_{01}^2, \\ P_{00} &= 1 - \frac{\kappa_a - \kappa_b}{\kappa_a} \frac{t}{S}, \\ P_{01} &= - \frac{\kappa_a - \kappa_b}{\kappa_a} \frac{\sqrt{2}}{\pi} \sin \pi \frac{t}{S}, \\ P_{11} &= P_{00} - \frac{\kappa_a - \kappa_b}{\kappa_a} \frac{1}{2\pi} \sin 2\pi \frac{t}{S}, \\ \kappa_2' &= \kappa_2 + \frac{(\kappa_a - \kappa_b)^2}{16\pi^2} \\ &\quad \cdot \left[32 \sin^2 \pi \frac{t}{S} + \sin^2 2\pi \frac{t}{S} \right] \frac{S^2}{\lambda_0^2}. \end{aligned} \quad (14b)$$

These two expressions were obtained by an application of the Rayleigh-Ritz method.³ Propagation in the yz plane was considered and a two term approximation used for Π_E and Π_M . The equivalent dielectric constants were defined so as to give the same phase velocity in an equivalent homogeneous medium as was actually found

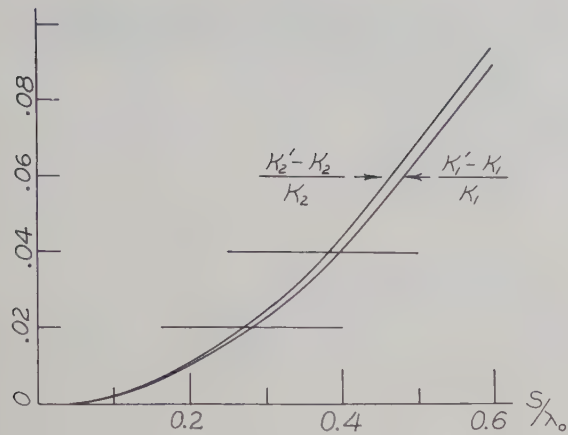


Fig. 2—Deviation of equivalent dielectric constants from static values. $\kappa_a = 2.56$, $\kappa_b = 1.03$.

for the stacked dielectric sheet medium. Quadratic expressions for κ'_1 and κ'_2 were obtained and (14a) and (14b) were derived by expanding the square roots and retaining only the lowest power term in S^2/λ_0^2 . It is seen that κ'_1 and κ'_2 reduce to κ_1 and κ_2 , respectively, whenever $k_0 S$ becomes negligible. Fig. 2 is a plot of

$$\frac{\kappa'_1 - \kappa_1}{\kappa_1} \quad \text{and} \quad \frac{\kappa'_2 - \kappa_2}{\kappa_2}$$

as a function of S/λ_0 for $\kappa_a = 2.56$, $\kappa_b = 1.03$, and the optimum value of t/S . For this case, the plane wave approximation is satisfactory for S less than about $0.3\lambda_0$.

This artificial anisotropic dielectric has been used as the basis of a broad-band quarter-wave plate and circular polarizer,⁵ as well as to improve the impedance characteristics of a periodically loaded waveguide for linear accelerator use.⁶ Another use for this medium is for a microwave version of a Nicol prism for analyzing

⁵ H. S. Kirschbaum and S. Chen, "A method of producing broad-band circular polarization employing an anisotropic dielectric," IRE TRANS., vol. MTT-5, pp. 199-203; July, 1957.

⁶ R. B. R. Harvie, *et al.*, "A theoretical and experimental investigation of anisotropic dielectric loaded linear electron accelerators," Proc. IEE (London), Pt. B, vol. 104, pp. 273-292; May, 1957.

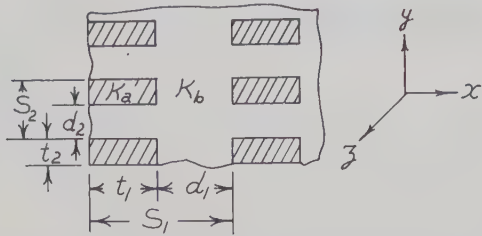


Fig. 3—A three-dimensional artificial anisotropic dielectric medium.

an arbitrary polarized wave into its basic components.

An artificial dielectric medium having three dimensional anisotropic properties can be obtained by making the structure periodic along two directions as in Fig. 3. The principal values of the dielectric constants for this medium can readily be evaluated when the periods S_1 and S_2 are small compared with the wavelength, so that the static values may be used. When the fringing fields around the dielectric prisms are neglected, it is found that

$$\kappa_x = \frac{S_1 \kappa_b (t_2 \kappa_b + d_2 \kappa_a)}{\kappa_b (S_2 d_1 + t_1 t_2) + t_1 d_2 \kappa_a}, \quad (15a)$$

$$\kappa_y = \frac{S_2 \kappa_b (t_1 \kappa_b + d_1 \kappa_a)}{\kappa_b (S_1 d_2 + t_1 t_2) + t_2 d_1 \kappa_a}, \quad (15b)$$

$$\kappa_z = \kappa_b + (\kappa_a - \kappa_b) \frac{d_1 d_2}{S_1 S_2}. \quad (15c)$$

CONCLUSION

The stacked dielectric sheet medium has been shown to behave like a homogeneous anisotropic dielectric when the spacing between sheets is small compared with the wavelength. Furthermore, the principal values of the dielectric constants are given to sufficient accuracy by their static values. For larger spacings, the equivalent dielectric constants are a few per cent greater than the static values, but the anisotropic properties are retained because of the existence of two distinct modes of propagation in the medium.



Calculation and Measurement of the Noise Figure of a Maser Amplifier*

J. C. HELMER† AND M. W. MULLER†

Summary—The noise performance of regenerative amplifiers is reviewed and equations are obtained which serve to interpret a measurement of noise from an ammonia molecular beam maser amplifier.

The measurement is accomplished by means of a double heterodyne system in which a detuned maser oscillator serves as second local oscillator. The measured noise figure is 3.5 ± 0.5 db, as predicted by theory for the slightly undercoupled circuit used. Although no beam noise is observed, the experimental uncertainty places an upper limit of 40°K on the spontaneous emission noise temperature of the ammonia beam.

INTRODUCTION

THE most important source of excess noise in electronic microwave amplifiers is the shot noise carried by the electron stream. This source of excess noise is absent in a maser¹ in which electromagnetic radiation is obtained from uncharged atomic systems. This fact was pointed out by Gordon, *et al.*, in their original report, in which it was shown that in the absence of other noise sources the maser technique might lead to a nearly ideal amplifier. The present measurement (the results of which have already been reported briefly elsewhere²) was undertaken to test this supposition in the specific instance of a regenerative maser employing a molecular beam of ammonia.

GENERAL DISCUSSION

Noise Performance of a Regenerative Amplifier

There appears to be some need for an elementary discussion of the noise performance of regenerative amplifiers because there has been a tendency among workers in this field to use various definitions of noise figure and noise temperature that differ from each other, as well as from the accepted standard. Such a variety is not especially serious in itself since a study of the particular definition can always make the specific result intelligible. It may, however, be less confusing to use the standard definitions as far as possible, even though, as we shall see presently, they are not completely adequate for the present purpose. The pertinent definitions are:^{3,4}

* Manuscript received by the PGMTT, September 25, 1957; revised manuscript received, December 5, 1957.

† Varian Associates, Palo Alto, Calif.

¹ J. P. Gordon, H. J. Zeiger, and C. H. Townes, "The maser—new type of microwave amplifier, frequency standard, and spectrometer," *Phys. Rev.*, vol. 99, p. 1264; 1955.

² J. C. Helmer, "A maser noise measurement," *Phys. Rev.*, vol. 107, pp. 902-903(L); August 1, 1957.

³ "IRE standards on electron tubes: definitions of terms, 1950," *PROC. IRE*, vol. 38, pp. 426-438; April, 1950.

⁴ "IRE standards on receivers: definitions of terms, 1952," *PROC. IRE*, vol. 40, pp. 1681-1685; December, 1952.

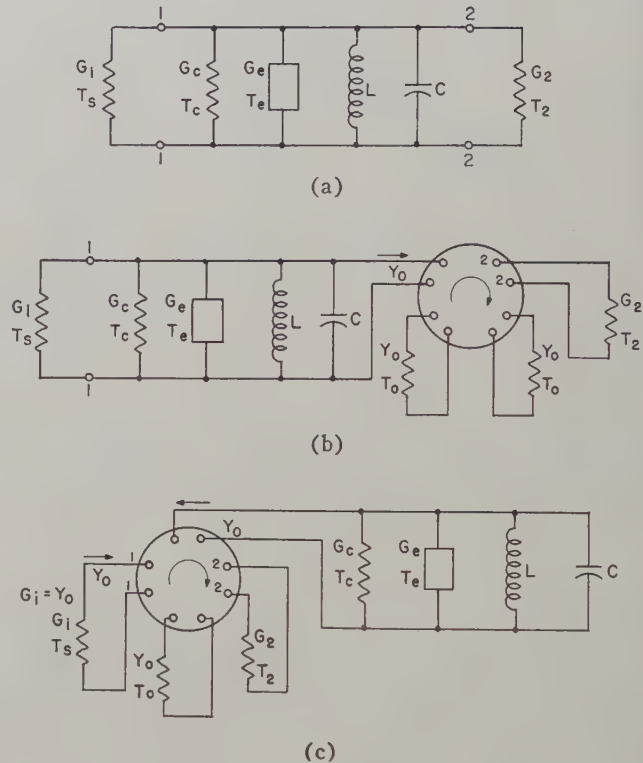


Fig. 1—(a) Transmission maser, (b) transmission maser with ideal load isolator, (c) reflection maser with ideal circulator.

Noise Figure: Of a linear system at a selected input frequency, the ratio of 1) the total noise power per unit bandwidth . . . available at the output terminals to 2) the portion thereof engendered at the input frequency by the input termination, the noise temperature of which is standard (290°K) at all frequencies.

Noise Temperature: At a pair of terminals and a specific frequency, the temperature of a passive system having an available noise power per unit bandwidth equal to that of the actual terminals.

Available Power: . . . the power that would be delivered to the output external termination . . . if the admittance of the external termination were the conjugate of the output driving-point admittance.

We shall choose as our "specific frequency" the center frequency of the ammonia resonance, and will consider the circuit configurations shown in Fig. 1, with the maser cavity used in transmission and reflection.

The circuit of Fig. 1(b) is very similar to the circuit actually used for this measurement.

The difficulty mentioned above arises in connection with the circuit configurations of Fig. 1(a), because the

driving point impedance at terminals 2 may have a negative real part under a set of possible operating conditions, and thus available power is undefined. In the circuit configurations of Fig. 1(b) and 1(c) the driving point admittance at the output terminals is just the characteristic admittance Y_0 of the transmission line, so that no problem arises.

It might be pointed out here that the circuit element G_e shown in Fig. 1 represents the negative conductance of the ammonia molecular beam. It has recently been shown⁵ that such a circuit representation is possible, and that an effective temperature T_e can be defined for this element, so that its available noise power is kT_e^6 watts per unit bandwidth.

We now write down the noise power per unit bandwidth at resonance flowing toward the load G_2 from all admittances G_i , G_c , G_e , Y_0 and G_2 , where

$T_s = 290^\circ\text{K}$, G_i = temperature and conductance of input coupling,

T_c , G_c = cavity temperature and conductance,

T_e , G_e = noise temperature and conductance of active medium. G_e is negative,

T_0 , Y_0 = temperature and characteristic conductance of isolator or circulator,

T_2 , G_2 = temperature and conductance of the load.⁷

For Fig. 1(b),

$$P_b = \frac{KT_s 4G_i Y_0 + KT_c 4G_c Y_0 + KT_e 4|G_e| Y_0}{(G_i + Y_0 + G_c + G_e)^2} + KT_0 \left(\frac{Y_0 - G_i - G_c - G_e}{Y_0 + G_i + G_c + G_e} \right)^2. \quad (1)$$

For Fig. 1(c),

$$P_c = KT_s \left(\frac{Y_0 - G_e - G_c}{Y_0 + G_c + G_e} \right)^2 + \frac{KT_c 4G_c Y_0 + KT_e 4|G_e| Y_0}{(Y_0 + G_c + G_e)^2}. \quad (2)$$

A measure of the sensitivity of the amplifier of Fig. 1(a) may be obtained by defining its noise figure, F_a , so that if it is connected to a receiver of noise figure F_r , the noise figure of the combination is given by

⁵ M. W. Muller, "Noise in a molecular amplifier," *Phys. Rev.*, vol. 106, pp. 8-12; April 1, 1957.

R. V. Pound, "Spontaneous emission and the noise figure of maser amplifiers," *Ann. Phys.*, vol. 1, pp. 24-32; April, 1957.

K. Shimoda, H. Takahasi, and C. H. Townes, "Fluctuations in amplification of quanta with application to maser amplifiers," *J. Phys. Soc. Japan*, vol. 12, pp. 686-700; June, 1957.

M. W. P. Strandberg, "Inherent noise of quantum-mechanical amplifiers," *Phys. Rev.*, vol. 106, pp. 617-620; May 15, 1957.

⁶ We use the approximation

$$\frac{\hbar\omega}{\exp(\hbar\omega/KT) - 1} = KT.$$

⁷ Note the sentence following (7).

$$F = F_a + \frac{F_r - 1}{\mu}, \quad (3)$$

where μ is the gain of the maser. In this way the definition of noise figure is tied to the way in which it is measured, as it always should be. A feature of the circuit of Fig. 1(a) is that noise generated by the load conductance G_2 is amplified by and reflected from the maser so that it adds coherently to the generating voltage. From this noise the power generated by G_2 , which contributes to the noise figure of the receiver, must be subtracted. Thus, we obtain

$$P_a = \frac{KT_s 4G_i G_2 + KT_c 4G_c G_2 + KT_e |G_e| G_2}{(G_i + G_2 + G_c + G_e)^2} + \frac{KT_2 4G_2^2}{(G_i + G_2 + G_c + G_e)^2} - KT_2. \quad (4)$$

In each case the power gain, μ , may be obtained by letting all temperatures, except T_s , be zero. Thus

$$\mu_a = \frac{4G_i G_2}{(G_i + G_2 + G_c + G_e)^2} \quad (5)$$

$$\mu_b = \frac{4G_i Y_0}{(G_i + Y_0 + G_c + G_e)^2} \quad (6)$$

$$\mu_c = \left(\frac{Y_0 - G_c - G_e}{Y_0 + G_c + G_e} \right)^2. \quad (7)$$

In Fig. 1(b) and 1(c) it has been assumed that G_2 is matched to Y_0 . A mismatch in G_2 does not affect the signal-to-noise ratio at the output, but it does affect the gain. The noise figures may be immediately obtained by the formula

$$F = \frac{P}{\mu K T_s}. \quad (8)$$

Thus

$$F_a = 1 + \frac{T_c G_c + T_e |G_e| + T_2 G_2}{T_s G_i} - \frac{1}{\mu_a} \cdot \frac{T_2}{T_s} \quad (9)$$

$$F_b = 1 + \frac{T_c G_c + T_e |G_e| + T_0 Y_0}{T_s G_i} + \frac{T_0}{T_s} \left\{ \frac{1}{\mu_b} - 2 \left(\frac{1}{\mu_b} \frac{Y_0}{G_i} \right)^{1/2} \right\} \quad (10)$$

$$F_c = 1 + \frac{(\sqrt{\mu_c} + 1)^2 \cdot T_c G_c + T_e |G_e|}{T_s G_i}. \quad (11)$$

Here the algebra has been arranged so that a limiting form is apparent. As the gain becomes sufficiently high, all equations have the form

$$F = \frac{\sum_x T_x |G_x|}{T_s G_i} \quad (12)$$

where the summation is taken over all conductances,

including G_s . Also, if $T_x = T_s$ for all x except e , then

$$F = \frac{\sum_{x \neq e} G_x}{G_i} + \frac{T_e}{T_s} \frac{|G_e|}{G_i}. \quad (13)$$

Since for high gain $G_e + \sum_{x \neq e} G_x \approx 0$, we have

$$F \approx \frac{Q_i}{Q_L} \left(1 + \frac{T_e}{T_s} \right), \quad (14)$$

where Q_i is the radiation Q of the input coupling and Q_L is the cold loaded Q of the cavity.

In the limit of high gain the reflection circuit of Fig. 1(c) inherently has the best noise figure because it has one less conductance to add noise to system. However, with the circuit of Fig. 1(a) it is possible to work at a lower gain, so that the amplifier is matched to the load G_2 . In this case the noise generated by G_2 is not reflected by the maser and the noise figure is simply

$$F'_a = 1 + \frac{T_e G_c + T_e |G_e|}{T_s G_i}. \quad (15)$$

This type of operation may require a very small value of G_2 which, in comparison with the circuit of Fig. 1(c), results in a tendency toward much greater gain instability due to fluctuations in cavity loading.

As the gain of the circuit of Fig. 1(a) is further reduced, a noise figure less than unity becomes possible. This is not mysterious, it is the consequence of a combination of low gain and mismatch which is such that the total noise power at terminals 2, due to all sources except G_i , is less than $K T_2$. If $T_e = 0$, this condition occurs for values of gain so that

$$\mu_a < \frac{T_2 G_i}{T_e G_c + T_2 G_2}. \quad (16)$$

In the circuit of Fig. 1(b) a noise figure of less than unity is not possible, as may be seen from (1). However, the possibility still exists that the maser cavity may be matched to the isolator, so that noise generated by Y_0 is absorbed and not reflected into the output. It also is possible to cool the isolator to reduce its noise contribution.

A quantity that is frequently quoted as a measure of the sensitivity of a maser amplifier under the improper designation "noise temperature" is the excess noise temperature per unit gain of the amplifier, or

$$\text{"Noise Temperature"} = 290^\circ \times (F - 1). \quad (17)$$

This quantity would be the true noise temperature if $\mu = 1$ and $T_i = 0^\circ\text{K}$.

Noise Temperature of the Ammonia Beam

We have regarded the ammonia beam in the maser as a negative conductance G_e which emits noise power $k T_e$ per unit bandwidth. It has been shown elsewhere⁵ that the noise temperature T_e can be defined in terms of the populations of the two quantum states of the

ammonia which participate in the interaction:

$$\exp(\hbar\omega/kT_e) = n_+/n_- \quad (18)$$

where n_+ and n_- are the populations of the upper and lower energy levels, respectively.

Since it is thought that the separating action of the inhomogeneous focusing field in an ammonia maser is quite efficient, one may expect the entering beam to consist almost entirely of upper-state molecules and thus to have a temperature near 0°K . Since $|G_e|$ is of the same order of magnitude as G_c and G_i , one thus would expect its contribution to the noise to be quite negligible, unless the amplifier were cooled to very low temperatures. It is indeed true that this noise contribution has not yet been observed.

Nevertheless, it should be pointed out that T_e might be substantially larger than the value one would compute from the population ratio of the entering beam. This is so because the populations n_+ and n_- should include all the molecules in these states in the cavity, including the "thermalized" molecules that have collided with the cavity walls or that have diffused into the cavity from the circumambient atmosphere. These molecules, of course, will contribute to n_- much more heavily than the entering beam and thus will tend to raise T_e .

It is very difficult to make an estimate of this contribution which depends on a number of parameters some of which are only very sketchily known, such as transverse velocities in the beam, the partial pressure of NH_3 in the vacuum envelope, and the flux of ammonia molecules into the cavity. We have made some estimates based on rough guesses of some of these quantities which indicate that the noise contribution of the ammonia might be between 0.1 and 0.5 db, corresponding to T_e between roughly 7°K and 35°K .

THE MEASUREMENT

The problem of measuring the noise figure of an ammonia beam amplifier is essentially the problem of overcoming the noise output of a K -band microwave receiver with a very narrow band noise signal. It is instructive to examine the conditions which must be met in order to obtain a ratio of signal noise to receiver noise of unity. Two cases arise. In one case the receiver bandwidth is greater than the maser bandwidth. Assuming a maser noise figure of 1, the necessary condition for unity signal to noise ratio is

$$\frac{\mu B_m}{(F_r - 1) B_r} = 1 \quad (19)$$

where

- μ = maser power gain,
- B_m = maser bandwidth,
- F_r = receiver noise figure,
- B_r = receiver bandwidth,
- $B_r > B_m$.

In the other case, the receiver bandwidth is less than the maser bandwidth and the necessary condition is simply

$$\frac{\mu}{F_r - 1} = 1. \quad (20)$$

For unity gain, the maser bandwidth is about 4000 cycles and it decreases in inverse proportion to the square root of the power gain of the maser. Thus, a maser with a gain of 20 db would have a bandwidth of about 400 cycles. On the other hand, *K*-band receivers typically have noise figures on the order of 20 db, primarily due to the crystal conversion loss, and have IF bandwidths on the order of 2 mc. Narrower IF bandwidths are difficult to use because of the stability requirements on the klystron local oscillator. For a 2-mc IF bandwidth, a local oscillator stability of 1 part in 10^6 is required, in order to keep received signals in the central portion of the IF amplifier response characteristic.

According to (19), we now see that fantastic maser gains are required in order to overcome the noise in the receiver. Such a measurement has been achieved by Alsop, *et al.*,⁸ using a super-regenerative maser in order to obtain the required gain. A somewhat different approach has been used at Bell Telephone Laboratories.⁹ Here, a maser preamplifier is attached to the front end of the receiver in order to lower the noise figure of the system. This requires the use of a circulator to which a second maser, whose noise figure is to be measured, is connected. In addition, modulation of the maser output and a lock-in detection system are employed, in order to reduce the noise bandwidth of the system.

Still a third solution to the problem has been tried by the authors. Here conditions are created such that (20) applies. The receiver shown in Fig. 2 is a double superheterodyne receiver with two mixers and two IF strips. The first mixer is driven by a klystron local oscillator and this is followed by a 2-mc wide IF strip. The second mixer works into a 50-cycle bandwidth audio strip. Ordinarily, the second local oscillator would be attached to the second mixer at this point. However, in order to keep the signal in the audio strip, the second local oscillator would have to follow the instability of the first. In other words, a receiver stability of about 1 part in 10^{10} is required in order to keep the signal centered in the pass band of the audio amplifier. The solution to this problem is to introduce a signal from a maser oscillator at the front end of the receiver along with the noise signal from the maser amplifier. These two signals are amplified independently in the first IF strip. Since they are both converted by the same local oscillator, the frequency difference between the two signals remains con-

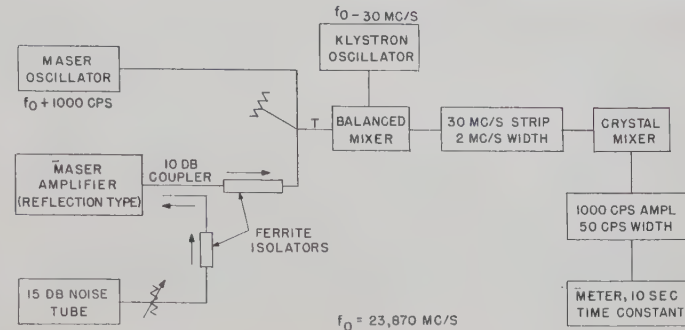


Fig. 2—Block diagram of apparatus.

stant. When the signal from the maser oscillator reaches the second mixer, it has an amplitude of a few volts and is capable of acting as a local oscillator. This local oscillator signal then converts the amplifier signal, which is originally detuned from it by 1000 cycles, so that it is amplified in the audio strip. Provided that the maser oscillator signal is strong enough, this double superheterodyne system will be linear and will have a bandwidth equal to the bandwidth of the audio amplifier. How strong does the maser signal have to be? With a receiver noise figure of 20 db, the effective noise power input to the receiver is about 10^{-12} watts. The available maser power, however, is about 10^{-10} watts, thus giving 20-db margin over the receiver noise. This is sufficient to ensure that the noise products generated by the maser oscillator in the second mixer override all other noise contributions.

The output of the audio amplifier is rectified and its average is determined by a meter. It is unfortunate that the narrower the bandwidth of the audio amplifier the greater will be the fluctuations in the reading of the output meter for a given meter time constant. This situation has been analyzed by Dicke,¹⁰ and one finds that the percentage fluctuation of the total output is given by

$$\frac{\Delta E}{E} \approx \frac{1}{\sqrt{B\tau}}$$

where B = bandwidth of audio amplifier and τ = meter time constant. With a meter time constant of 10 seconds, a 4 per cent fluctuation is obtained. Since part of this fluctuation is due just to receiver noise, the fluctuation in the computed value of the maser noise is greater than 4 per cent. A longer meter time constant is not useful because of instabilities in the maser gain. However it should be pointed out that n measurements with a meter of time constant τ are equivalent to a single measurement with a meter of time constant $n\tau$. In principle, by taking a sufficient number of measurements one can obtain a noise figure to any desired degree of accuracy. Thus the ultimate accuracy is limited only by the patience of the observer and the uncertainty in

⁸ L. E. Alsop, J. A. Giordmaine, C. H. Townes, and T. C. Wang, "Measurement of noise in a maser amplifier," *Phys. Rev.*, vol. 107, pp. 1450-1451(L); September 1, 1957.

⁹ J. P. Gordon and L. D. White, "Experimental determination of the noise figure of an ammonia maser," *Phys. Rev.*, vol. 107, p. 1728(L); September 15, 1957.

¹⁰ R. H. Dicke, "Measurement of thermal radiation at microwave frequencies," *Rev. Sci. Inst.*, vol. 17, pp. 268-275; July, 1946.

the calibration of the noise standard and the microwave components.

Referring again to Fig. 2 when the maser amplifier is turned on the noise power output of the receiver rises by an amount P_1 . Then a known amount of noise ΔP per unit frequency interval is introduced through a calibrated directional coupler and is amplified by the maser, thereby causing the receiver noise power output to increase again by an amount P_2 . The maser noise figure is then given by

$$F = \frac{\Delta P}{kT} \frac{P_1}{P_2} + \frac{1}{\mu}. \quad (21)$$

The results of a number of such measurements as a function of amplifier gain are shown in Fig. 3. Excluding the two high measurements at low gain, the average value of the set is $3\frac{1}{2}$ db with a standard deviation of $\frac{1}{2}$ db. A measurement of the cavity coupling shows that the cavity, being slightly undercoupled, has a circuit noise figure of $3\frac{1}{2}$ db as given by (14) with $T_e = 0$. Therefore, it is concluded that no spontaneous emission noise from the beam is observed. However, from the standard deviation of the measurements it is possible to set an upper limit to the beam noise. We conclude that the beam temperature is less than 40°K .

The high noise figure measurements at low gain can be caused by interaction between the maser oscillator and maser amplifier arising from a relatively large am-

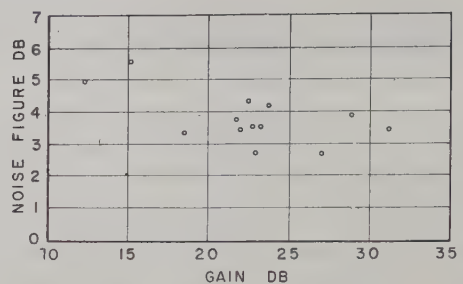


Fig. 3—Noise figure measurement.

plifier bandwidth at low gain. It is also true, as shown by (11), that the noise figure of the reflection amplifier rises at low gain. Since the accuracy of the gain measurements is somewhat uncertain, quantitative information is taken from the high-gain region of constant noise figure.

Theoretically, we expect that the effective beam temperature can be very low. If so, the beam radiation will not be easy to detect, but it may be possible with sufficiently refined techniques. By using low-noise maser preamplifiers and by cooling the cavity and its loads, we may eventually measure spontaneous emission.

ACKNOWLEDGMENT

The authors wish to acknowledge helpful conversations with Drs. C. H. Townes, J. P. Gordon, and M. L. Stitch.



Propagation in Dielectric Slab Loaded Rectangular Waveguide*

P. H. VARTANIAN†, W. P. AYRES†, AND A. L. HELGESSON‡

Summary—Propagation in dielectric loaded rectangular waveguide is investigated theoretically for varying slab thickness and dielectric constant. The slabs are placed across the center of the waveguide in the E plane. This geometry is found to offer bandwidths in excess of double that of rectangular waveguide for dielectrics having dielectric constants of approximately 18. Power handling capacities which are double or triple that of standard waveguide are achievable using the dielectric loaded waveguide. In addition to the theory, design curves of bandwidth, guide wavelength, cutoff wavelength, impedance, power handling capacity, wall losses, and dielectric losses are presented and compared to experiment where possible.

LIST OF SYMBOLS

$k = \omega/c = \omega\sqrt{\mu_0\epsilon_0} = 2\pi/\lambda_0$.
 $k_c = 2\pi/\lambda_c$.
 $\beta = 2\pi/\lambda_g$.
 λ_0 = free-space wavelength.
 λ_g = guide wavelength.
 λ_c = guide cutoff wavelength.
 μ_0 = free-space permeability.
 ϵ_0 = free space permittivity.
 $\epsilon = \epsilon\epsilon_0$ = complex permittivity.
 $= \epsilon_0 (\epsilon' - j\epsilon'')$
 ϵ' = relative dielectric constant.
 ϵ'' = loss factor.
 $\tan \delta = \epsilon''/\epsilon'$ = loss tangent.
 $\eta = \sqrt{\mu_0/\epsilon_0} = 377$ ohms.
 $r = s/d = (c/a)/(1 - c/a)$.

INTRODUCTION

WITH the development of low-loss, high-dielectric constant materials, a new type of waveguide transmission line offers advantages in bandwidth and power handling capacity over conventional waveguides. The geometry to be considered is a rectangular waveguide loaded with a dielectric slab placed across the center of the waveguide in the E plane. That this geometry would broaden the rectangular waveguide is readily apparent by comparison with the ridged waveguide. Both the ridged and the dielectric loaded waveguides add capacitance to the dominant mode, while only slightly affecting the capacitance associated with the next higher mode. The dielectric loaded waveguide, unlike the ridged guide, does not reduce the air

gap and, consequently, the power handling capacity, but instead adds material having a higher breakdown strength to the region where breakdown is most likely. Consequently, the power handling capacity is higher with the loaded waveguide. The general results, if compared to ridged waveguide, are that the dielectric loaded waveguide is superior in every respect, with the assumption that suitably low-loss dielectric materials are available.

This work theoretically investigates the propagation characteristics of the TE_{n0} modes in dielectric loaded waveguide. The analysis yields design curves of bandwidth, guide wavelength, cutoff wavelength, impedance, power handling capacity, wall losses, and dielectric losses. Previous treatments of dielectric loaded rectangular waveguide have considered the cutoff relations¹ and other loading geometries.² Berk,³ by variational methods, has derived approximate relations for the guide wavelength.

GENERAL THEORY

The geometry of the dielectric slab loaded waveguide is shown in Fig. 1. It consists of a dielectric slab mounted in the E plane at the center of a rectangular waveguide.

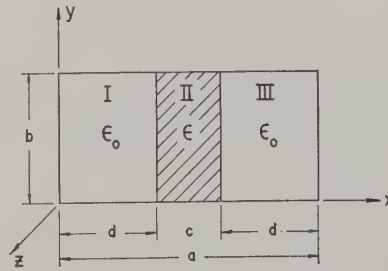


Fig. 1—Dielectric loaded waveguide geometry.

The two types of modes corresponding to TE and TM modes are called the longitudinal section electric (LSE) and longitudinal section magnetic (LSM) modes. The LSE mode is characterized by $E_x = 0$ and the LSM mode by $H_x = 0$. Considerations of the boundary conditions lead to the fact that for modes having no y dependence

* Manuscript received by the PGM TT, October 4, 1957; revised manuscript received, December 6, 1957. This work was performed at the Microwave Physics Lab., Sylvania Elec. Products, Inc., and was sponsored in part by the U. S. Army Signal Corps under Contract No. DA 36-039-SC-73188.

† Microwave Eng. Labs., Inc., Palo Alto, Calif.; formerly with Sylvania Microwave Phys. Lab., Mountain View, Calif.

‡ Massachusetts Institute of Technology, Cambridge, Mass., on educational leave from Sylvania Microwave Phys. Lab., Mountain View, Calif.

1 C. Montgomery, R. Dicke, and E. Purcell, "Principles of Microwave Circuits," McGraw-Hill Book Co., Inc., New York, N. Y., Rad. Lab. Ser., vol. 8, pp. 386-387; 1948. This work appears to have typographical errors in several of the equations. The curves, however, are correct at the calculated points.

2 L. Pincherle, "Electromagnetic waves in metal tubes filled longitudinally with two dielectrics," *Phys. Rev.*, vol. 66, pp. 118-130; September, 1944.

3 A. D. Berk, "Variational principles for electromagnetic resonators and waveguides," *IRE TRANS.*, vol. AP-4, pp. 104-111; April, 1956.

of fields, the LSE mode is a TE mode (*i.e.*, E_z is zero). Thus, for these modes with propagation according to $\exp j(\omega t - \beta z)$, Maxwell's equations give the following relations:

$$E_y = -\frac{\omega\mu_0}{\beta} H_z \quad (1)$$

$$\frac{\partial E_y}{\partial x} = -j\omega\mu_0 H_z \quad (2)$$

$$\frac{\partial H_z}{\partial x} + j\beta H_z + j\omega\epsilon E_y = 0. \quad (3)$$

From (1) through (3), it can be shown that

$$\frac{\partial^2 H_z}{\partial x^2} + (\epsilon k^2 - \beta^2) H_z = 0 \quad (4)$$

where $\epsilon = \epsilon_0$ is the dielectric constant in the region under consideration and $k^2 = \omega^2\epsilon_0\mu_0$, the square of the free-space wave number. Since we have assumed modes having fields which are independent of y , let

$$H_z = Ag(x)e^{j(\omega t - \beta z)} \quad (5)$$

and from (1) and (3)

$$E_y = j\omega\mu_0 \frac{\partial H_z}{\partial x} \begin{cases} \frac{1}{k^2 - \beta^2} & \text{in I} \\ \frac{1}{\epsilon k^2 - \beta^2} & \text{in II} \\ \frac{1}{k^2 - \beta^2} & \text{in III.} \end{cases} \quad (6)$$

For the purpose of analysis, the TE modes are separated into $TE_{odd,0}$ and $TE_{even,0}$ modes. For the $TE_{odd,0}$ modes, $g(x)$ is an antisymmetric function about the center of the guide. Hence, let

$$g(x) = \begin{cases} \cos \frac{px}{d} & \text{in I} \\ B \sin \frac{q}{s} \left(\frac{a}{2} - x \right) & \text{in II} \\ -\cos \frac{p}{d} (a - x) & \text{in III} \end{cases} \quad (7)$$

where p and q are unknowns and $s = c/2$. From (4), (and for all TE modes),

$$\left(\frac{p}{d} \right)^2 = k^2 - \beta^2 \quad (8)$$

$$\left(\frac{q}{s} \right)^2 = \epsilon k^2 - \beta^2. \quad (9)$$

The boundary conditions that H_z and E_y be continuous require

$$B = \frac{\cos p}{\sin q} \quad (10)$$

$$\frac{\tan p}{p} = r \frac{\cot q}{q} \quad (11)$$

where

$$r = \frac{s}{d} = \frac{c/a}{1 - c/a}.$$

The limits on p and q for the $TE_{n,0}$ modes (n odd) are

$$0 \leq q \leq \frac{n\pi}{2} \\ -\infty \leq p^2 \leq \left(\frac{n\pi}{2} \right)^2. \quad (12)$$

Eliminating β from (8) and (9), there results

$$q^2 = r^2 p^2 + \frac{(\epsilon - 1)}{4} \left(\frac{rka}{1 + r} \right)^2 \quad (13)$$

which along with (11) and (12) permits finding p and q .

As a function of slab thickness, q^2 is zero for zero slab thickness and increases monotonically to $(n\pi/2)^2$ for increasing slab thickness. The quantity p^2 , on the other hand, is $(n\pi/2)^2$ for zero slab thickness. As the slab is increased in width, p^2 decreases to a negative minimum returning asymptotic to zero for a dielectric filled guide. The negative values of p^2 indicate that the fields are experiencing exponential decay outside the slab. For such values of p^2 , it would be imagined that the metallic walls at $x=0$ and $x=a$ could be removed with little effect on the propagation characteristics. This has been experimentally verified for a slab of $\epsilon = 9$. Curves showing the transverse electric field as a function of frequency are shown in Fig. 2. It is seen that for frequencies

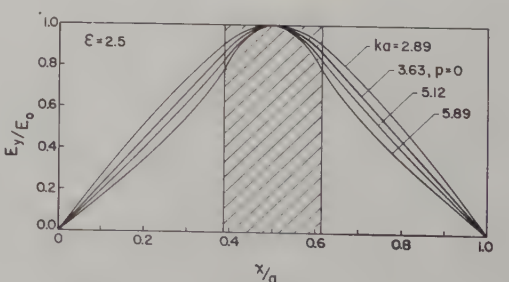
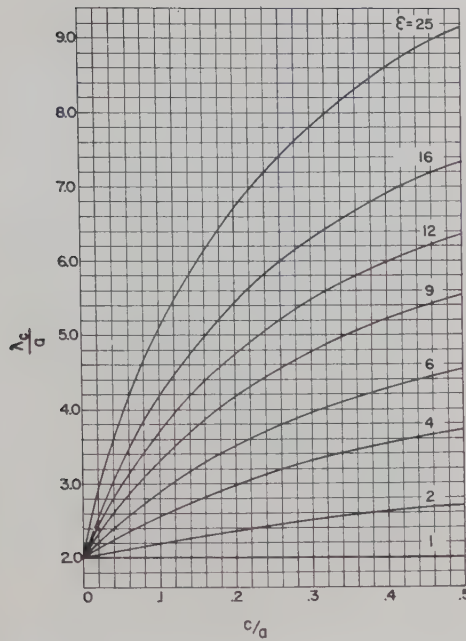
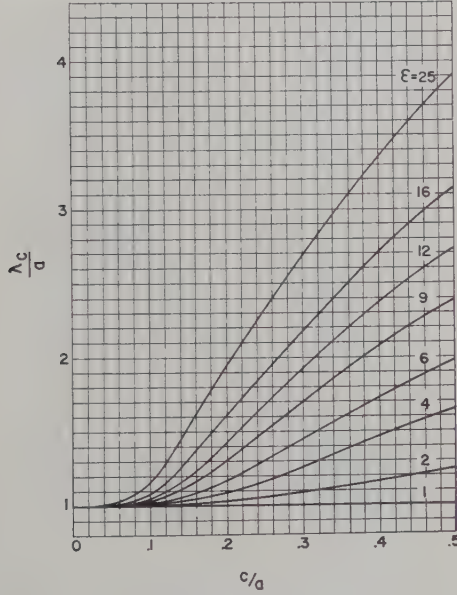


Fig. 2—Electric fields in dielectric loaded waveguide for several frequencies.

and slab thicknesses producing large negative values of p^2 , the energy is highly concentrated in the dielectric slab. The $p^2 = 0$ condition is of interest since the electric field in the air space has a constant gradient. For $ka = 3.63$, the fields are linear in the air space. For a higher frequency, the fields decay exponentially in the air spaces.

Fig. 3—Cutoff wavelength for the TE_{10} mode.Fig. 4—Cutoff wavelength for the TE_{20} mode.

PROPAGATION CHARACTERISTICS

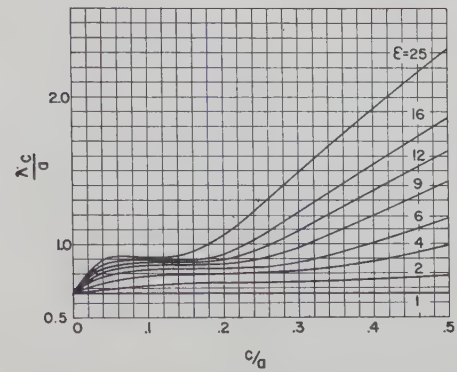
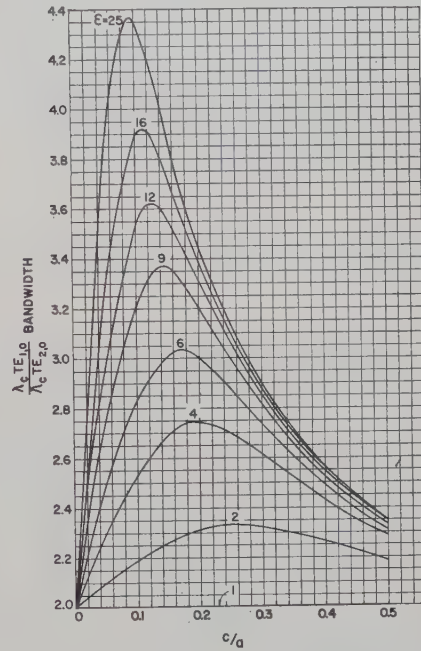
The cutoff frequency relations are easily found by setting $\beta=0$ in (8), (9), and (11). This leads to the equation for cutoff for the $TE_{odd,0}$ modes

$$\tan \frac{k_c a}{2(1+r)} = \frac{1}{\sqrt{\epsilon}} \cot \frac{\sqrt{\epsilon} k_c a r}{2(1+r)} \quad (14)$$

where

$$k_c = \frac{2\pi f_{cutoff}}{c}.$$

Similarly, it can be shown that for the $TE_{even,0}$ modes that

Fig. 5—Cutoff wavelength for the TE_{30} mode.Fig. 6—Bandwidth defined on the basis of the ratios of cutoff wavelengths for the TE_{10} and TE_{20} modes.

$$\tan \frac{k_c a}{2(1+r)} = -\frac{1}{\sqrt{\epsilon}} \tan \frac{\sqrt{\epsilon} k_c a r}{2(1+r)}. \quad (15)$$

The normalized cutoff wavelengths calculated from (14) and (15) for the TE_{10} , TE_{20} , and TE_{30} modes are shown in Fig. 3 through Fig. 5 as a function of slab thickness and dielectric constant. The bandwidth, defined as the ratio of the cutoff wavelength for the TE_{10} mode to the cutoff wavelength for the TE_{20} mode is shown in Fig. 6. It is shown that for each dielectric constant there is a slab thickness which gives maximum bandwidth. This slab thickness, called the optimum slab thickness, and the associated maximum bandwidth are plotted in Fig. 7. It is seen that a slab of dielectric constant 18.1 can double the bandwidth of air filled waveguide. A dielectric constant of 9 gives a 1.68 improvement in bandwidth.

For the TE_{10} mode, the ka vs βa plot is calculated from (11) and (13). The quantities ka and βa are the reciprocals of the free space and guided wavelengths

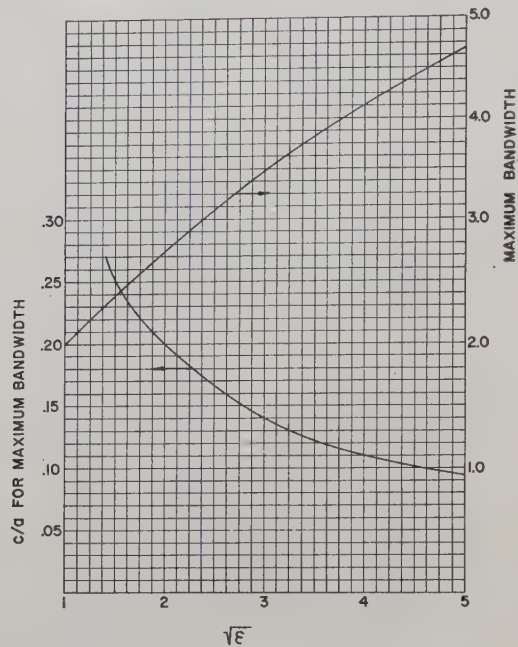


Fig. 7—Maximum bandwidth achievable for a given dielectric constant and the dielectric thickness which gives this maximum bandwidth.

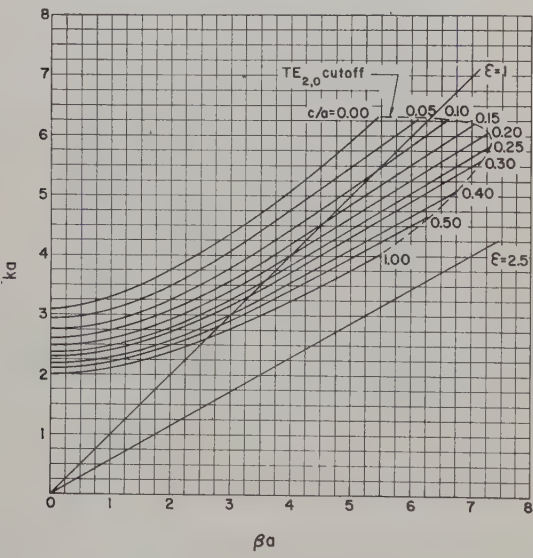


Fig. 8— ka vs βa plot for $\mathcal{E}=2.5$.

normalized to the waveguide width. Fig. 8 through Fig. 10 are the results for dielectric constants of 2.5, 9, and 16.⁴ Asymptotes for $ka = \beta a$ and $ka = \beta a / \sqrt{\mathcal{E}}$ also are shown. For sufficiently high frequency, the curves are all asymptotic to $ka = \beta a / \sqrt{\mathcal{E}}$. The $c/a = 0$ curve is, of course, asymptotic to $ka = \beta a$. From (8) it can be shown that

$$\frac{\lambda_g}{\lambda_0} = \left\{ 1 - \left[\frac{2p(1+r)}{ka} \right]^2 \right\}^{-1/2}, \quad (16)$$

⁴ These dielectric constants were chosen to give a range of data which would be useful for commonly used low-loss dielectrics. These materials are available in the form of titanium dioxide loaded polystyrene ($\mathcal{E}=2.5$ to 25).

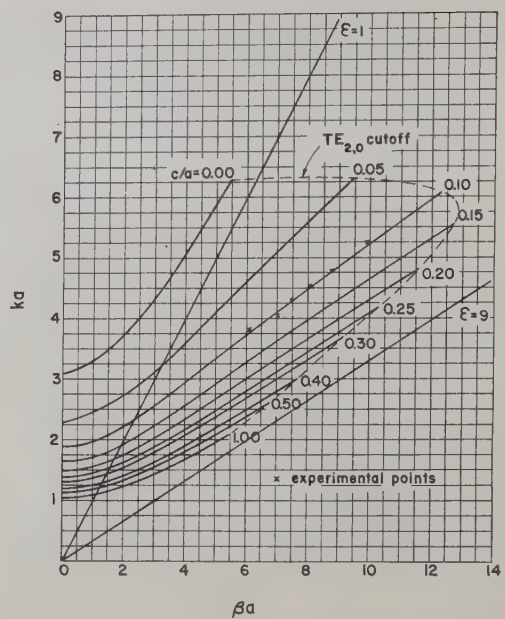


Fig. 9— ka vs βa plot for $\mathcal{E}=9$. Experimental points taken in X -band waveguide are shown.

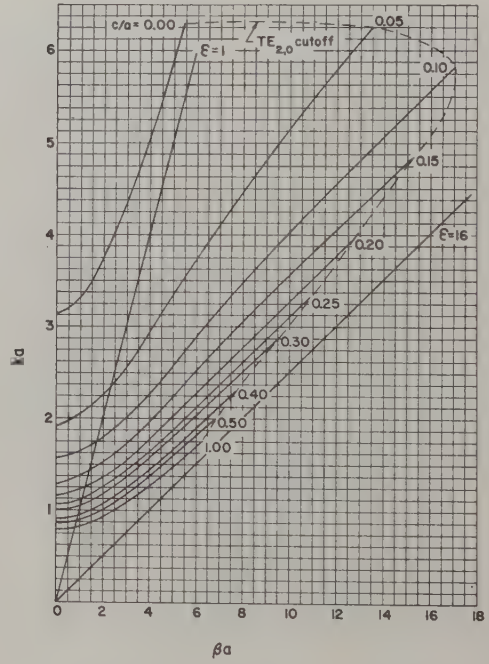
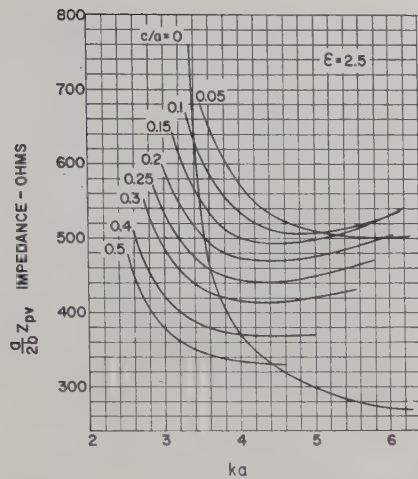
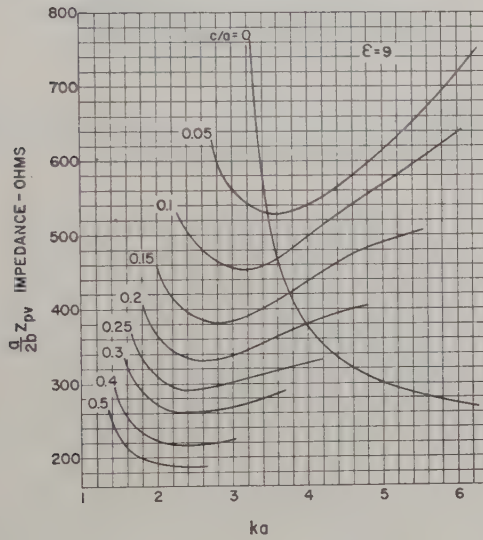


Fig. 10— ka vs βa plot for $\mathcal{E}=16$.

where λ_g and λ_0 are the guide and free-space wavelengths. This shows that for frequencies and geometries where $2p(1+r) < ka$, the guide and free-space wavelengths are approximately equal. This also shows that the points where $p^2 = 0$ lie on the $ka = \beta a$ line in Fig. 8 through Fig. 10.

Experimental points are shown on the $\mathcal{E}=9$ curve and show very good agreement with the theory. These measurements were made in X -band waveguide. It is interesting to note in passing that this X -band waveguide with a dielectric slab 0.126-inch thick has upper and lower frequency cutoffs of 11.93 and 3.54 kmc.

The slope of the line from the origin to points on the

Fig. 11—Normalized power voltage impedance for $\epsilon = 2.5$.Fig. 12—Normalized power voltage impedance for $\epsilon = 9$.

ka vs βa plot gives the group velocity of the structure. It is seen that over certain frequency ranges the dielectric loading can give a relatively constant group velocity. As such, this type waveguide could be useful in devices requiring a slow wave structure.

IMPEDANCE

The wave impedance defined by

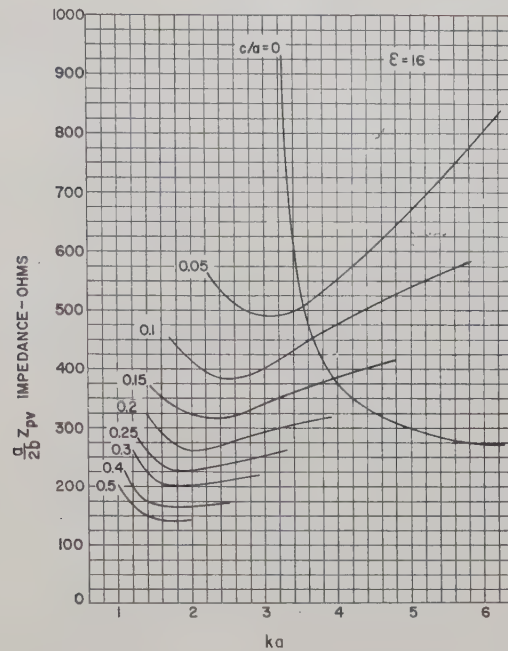
$$Z_0 = \frac{E_y}{H_x} = \eta \frac{ka}{\beta a}$$

where $\eta = 377$ ohms can easily be found from the ka vs βa curves.

The power-voltage impedance can be defined by

$$Z_{PV} = \frac{VV^*}{2P}$$

where P is the power carried by the guide and V is the voltage across the center of the guide. From (6)

Fig. 13—Normalized power voltage impedance for $\epsilon = 16$.

$$E_y = \begin{cases} E_0 \frac{\cos q}{\sin p} \sin \frac{px}{d} \\ E_0 \cos \frac{q}{s} \left(\frac{a}{2} - x \right) \\ E_0 \frac{\cos q}{\sin p} \sin \frac{p}{d} (a - x) \end{cases} \quad (17)$$

where

$$E_0 = - \frac{j\omega\mu_0 A p \sin p}{(k^2 - \beta^2)d \cos q} = - \frac{j\omega\mu_0 A B q}{(\epsilon k^2 - \beta^2)s}.$$

The power in the waveguide is

$$P = - \frac{1}{2} \int E_y H_x^* dx dy = \frac{E_0^2 abR}{4Z_0(1+r)} \quad (18)$$

where

$$R = r \left(1 + \frac{\sin 2q}{2q} \right) + \left(\frac{\cos q}{\sin p} \right)^2 \left(1 - \frac{\sin 2p}{2p} \right).$$

Hence, from (18)

$$Z_{PV} = \frac{2\eta(1+r)}{R} \frac{b}{a} \frac{ka}{\beta a}. \quad (19)$$

This impedance has been calculated and is plotted for $\epsilon = 2.5, 9$, and 16 in Fig. 11 through Fig. 13.

POWER HANDLING CAPACITY

The power handling capacity is calculated from (17) and (18). It is assumed that the waveguide will break down at the point of highest field in the air space. This point obviously is at the surface of the dielectric or at $x = d$. With this assumption

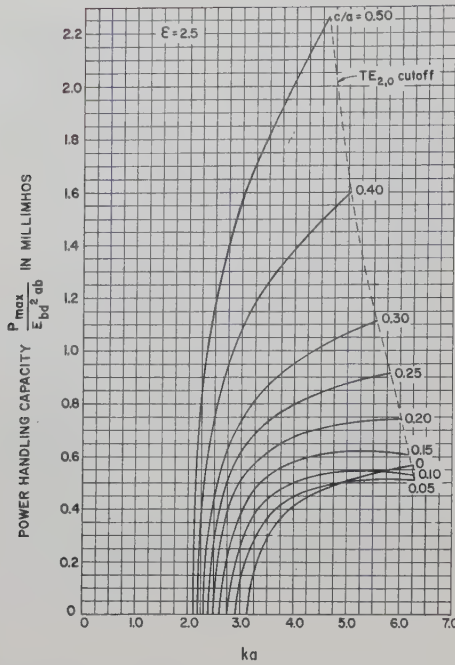


Fig. 14—Power handling capacity for $\epsilon = 2.5$. The $c/a = 0$ curve represents unloaded waveguide.

$$P_{\max} = \frac{E_{bd}^2 ab R}{4\eta(1+r) \cos^2 q} \left(\frac{\beta a}{ka} \right) \quad (20)$$

where E_{bd} is the breakdown electric field in air. The quantity $P_{\max}/E_{bd}^2 ab$ is plotted as a function of frequency with slab thickness as a parameter for dielectric constants 2.5, 9, and 16 in Fig. 14 through Fig. 16. The $c/a = 0$ curves give the maximum power for the unloaded guide.

It is noted that for very thin slabs the power handling capacity is below that for the unloaded guide. This is because the energy is drawn toward the slab, but the slab is not thick enough to contain the region of high field. As the slab thickness is increased, the energy is further concentrated, but the high fields are now contained in the dielectric. Consequently, the power handling capacity exceeds that for the unloaded waveguide. For the $\epsilon = 9$ case, for the slab thickness corresponding to maximum bandwidth, the power handling capacity is almost twice that for unloaded waveguide.

The assumption of breakdown at the dielectric surface fails when the field for breakdown in the dielectric becomes less than $E_{bd}/\cos q$. In this case, $E_{bd}/\cos q$ should be replaced by the breakdown electric field for the dielectric.

A practical problem in achieving high-power handling capability is the complete elimination of air gaps between the dielectric slab and the waveguide. A small air gap is equivalent to a small capacity in series with a large capacity (the dielectric slab) and breakdown is very likely across this small gap. As seen from Fig. 14 through Fig. 16, the power handling capacity of the loaded waveguide can be considerably in excess of the

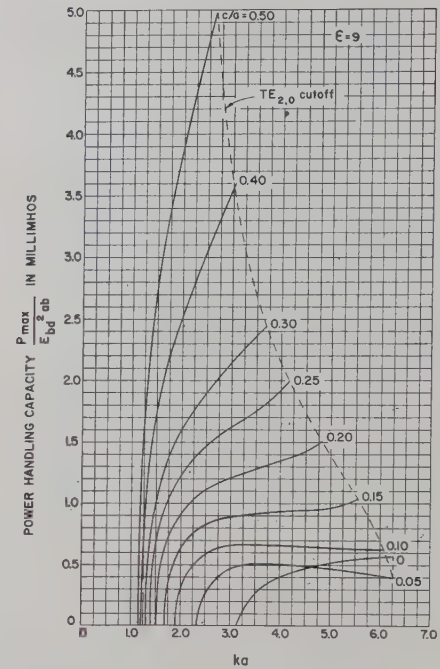


Fig. 15—Power handling capacity for $\epsilon = 9$. The $c/a = 0$ curve represents unloaded waveguide.

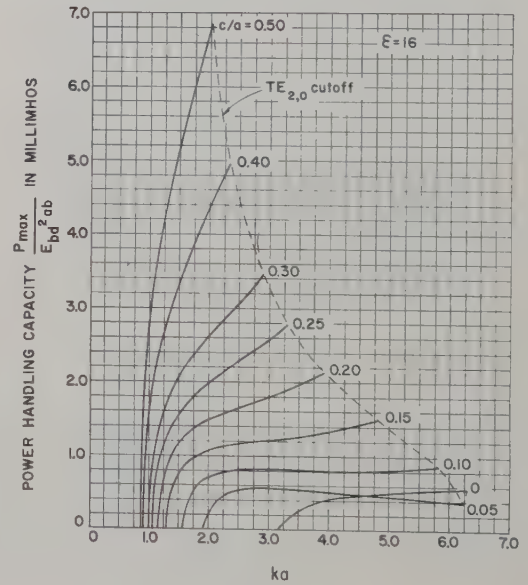
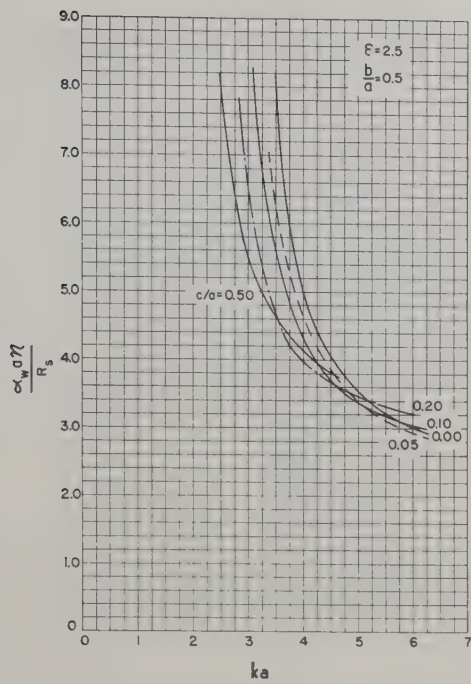


Fig. 16—Power handling capacity for $\epsilon = 16$. The $c/a = 0$ curve represents unloaded waveguide.

unloaded waveguide. In general, transforming sections from unloaded to loaded waveguide (especially those utilizing thin slab matching sections) will limit the power handling ability of the transmission line.

WAVEGUIDE LOSSES

Since the magnetic fields are being concentrated about the slab, it might be expected that the waveguide wall losses might be considerably increased by the addition of the dielectric slab. In general, while the losses are increased, the increase is not significant. The power dissipated in the waveguide walls is

Fig. 17—Wall losses in dielectric loaded waveguide for $\mathcal{E}=2.5$.

$$P_w = \frac{R_s}{2} \int |H_t|^2 dS$$

where R_s is the surface resistivity of the metal waveguide walls and H_t is the magnetic field tangential to the waveguide wall. Here as usual it is assumed that the loss free H_t is a good approximation to the actual H_t . The attenuation per unit length due to wall losses is

$$\alpha_w = \frac{P_w}{2P}$$

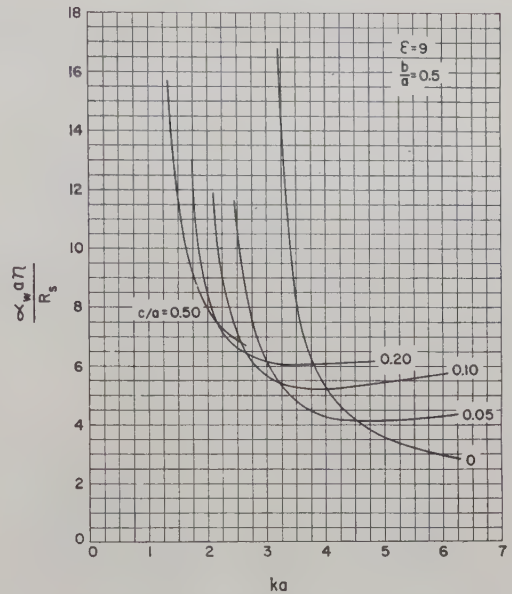
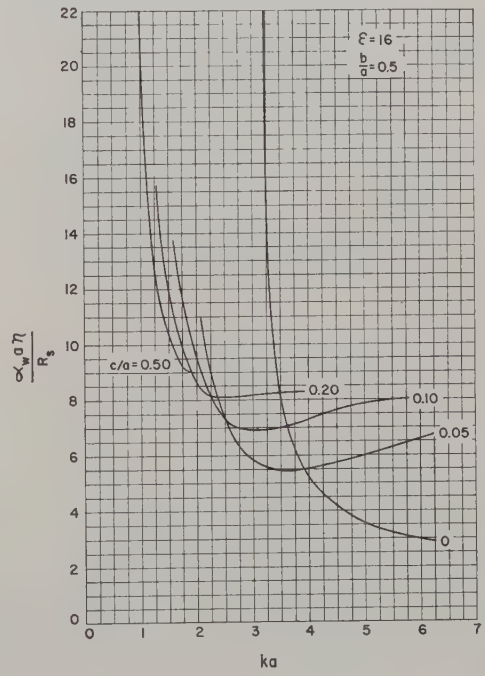
Performing the indicated integrations and substituting from (1), (5), (17), and (18), we find

$$\frac{\alpha_w a \eta}{R_s} = \left(\frac{\beta a}{ka} \right) \left(\frac{a}{b} \right) \left\{ \left[\left(\frac{ka}{\beta a} \right)^2 - 1 \right] \left[R' + 2(1+r) \frac{b}{a} \left(\frac{\cos q}{\sin p} \right)^2 \right] \frac{1}{R} + 1 \right\} \quad (21)$$

where

$$R' = \left(\frac{\cos q}{\sin p} \right)^2 \left(1 + \frac{\sin 2p}{2p} \right) + \left(\frac{q}{p} \right)^2 \frac{1}{r} \left(1 - \frac{\sin 2q}{2q} \right).$$

These waveguide losses are plotted in Fig. 17 through Fig. 19 for dielectric constants of 2.5, 9, and 16. The aspect ratio has been chosen to be 2:1. The losses are found to be comparable in magnitude to the unloaded waveguide losses except for effects connected with the lowering of the low-frequency cutoff by the dielectric addition. An interesting point is seen where the addition of a dielectric slab actually reduces the waveguide losses. This is because the low-frequency cutoff is reduced, thus reducing the transverse currents in the waveguide and consequently reducing the waveguide losses.

Fig. 18—Wall losses in dielectric loaded waveguide for $\mathcal{E}=9$.Fig. 19—Wall losses in dielectric loaded waveguide for $\mathcal{E}=16$.

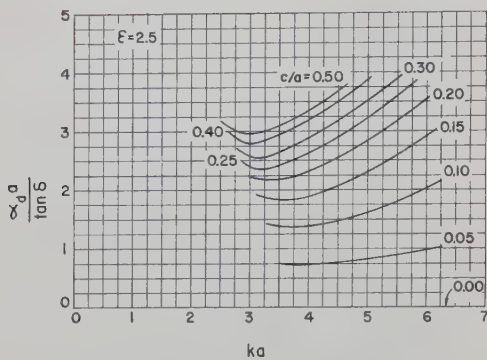
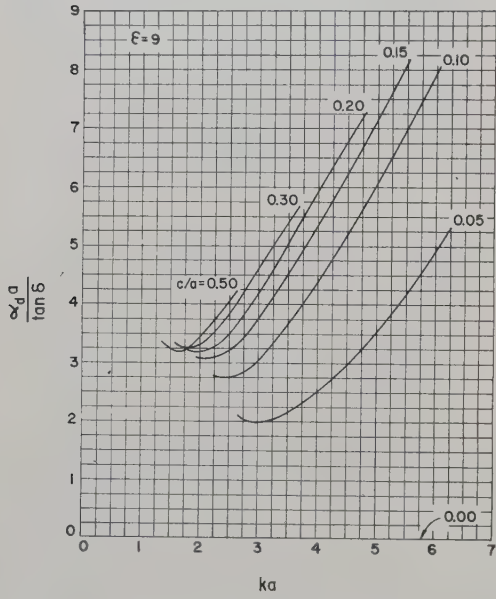
DIELECTRIC LOSSES

Dielectric losses are calculated from

$$P_d = 2 \int_d^{a/2} \int_0^b \frac{|E_y| |J_y|}{2} dx dy = \sigma \int_d^{a/2} \int_0^b |E_y|^2 dx dy,$$

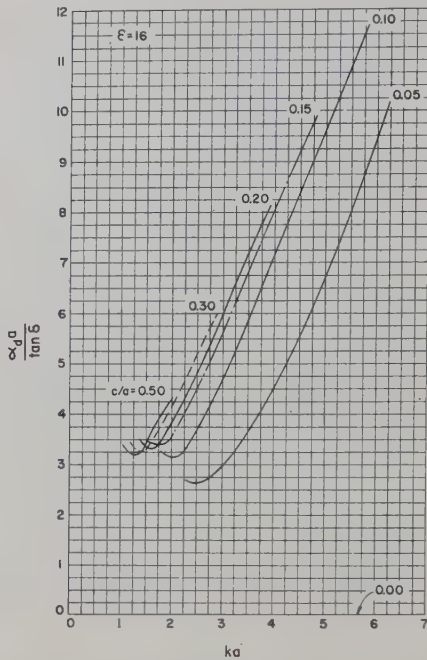
$$\sigma = \omega \mathcal{E}'' \epsilon_0, \quad \alpha_d = \frac{P_d}{2P}.$$

Performing the indicated integration, and substituting from (17) and (18), the dielectric loss is found to be given by

Fig. 20—Dielectric losses for $\epsilon = 2.5$.Fig. 21—Dielectric losses for $\epsilon = 9$.

$$\frac{\alpha_d a}{\tan \delta} = \frac{\epsilon' k a}{2} \left(\frac{k a}{\beta a} \right) \frac{r \left(1 + \frac{\sin 2q}{2q} \right)}{R} \quad (22)$$

Plots of dielectric loss as a function of frequency with slab thickness as a parameter are shown in Fig. 20 through Fig. 22. It is apparent that, as might be expected, losses are highest for thick slabs and high fre-

Fig. 22—Dielectric losses for $\epsilon = 16$.

quencies. For a typical dielectric with $\epsilon' = 9$, $\epsilon'' = 0.005$, the loss per meter in X -band waveguide with $c/a = 0.15$ and $ka = 4.0$ is approximately 1.1 db/meter.

CONCLUSION

Dielectric slab loaded rectangular waveguide can afford significant advantage in bandwidth and power handling capacity over unloaded rectangular waveguide. It has been shown that by proper choice of dimensions and dielectrics, the bandwidth and power handling capacity can be significantly increased. The waveguide wall losses were found to be larger than, but still comparable to, those of unloaded waveguide. Finally, low-dielectric loss materials should permit reasonably low-loss transmission properties.

ACKNOWLEDGMENT

The authors are indebted to Mrs. R. Farrand for many of the numerical calculations.



Parallel-Coupled Transmission-Line-Resonator Filters*

SEYMOUR B. COHN†

Summary—This paper describes the synthesis of band-pass transmission-line filters consisting of series of half-wavelength resonant conductors such as strips. The design differs from the usual end-coupled strip configuration in that successive strips are parallel coupled along a distance of a quarter-wavelength. The resulting coupling between resonators is partly electric and partly magnetic. Several important advantages are gained by this arrangement: 1) the length of the filter is approximately half that of the end-coupled type; 2) the gaps are larger and therefore less critical; and 3) the insertion-loss curve is symmetrical on a frequency scale with the first spurious response occurring at three times the center frequency of the pass band.

Formulas are derived for the parallel-coupled-resonator transmission-line filter that permit accurate design for Tchebycheff, maximally flat, or any other physically realizable response. The formulas are theoretically exact in the limit of zero bandwidth, but frequency-response calculations show them to give good results for bandwidths up to about 30 per cent. An experimental strip-line filter of this type has been constructed, and the data given in this paper show that excellent performance has been obtained.

INTRODUCTION

AS shown in Fig. 1(a),¹⁻³ multiple-coupled-resonator band-pass filters in strip line (or other TEM transmission line) have been most commonly composed of half-wavelength strips coupled end to end. In this paper, an alternative arrangement is treated in which the half-wavelength strips are parallel-coupled, as in Fig. 1(b) and 1(c). Parallel coupling offers a number of important advantages over end coupling: 1) the length of the filter is reduced approximately by half; 2) a symmetrical insertion-loss-vs-frequency response is obtained with the first spurious response occurring at three times the center frequency, and 3) a much larger gap between adjacent strips is permitted. The last advantage is of particular importance, since it eases the tolerance on the gaps for a given bandwidth, or permits a broader bandwidth for a given tolerance. Furthermore, the larger gap permits a higher power rating of the filter.

Formulas have been derived that allow the parallel-coupled-resonator filter to be designed in a straightforward manner, and to have any desired physically realizable response, such as maximally flat or equal-

ripple. The accuracy of the design formulas has been checked by exact computation, and they have been found to give excellent results for bandwidths up to about 20 per cent in the case of maximally flat response and 30 per cent in the case of equal ripple response. The method of analysis is basically that used in an earlier paper³ for a number of other types of direct-coupled-resonator filters. In this method, the lumped-constant low-pass prototype filter having the desired response is made equivalent to a set of either series- or parallel-resonant *LC* arms interconnected by broad-band quarter-wavelength transformers. An approximate equivalence then is established between the latter circuit and the actual coupled-resonator structure.

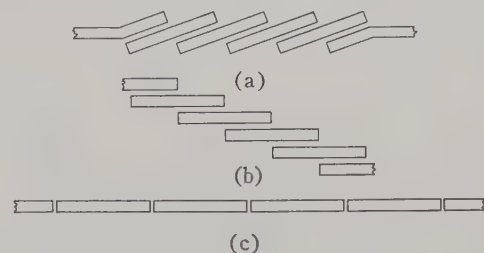


Fig. 1—Coupled-resonator strip-line filters: (a) end coupled; (b) and (c) parallel coupled.

DESIGN PROCEDURE

The design formulas for an *n*-resonator parallel-coupled filter are given in Table I. They utilize the element values g_1, g_2, \dots, g_n of the prototype low-pass filter, which may be computed for either maximally flat or equal-ripple response by means of formulas given in Table II.³ The schematic diagram in Fig. 2 shows that the filter is assembled from $n+1$ sections, resulting in a structure containing n resonators. The sections are of equal length (one-quarter wavelength at the center frequency), and their electrical design is completely specified by two characteristic impedances— Z_{oe} of the even-mode wave on the parallel conductors, and Z_{oo} of the odd-mode wave. These characteristic impedances have previously been defined, and formulas and graphs relating them to the dimensions of the cross section are available.⁴ The total filter structure always will be symmetrical for maximally flat or equal-ripple response.

In the design of a parallel-coupled-resonator filter, one should first select the type of response function and the number of resonators that will yield the desired in-

* Manuscript received by the PGMTT, October 21, 1957. The work described in this paper was supported by the U. S. Army Signal Eng. Labs. under Contract No. DA 36-039-sc-64625.

† Stanford Research Institute, Menlo Park, Calif.

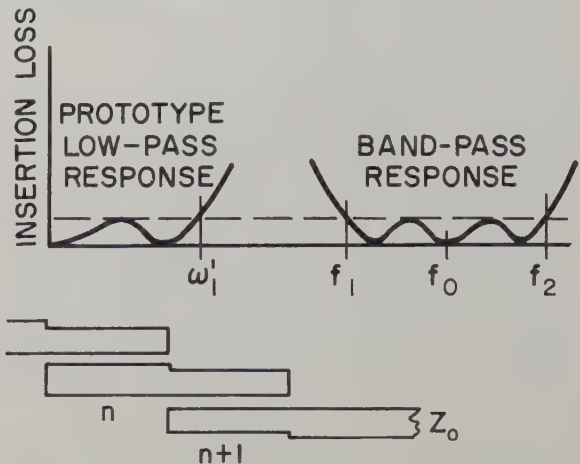
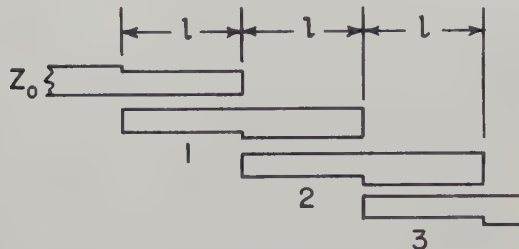
¹ E. G. Fubini, W. E. Fromm, and H. S. Keen, "Microwave applications of high-*Q* strip components," IRE CONVENTION RECORD, Pt. 8, pp. 98-103; March, 1954.

² E. A. Bradley, "Design and development of strip-line filters," IRE TRANS., vol. MTT-4, pp. 86-93; April, 1956.

³ S. B. Cohn, "Direct-coupled-resonator filters," PROC. IRE, vol. 45, pp. 187-196; February, 1957.

⁴ S. B. Cohn, "Shielded coupled-strip transmission line," IRE TRANS., vol. MTT-3, pp. 29-38, October, 1955.

TABLE I
FORMULAS FOR PARALLEL-COUPLED TRANSMISSION-LINE-RESONATOR FILTER



(For either maximally-flat or equal-ripple response, the structure is symmetrical.)

$l = \lambda_0/4$, where λ_0 = wavelength in transmission line at f_0

$$f_0 = (f_1 + f_2)/2$$

$$Z_{oe_i} = Z_0 \left\{ 1 + \frac{Z_0}{K_{i-1,i}} + \left(\frac{Z_0}{K_{i-1,i}} \right)^2 \right\}, \quad i = 1 \text{ to } n+1$$

$$Z_{oo_i} = Z_0 \left\{ 1 - \frac{Z_0}{K_{i-1,i}} + \left(\frac{Z_0}{K_{i-1,i}} \right)^2 \right\}, \quad i = 1 \text{ to } n+1$$

$$\frac{Z_0}{K_{i-1,i}} = \frac{\pi}{\omega_1'} \left(\frac{f_2 - f_1}{f_2 + f_1} \right) \left(\frac{1}{g_{i-1} g_i} \right)^{1/2}$$

g_1, g_2, \dots, g_n = prototype elements in farads and henries from Table II.

$$g_0 = \frac{\pi}{\omega_1'} \left(\frac{f_2 - f_1}{f_2 + f_1} \right)$$

$$g_{n+1} = \frac{\pi}{r\omega_1'} \left(\frac{f_2 - f_1}{f_2 + f_1} \right)$$

r = right-hand load resistance in schematic of Table II.

ω_1' = pass band edge of prototype filter.

f_1, f_2 = corresponding pass band edges of transmission-line filter.

Z_{oe_i} = even-mode characteristic impedance with respect to ground of each conductor in i th section.

Z_{oo_i} = odd-mode characteristic impedance with respect to ground of each conductor in i th section.

(The dimensions for strip-line construction may be obtained as function of Z_{oe_i} and Z_{oo_i} from Cohn.⁴)

sertion-loss function in the pass and stop bands. This may be done with the aid of the insertion-loss formulas in Table II and the following approximate relationship between the frequency scales of the prototype filter and the parallel-coupled-resonator filter:

$$\omega' = 2\omega_1' \left(\frac{f - f_0}{f_2 - f_1} \right). \quad (1)$$

The exact response curves and the bandwidth-error curve (which appear later) show how response errors are introduced when the relative bandwidth exceeds 0.1. The bandwidth error may be reduced by preadjusting the design with the aid of these curves.

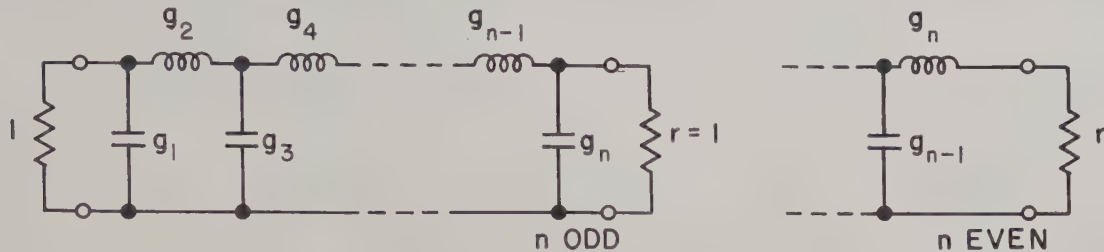
Next, the element values g_1, g_2, \dots, g_n may be computed, and in terms of these the Z_{oe} and Z_{oo} values of each of the $n+1$ sections. Then, the transmission-line

dimensions in each section should be designed to yield these characteristic impedances. This may be done easily in the case of thin strip conductors, and with somewhat more difficulty in the case of thick strips, by means of the available graphs and formulas.⁴ It is noted that the strip widths and spacings will, in general, differ from section to section, and hence the width of the resonators will not be constant, as shown in Fig. 2. This variation in width is necessary to compensate for differences in the coupling gap. The amount of variation decreases as the bandwidth is reduced and, except perhaps for the first and last section, the variation is negligible in the case of bandwidths less than a few per cent.

One further important step in the filter design is to alter the length of the resonators to compensate for fringing capacitance at their ends. This may be done

TABLE II

PROTOTYPE LOW-PASS FILTER AND ITS DESIGN EQUATIONS FOR MAXIMALLY-FLAT AND TCHEBYCHEFF RESPONSE

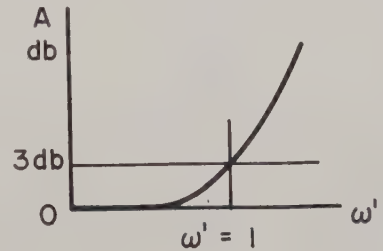


Maximally-Flat Response

$$r = 1 \text{ for all } n$$

$$g_k = 2 \sin \left[\frac{(2k-1)\pi}{2n} \right], \quad k = 1, 2, \dots, n$$

$$A = 10 \log_{10} (1 + \omega'^{2n}) \text{ db}$$



Tchebycheff Response

$$r = 1 \text{ for } n \text{ odd}, \quad r = \tanh^2(\beta/4) \text{ for } n \text{ even}$$

$$g_1 = 2a_1/\gamma$$

$$g_k = \frac{4a_{k-1}a_k}{b_{k-1}g_{k-1}}, \quad k = 2, 3, \dots, n$$

$$\text{check: } g_n = g_1 r$$

$$a_k = \sin \left[\frac{(2k-1)\pi}{2n} \right], \quad k = 1, 2, \dots, n$$

$$b_k = \gamma^2 + \sin^2 \left(\frac{k\pi}{n} \right), \quad k = 1, 2, \dots, n$$

$$\beta = \log_e \left(\coth \frac{A_m}{17.37} \right), \quad A_m \text{ in db}$$

$$\gamma = \sinh \left(\frac{\beta}{2n} \right)$$

$$A = 10 \log_{10} [1 + (10^{A_m/10} - 1) \cos^2 (n \cos^{-1} \omega')] \text{ db}, \quad \omega' \leq 1$$

$$A = 10 \log_{10} [1 + (10^{A_m/10} - 1) \cosh^2 (n \cosh^{-1} \omega')] \text{ db}, \quad \omega' \geq 1$$

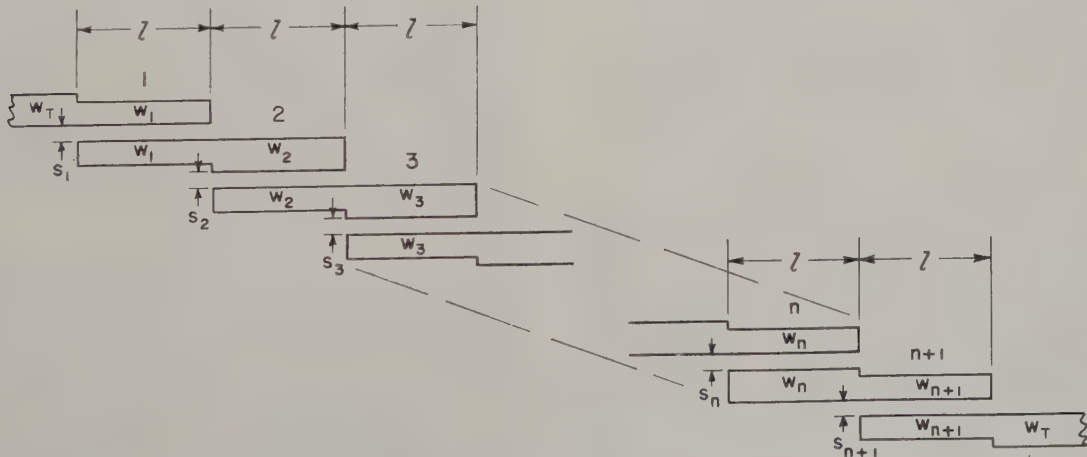
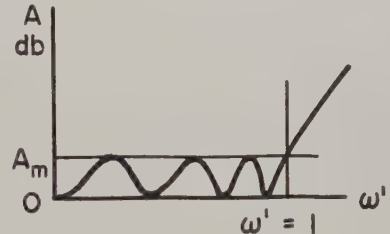


Fig. 2—Basic dimensions of the strip-line parallel-coupled-resonator filter.

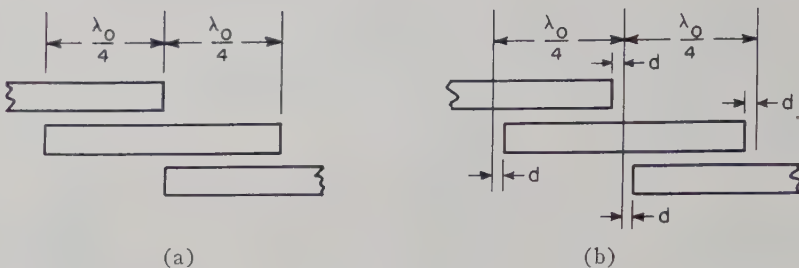


Fig. 3—(a) Strip-resonator design neglecting fringing capacitance at ends. (b) Suggested compensation for fringing capacitance at ends of resonators.

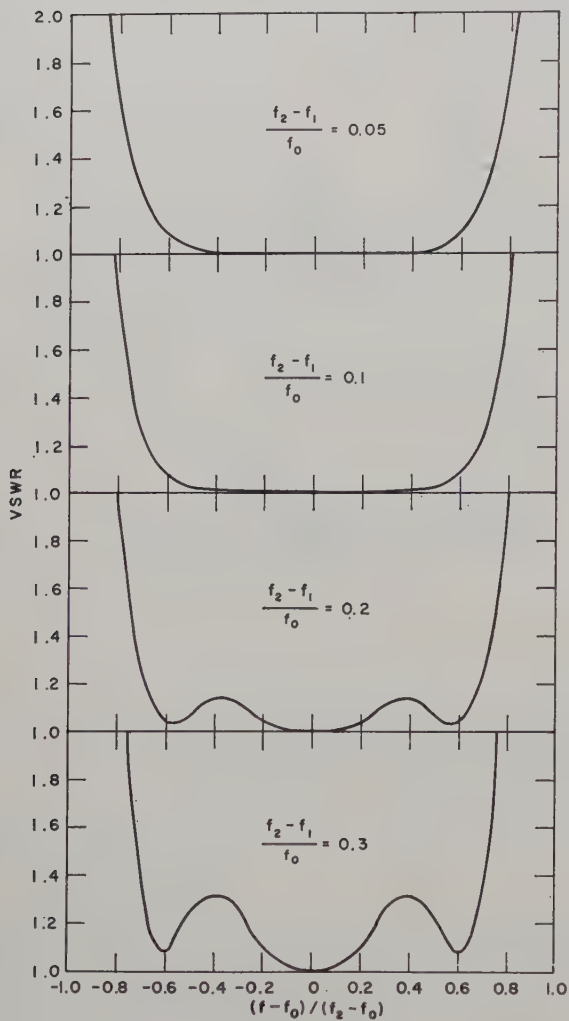


Fig. 4—VSWR curves of six-resonator, parallel-coupled filter designed for maximally-flat response.

as shown in Fig. 3(b), where each end is cut back by the average length, d . The dimension d would be expected to be somewhat less than $(C_f'/\epsilon) \cdot (b/2)$, where C_f'/ϵ is a quantity plotted elsewhere as a function of the strip-thickness-to-plate-spacing ratio, t/b .⁵ Measurements on the experimental filter described below indicate that d should be approximately $0.75 (C_f'/\epsilon) \cdot (b/2)$. For very thin strips, this would be $0.75 (0.220b) = 0.165b$. In wide-

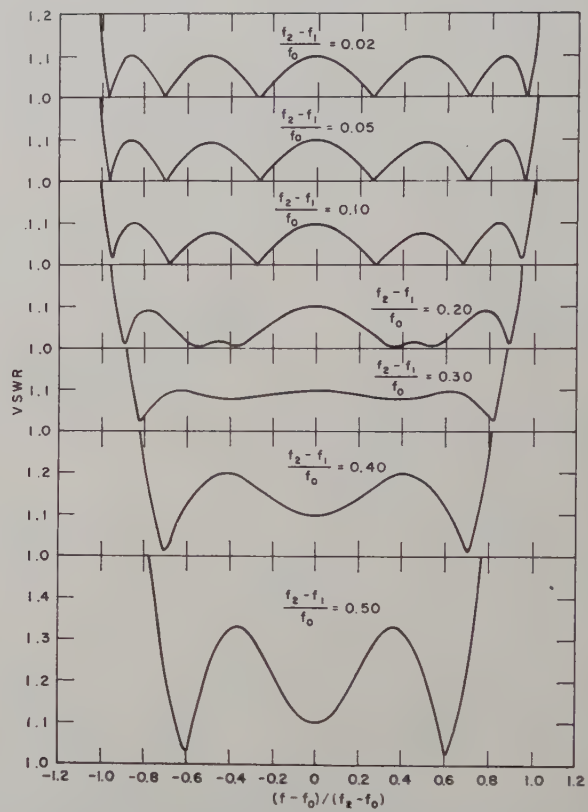


Fig. 5—VSWR curves of six-resonator, parallel-coupled filter designed for equal-ripple response— $VSWR = 1.10$.

bandwidth filters an error in d would be unimportant, while in narrow-bandwidth filters the error would be cancelled by the tuning adjustments that are already needed to overcome the effects of constructional tolerances. This tuning may be done, for example, by means of screws or dielectric slugs in high-electric-field regions of the resonators.

VERIFICATION OF DESIGN ACCURACY

Because of the approximations necessary in the derivation of the design formulas, their accuracy was checked theoretically. This was done by exact computation of the insertion-loss and vswr responses of the actual transmission-line filter networks specified by the formulas for various bandwidths and for either maximally flat or Tchebycheff response. The computations were performed on an electronic computer by a matrix-

⁵ S. B. Cohn, "Problems in strip transmission line," IRE TRANS., Vol. MTT-3, pp. 119-126; March, 1955.

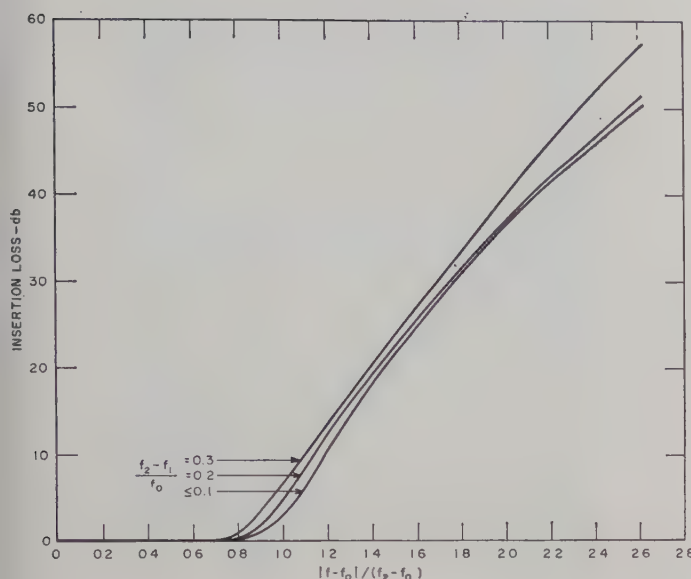


Fig. 6—Insertion-loss curves of six-resonator, parallel-coupled filter designed for maximally-flat response.

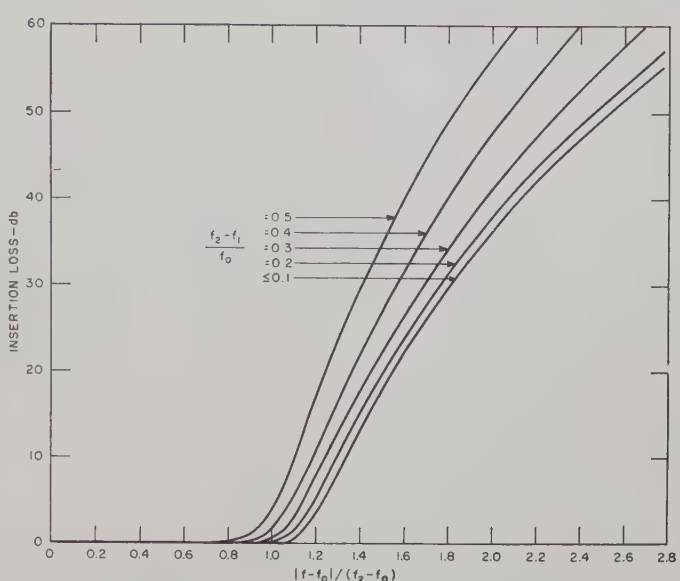


Fig. 7—Insertion-loss curves of six-resonator, parallel-coupled filter designed for equal-ripple response—vswr = 1.10.

multiplication method.⁶ Because the filter is symmetrical, it is sufficient to compute the matrix of half the filter. The insertion loss and vswr then were computed as functions of the elements of this matrix.

The pass band vswr curves for six-resonator maximally flat filters of various bandwidths are shown in Fig. 4. The relative bandwidth is defined as

$$W = \frac{f_2 - f_1}{f_0}, \quad (2)$$

where $f_0 = (f_1 + f_2)/2$, and f_1 and f_2 are the 3-db points of the response curve. The response is seen to be truly maximally flat for relative bandwidths up to 0.1, while at 0.2 the deviation from maximally flat is slight. At 0.3, however, the deviation would be serious in the more critical applications. The corresponding curves are shown in Fig. 5 for six-resonator filters designed to have an equal ripple vswr of 1.10 in the pass band. In this case, f_1 and f_2 are the pass band limits for the equal ripple-level vswr of 1.10. The desired response is obtained very accurately for relative bandwidths up to 0.05, and gradually deteriorates as the bandwidth is increased further. In spite of this deterioration, the pass band vswr limit of 1.10 is not exceeded for relative bandwidths up to 0.3, and even at 0.4 or 0.5 the response is adequate for many applications. But, it is important to note that these conclusions are drawn from specific cases considered, and may vary somewhat with other numbers of resonators or with other equal ripple levels.

The insertion-loss curves for the above cases are plotted against a normalized frequency scale in Fig. 6 and Fig. 7. Because the response is symmetrical with

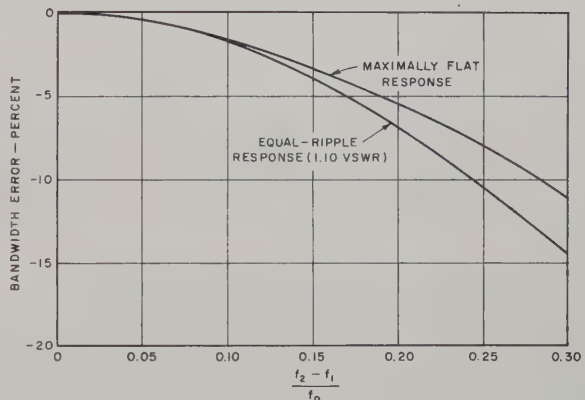


Fig. 8—Bandwidth error vs relative bandwidth for six-resonator parallel-coupled filter. Error is expressed as a percentage of the bandwidth; e.g., at $(f_2 - f_1)/f_0 = 0.10$, corrected bandwidth = 0.098.

frequency, only half of each pass band is shown. In both figures, the insertion loss is virtually identical with that of the prototype function for relative bandwidths up to 0.1, and even for greater bandwidths, the deviation is quite small.

In addition to the errors in response-curve shape that develop as the bandwidth is increased, the predicted bandwidth is slightly in error. In Fig. 8 the bandwidth error in per cent is plotted vs relative bandwidth for the cases considered above. It is seen that the discrepancy does not exceed 2 per cent of the bandwidth for relative bandwidths up to 0.1, and is only about 6 per cent at 0.2. The actual bandwidth of the filter appears to be always less than the value assumed in the design, and therefore, in the case of the wider bandwidths, it would be desirable in calculating the parameters of a given filter to use a somewhat larger bandwidth than actually is required. Fig. 8 may be used as an approximate guide in selecting the bandwidth design value.

⁶ P. I. Richards, "Applications of matrix algebra to filter theory," Proc. IRE, vol. 34, pp. 145P-150P; March, 1946.

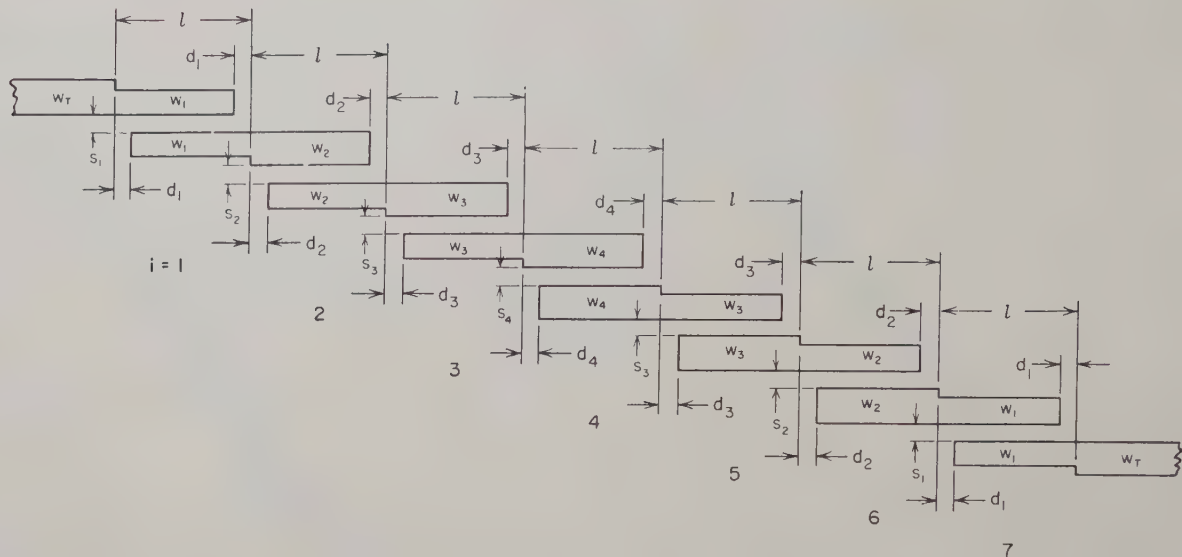


Fig. 9—Layout of parallel-coupled-resonator filter.

TABLE III
DESIGN PARAMETERS FOR EXPERIMENTAL PARALLEL-COUPLED STRIP-LINE-RESONATOR FILTER

i	Z_o	Z_{oei}	Z_{ooi}	w_i	s_i	d_i
	$K_{i-1,i}$					
1	0.449	82.5 ohms	37.6 ohms	0.236 inch	0.021 inch	0.073 inch
2	0.1529	58.8 ohms	43.5 ohms	0.346 inch	0.110 inch	0.084 inch
3	0.1038	55.7 ohms	45.3 ohms	0.360 inch	0.158 inch	0.085 inch
4	0.0976	55.4 ohms	45.6 ohms	0.361 inch	0.163 inch	0.085 inch

DESIGN OF EXPERIMENTAL FILTER

A strip-line parallel-coupled-resonator filter has been constructed and tested in order to demonstrate the feasibility of this type of design. As shown in Fig. 9, the filter has six resonators. The two ground planes were spaced 0.5 inch apart by a polystyrene dielectric. The strips are of copper foil, 0.0017 inch thick. The filter was designed for 10-per cent bandwidth, centered at 1200 mc, and an equal ripple pass band vswr of 1.10. The exact theoretical vswr and the insertion-loss curves of the actual transmission-line filter network, as calculated by an electronic computer, are shown in Fig. 5 and Fig. 7. In each figure the appropriate curve is labeled $(f_2 - f_1)/f_0 = 0.1$. The details of the design procedure and a discussion of the experimental results are given below.

Fig. 9 shows that the filter has seven sections, but because of the symmetry of the filter, it is necessary to compute the parameters of only the first four sections. The first step in the design procedure is to compute the element values g_1, g_2, g_3 , and g_4 of the prototype seven-element, low-pass filter. This is done by means of the formulas for Tchebycheff response in Table II, with $n=7$ and $A_m=0.00986$ db (which corresponds to an input vswr of 1.10). The resulting values are

$$g_1 = 0.77968, \quad g_2 = 1.35921, \quad g_3 = 1.68800, \quad g_4 = 1.53454.$$

Next, the quantity $Z_o/K_{i-1,i}$ and the even- and odd-

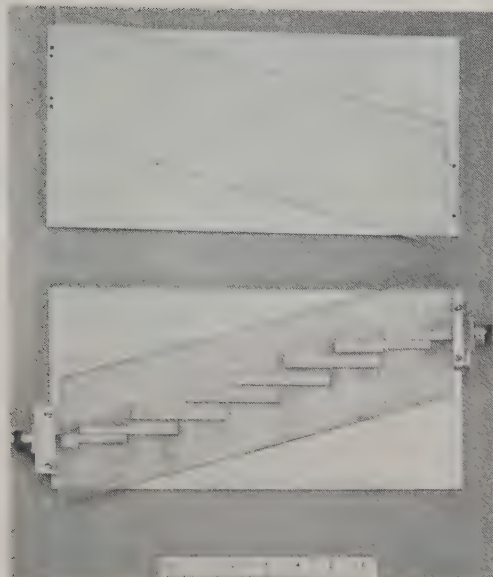
mode characteristic impedances Z_{oei} and Z_{ooi} are computed from the formulas in Table I. In this calculation $(f_2 - f_1)/f_0$ is set equal to 0.1, and Z_o to 50 ohms. Then the strip widths w_i and separations s_i of the various sections are obtained from the nomograms of a previous paper,⁴ with ϵ_r equal to 2.55, b equal to 0.5 inch, and strip thickness assumed to be zero. Finally, the resonators are shortened at their ends by d_i to compensate for fringing capacitance. The various quantities referred to above are contained in Table III.⁷

A further quantity required is the width w_T of the terminating 50-ohm strips. This may be obtained from a graph of characteristic impedance vs strip width.^{5,8} The result is $w_T/b = 0.744$ or $w_T = 0.372$ inch. The section length l is a quarter-wavelength in the dielectric, and hence equals 1.540 inch.

Photographs of the completed filter are shown in Fig. 10. The structure is a sandwich of copper foil separated by a pair of polystyrene plates each machined to have flat surfaces and a thickness of 0.250 inch. Thus, the total ground-plane spacing is one-half inch. The copper foil was cemented to the polystyrene plates with Dow

⁷ The values of d_i in Table III were computed from an approximate formula, and are quite close to the value $0.165b$ mentioned above. Because the formula is rather complex, and its assumptions are as yet unproved, it is not given here.

⁸ S. B. Cohn, "Characteristic impedance of the shielded-strip transmission line," IRE TRANS., vol. MTT-2, pp. 52-57; July, 1954.



(a)



(b)

Fig. 10—Photographic views of parallel-coupled resonator filter:
(a) with upper plate removed; (b) completely assembled.

Corning XC-271 adhesive, which was applied to the copper and air dried for 45 minutes before pressing the foil onto the polystyrene. The strip circuit then was cut on one surface with a sharp knife and the unwanted foil peeled off.

DATA FOR EXPERIMENTAL FILTER

A preliminary model of the parallel-coupled resonator filter was tested first with the resonator ends uncompensated; *i.e.*, with $d_i = 0$. The center frequency was lower than the design value by 4.4 per cent. Then, the open-circuited strip ends all were cut back uniformly a distance $d = 0.220b$, the value of $(C_f'/\epsilon)/(b/2)$ for very thin strips, and the center frequency was higher than the design value by 1.7 per cent. Finally, the filter was reconstructed with the values of d_i given in Table III. The center frequency of this model is 1207 mc, rather than the design value of 1200 mc—an error of only 0.6 per cent. In the three cases the bandwidth and response curves are quite similar. Although the best pass band response was obtained with the last case, it may have been due to more accurate construction.

Fig. 11 shows a comparison between the measured

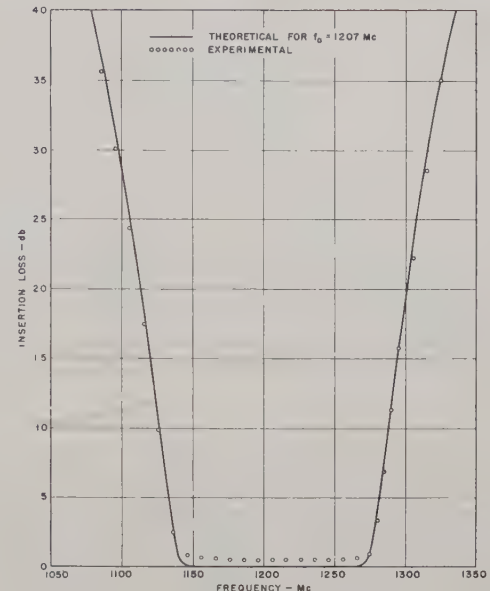


Fig. 11—Insertion loss of parallel-coupled-resonator filter.

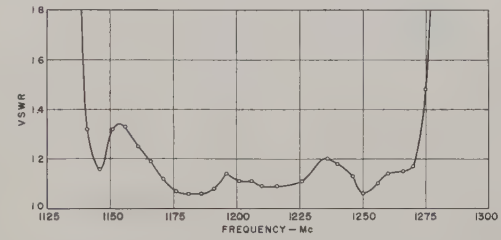


Fig. 12—Measured vswr of parallel-coupled-resonator filter.

insertion loss of the filter and the exact theoretical curve for the transmission-line network computed for a center frequency of 1207 mc and neglecting dissipation. Above 2 db, the agreement is excellent. The bandwidth error is seen to be only about 1.0 per cent of the bandwidth. In the pass band, however, disagreement is inevitable because of the finite Q of the strip-line resonators. Nevertheless, the measured pass band insertion loss is quite uniform at 0.5 to 0.7 db.

The input vswr of the filter measured with a 50-ohm termination on the output is shown in Fig. 12. Although the vswr exceeds the theoretical ripple level of 1.10, it would be quite acceptable for most applications. The highest vswr peak in the pass band occurs near the low frequency end, where it reaches a value of 1.33, while the vswr elsewhere in the pass band is under 1.20. It is believed that the vswr could be made to conform more closely to theory if tuning adjustments were provided for the resonators. These adjustments also could serve to set the center frequency of the filter exactly on the desired value.

DERIVATION OF DESIGN FORMULAS

The analysis of the parallel-coupled-resonator filter is based upon the characteristics of the individual section of Fig. 13(a). The image impedance Z_I and image phase shift β of this section are given in a paper by Jones and

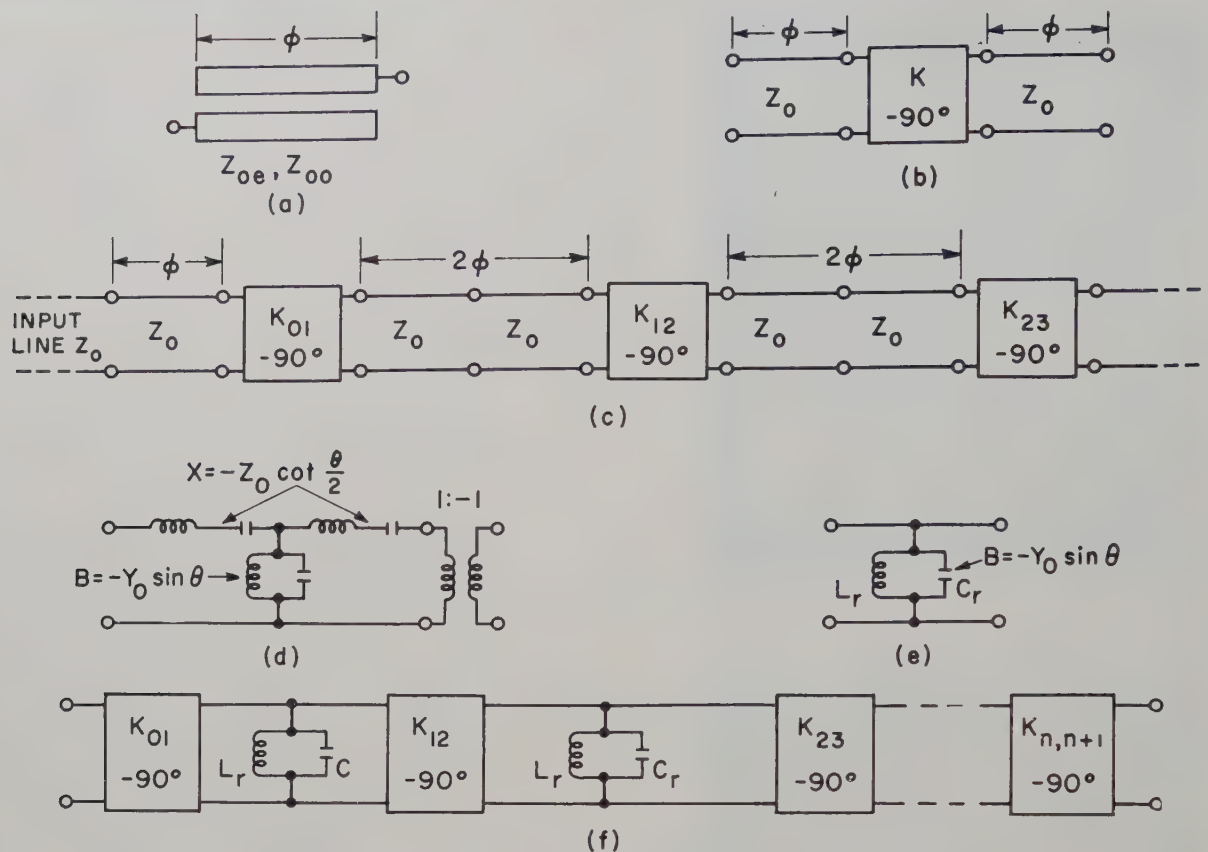


Fig. 13—Development of equivalent circuit of the parallel-coupled-resonator filter.

Bolljahn⁹ as follows

$$Z_I = \frac{[(Z_{oe} - Z_{oo})^2 - (Z_{oe} + Z_{oo})^2 \cos^2 \phi]^{1/2}}{2 \sin \phi} \quad (3)$$

$$\cos \beta = \left(\frac{Z_{oe} + Z_{oo}}{Z_{oe} - Z_{oo}} \right) \cos \phi, \quad (4)$$

where ϕ is the electrical length of the coupled transmission lines and Z_{oe} and Z_{oo} are the characteristic impedances of each conductor with respect to ground for the even and odd modes, respectively.

It is now shown that the filter section of Fig. 13(b) is approximately equivalent to that of Fig. 13(a). The box represents an ideal impedance inverter having a constant image impedance, K , and a phase shift of -90° at all frequencies. The image impedance, Z_I , and image phase shift, β , of the section will be derived by means of the $ABCD$ matrix parameters.^{5,10}

The $ABCD$ matrix of a transmission line of length ϕ and characteristic impedance Z_o is

$$\begin{bmatrix} \cos \phi & jZ_o \sin \phi \\ j \sin \phi & \cos \phi \end{bmatrix}.$$

⁹ E. M. T. Jones and J. T. Bolljahn, "Coupled-strip-transmission-line filters and directional couplers," IRE TRANS., vol. MTT-4, pp. 75-81; April, 1956.

¹⁰ Radio Research Laboratory Staff, "Very High Frequency Techniques," McGraw-Hill Book Co., Inc., New York, N. Y., vol. 2, ch. 26; 1947.

The matrix of the ideal inverter is obtained from this by substituting $\phi = -90^\circ$ and $Z_o = K$, as follows

$$\begin{bmatrix} 0 & -jK \\ -j & 0 \end{bmatrix}.$$

Therefore, the $ABCD$ matrix of the complete filter section of Fig. 13(b) is

$$\begin{aligned} \begin{bmatrix} A & B \\ C & D \end{bmatrix} &= \begin{bmatrix} \cos \phi & jZ_o \sin \phi \\ j \sin \phi & \cos \phi \end{bmatrix} \times \begin{bmatrix} 0 & -jK \\ -j & 0 \end{bmatrix} \\ &\times \begin{bmatrix} \cos \phi & jZ_o \sin \phi \\ j \sin \phi & \cos \phi \end{bmatrix} \\ &= \begin{bmatrix} \left(\frac{K}{Z_o} + \frac{Z_o}{K} \right) \sin \phi \cos \phi & j \left(\frac{Z_o^2}{K} \sin^2 \phi - K \cos^2 \phi \right) \\ j \left(\frac{K}{Z_o^2} \sin^2 \phi - \frac{\cos^2 \phi}{K} \right) & \left(\frac{K}{Z_o} + \frac{Z_o}{K} \right) \sin \phi \cos \phi \end{bmatrix}. \end{aligned}$$

The image parameters are related to the matrix elements by $Z_I = \sqrt{B/C}$ and $\cos \beta = A$, and, hence,

$$Z_I = Z_o \left[\frac{\frac{Z_o}{K} \sin^2 \phi - \frac{K}{Z_o} \cos^2 \phi}{\frac{K}{Z_o} \sin^2 \phi - \frac{Z_o}{K} \cos^2 \phi} \right]^{1/2} = Z_o \left[\frac{\frac{Z_o}{K} - \left(\frac{K}{Z_o} + \frac{Z_o}{K} \right) \cos^2 \phi}{\left(\frac{K}{Z_o} + \frac{Z_o}{K} \right) \sin^2 \phi - \frac{Z_o}{K}} \right]^{1/2}$$

$$= \frac{1}{2 \sin \phi} \left[\frac{\frac{4Z_o^3}{K}}{\frac{K}{Z_o} + \frac{Z_o}{K} - \frac{Z_o}{K \sin^2 \phi}} - \frac{\frac{4Z_o^2 \left(\frac{K}{Z_o} + \frac{Z_o}{K} \right) \cos^2 \phi}{K}}{\frac{K}{Z_o} + \frac{Z_o}{K} - \frac{Z_o}{K \sin^2 \phi}} \right]^{1/2} \quad (5)$$

$$\cos \beta = \left(\frac{K}{Z_o} + \frac{Z_o}{K} \right) \sin \phi \cos \phi. \quad (6)$$

A comparison between (3) and (5), and between (4) and (6), shows that the sections of Fig. 13(a) and 13(b) would be electrically equivalent if the following conditions were met,

$$\left(\frac{K}{Z_o} + \frac{Z_o}{K} \right) \sin \phi = \frac{Z_{oe} + Z_{oo}}{Z_{oe} - Z_{oo}} \quad (7)$$

$$\frac{\frac{4Z_o^3}{K}}{\frac{K}{Z_o} + \frac{Z_o}{K} - \frac{Z_o}{K \sin^2 \phi}} = (Z_{oe} - Z_{oo})^2 \quad (8)$$

$$\frac{\frac{4Z_o^2 \left(\frac{K}{Z_o} + \frac{Z_o}{K} \right)}{K}}{\frac{K}{Z_o} + \frac{Z_o}{K} - \frac{Z_o}{K \sin^2 \phi}} = (Z_{oe} + Z_{oo})^2. \quad (9)$$

The presence of $\sin \phi$ in the left side of each of the above makes a frequency-independent equality impossible. However, $\sin \phi$ is stationary in the vicinity of $\phi = 90^\circ$, and hence may be replaced by unity with negligible error over a moderate bandwidth. Thus,

$$\frac{K}{Z_o} + \frac{Z_o}{K} = \frac{Z_{oe} + Z_{oo}}{Z_{oe} - Z_{oo}} \quad (10)$$

$$\frac{2Z_o^2}{K} = Z_{oe} - Z_{oo} \quad (11)$$

$$\frac{4Z_o^3 \left(\frac{K}{Z_o} + \frac{Z_o}{K} \right)}{K} = (Z_{oe} + Z_{oo})^2. \quad (12)$$

From these equations, formulas for Z_{oe}/Z_o and Z_{oo}/Z_o as functions of Z_o/K may be found. Only two of the three equations are needed for this purpose, and since the three do not form a consistent set, a judicious choice must be made among them. Examination of (3) to (6) indicates that the third relation is the least important of the three. Therefore, (10) and (11) are solved simultaneously to yield

$$\frac{Z_{oe}}{Z_o} = 1 + \frac{Z_o}{K} + \frac{Z_o^2}{K^2} \quad (13)$$

$$\frac{Z_{oo}}{Z_o} = 1 - \frac{Z_o}{K} + \frac{Z_o^2}{K^2}. \quad (14)$$

It may now be noted that, for narrow bandwidth, $Z_o/K \ll 1$ and, therefore, (12) is satisfied approximately by (13) and (14). Thus the effect of the approximations involved in relating the sections of Fig. 13(a) and 13(b) is negligible for narrow bandwidth, but increases in importance as the bandwidth is increased.

When the individual sections of the filter are assembled, it is seen that the original parallel-coupled-resonator filter of Fig. 1(b) or 1(c) is approximately equivalent to the circuit of Fig. 13(c), in which transmission lines approximately $\lambda_o/2$ long are separated by inverters. A lumped-constant equivalent of a line of length θ is shown in Fig. 13(d). This exact equivalent circuit is particularly convenient for θ near 180° . In Fig. 13(e) the equivalent circuit has been simplified by omitting the phase-reversing transformer which has no effect on the insertion-loss response. Also, the series reactances of Fig. 13(f) are small near $\theta = 180^\circ$ and are negligible in comparison with the high characteristic impedances of the inverting elements. Thus, the circuit of Fig. 13(f) is approximately equivalent to that of Fig. 13(c), and hence to the original parallel-coupled-resonator filter.

The analysis will be shortened at this point by comparing the filter circuit of Fig. 13(f) with that shown in Fig. 11(c) of a previous paper.³ They are seen to be the same, except that the former contains parallel-resonant arms while the latter contains series-resonant arms. Hence, the circuits are duals, and the formulas obtained for the latter may be used in the present analysis if K is replaced by $1/K$, Z_o by $1/Z_o$, and if L and C are interchanged. Thus,

$$\frac{Z_o}{K_{i,i+1}} = \frac{\pi W}{2\omega_1' \sqrt{g_i g_{i+1}}}, \quad i = 1 \text{ to } n-1, \quad (15)$$

where W is the relative bandwidth defined by (2). For the first and last section of the filter,

$$\frac{Z_o}{K_{01}} = \sqrt{\frac{\pi W}{2\omega_1' g_1}}, \quad \frac{Z_o}{K_{n,n+1}} = \sqrt{\frac{\pi W r}{2\omega_1' g_n}}. \quad (16)$$

The formulas in Table I follow directly from (13) through (16).

A New Class of Broad-Band Microwave 90-Degree Phase Shifters*

B. M. SCHIFFMAN†

Summary—In the type of circuits considered here, the input power is divided equally between two channels whose outputs are caused to have a very nearly 90° phase difference over a broad frequency range. Networks suitable for application at low frequencies which perform the above function have been widely investigated.¹⁻⁹ This report describes a new type of 90° differential phase shifter which has a constant resistance input, and which is useful over bandwidths as large as 5:1 in the microwave region.

THEORY

Basic Phase-Shifting Element

THE circuits to be described employ sections of coupled-strip transmission lines operating in the TEM mode as key elements. One such coupled-strip transmission-line phase-shift element is shown in Fig. 1. Two parallel-coupled lines of equal length are connected at one end; ideally this connection should be of zero length. The unconnected ends serve as the input and output of a two-terminal-pair network. The frequency behavior of a coupled-line network connected in this manner, and also that of other related coupled-line circuits, has been derived by Jones and Bolljahn.¹⁰

The equations for the image impedance Z_I , and phase constant, ϕ , of coupled lines connected as shown in Fig. 1 are, in terms of the even- and odd-mode characteristic impedances of the lines and their length,

$$Z_I = \sqrt{Z_{0e}Z_{0o}}, \quad (1)$$

and

$$\cos \phi = \frac{\frac{Z_{0e}}{Z_{0o}} - \tan^2 \theta}{\frac{Z_{0e}}{Z_{0o}} + \tan^2 \theta}, \quad (2)$$

† Manuscript received by the PGMTT, November 4, 1957. This work was sponsored by the Air Force Cambridge Res. Ctr., Air Res. Dev. Command, Laurence G. Hanscom Field, Bedford, Mass., under Contract AF 19(604)-1571, and was first described in Sci. Rep. 2 for that contract.

† Stanford Research Institute, Menlo Park, Calif.

¹ R. V. L. Hartley, U. S. Patent No. 1,666,206; April 17, 1928.

² B. Lenehan, "A new single-sideband carrier system for power lines," *Elec. Eng.*, vol. 66, pp. 549-592; June, 1947.

³ R. B. Dome, "Wideband phase shift networks," *Electronics*, vol. 19, pp. 112-115; December, 1946.

⁴ Sidney Darlington, "Realization of a constant phase difference," *Bell Syst. Tech. J.*, vol. 29, pp. 94-104; January, 1950.

⁵ H. J. Orchard, "Synthesis of wide-band two-phase networks," *Wireless Eng.*, vol. 27, pp. 72-81; March, 1950.

⁶ Oswald G. Villard, Jr., "Cascade Connection of 90-degree phase-shift network," *PROC. IRE*, vol. 40, pp. 334-337; March, 1952.

⁷ Donald K. Weaver, Jr., "Design of wide-band 90-degree phase-difference network," *PROC. IRE*, vol. 42, pp. 671-676; April, 1954.

⁸ D. G. C. Luck, "Properties of some wide-band phase-splitting networks," *PROC. IRE*, vol. 37, pp. 147-151; April, 1949.

⁹ Harry Sohon, "Wide-band phase-delay circuit," *PROC. IRE*, vol. 41, pp. 1050-1052; August, 1953.

¹⁰ E. M. T. Jones and J. T. Bolljahn, "Coupled-strip-transmission-line filters and directional couplers," *IRE TRANS.*, vol. MTT-4, pp. 75-81; April, 1956.

where

Z_{0e} is the characteristic impedance of one line to ground when equal in-phase currents flow in both lines,

Z_{0o} is the characteristic impedance of one line to ground when equal out-of-phase currents flow in both lines.

$\theta = \beta l$ is the electrical length of a uniform line of length l and phase constant β .

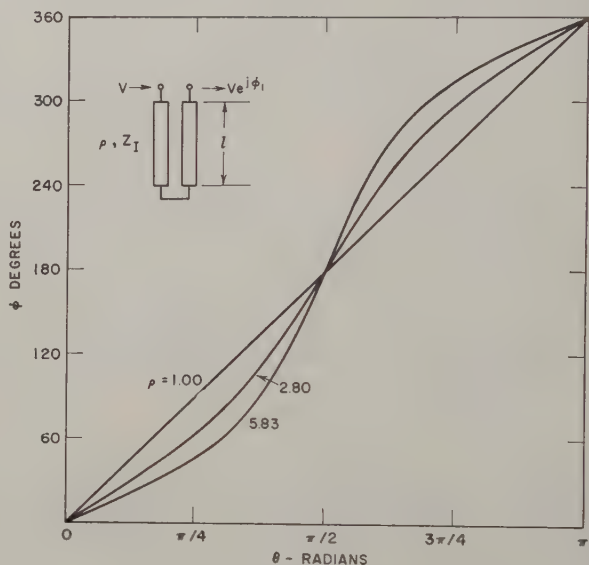


Fig. 1—Coupled-transmission-line element with ends connected and curves of its phase response for three values of ρ .

From (1) Z_I is seen to be a constant independent of frequency. The phase-shift function, ϕ , of such a coupled-line element is plotted against θ , the frequency variable, in Fig. 1 for three values of ρ , where ρ is defined as $\rho = Z_{0e}/Z_{0o}$. Such a network element possesses a sufficient number of independent design parameters to permit its use in a variety of phase-shift networks. This can be demonstrated as follows.

From the orthogonality relations that define them,¹¹ it is seen that Z_{0e} and Z_{0o} are independent quantities. Hence, the product $(Z_{0e}Z_{0o})$ and the ratio $\rho = Z_{0e}/Z_{0o}$ can be independently specified. It then follows, using (1) and (2), that the image impedance of the coupled-line network can be chosen independently of its image phase constant, ϕ . Therefore, provided that ϕ can be properly specified by suitable choices of ρ and line length l , and that a power divider can be designed that

¹¹ S. B. Cohn, "Shielded coupled-strip transmission line," *IRE TRANS.*, vol. MTT-3, pp. 29-38; October, 1955.

is matched at all frequencies, it follows that a network with a desirable differential-phase response can be obtained by connecting in parallel a coupled-line network and a suitable length of uniform transmission line. Such a network is described below.

Type-A Network

The most elementary form of such a network, termed a Type-A network, is shown schematically in Fig. 2, together with a plot of phase shifts, ϕ_1 through the coupled portion, and ϕ_2 through the uniform portion. The characteristic impedance of the length of uniform line is $Z_0 = Z_I$, and the outputs of both branches are assumed to be matched. The input impedance of the network is $Z_I/2$, a constant independent of frequency.

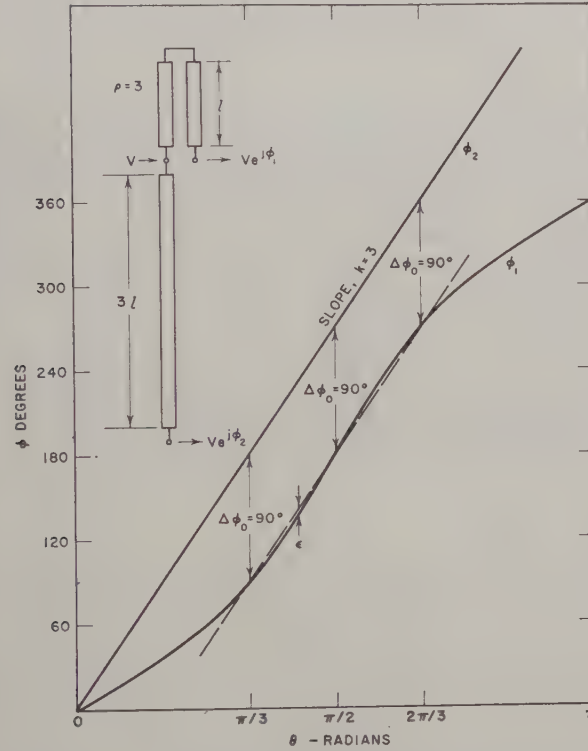


Fig. 2—A Type-A network and curves of phase response for each of its two branches.

The phase shift through the uniform transmission line, ϕ_2 , is represented by the straight line of slope k through the origin, where k is the ratio of the length of the uniform line to that of the coupled lines. Inspection of (2) for phase shift through the coupled-line portion indicates that ϕ_1 has odd symmetry about $\theta = n\pi/2$. Thus a dashed line, also of slope k , drawn through the point $(\theta = \pi/2, \phi = \pi)$ as shown in Fig. 2, intersects the ϕ_1 curve in two other points equal distances from $\theta = \pi/2$. It now can be seen that the output phase difference, $\Delta\phi = \phi_2 - \phi_1$, can be made equal to 90° for three desired values of θ by means of (2). For the case illustrated in Fig. 2, $k = 3$, $\rho = 3.00$, and $\Delta\phi = 90^\circ$ at $\theta = \pi/3, \pi/2$, and $2\pi/3$. The output phase difference at these three values of θ will be called $\Delta\phi_0$. At other points in the interval $\pi/3 < \theta < 2\pi/3$ and for a small distance outside this in-

terval, the phase difference, $\Delta\phi$ will vary from $\Delta\phi_0$ by some small amount which is the phase error. A graph of the theoretical differential phase shift through the Type-A network of Fig. 2 is shown in Fig. 3. The differential phase shift is $90 \pm 4.8^\circ$ over a 2.34:1 bandwidth, as shown. Other values of ρ yield different values of maximum phase errors and bandwidths for the Type-A network. For example, $\rho = 2.7$ yields a differential phase shift of $90 \pm 2.5^\circ$ over a 1.95:1 bandwidth.

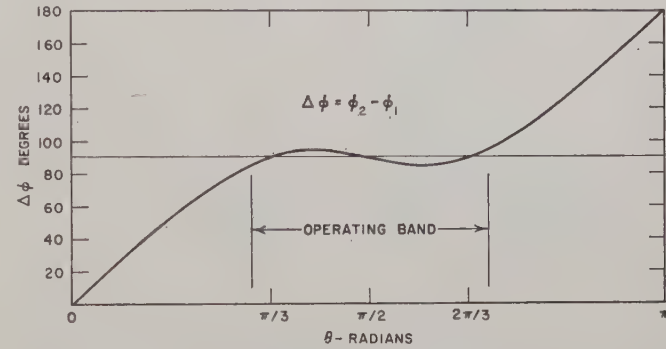


Fig. 3—Differential phase response of the Type-A network shown in Fig. 2.

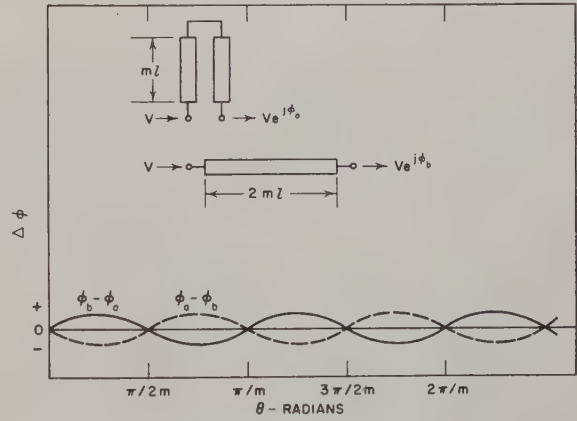


Fig. 4—Error-correcting network and its two possible differential phase responses.

Phase-Error-Correcting Network

It is possible to reduce the maximum phase error of a Type-A differential-phase-shift network by connecting another differential-phase-shift network in tandem. This second network is so designed that $\Delta\phi_0 = 0$ and its $\Delta\phi$ vs θ curve is approximately the negative of the error curve of the Type-A network in the band of interest. Such a network is shown in Fig. 4. It consists of two entirely separate parts, a section of uniform transmission line of length $2ml$ and a coupled-line section of length ml . It is possible, therefore, to connect the error-correcting network to the Type-A network in two ways. Consequently, the former has two $\Delta\phi$ vs θ curves which are the negatives of each other, as shown in Fig. 4. In a given case the parameters m and ρ of the error-correcting network, and the method of connecting the latter to the Type-A network must be chosen so that the net phase error in a given bandwidth is minimized.

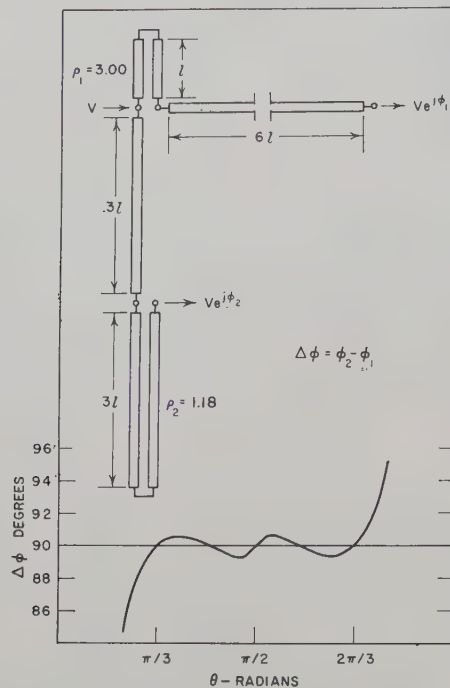


Fig. 5—A Type-B network and its differential phase response.

Type-B Network

A differential phase shifter that was designed as outlined above is shown in Fig. 5. In this case, m is set equal to 3. (A nonintegral value of m would destroy symmetry and almost certainly reduce the bandwidth of a given network configuration.) Thus, the error-correcting network differential-phase response is zero at $\theta = \pi/3$, $\pi/2$, and $2\pi/3$; and the resulting combination called a Type-B network is suitable for an approximately 2:1 bandwidth. Equal-ripple response may then be obtained in the band of interest with two additional points of zero phase error by properly choosing ρ_1 and ρ_2 . The subscript 1 applies to the differential-phase-shifting coupled-line portion and the subscript 2 applies to the error-correcting coupled-line portion. Here again it is possible to choose various combinations of these parameters to obtain slightly different bandwidths and maximum phase errors. A natural choice is to have zero phase error at $\theta = \pi/3$ and at $\theta = 2\pi/3$ as in the Type-A network. Since the error-correcting curve goes through zero at $\theta = \pi/3$ and at $\theta = 2\pi/3$, $\Delta\phi_0$ of the differential-phase-shifting element is made equal to 90° at these points. Therefore, $\rho_1 = 3.00$ as in the Type-A network described in the preceding section. By choosing a point midway between bandedge and bandcenter for complete error cancellation, ρ_2 is found to be 1.18 by trial and error, and an almost equal-ripple response is obtained. The maximum phase error is thus 0.7° over a 2.13:1 bandwidth. The theoretical differential-phase response of this Type-B network is plotted in Fig. 5.

By shifting the points of zero phase error from $\theta = \pi/3$ and $\theta = 2\pi/3$ and allowing a maximum phase error of 1.2° , the bandwidth can be extended to 2.32:1. For such

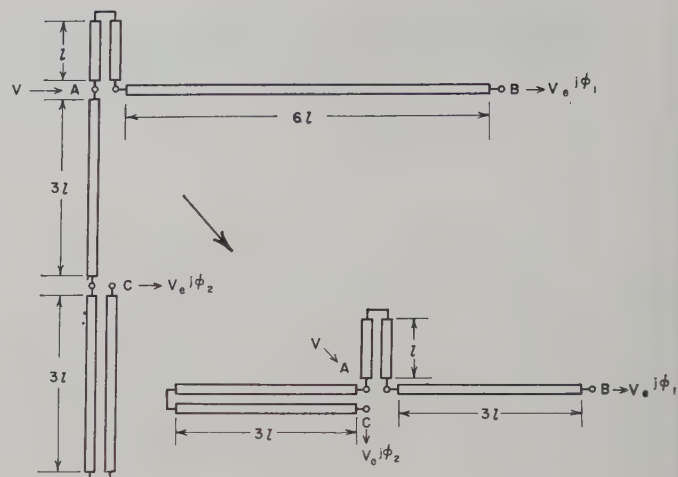


Fig. 6—Type-B network before and after removing equal lengths of uniform transmission line.

a network, $\rho_1 = 4.10$, and $\rho_2 = 1.24$. Still greater bandwidths with resulting larger phase errors are possible with this type of network. Conversely, the maximum phase error can be reduced well below the 0.7° maximum of the first example, if a reduced bandwidth is acceptable, although such configurations have not been investigated.

Composite networks as described above often can be made more compact by removing equal lengths of uniform transmission line from each branch, without affecting the differential-phase response. Such a reduction in size is illustrated in Fig. 6, for the Type-B network.

Type-C Network

By reversing the connection of the error-correcting network, a third type, the Type-C network, is obtained. In this case, putting $m = 2$ secures error cancellation over a broader frequency band than does the Type-B network and preserves the symmetry of the response. For the error-correcting network, $\Delta\phi_0 = 0$ at $\theta = \pi/4$ and at $\theta = 3\pi/4$. By arbitrarily setting $\Delta\phi_0 = 90^\circ$ for the differential-phase-shift network at $\theta = \pi/4$ and at $3\pi/4$, we find by means of (2) that $\rho_1 = 5.83$. Three values of ρ_2 were tried to minimize the phase error over as broad a band as possible. A value of $\rho_2 = 2.35$ yielded a 90° differential phase shifter with a $\pm 5^\circ$ error over a 5:1 band. Such a Type-C network and its theoretical $\Delta\phi$ vs θ curve are shown in Fig. 7. Further improvement in the theoretical performance of this type of network may be obtained by changing the value of ρ_1 a small amount and then optimizing the value of ρ_2 .

Type-D and Type-E Networks

Other configurations of differential-phase-shift networks employing coupled lines have been investigated. Type D and its derived Type E are shown in Fig. 8. In these types, the band center is at $\theta = \pi$, instead of at $\theta = \pi/2$ as in Types A, B, and C. A Type-E network having $\rho_1 = 3.0$ and $\rho_2 = 1.37$ yields a maximum phase error

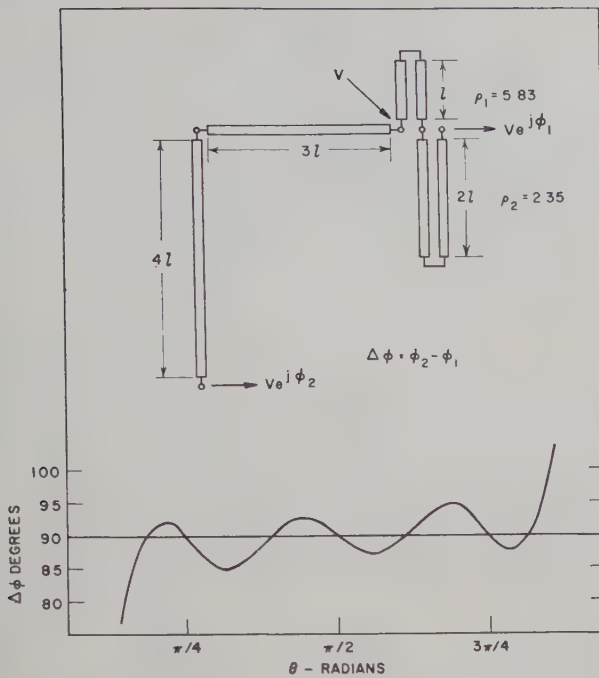


Fig. 7—A Type-C network and its differential phase response.

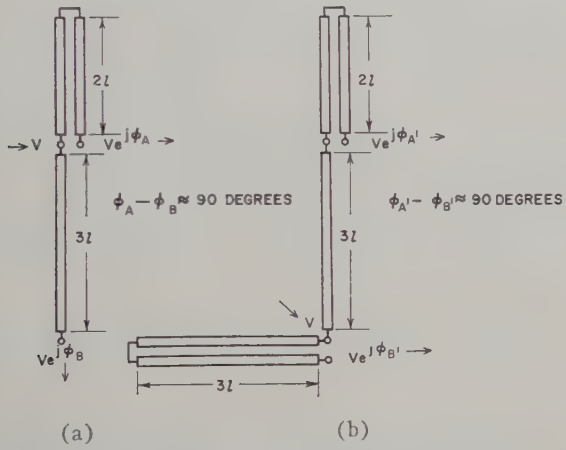


Fig. 8—(a) Type-D network. (b) Type-E network.

of the order of 2° for a 2:1 band. Since this performance is poorer than that of the Type-B network which is its counterpart, Types D and E will not be discussed further.

Type-F Network

A more complex phase-shifting element is illustrated in Fig. 9. It consists of a coupled-line section with two degrees of coupling along different portions of its length. If the even- and odd-mode characteristic impedances are so chosen that

$$\frac{Z_{0e1}}{Z_{0e2}} = \frac{Z_{0o2}}{Z_{0o1}}, \quad (3)$$

the image impedance is

$$Z_I = \sqrt{Z_{0e1}Z_{0o1}} = \sqrt{Z_{0e2}Z_{0o2}},$$

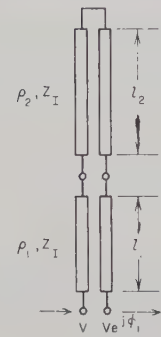


Fig. 9—A more complex type of phase-shifting element.

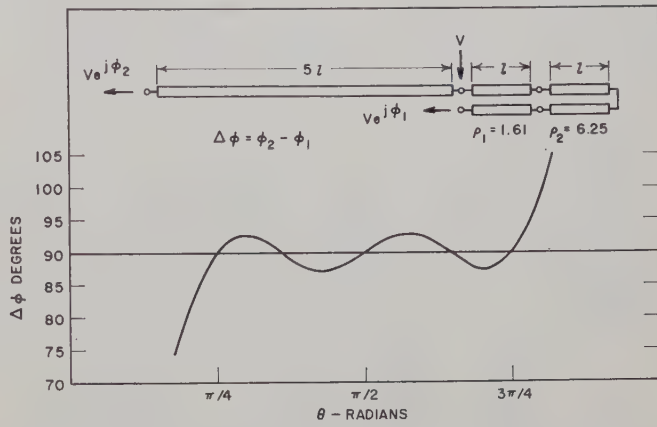


Fig. 10—A Type-F network and its differential phase response.

and the phase shift, ϕ , is

$$\phi_1 = \cos^{-1} \frac{\rho_1 - \tan^2 \left(\tan^{-1} \left[\frac{Z_{0o2}}{Z_{0e1}} \tan \theta_2 \right] + \theta_1 \right)}{\rho_1 + \tan^2 \left(\tan^{-1} \left[\frac{Z_{0o2}}{Z_{0e1}} \tan \theta_2 \right] + \theta_1 \right)}. \quad (4)$$

Here the subscripts 1 and 2 refer to the two sections of the coupled transmission line as shown in Fig. 9. A differential phase shifter employing this element, designated Type F, is shown in Fig. 10. The length of the uniform transmission line is $5l$. The two portions of the coupled lines with different degrees of coupling are each of length l . This equality of lengths is necessary in order to obtain a differential-phase response that is symmetrical about the center frequency. Such a symmetrical output is desired because it is reasonable to expect that the useful bandwidth of the network is thereby maximized. A consequence of making the two coupled portions of equal length, however, is that $\Delta\phi_0 = 90^\circ$ at $\theta = \pi/4$ and at $\theta = 3\pi/4$. This network is suitable for bandwidths of about 3:1, for this reason.

Three sets of values of the parameters ρ_1 and ρ_2 for the two coupled portions have been tried. The values $\rho_1 = 1.612$ and $\rho_2 = 6.25$ yield a 3.24:1 bandwidth with a phase error of $\pm 2.8^\circ$ as shown in Fig. 10.

Comparison of the Various Networks

A summary of the differential-phase-shift network types and their approximate characteristics is given below in Table I.

EXPERIMENTAL MODEL

Design

A Type-C network was constructed in strip-line for the 300-1500 mc band, to test the foregoing theory. The layout of the circuit is shown in Fig. 11. The characteristic impedance of each branch is 50 ohms; the input impedance at the *T* junction is 25 ohms, therefore, but no attempt was made to match the input since the differential phase shift is not affected by such a mismatch provided the tee is symmetrical. Symmetry was maintained to the extent that this was possible in the re-

TABLE I
NETWORK TYPES AND THEIR CHARACTERISTICS

Type	Ratio-Upper to Lower Frequency	Maximum Theoretical Phase Error	Remarks
A	2.0	$\pm 2.8^\circ$	Simplest and most compact design (Fig. 2)
B	2.0-2.5	$\pm 0.7^\circ$ - 2.0°	(Fig. 5 and Fig. 6)
C	5.0	± 5.0	Bulky, most sensitive to mechanical tolerances (Fig. 7)
D, E	—	Excessive	Not recommended (Fig. 8)
F	3.2	$\pm 2.8^\circ$	Simpler and more compact than Types B and C (Fig. 10)

Note: the above values of bandwidth and phase error are typical of each type of network and are not necessarily optimum.

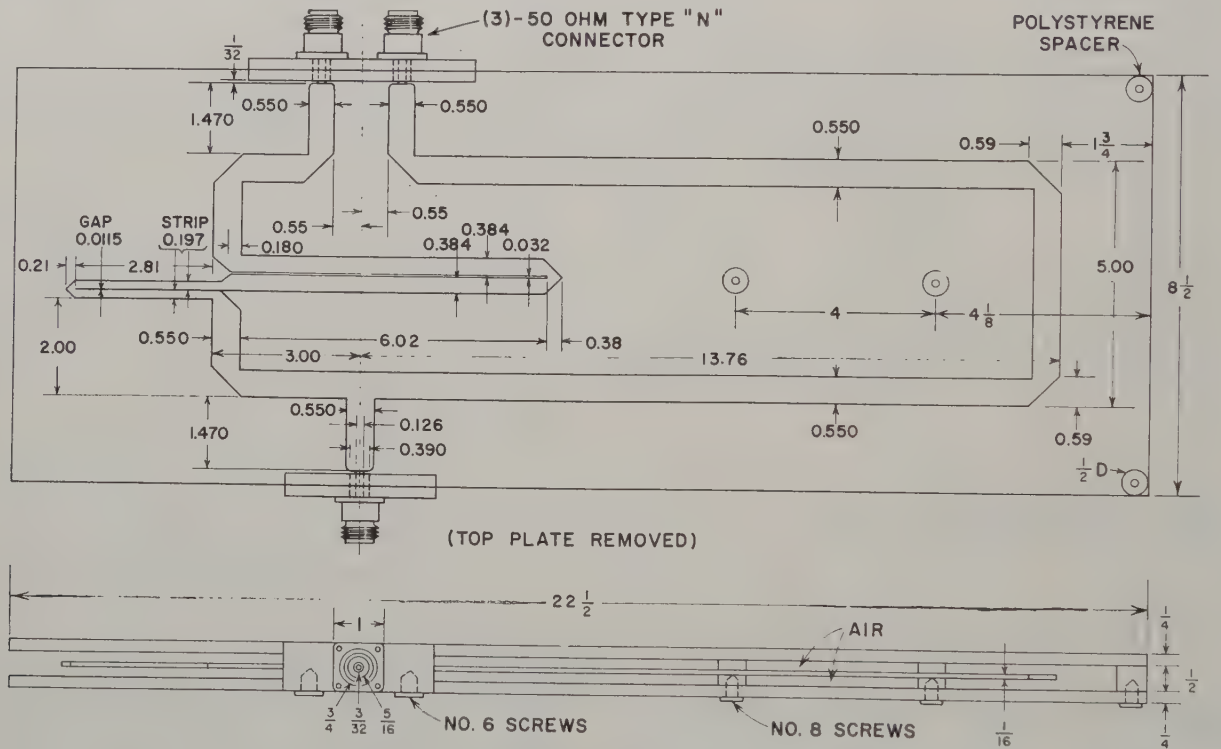


Fig. 11—Experimental Type-C phase shifter for the 300-1500-mc band. Note: dimensions in inches; all corner bevels 45° .

mainder of the network.

The ground-plane spacing was chosen as one-half inch and the thickness of the center conductor as $1/16$ inch. The dielectric is air, except for some polyfoam strips supporting the center conductor. Four polystyrene cylinders and the two connector blocks separate the ground planes. The width of the center strip of the 50-ohm characteristic-impedance portion is obtained from design curves for strip transmission lines¹² and the widths and spacings of the coupled-strip portions of the net-

work are obtained from coupled-strip transmission-line design formulas¹¹ developed at Stanford Research Institute by S. B. Cohn.

The three right angle transmission-line bends in each branch were mitered in a manner known to reduce reflections to a very low value. The junctions between the transmission line and phase shifting coupled-line elements were similarly mitered, as were the short lengths of line which connect each pair of coupled lines.

In calculating the required lengths of uniform transmission line and coupled lines the following simplifying assumptions were made: 1) the uniform line and the right-angle bends in each branch behave as uniform lines

¹² S. B. Cohn, "Characteristics impedance of the shielded-strip transmission line," IRE TRANS., vol. MTT-2, pp. 52-57; July, 1954.

of different length; 2) the short lines which connect the coupled lines are uniform 50-ohm lines whose lengths can be found by measuring along their centerlines. A simple analysis then showed that if assumption 2) is correct, these connecting lines produce a phase shift at bandcenter which is proportional to their lengths multiplied by $\sqrt{\rho}$. All lengths were then calculated for exactly 90° phase difference at bandcenter, which is 900 mc.

Results

The differential-phase output of the experimental network was measured by a substitution method. First tests showed a slightly rising average characteristic in the $\Delta\phi$ vs frequency curve as seen in Curve B of Fig. 12. This indicated either that the uniform transmission-line branch was too long or that the coupled portions were too short. However, the peaks of the experimental Curve B were displaced toward the higher frequencies, as compared with the theoretical Curve A, and this fact alone indicated that the coupled-line elements were made too short.

The experimental differential phase shifter was then adjusted to make the phase difference 90° on the average, as follows. A straight line was drawn through the 90° point on the ordinate of Fig. 12 so that Curve B oscillates about this line approximately uniformly. The slope of this line was then used to calculate the length by which the uniform-line branch of the phase shifter must be reduced in order to match the unwittingly shortened coupled-line portions. Thus the amount calculated is

$$\text{Slope} \times \text{wavelength} = \frac{(137^\circ - 90^\circ)}{360^\circ} \times \frac{\text{velocity of light}}{1800 \text{ mc}} \\ = 0.86 \text{ inch.}$$

The dimensions given in Fig. 11 reflect this adjustment and Curve D of Fig. 12 is the resultant differential phase

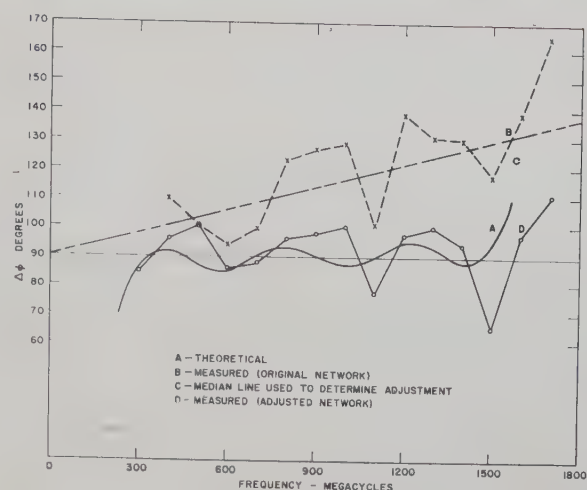


Fig. 12—Performance of a Type-C experimental phase shifter.

output. It is seen that the differential phase output oscillates about an average value of 90°, although the maximum phase error is larger than that predicted.

It is believed that the performance of the experimental phase shifter could be further improved by compensating for the discontinuities at the input to the coupled lines and at the connection between coupled lines.

CONCLUSION

The use of coupled transmission-line elements makes possible the design of broad-band, matched differential phase-shift networks for the microwave region. The techniques employed here in the design of 90° differential phase shifters also may be used to provide any other amount of differential phase shift over very broad frequency bands.

ACKNOWLEDGMENT

The author wishes to thank S. B. Cohn for his contribution of the basic idea, and R. C. Honey for his valuable aid in the course of its development.



Correspondence

Fourier Transforms and Directional Couplers*

The excellent review of Bolinder¹ on the applications of Fourier transforms in wave theory, particularly the section on "Coupling of Waves," suggested that the readers of these TRANSACTIONS might also be interested in some related work performed by this writer some time ago. A report² on this work contains a section on the use of Fourier integral and series methods for directional coupler design. In connection with directional couplers, this letter also can be considered as noting a further addition to the useful bibliography of Schwartz.³ Although not widely distributed, the aforementioned report² has been available since late 1947 in the Document Room of the Research Laboratory of Electronics at the Massachusetts Institute of Technology as No. SPE-239. It should be emphasized that this letter is not intended to start a controversy as to who did what first, but rather to bring to the readers' attention a report of possible interest.

SAMUEL SENSIPER
Hughes Aircraft Co.
Culver City, Calif.

* Received by the PGM TT, November 11, 1957.

¹ E. F. Bolinder, "The relationship of physical applications of Fourier transforms in various fields of wave theory and circuitry," IRE TRANS., vol. MTT-5, pp. 153-158; April, 1957.

² S. Sensiper, "Notes on Theory of Directional Couplers," Sperry Gyroscope Co., Inc., Great Neck, N. Y., Rep. No. 5224-1095; August 1, 1947.

³ R. F. Schwartz, "Bibliography on directional couplers," IRE TRANS., vol. MTT-2, pp. 58-63; July, 1954. See also, IRE TRANS., vol. MTT-3, pp. 42-43; April, 1955.

Analysis of the Variable-Ratio Microwave Power Divider*

It has been shown experimentally that a variable-ratio microwave power divider is easily assembled from two identical 3-db directional couplers and a phase changer.¹ The scattering matrix² of this structure is readily obtained from the flow graph³ showing the interconnections between the couplers. The following shows that the whole structure is still a directional coupler, derives the conditions to optimize the power transfer, and finally, gives the phase angles of the scattering coefficients.

The type of lossless directional couplers that are considered here have the following scattering matrix

* Received by the PGM TT, November 11, 1957.

¹ W. L. Teeter and K. R. Bushore, "A variable-ratio microwave power divider and multiplexer," IRE TRANS., vol. MTT-5, pp. 227-229; October, 1957.

² C. G. Montgomery, R. H. Dicke, and E. M. Purcell, "Principles of Microwave Circuits," McGraw-Hill Book Co., Inc., New York, N. Y., M.I.T. Rad. Lab. Ser., vol. 8, ch. 5; 1948.

³ S. J. Mason, "Feedback theory—some properties of signal flow graphs," PROC. IRE, vol. 41, pp. 1144-1156; September, 1953.

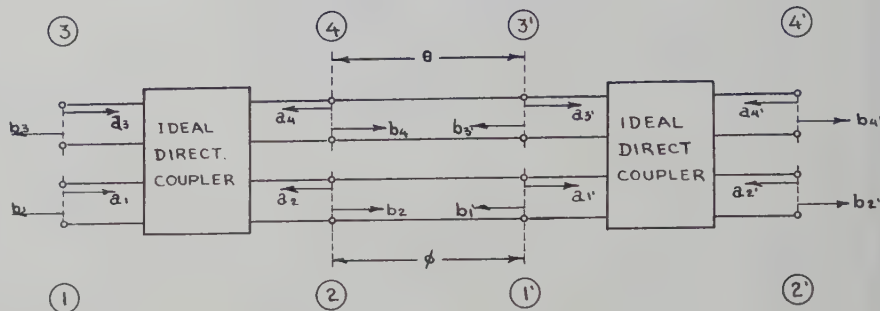


Fig. 1

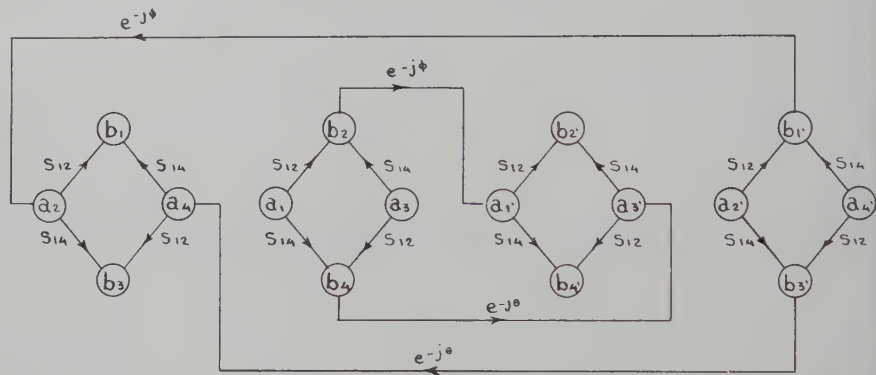


Fig. 2

$$\begin{bmatrix} b_1 \\ b_2 \\ b_3 \\ b_4 \end{bmatrix} = \begin{bmatrix} 0 & S_{12} & 0 & S_{14} \\ S_{12} & 0 & S_{14} & 0 \\ 0 & S_{14} & 0 & S_{12} \\ S_{14} & 0 & S_{12} & 0 \end{bmatrix} \begin{bmatrix} a_1 \\ a_2 \\ a_3 \\ a_4 \end{bmatrix}, \quad (1)$$

$$\begin{bmatrix} b_1 \\ b_2' \\ b_3' \\ b_4' \end{bmatrix} = \begin{bmatrix} 0 & S_{12'} & 0 & S_{14'} \\ S_{12'} & 0 & S_{14'} & 0 \\ 0 & S_{14'} & 0 & S_{34'} \\ S_{14'} & 0 & S_{34'} & 0 \end{bmatrix} \begin{bmatrix} a_1 \\ a_2' \\ a_3' \\ a_4' \end{bmatrix}. \quad (4)$$

where a_i and b_i are, respectively, the complex amplitudes of the incident and emergent waves referred to planes $i=1, 2, 3, 4$ and have been normalized in such a way that $a_i a_i^*$ and $b_i b_i^*$ are respectively proportional to the incident and emergent power at terminal i .

Fig. 1 shows the structure to be analyzed and Fig. 2 its flow graph. The whole structure can be specified by the following scattering matrix referred to planes 1, 2', 3 and 4'

$$\begin{bmatrix} b_1 \\ b_2' \\ b_3' \\ b_4' \end{bmatrix} = \begin{bmatrix} S_{11} & S_{12'} & S_{13} & S_{14'} \\ S_{2'1} & S_{2'2'} & S_{2'3} & S_{2'4'} \\ S_{31} & S_{32'} & S_{33} & S_{34'} \\ S_{4'1} & S_{4'2'} & S_{4'3} & S_{4'4'} \end{bmatrix} \begin{bmatrix} a_1 \\ a_2' \\ a_3' \\ a_4' \end{bmatrix}. \quad (2)$$

From the flow graph the coefficients s_{ij} are found to be

$$\begin{aligned} S_{11} &= S_{2'2'} = S_{33} - S_{4'4'} = 0 \\ S_{12} &= S_{31} = S_{2'4'} = S_{4'2'} = 0 \\ S_{12'} &= S_{12}^2 e^{-j\phi} + S_{14}^2 e^{-j\theta} = S_{2'1} \\ S_{14'} &= S_{12} S_{14} (e^{-j\phi} + e^{-j\theta}) = S_{4'1} = S_{2'3} = S_{32} \\ S_{34'} &= S_{12}^2 e^{-j\theta} + S_{14}^2 e^{-j\phi} = S_{4'3}. \end{aligned} \quad (3)$$

After substituting (3) in matrix (2), one obtains

Since the analysis is based on the assumption of ideal lossless components, the scattering matrix (4) is unitary and of the same type as matrix (1). Thus the whole structure is still a directional coupler whose coefficients are functions of θ and ϕ . Let $\psi = \theta + \psi$, where ψ is variable at will (variable phase changer). Then,

$$S_{14'} = 2 |S_{12}| |S_{14}| \cos \frac{\psi}{2} \exp j(\varphi_{12} + \varphi_{14} - \theta - \frac{\psi}{2})$$

where φ_{12} = phase of S_{12} ; φ_{14} = phase of S_{14} . The amplitude of $S_{14'}$ is then given by

$$|S_{14'}| = 2 |S_{14}| [1 - |S_{14}|^2]^{1/2} \cos \frac{\psi}{2} \quad (5)$$

since $|S_{12}|^2 + |S_{14}|^2 = 1$.

The optimization of $|S_{14'}|$ with respect to $|S_{14}|$ is obtained by making

$$\frac{d |S_{14'}|}{d |S_{14}|} = 0$$

for all possible values of ψ ; i.e.;

$$\frac{d |S_{14'}|}{d |S_{14}|} = 2 \cos \frac{\psi}{2} \sqrt{1 - |S_{14}|^2} \cdot \left[1 - \frac{|S_{14}|^2}{1 - |S_{14}|^2} \right] = 0.$$

The only acceptable value of $|S_{14}|$ is then $1/\sqrt{2}$ which implies that $|S_{12}| = 1/\sqrt{2}$. Substitution of $|S_{14}| = |S_{12}| = 1/\sqrt{2}$ in (5) gives,

$$|S_{14'}| = \cos \frac{\psi}{2}$$

while the power transmission is:

$$|S_{14'}|^2 = \cos^2 \frac{\psi}{2}$$

and $0 \leq |S_{14'}|^2 \leq 1$ for $0 \leq \psi \leq \pi$.

For all other values of $0 < |S_{14}| < 1$

$$0 \leq |S_{14'}|^2 = 4 |S_{14}|^2 [1 - |S_{14}|^2] \cos^2 \frac{\psi}{2} < 1 \text{ for } 0 \leq \psi \leq \pi.$$

The phase angles of the scattering coefficients are given by

$$\not S_{14'} = \varphi_{12} + \varphi_{14} - \theta - \frac{\psi}{2} = \varphi_{12} + \varphi_{14} - \frac{(\theta + \phi)}{2}$$

$$\not S_{12'} = \tan^{-1} \frac{|S_{12}|^2 \sin (2\varphi_{12} - \phi) + |S_{14}|^2 \sin (2\varphi_{14} - \theta)}{|S_{12}|^2 \cos (2\varphi_{12} - \phi) + |S_{14}|^2 \cos (2\varphi_{14} - \theta)}$$

$$\not S_{34'} = \tan^{-1} \frac{|S_{12}|^2 \sin (2\varphi_{12} - \theta) + |S_{14}|^2 \sin (2\varphi_{14} - \phi)}{|S_{12}|^2 \cos (2\varphi_{12} - \theta) + |S_{14}|^2 \cos (2\varphi_{14} - \phi)}$$

and for $|S_{12}| = |S_{14}| = 1/\sqrt{2}$ they reduce to

$$\not S_{14'} = \not S_{12'} \pm \pi = \not S_{34'} = \varphi_{12} + \varphi_{14} - \frac{(\theta + \phi)}{2}.$$

From a general viewpoint there are other possible interconnections of two directional couplers which still give a new directional

coupler. These cases are being studied in a Master of Science thesis at Laval University, Quebec, Can., and will be published later.

R. M. VAILLANCOURT
Canadian Armament Res. and Dev. Estab
Valcartier, Quebec, Can.

WESCON PAPERS DEADLINE SET FOR MAY 1, 1958

Authors wishing to present papers at the 1958 WESCON Convention to be held in Los Angeles, Calif., August 19-22, should send 100-word abstracts and either the complete text or a detailed summary to the Technical Program Committee Chairman:

Dr. Robert C. Hansen
Microwave Laboratory
Hughes Aircraft Co.
Culver City, Calif.

There will be again an IRE WESCON CONVENTION RECORD. Authors will be notified of acceptance or rejection by June 1, 1958.

1958 PGMTT National Symposium

The 1958 PGMTT National Symposium, sponsored by the IRE Professional Group on Microwave Theory and Techniques and hosted by the IRE San Francisco Section, will be held at Cubberley Auditorium, Stanford University, Stanford, Calif. May 5-7.

Arthur L. Aden is Symposium Chairman. Kiyo Tomiyasu is in charge of the technical program; Henry Schroeder, local arrangements; Glenn Keitel, publicity; and Theodore Moreno, finance. Members of the Steering Committee are A. L. Aden, T. N. Anderson, S. B. Cohn, W. A. Edson, H. Heffner, P. D. Lacy, J. L. Melchor, T. Moreno, W. H. Thon, K. Tomiyasu, and J. R. Whinnery.

The Technical Program Committee is K. Tomiyasu, Chairman, S. B. Cohn, E. M. T. Jones, P. D. Lacy, H. J. Shaw, P. H. Vartanian, Jr., and G. J. Wheeler.

Advance registration for this Symposium is urged. Registration fees are \$3.00 for IRE members, \$1.00 for IRE student members, and \$5.00 for nonmembers. The banquet is \$5.00 per person extra. Checks should be made payable to T. Moreno, Finance Chairman, and should be mailed to T. Moreno, Finance Chairman, 1958 PGMTT National Symposium, Varian Associates, 611 Hansen Way, Palo Alto, Calif.

PROGRAM

REGISTRATION

Mon.

8:00-8:45 A.M.

SESSION 1

Mon.

8:45 A.M.-NOON

FERRITES I

Chairman: S. SENSIPER, *Hughes Aircraft Co., Culver City, Calif.*

Opening Addresses

A. L. ADEN, *Symposium Chairman, Sylvania Microwave Physics Lab., Mountain View, Calif.*

H. H. SKILLING, *Chairman, Dept. of Elec. Eng., Stanford University, Stanford, Calif.*

W. L. PRITCHARD, *Chairman, PGMTT Administrative Committee, Raytheon Mfg. Co., Wayland, Mass.*

Applications of the Nonlinear Properties of Ferromagnetic Resonance

C. L. HOGAN, *Dept. of Applied Physics, Harvard University, Cambridge, Mass.*

Microwave Radiation from Ferrimagnetically Coupled Electrons in Transient Magnetic Fields

F. R. MORGENTHALER, *Antenna Lab., AF Cambridge Res. Center, Bedford, Mass.*

Ferrite High-Power Effects in Waveguide

E. STERN AND R. MANGIARACINA, *Sperry Gyroscope Co., Great Neck, N. Y.*

Shape Effects in Microwave Ferrite Devices
J. L. MELCHOR AND P. H. VARTANIAN, *Microwave Engineering Labs., Inc., Palo Alto, Calif.*

Characteristics of Ferrite Microwave Limiters

G. S. UEBELE, *Hughes Aircraft Co., Culver City, Calif.*

SESSION 2

Mon.

2:00-5:00 P.M.

FERRITES II

Chairman: T. N. ANDERSON, *Airtron, Inc., Linden, N.J.*

Theory of Nonreciprocal Ferrite Phase Shifters in Dielectric-Loaded Coaxial Line

K. J. BUTTON, *Lincoln Lab., M.I.T., Lexington, Mass.*

Nonreciprocity in Dielectric Loaded TEM Mode Transmission Lines

D. FLERI AND G. HANLEY, *Sperry Gyroscope Co., Great Neck, N.Y.*

Ferrite Phase Shifter for the UHF Region

C. M. JOHNSON, *Electronic Communications, Inc., Timonium, Md.*

A Ferrite Serrodyne for Microwave Frequency Translation

F. J. O'HARA, *Missile Systems Div., Raytheon Mfg. Co., Bedford, Mass., AND H. SCHARFMAN, Research Div., Raytheon Mfg. Co., Waltham, Mass.*

Broad-Band Ferrite Rotators Using Quadruply Ridged Circular Waveguide

H. N. CHAIT AND N. G. SAKIOTIS, *U. S. Naval Res. Lab., Washington 25 D. C.*

A Broad-Band Rotational Ferrite Duplexer for Microwave Relay Applications

T. ANDERSON, K. CARR, AND E. WANTUCH, *Airtron, Inc., Cambridge, Mass.*

Broad-Band High-Power Ferrite Load Isolator for S-Band

E. N. SKOMAL, *Sylvania Microwave Physics Lab., Mountain View, Calif.*

Low-Energy Ferrite Switch

L. M. SILBER AND M. A. TREUHAFT, *Micro-wave Research Inst., Polytechnic Inst. Brooklyn, Brooklyn, N.Y.*

SESSION 3

Tues.

8:45 A.M.-NOON

MICROWAVE PHYSICS I

Chairman: D. D. KING, *Electronic Communications, Inc., Timonium, Md.*

The Present State of the Millimeter Wave Generation and Technique Art

P. D. COLEMAN, *Dept. of Elec. Eng., University of Illinois, Urbana, Ill.*

Millimeter-Wave Generation Utilizing Ferrites

W. P. AVRES, *Microwave Engineering Lab., Inc., Palo Alto, Calif.*

Some Characteristics of Dielectric Image Lines at Millimeter Wavelengths

J. C. WILTSE, *Radiation Lab., The Johns Hopkins University, Baltimore 2, Md.*

Microwave Properties of Gas Discharges

S. C. BROWN, *Dept. of Physics, M.I.T., Cambridge, Mass.*

Investigations of Microwave Phase Shift in Gas Discharge and Ferrite Loaded Coaxial Lines

J. ROWLEY, H. BANDEL, E. SKOMAL, A. L. ADEN, AND O. T. FUNDINGSLAND, *Sylvania Microwave Physics Lab., Mountain View, Calif.*

Recent Advances in Microwave Gas Discharge Duplexer Devices

L. GOULD, *Microwave Associates, Inc., Burlington, Mass.*

High-Power, Magnetic Field Controlled Microwave Gas Discharge Switches

S. J. TETENBAUM AND R. M. HILL, *Sylvania Microwave Physics Lab., Mountain View, Calif.*

SESSION 4

Tues.

2:00-5:00 P.M.

MICROWAVE PHYSICS II

Chairman: J. R. WHINNERY, *Dept. of Elec. Eng., University of California, Berkeley, Calif.*

Solid-State Microwave Amplifiers

H. HEFFNER, *Dept. of Elec. Eng., Stanford University, Stanford, Calif.*

On the Design of Reflection Cavity Solid-State Masers

A. L. McWHORTER AND J. W. MEYER, *Lincoln Lab., M.I.T., Lexington, Mass.*

AUHF Solid-State Maser

R. H. KINGSTON, *Lincoln Lab., M.I.T., Lexington, Mass.*

At the Frontiers in Radio Astronomy

H. I. EWEN, *Ewen Knight Corp., Needham Heights, Mass.*

A Microwave Frequency Standard Employing Optically Pumped Sodium Vapor

W. E. BELL, A. BLOOM, AND R. WILLIAMS, *Varian Associates, Palo Alto, Calif.*

SYMPOSIUM BANQUET

Place—Rickey's Studio Inn, Rose Room, 4219 El Camino Real, Palo Alto, Calif.

Time—Tuesday, Cocktail Hour: 6:00-7:00 P.M., Dinner: 7:00 P.M.

Toastmaster—M. LEIFER, Chairman, San Francisco Section, IRE, Sylvania Electric Products, Mountain View, Calif.

Opening Address—F. E. TERMAN, Dean of Engineering and Provost, Stanford University, Stanford, Calif.

Microwave Prize—Announced by W. L. PRITCHARD, Chairman, PGM TT Administrative Committee, Raytheon Mfg. Co., Wayland, Mass.

Industry's Role In Basic Research
C. G. SUITS, Vice-President and Director of Res., General Electric Res. Lab., Schenectady, N.Y.

SESSION 5

Wed. 8:45 A.M.—NOON

MICROWAVE TECHNIQUES

Chairman: T. S. SAAD, Sage Labs., Inc., Wellesley, Mass.

How to Explain the Smith Chart to a Digital Computer

L. YOUNG, Westinghouse Electric Corp., Baltimore 3, Md.

Measurement of Two-Mode Discontinuities in a Multimode Waveguide by a Resonance Technique

L. B. FELSEN, W. K. KAHN, AND L. LEVEY, *Microwave Res. Inst. Polytechnic Inst. Brooklyn, Brooklyn, N.Y.*

Mode Couplers and Multimodal Measurement Techniques
D. J. LEWIS, *Moore School of Elec. Eng., University of Pennsylvania, Philadelphia 4, Pa.*

Measurement of Harmonic Power Generated by Microwave Transmitters
V. G. PRICE, *General Electric Microwave Lab., Palo Alto, Calif.*

Design Data for Optimum Multicoupler Networks
J. F. CLINE AND B. M. SCHIFFMAN, *Stanford Res. Inst. Menlo Park, Calif.*

A Wide-Band Strip-Line Balun
E. M. T. JONES AND J. K. SHIMIZU, *Stanford Res. Inst., Menlo Park, Calif.*

Periodic Structures in Trough Waveguide
A. A. OLINER, *Microwave Res. Inst., Polytechnic Inst. Brooklyn, Brooklyn, N.Y.*, AND W. ROTMAN, *AF Cambridge Res. Center, Bedford, Mass.*

A Study of a Serrated-Ridged Waveguide
H. S. KIRSCHBAUM, *Battelle Memorial Inst., Columbus, Ohio*, AND R. TSU, *Ohio State University, Columbus, Ohio*

SESSION 6

Wed.

2:00—5:00 P.M.

MICROWAVE FILTERS

Chairman: W. W. MUMFORD, Bell Telephone Labs., Whippany, N.J.

Design Considerations for High-Power Microwave Filters
S. B. COHN, *Stanford Res. Inst., Menlo Park, Calif.*

Waveguide Filter for Suppressing Spurious Transmission from High-Power S-Band Radar

H. A. WHEELER AND H. L. BACHMAN, *Wheeler Labs., Great Neck, N.Y.*

High-Power Filters Using Higher-Order Mode Resonance

J. H. VOGELMAN, *Rome Air Development Center, Griffiss Air Force Base, N.Y.*

Hybrid Junction-Cutoff Waveguide Filters
E. N. TORGOW, *Microwave Res. Inst., Polytechnic Inst. Brooklyn, Brooklyn, N.Y.*

Corrugated-Waveguide Filters with Specified Stop-Band Characteristics
M. CRANE AND D. GRACE, *Electronics Labs., Stanford University, Stanford, Calif.*

Practical Design of Strip-Line Half-Wavelength Resonator Directional Filters
R. D. WANSELOW AND L. P. TUTTLE, *Melpa Inc., Falls Church, Va.*



Contributors

W. P. Ayres, for a photograph and biography please see page 268 of the October, 1957, issue of these TRANSACTIONS.



Morris E. Brodwin (A'49-M'55) was born in New York, N. Y., on July 14, 1924. He received the B.S. degree in electrical engineering from the University of Nebraska in 1947. In 1951, he received the M.S. degree and in 1957, the Dr.Eng. degree from The Johns Hopkins University, Baltimore, Md.

He was a member on the staff of the Martin Company for nine months in 1948. In October, 1949, he joined the Radiation Laboratory of The Johns Hopkins University. He is presently research scientist in charge of microwave research at the Radiation Laboratory.

Dr. Brodwin is a member of Sigma Xi and Pi Mu Epsilon.



M. E. BRODWIN

joined the Radiation Laboratory of The Johns Hopkins University. He is presently research scientist in charge of microwave research at the Radiation Laboratory.

Dr. Brodwin is a member of Sigma Xi and Pi Mu Epsilon.



H. J. Carlin (M'47-SM'50-F'56) was born in New York, N. Y., on May 1, 1917. He attended Columbia University, receiving the B.S. degree in 1938, and the M.S. degree in 1940. In 1947 he was awarded the D.E.E. degree from Polytechnic Institute of Brooklyn.

Dr. Carlin was with Westinghouse from 1940-1945. In the latter part of 1945, he joined the Polytechnic Institute of Brooklyn, where he now holds the position of research professor and associate director of the Microwave Research Institute. His major work has been in the fields of microwave devices and network theory.

He is a member of the AAAS, Tau Beta Pi, Sigma Xi, and Eta Kappa Nu.



H. J. CARLIN

he now holds the position of research professor and associate director of the Microwave Research Institute. His major work has been in the fields of microwave devices and network theory.

He is a member of the AAAS, Tau Beta Pi, Sigma Xi, and Eta Kappa Nu.



Seymour B. Cohn (S'41-A'44-M'46-SM'51) was born in Stamford, Conn., on October 21, 1920. He received the B.E. degree in electrical engineering from Yale Uni-

versity in 1942. The M.S. degree in communication engineering, in 1946, and the Ph.D. degree in engineering sciences and applied physics, in 1948, were awarded by Harvard University. From 1942 to 1954, he was employed as a special research associate by the Radio Research Laboratory of Harvard University, also representing that Laboratory as a technical observer with the U. S. Army Air Force in the Mediterranean Theater of Operations. Dr. Cohn worked at Sperry Gyroscope Co. from 1948 to 1953, where he held the position of research engineer in the Microwave Instruments and Components Department.

Since February, 1953, Dr. Cohn has been with the Stamford Research Institute as head of the Microwave Group, and since 1957 as manager of the Antenna Systems Laboratory.

He is a member of Tau Beta Pi and Sigma Xi.



S. B. COHN

R. E. Collin, for a photograph and biography please see page 219 of the July, 1957, issue of these TRANSACTIONS.

Alexander L. Cullen (M'56) was born in Lincoln, England, on April 30, 1920. He studied electrical engineering at Imperial College, London, England, and in 1940, joined the staff of the Radio Department of the Royal Aircraft Establishment, Farnborough, where he worked on radar.

In 1946, Professor Cullen joined the staff of University College, London, England, as lecturer in electrical engineering, where he collaborated with Professor H. M. Barlow in microwave research and in writing a textbook on "Microwave Measurements."

In 1955, he was appointed to the Chair of Electrical Engineering in the University of Sheffield.

Prof. Cullen is an Associate Member of the IEE, and is a member of several committees connected with work in the microwave field.



Glenn F. Engen was born in Battle Creek, Mich., on April 26, 1925. He received the B.A. degree in physics and mathematics from Emmanuel Missionary College, Berrien Springs, Mich., in June, 1947. He has done graduate work at the Universities of Michigan, Maryland, and Colorado. After employment with the U. S. Naval Ordnance Laboratory and The Johns Hopkins University Applied Physics Laboratory, he joined the National Bureau of Standards in 1954. His present work is in the field of microwave power measurement techniques and standards.

Mr. Engen is a member of the Boulder Branch of RESA.



G. F. ENGEN

Alan L. Helgesson was born in Gary, Ind., on March 28, 1933. He received the B.S. degree in electrical engineering from the California Institute of Technology, Pasadena, Calif., in 1955 and the M.S. degree from Stanford University, Stanford, Calif., in 1957.



A. L. HELGESSON

He has been a member of the technical staff at Bell Telephone Laboratories and a part-time assistant instructor in the mathematics department of Ohio State University. Since June, 1956, he has been an engineer at the Sylvania Microwave Physics Laboratory engaged in the study of microwave ferrite devices and dielectric loaded waveguide. At present, he is on leave of absence at the Massachusetts Institute of Technology where he is studying for the Sc.D. degree.

Mr. Helgesson is a member of Tau Beta Pi.



J. C. Helmer was born in Evanston, Ill., on November 18, 1926. He received the B.S. degree in mathematics from Lawrence College in 1950, the M.S. degree in physics from the California Institute of Technology in 1952, and the Engr. and Ph.D. degrees in electrical engineering from Stanford University in 1954 and 1957, respectively.

At various times Dr. Helmer has worked

as a computer engineer for Northrop Aviation Corp. and Bendix Aviation Corp. in Los Angeles, Calif., and as a microwave engineer for Bell Telephone Laboratories. From 1953 to 1956, he was a research assistant at the Hansen Laboratories at Stanford University. Since August, 1956, he has been a member of the research staff of Varian Associates.

Dr. Helmer is a member of Phi Beta Kappa, Tau Beta Pi, and Sigma Xi.

J. C. HELMER

and Sigma Xi.

Allan V. James (S'51-A'56) was born in Kingston, Jamaica, British West Indies, on March 23, 1913. He attended elementary and high schools in Brooklyn, N. Y. During 1946 and 1947, he served in the U. S. Army as a radar repairman with the Signal Corps. He received the B.S. degree in electrical engineering from the Milwaukee School of Engineering in 1950, and the M.S. degree in electrical engineering from the Polytechnic Institute of Brooklyn in 1956.

A. V. JAMES

Mr. James was employed by the Polytechnic Institute of Brooklyn, Microwave Research Institute, from 1951 to 1956, where he designed several bolometric and calorimetric power meters for operation in the microwave region. He is presently employed as microwave design engineer by the Polytechnic Research and Development Company.

Kaneyuki Kurokawa was born on August 14, 1928, in Tokyo, Japan. He received the B.S. degree in electrical engineering from the

University of Tokyo in 1951. Since then, first as a graduate student and later as an assistant of the university, he has been engaged in research on microwave measurements. In 1954, he participated in the Foreign Student Summer Project held at the Massachusetts Institute of

K. KUROKAWA



Technology. Mr. Kurokawa became an assistant professor of the University of Tokyo in August, 1957.

He is a member of the Institute of Electrical Engineers of Japan and the Institute of Electrical Communication Engineers of Japan.



Katsu Matsumaru (A'55) was born on May 30, 1913, in Tokyo, Japan. He was graduated from Tokyo University with the B.S. degree in 1939.

From 1940 to 1943, he served as an assistant at Tokyo University and later, from 1944-1951, he served in the same capacity at the Tokyo Institute of Technology.

In 1951, Mr. Matsumaru joined the Radio Development

Section of the Electrical Communication Laboratory, Nippon Telegraph and Telephone Public Corporation in Tokyo, Japan, where he has participated in the microwave research program.



K. MATSUMARU



Ljubimko Milosevic was born in Zajecar, Yugoslavia, on June 23, 1916. He was graduated from Faculté Technique of Belgrade University in 1939. He attended the Sorbonne (Études Supérieures des Sciences Physiques) in Paris, and was graduated in 1940. In 1943, he was graduated from École Nationale Supérieure des Télécommunications. He joined the Compagnie Française Thomson-Houston in

Paris in 1943, and was in charge of electroacoustics studies until 1949. He then was put in charge of hf heads studies in the vhf research laboratory. He is, at present, head of high-power radar development in the division Matériel Électronique. Mr. Milosevic is a member of the Société des Radio Électriciens.



L. MILOSEVIC



Frederic R. Morgenthaler (S'55-M'57) was born in Shaker Heights, Ohio, on March 12, 1933. He was associated with Bell Telephone Laboratories, New York, N. Y., and Murray Hill, N. J., from 1953 to 1955 as a cooperative course student and received the

degrees of S.B. and S.M. in electrical engineering in 1956 from the Massachusetts Institute of Technology, Cambridge, Mass.

Mr. Morgenthaler presently is on active duty as a Lieutenant in the United States Air Force and is stationed at the Antenna Laboratory, Electronics Research Directorate, Air Force Cambridge Research Center, Bedford, Mass. He is currently engaged in the study of microwave properties of solid state materials.

He is a member of Eta Kappa Nu, Tau Beta Pi, and Sigma Xi.



F. MORGENTHALER

❖

John A. Morrison was born in Beckenham, Kent, England, on June 10, 1927. He received the B.Sc. (Special) Mathematics degree from the University of London in 1952. He did his graduate study at Brown University, Providence, R. I., receiving the Sc.M. degree in 1954 and the Ph.D. degree in applied mathematics in 1956.

Dr. Morrison has been at Bell Telephone Laboratories, Murray Hill, N. J., since February, 1956, where he has been mainly concerned with electromagnetic theory.

Dr. Morrison is a member of Sigma Xi.



J. A. MORRISON



Marcel W. Muller (SM'57) was born in Vienna, Austria, on November 1, 1922. He received the B.S. degree in electrical engineering in 1949 and the A.M. degree in physics in 1952 from Columbia University, New York, N. Y., and the Ph.D. in physics in 1957 from Stanford University, Stanford, Calif.

Since 1952, he has been a research engineer at Varian Associates, where he has engaged in research on microwave electronics and physics.

Mr. Muller is a member of the American Physical Society, Sigma Xi, and Tau Beta Pi.



M. W. MULLER



Sogo Okamura (A'52-M'57) was born in Mie Prefecture, Japan, on March 18, 1918. He graduated from the Tokyo Imperial University (now the University of Tokyo) in 1940, and received the Doctor of Engineering degree from the same university in 1951.

He was appointed an instructor in the Electrical Engineering Department of the Tokyo Imperial University in 1940. During World War II, he served as a naval officer and was engaged on the microwave radar at the Naval Technical Research Institute in Tokyo.

After the war he was appointed an assistant professor in 1947, and became a professor in 1951, at the University of Tokyo.

Awarded a scholarship by the British Council, he studied at University College, London, from 1953 to 1954. He has been lecturing on electrical engineering subjects and is now working on microwave electronics.

Dr. Okamura is a member of the Institute of Electrical Engineers of Japan, the Institute of Electrical Communication Engineers of Japan, the Physical Society of Japan, the Institute of Illuminating Engineers of Japan, and the Institute of Television Engineers of Japan. He is also a member of the National Committee of URSI.

B. Rogal was born in Kielce, Poland, on April 9, 1920. During World War II, he served as a signals officer. After the war he obtained the B.Sc. (Hons) degree in electrical engineering at the University of London.

He joined Wayne-Kerr Laboratories, Ltd., in February, 1950, as a development engineer and has been engaged on work in uhf and vhf bands.

Since 1952, his main interest has been in the microwave field where he has worked on a number of high precision measuring instruments. In April, 1956, he was appointed chief engineer of Wayne-Kerr.

Mr. Rogal is a graduate member of the Institute of Electrical Engineers, England.

Bernard M. Schiffman (S'51-A'53) was born on December 5, 1915, in New York, N. Y. He received the B.S. degree in electrical engineering in 1932 from the State University of Iowa. He did graduate work at the Polytechnic Institute of Brooklyn and Stanford University. From 1941 to 1945, he served in the U. S. Army. During part of

this period, he was a radio technician in the Signal Corps. From 1946 to 1951, Mr. Schiffman was a junior civil engineer with the City of New York. From 1952 to 1954, he was employed by the Hazeltine Electronics Corp. in a radar indicator development group. In 1954, he joined the Sylvania Electronic Defense Laboratory, where he worked on transmitter development and in the microwave group.

In July, 1956, he joined the staff of the Stanford Research Institute, where he has been engaged in microwave circuit research and development.

Mr. Schiffman is a member of Eta Kappa Nu and RESA.



A. SINGH

From 1949 to 1953, Dr. Singh was lecturer in radio physics at the University of Delhi.

In 1953 he became a member of the Scientific staff of the National Physical Laboratory of India, leading a project on microwave tubes, and in 1956 he became Senior Scientific Officer. Dr. Singh joined the Central Electronics Engineering Research Institute in 1957. He now holds the position of Assistant Director.

Jadwiga Smolarska was born on July 2, 1931, in Cracow, Poland. She began her engineering studies at the Gliwice Polytechnical College and later transferred to the Wroclaw Polytechnical College where she obtained an electrical engineering certificate in 1954. In 1956, she received the M.Sc. degree from the Warsaw Polytechnical College.

The material for Miss Smolarska's article is derived from her diploma work which was done at the In-

J. SMOLARKA

stitute of Basic Technical Problems of the Polish Academy of Science in the Department of Communications Theory, where she has been employed since 1956 on waveguide theory research.

Max Sucher was born in Poland in 1913. He received the B.S. degree in physics from Brooklyn College, Brooklyn, N. Y., in 1933 and the M.S. degree in physics from Brooklyn Polytechnic Institute, Brooklyn, N. Y., in 1947.



M. SUCHER

From 1936 to 1938, Mr. Sucher was with the National Bureau of Standards and from 1940 to 1946, with the Bureau of Ships of the Navy Department. From 1946 to 1947, he served as a research fellow in the physics department of Brooklyn Polytechnic Institute, joining the staff of the Polytechnic Research and Development Company in 1947. Since 1950 he has been with the Microwave Research Institute of Brooklyn Polytechnic Institute as a research associate and project engineer.

Mr. Sucher is a member of the American Physical Society and Sigma Xi.

L. O. Sweet (S'51-A'53) was born in Brooklyn, N. Y. on October 19, 1929. He received the B.E.E. degree from the College

of the City of New York in 1951 and the M.E.E. degree from the Polytechnic Institute of Brooklyn in 1952. He was at the Microwave Research Institute of Brooklyn Polytech from 1951 to 1953 and from 1955 to 1956. While there, he worked on the development of microwave power standards. From 1953 to 1955, he served as a lieutenant in the United States Air Force and was engaged in the airborne testing and evaluation of bombing and navigation systems.

He joined the engineering staff of the Polytechnic Research and Development Company in 1956 and is presently concerned with the development of microwave components. Mr. Sweet is a member of Sigma Xi.

P. H. Vartanian (S'52-M'56-SM'56) was born in Rochester, N. Y., on June 14, 1931. He received the Bachelor of Science degree in

electrical engineering in 1953 from the California Institute of Technology, Pasadena, Calif., and the Master of Science degree from Stanford University, Stanford, Calif., in 1954.

At Stanford he was a Tau Beta Pi Fellow and later a research assistant at the Electronics Research Laboratory. In 1951 and 1952 Dr. Vartanian worked part-time at the United States Naval Radiological Defense Laboratory on radia-

tion detectors. In 1954, he joined the Electronic Defense Laboratory of Sylvania Electric Products Inc., Mountain View, Calif., where he was engaged in research on microwave ferrites.

In 1956, he received the Ph.D. degree in electrical engineering at Stanford University under the Honors Cooperative Program.

During that same year, Dr. Vartanian assisted in the formation of the Microwave Engineering Laboratories, Incorporated, Palo Alto, Calif., where he is presently engaged in research and development on solid-state components.

Dr. Vartanian is a member of Tau Beta Pi and RESA.



P. H. VARTANIAN

Radiological Defense Laboratory on radia-

Réné Vautey was born in Paris, France, on April 29, 1929. He was graduated from the École Nationale Supérieure des Télécommunications in 1953.

In 1954, Mr. Vautey joined the Compagnie Française Thomson-Houston in Paris, France, where he is, at present, in charge of microwave research and development in the division Matériel Électronique.



R. VAUTEY



microwave engineers

• The Hughes Research and Development Laboratories are engaged in basic and applied research and development programs in a wide variety of fields, including antennas, radomes, microwave and storage tubes, masers, ferrite devices, microwave circuitry, instrumentation, and other fields.

One of the several interesting problems is the design of feedback loops for locking the local oscillator klystron to an available reference signal. The requirements—good stability and low noise in a very trying environment.

Your inquiry is invited.

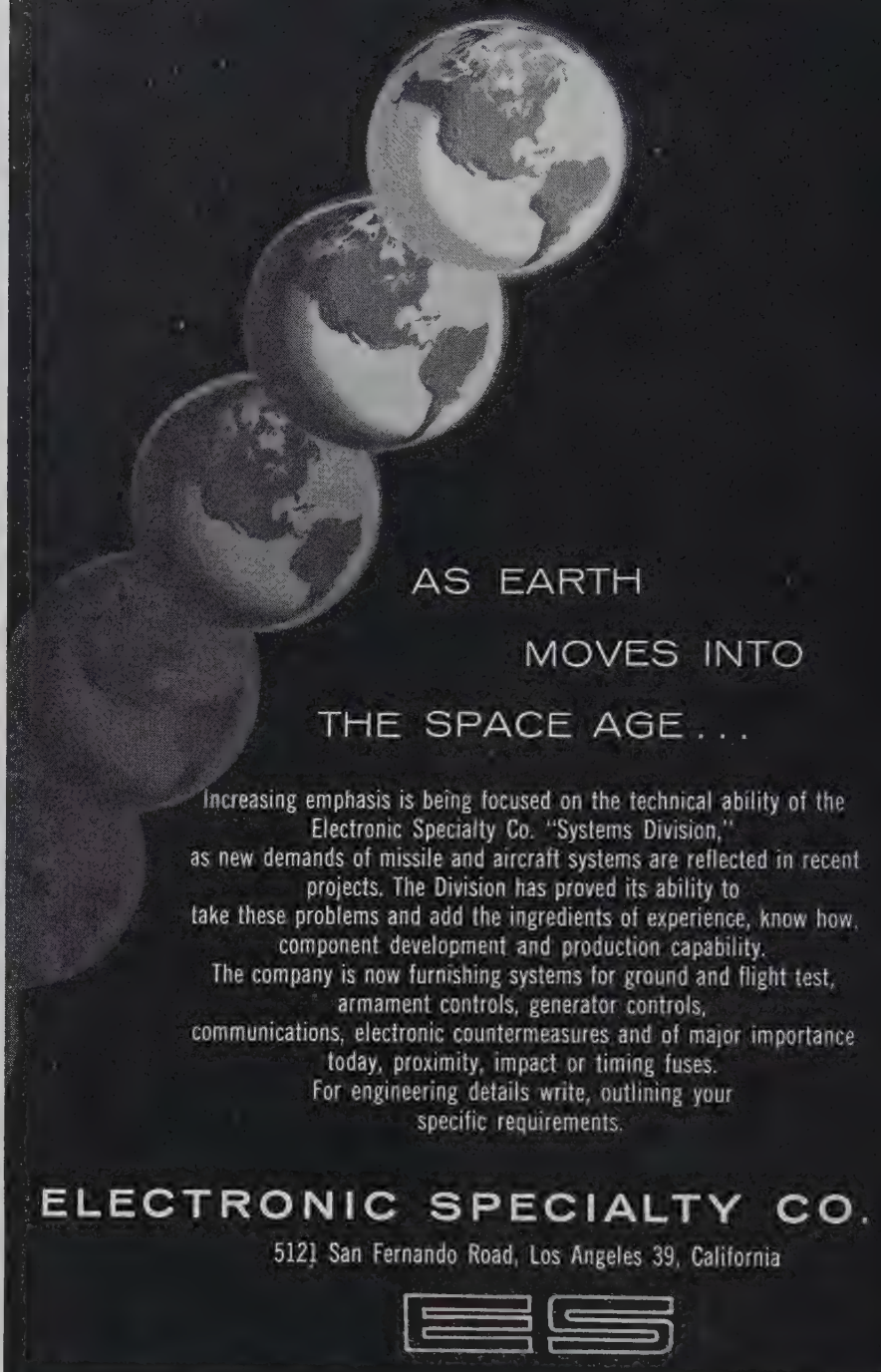
Please write Mr. John Bailey.

the West's leader in advanced electronics

HUGHES

RESEARCH & DEVELOPMENT
LABORATORIES

Hughes Aircraft Co., Culver City, Calif.



AS EARTH
MOVES INTO
THE SPACE AGE...

Increasing emphasis is being focused on the technical ability of the Electronic Specialty Co. "Systems Division," as new demands of missile and aircraft systems are reflected in recent projects. The Division has proved its ability to take these problems and add the ingredients of experience, know how, component development and production capability. The company is now furnishing systems for ground and flight test, armament controls, generator controls, communications, electronic countermeasures and of major importance today, proximity, impact or timing fuses. For engineering details write, outlining your specific requirements.

ELECTRONIC SPECIALTY CO.

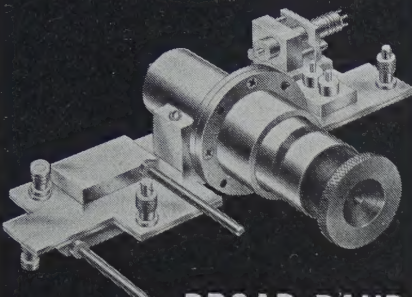
5121 San Fernando Road, Los Angeles 39, California



NOTICE TO ADVERTISERS

Effective immediately the IRE TRANSACTIONS ON MICROWAVE THEORY AND TECHNIQUES will accept display advertising. For full details contact Tore N. Anderson, Advertising Editor, PGM TT TRANSACTIONS, 1539 Deer Path, Mountainside, N. J.

NEW



**BROAD BAND
STRIP-LINE ASSEMBLY
REDUCES
-SIZE by 65%
-WEIGHT by 60%**

*The Newest Concept in
Microwave Plumbing*

Printed circuitry in a sandwich type of construction has been adapted to produce microwave plumbing that offers a substantial reduction in size and weight. By standardizing on component parts, system package design for units within a frequency range of 500MC to 12,000MC can be accomplished. Electrical characteristics, in general, compare with coaxial.

OTHER KEARFOTT products include: Ferrite Isolators and Duplexers in a wide range of sizes and band widths and facilities to produce special configurations if desired. Our engineers can help you.

SALES OFFICES:

Eastern Office: 1378 Main Avenue
Clifton, N.J.

Midwest Office: 23 W. Calendar Ave.
La Grange, Ill.

South Central Office: 6211 Denton Drive
Dallas, Texas

Northwest Area Office: 530 University Avenue
Palo Alto, California

Kearfott



KEARFOTT COMPANY, INC.

MICROWAVE DIVISION
DEPT. 19D, 14844 OXNARD ST.
VAN NUYS, CALIF.

AVAILABLE BACK ISSUES OF
IRE TRANSACTIONS
ON
MICROWAVE THEORY AND
TECHNIQUES

PUBLICATION	PRICES		
	Group Members	IRE Members	Non-* Members
Vol. MTT-2, No. 3 September, 1954	\$1.10	\$1.65	\$3.30
Vol. MTT-3, No. 1 January, 1955	\$1.50	\$2.25	\$4.50
Vol. MTT-3, No. 4 July, 1955	\$1.60	\$2.40	\$4.80
Vol. MTT-4, No. 1 January, 1956	\$1.65	\$2.45	\$4.95
Vol. MTT-4, No. 3 July, 1956	\$1.25	\$1.85	\$3.75
Vol. MTT-4, No. 4 October, 1956	\$1.85	\$2.75	\$5.55
Vol. MTT-5, No. 2 April, 1957	\$1.90	\$2.85	\$5.70
Vol. MTT-5, No. 3 July, 1957	\$1.15	\$1.70	\$3.45
Vol. MTT-5, No. 4 October, 1957	\$1.20	\$1.80	\$3.60
Vol. MTT-6, No. 1 January, 1958	\$2.65	\$3.95	\$7.95

* Colleges, Universities, Subscription Agencies, and all Libraries, may purchase at IRE Member rate.

INSTITUTIONAL LISTINGS

The IRE Professional Group on Microwave Theory and Techniques is grateful for the assistance given by the firms listed below, and invites application for Institutional Listing from other firms interested in the Microwave field.

AIRTON, INC., 1101 W. Elizabeth Ave., Linden, N.J.

Designers and Producers of Complete Line of Microwave, Electronic and Aircraft Components.

COLLINS RADIO CO., Cedar Rapids, Iowa

Complete Industrial Microwave, Communication, Navigation and Flight Control Systems

HUGHES AIRCRAFT COMPANY, Culver City, Calif.

Radar Systems, Guided Missiles, Antennas, Radomes, Tubes, Solid State Physics, Computers

MARYLAND ELECTRONIC MANUFACTURING CORPORATION, College Park, Md.

Development and Production of Microwave Antennas and Waveguide Components

MICRODOT, INC., South Pasadena, Calif.

Microminiature Coaxial Connectors, Cables, and Assemblies

MICROWAVE DEVELOPMENT LABS., INC., 92 Broad St., Babson Park 57, Mass.

Design, Development & Production of Waveguide Components & Complete RF Assemblies

MICROWAVE TUBE LAB., SYLVANIA ELECTRIC PRODUCTS, INC., 500 Evelyn Ave., Mountain View, Calif.

Traveling-Wave Tubes, Backward-Wave Oscillators (Helix and Oscillators), Klystrons

WEINSCHL ENGINEERING CO., INC., Kensington, Md.

Attenuation Standards, Coaxial Attenuators and Insertion Loss Test Sets

WHEELER LABORATORIES, INC., 122 Cutter Mill Road, Great Neck, N. Y.

Consulting Services, Research & Development, Microwave Antennas & Waveguide Components

The charge for an Institutional Listing is \$50.00 per issue or \$140.00 for four consecutive issues. Applications for Institutional Listings and checks (made out to the Institute of Radio Engineers) should be sent to Mr. L. G. Cumming, Technical Secretary, Institute of Radio Engineers, 1 East 79th Street, New York 21, N. Y.

NOTICE TO ADVERTISERS

Effective immediately the IRE TRANSACTIONS ON MICROWAVE THEORY AND TECHNIQUES will accept display advertising. For full details contact Tore N. Anderson, Advertising Editor, PGM TT TRANSACTIONS, 1539 Deer Path, Mountainside, N.J.



New MICROWAVE INSTRUMENTATION

FILED IN STACKS

BROADBAND SPECTRUM ANALYZER

Type L701A: 950 to 2000 Mc/s (Fund.)
Type S701A: 1900 to 4000 Mc/s (Fund.)

Harmonic Operation: to 16,000 Mc/s

Swept IF: 7 Kc and 50 Kc

Sweep Width: 50 Mc

RF Attenuator: 100 db Range

Video Markers



701

UNIVERSAL KLYSTRON POWER SUPPLY

Beam: 200 to 2000 V, 125 ma max.
1800 to 3600 V, 100 ma or 250 W max.

Reflector: 0 to 1000 V

Control Grid: -300 to 0 to +150 V, 5 ma max.

Regulation: 0.03%

Ripple: 3 mv max.

Internal Reflector Modulation:
Square Wave, Pulse, Sawtooth,
Sine Wave



815

UNIVERSAL MICROWAVE POWER SUPPLY

Helix or Beam: 0 to 1800 V, 125 ma max.
1700 to 3500 V, 100 ma or 250 W max.

Collector: 0 to 300 V, 100 ma max.

Anode: 0 to 600 V, 60 ma max.

G-1: 0 to 300 V, 5 ma max.

G-2 or Reflector: 0 to \pm 1200, 1 ma max.

G-3: 0 to \pm 750, 1 ma max.

G-4: 0 to \pm 500, 1 ma max.

Regulation: 0.03%. Ripple: 3 mv max.

Heater: 0 to 15 V D.C., Regulated.

Internal G-1 or G-2 Modulation: Sine Wave,
Square Wave, Pulse, Sawtooth.



817

UNIVERSAL RATIO METER

(COMBINED RATIO METER AND STANDING WAVE AMPLIFIER)

RATIO METER—1000 cps operation

VSWR Ranges: 1.02 to 1.22, 1.20 to ∞

Reflection Coefficient: .01 to .1, .1 to 1.0

Other Scales: db, Slotted Line VSWR

Standing Wave Amplifier—1000 cps operation

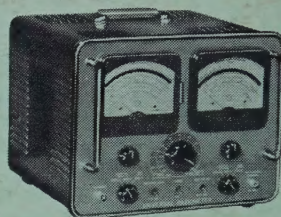
Range: 70 db in six 10 db steps

Noise Level: .03 mv

Scales: VSWR, db, Expanded VSWR

Bolometer Bias: 4.5 and 8.75 ma

Input Impedance: 200 ohms or 200 K ohms



811

KLYSTRON POWER SUPPLY

Beam: 300 to 1000 V, 85 ma max.

Reflector: 0 to 900 V, 20 μ a max.

Control Grid: -300 to 0 to +150 V, 5 ma max.

Regulation: 1%

Ripple: 7 mv max.

Internal Reflector Modulation:
Square Wave, Pulse, Sawtooth



819

Precision Microwave Equipment

F-R MACHINE WORKS, Inc.
WOODSIDE 77, N. Y. ASTORIA 8-2800

TEST
EQUIPMENT

RADAR
COMPONENTS

HIGH-POWER
MODULATORS

Write today for complete



REPRESENT

FLORIDA
GEORGIA
ALABAMA

J. NEAL CO.
1941 S.W. 33rd
MIAMI, FLA.

WASHINGTON
OREGON

AHMCO
BOEING FIELD
KING CITY AIR
SEATTLE 8, W.

WASHINGTON

A & M ASSOC
1145 19th ST
WASHINGTON,

COLORADO
NEW MEXICO
UTAH
WYOMING

HYTRONIC
MEASUREMENT
1295 S. BANNISTER
DENVER 23, CO

ILLINOIS
INDIANA
WISCONSIN

KADELL SALES CO.
5875 N. LINCOLN
CHICAGO 45, IL

CALIFORNIA
ARIZONA

VAN GROOS CO.
21051 COSTANZA
WOODLAND HILLS

EXPORT

SZUCS INT'L CO.
50 BROAD ST.
NEW YORK 4,